# Superconducting magnetic energy storage with second-generation high temperature superconductors

Jérémie Ciceron

Communauté
UNIVERSITÉ Grenoble Alpes

# THÈSE

Pour obtenir le grade de

**DOCTEUR DE LA COMMUNAUTE UNIVERSITE GRENOBLE ALPES**

Spécialité : **Génie électrique**

Arrêté ministériel : 25 mai 2016

Présentée par

**Jérémie CICERON**

Thèse dirigée par **Pascal TIXADOR**, et
codirigée par **Arnaud BADEL**

préparée au sein du **Laboratoire G2ELab, INP Grenoble**
dans **l'École Doctorale Électrotechnique, Électronique, Automatique et Traitement du Signal**

# High energy density Superconducting Magnetic Energy Storage with second generation high temperature superconductors

Thèse soutenue publiquement le **20 mars 2019**,
devant le jury composé de :

**M. Satoshi Awaji**
Professeur à l'université du Tohoku, Rapporteur
**M. Jean-Pascal Cambronne**
Professeur à l'université Paul Sabatier Toulouse III, Président
**M. Michel AMIET**
Ingénieur, expert indépendant DGA, Examinateur
**M. Pierre VEDRINE**
Docteur, Responsable du DACM, CEA Saclay, Examinateur
**M. Pascal TIXADOR**
Professeur à Grenoble-INP, Directeur de thèse
**M. Arnaud BADEL**
Chargé de recherche CNRS, Co-encadrant
**M. Frédérick FOREST**
Ingénieur, Directeur technique SigmaPhi, Invité

# Acknoledgments

Je tiens à remercier Arnaud Badel, pour ses conseils, ses idées et son soutien tout au long de cette thèse.
Je remercie Pascal Tixador pour avoir fait émerger le projet BOSSE et rendu cette thèse possible, pour l'encadrement de mon travail, pour avoir partagé (une partie de) ses compétences techniques avec moi et pour son soutien.
Je remercie l'ensemble des membres du jury pour l'intérêt qu'il porte à mes travaux.

Je remercie l'ensemble des personnes qui ont travaillé sur le projet BOSSE, chez nos partenaires sur ce projet. En particulier Michel Amiet et Mathieu Bervas de la Direction Générale de l'Armement, Frédérick Forest, Raphaël Pasquet, Emmanuel Voisin et Christophe Lecrenn de la société SigmaPhi, Markus Schneider, Volker Brommer et Martin ROCH de l'Institut Saint-Louis.

Je remercie les membres d'universités et de laboratoires qui nous ont accueillis dans leurs locaux, ont mis à notre disposition leur matériel, ont partagé avec nous leurs compétences et ont consacré du temps à notre projet : Carmine Senatore et Christian Barth de l'Université de Genève et Franck Borgnolutti du CEA Saclay. Je remercie tout particulièrement Satoshi Awaji de l'Université du Tohoku pour nous avoir accueilli et donné accès aux installations du HFLSM pendant toute une semaine. Je remercie également Thibault Lecrevisse du CEA Saclay pour ses conseils et les discussions techniques que nous avons eues.

Je remercie tous les doctorants de mon équipe à l'Institut Néel avec qui j'ai eu l'occasion de travailler et d'échanger des points de vue et des compétences : Tara Benkel, John Himbele, Guillaume Escamez, Blandine Rozier et en particulier André-Julien Vialle. Je remercie également Guillaume Coché, qui a travaillé sur le projet BOSSE dans le cadre de son stage dans notre équipe.

Je remercie chaleureusement les chercheurs du LNCMI Grenoble avec qui nous avons travaillé et échangé, et pour leur disponibilité lorsque nous avons travaillé sur les sites d'aimants du LNCMI Grenoble : Benjamin Vincent, François Debray et en particulier Xavier Chaud.

Enfin, je remercie l'ensemble du personnel de l'Institut Néel et du LNCMI Grenoble, qui ont permis de faire avancer le projet BOSSE. En particulier parmis eux : André Sulpice, Thibaut Gandit, Julien Marpaud, Pierre-Alexandre Bertrand, Cyril Bruyère, Mathilde Heigeas, Loïc Jean, Robert Pankow, Gilles Pont, Gregory Garde, Ghenadie Novitchi, Abdellali Hadj-Azzem, Jung bin Song, Philippe Jeantet, Emmanuel Roy et Guillaume Donnier-Valentin.

# Table of contents

# Introduction

SMES (Superconducting Magnetic Energy Storage) is an interesting solution for high power pulsed source. Since 2004 a SMES program funded by the DGA (French Delegation on Armament) has been started at the Grenoble CNRS. An 800 kJ device made of first generation HTS tapes and conduction cooled was rather successfully tested in 2008 and proved the feasibility of a HTS coil with user-friendly cooling. This work is now continued in the context of a new project, called BOSSE for BObine Supraconductrice pour le Stockage d'Energie (Superconducting Coil for Energy Storage). This project is still funded by the DGA and is a cooperation between the Grenoble CNRS, the SigmaPhi Company and the Saint Louis Institute (ISL). The BOSSE project has the objective to develop two devices. The first one is a demonstrator of the $S^3EL$ (Superconducting Self-Supplied Electromagnetic Launcher) concept, but this topic is not addressed in this work. The second objective is to develop a new SMES in the MJ range, focusing on the energy density and compactness. The objective with this SMES is to reach a specific energy of 20kJ/kg for the winding, i.e. 50 % higher than the current world record for a superconducting winding. This performance will be achieved by taking advantage of new possibilities offered by impressive performances of second generation HTS tapes in liquid helium.

This manuscript aims to describe what has been achieved during this PhD in the frame of the BOSSE project, but also to offer a global reflection and guidelines about SMES design.

In the first chapter are presented the prerequisites that are necessary to design a SMES and especially the high specific energy SMES of the BOSSE project. So in this part is given information about the current transport properties of superconductors, generalities about SMES (history, applications, topologies) and superconducting windings (stability, protection, cooling, losses) and mechanics of superconducting windings.

In the second chapter, reflections and solutions about the optimization of a SMES winding are proposed. The design of the SMES of the BOSSE project, partially based on this approach, is presented in detail. Elements about the manufacturing process are also given.

The third chapter is dedicated to the presentation of experimental work. Some modular elements (pancakes of REBCO tapes) of the SMES have been manufactured and tested in self-field and under background magnetic field. During these tests, transitions from superconducting state to normal state have been detected. These early detections, based on voltage measurements, have prevented the pancakes to be damaged when transitions occurred, even at very high current density (980 $A/mm^2$ in the bare conductor). The measurement method is presented, as well as the results of the tests and their interpretation. The performances achieved with the prototype pancakes show that the specifications of the high specific energy SMES can be reached.

# Chapter 1: Introduction to superconducting windings and Superconducting Magnetic Energy Storage (SMES)

# 1. General introduction to superconductivity and superconductors

## 1.1. Superconductivity

### 1.1.1. Critical surface:

Superconductivity, from the electrical point of view, is a phenomenon in which a material exhibits zero electrical resistivity. Until now, superconductivity has been observed only at very low temperature (see Fig. 2) or under extremely high pressure [DETK15]. It has been discovered by Heike Kamerlingh Onnes in 1911 who was measuring the electrical resistivity of mercury at low temperatures.

It is known from the general public that the superconducting state is related to the temperature. But it is also related to the value of the magnetic induction B, the amount of current passing in the material and to the mechanical strain. Most of the time in a first approximation, the strain effect is neglected. Thus, the superconducting state of a material used in electrical engineering applications is generally described by the so-called "critical surface", i.e. the surface describing the critical current $I_C$ depending on the temperature T and the value of the B field. The material shifts from a superconducting non dissipative state to a dissipative state when the current is exceeding $I_C$, which value depends on B and T. The critical temperature, $T_C$, is the maximum temperature at which the superconducting state can be maintained, being implied that the B field and $I_C$ are null at this point. The dissipative state is usually not stable thermally so that overstepping the critical surface leads rapidly to a transition to the normal resistive state.

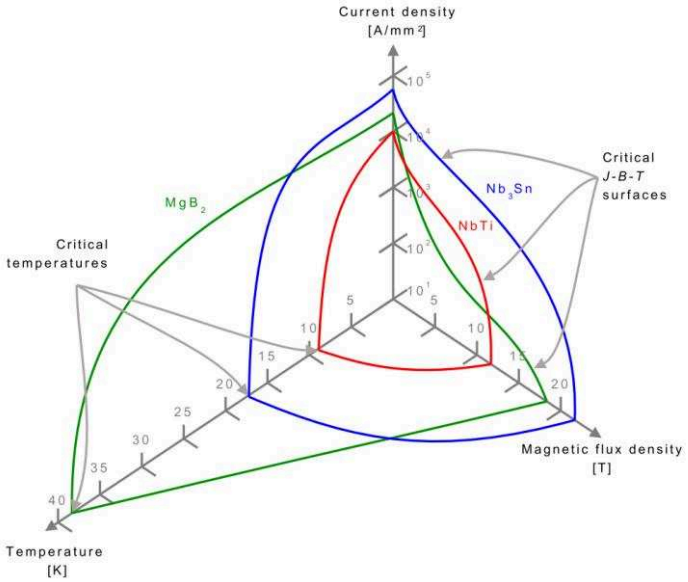


*Figure 1: Critical surfaces of superconductors used in electrical engineering applications [Esca16].*

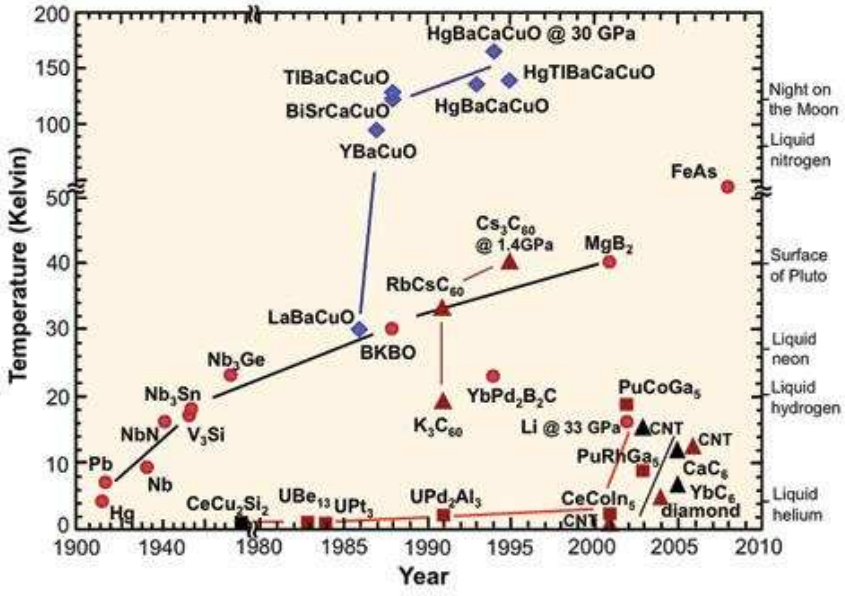


*Figure 2: Critical temperature of discovered superconductors over the years [Esca16].*

### 1.1.2. Superconductors

Superconductors, i.e. materials which exhibit superconductivity under specific conditions, are numerous and are classified in type I or type II depending on their behaviour [Tixa95]. Practically, almost only type II superconductors are used in electrical engineering applications. As an exception, we can cite the superconducting radio-frequency cavities for particle accelerators which are plated with pure niobium. Type I superconductors are also used in superconducting electronics and superconducting detectors. But as this is far beyond the scope of this PhD, only type II superconducting materials will be presented in this work.

Type II Superconductors are further classified depending on their critical temperature. They are generally classified as Low Temperature Superconductors (LTS) or High Temperature Superconductors (HTS). LTS have critical temperature (CT) below 30 K. Their physics is well understood and is described by the BCS (Bardeen Cooper Schrieffer) theory [BaCS57]. Industrially used LTS are Niobium Titanium (NbTi) and Niobium Tin ($Nb_3Sn$).

$MgB_2$ is sometimes classified as LTS because its physical behaviour is explained by the BCS theory [ViVS07] but is sometimes classified as HTS because its critical temperature is 39 K. It is also sometimes defined as an Intermediate Critical Temperature Superconductor [Mgb215].

HTS have been discovered in the 80's. A superconducting phase transition has been measured at 30 K in LaBaCuO in 1986 then at 90 K in YBaCuO in 1987. These discoveries had led to a new rise of interest in superconducting electrotechnics and was giving hope to discover materials which would be superconducting at room temperature and pressure. This hope has not been fulfilled until now and obtaining conductors using HTS suitable for electrotechnics proved to be very challenging. This explains the long delay between the discovery of the superconducting properties of cuprates and the commercialisation of conductors incorporating cuprate-based superconductors. Currently, 2 families of HTS conductors are commercially available. On one side BSCCO conductors incorporating Bismuth and cuprates ($Bi_2Sr_2Ca_1Cu_2O_X$ or $B_2iSr_2Ca_2Cu_3O_X$), which are referred as "1$^{st}$ generation HTS conductors". On the other side, REBCO conductors (Rare-Earth$_1$Ba$_2$Cu$_3$O$_X$), based on the association of rare-earth atoms with barium and cuprates, referred as "2$^{nd}$ generation HTS conductors". HTS conductors and especially REBCO are bringing the hope to widen the range of applications of superconducting systems, as they not only display higher $T_C$ but also have much broader critical surface, with large critical

currents up to very high fields (See Fig. 9). Worldwide production of these conductors is currently rising, going with the expectation to use HTS conductors into industrial applications. It is a noticeable fact that the physics of the superconductivity in HTS is currently not fully understood and that the hope to discover superconductors with higher performances or easier to implement in applications is still very high.

### 1.1.3. Transition

When the current in a conductor is exceeding $I_C$, an electric field is appearing in a very sudden way and energy is dissipated. Nevertheless, the slope of this transition is not infinitely sharp. Recording the electric field versus current, the electric field sharply increases at one point and the electric field can be then described by a "power law":

$$E = E_C \left(\frac{|I|}{I_C}\right)^n \left(\frac{I}{|I|}\right) \quad (1)$$

$E_C$ and $I_C$ are called the critical field and current. Most of the time and if not specified, $E_C$ is chosen equal to 1 µV/cm (international standard for HTS). This value is an arbitrary convention, but comes from experimental practical aspects [Esca16]. The power exponent "n" is the resistive transition index. From equation 1, we can now refine the definition of $I_C$: it is the value of current at which the conductor exhibits an electric field of 1 µV/cm. The n value is depending mainly on the material (including doping) but also on the temperature and magnetic field and at the macroscopic scale about the homogeneity of the sample. For example, n values of LTS materials such as NbTi or $Nb_3Sn$ at 4.2 K are around 100 while REBCO conductors in same conditions have generally n values around 30.

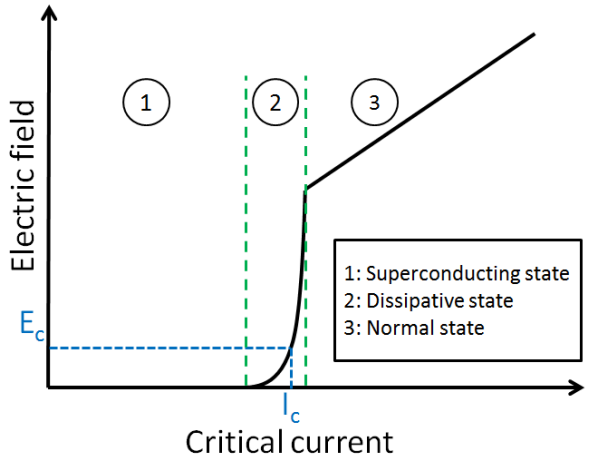


*Figure 3: Electrical field depending on the current in a superconductor following a power law until the normal resistive state [Esca16].*

Two remarks must be emphasized:

- The power law (equation 1) is generally valid only at the vicinity of $I_C$. When I is exceeding $I_C$, the experimental curve E(I) starts to get away from the power law. This can be due to two different things. First as the superconductor starts to dissipate energy, the temperature of the sample is rising and the value of $I_C$ is changing. Moreover part of the current may go to resistive parts of the conductor. For current much lower than $I_C$ the power may be no more valid as well depending on the temperature.

- Experimentally, only the voltage is measured. The electric field, and therefore $I_C$, are deduced from the length of the conductor. In the case of REBCO tapes, $I_C$ and n value may change along the length of the conductor [CCKP15], making the power law somewhat inappropriate to fit the E(I) curve of a long length of conductor (see part I-1.3.4)

To determine the value of $I_C$ and n with a good precision is of major importance in order to calculate correctly the margins and the AC losses (see I-3.4.2) in a superconducting winding. An alternative to the power law called "percolation law" is sometimes used [ESBM16][DAMD01], especially in order to calculate the AC losses of superconducting conductors.

## 1.2. Superconductors for electrical engineering

Materials that exhibits Type II superconducting properties are numerous and very varied from the chemical point of view. For electrical engineering applications they have to exhibit a large critical surface: a high critical current density at relatively elevated temperature and/or under high magnetic field. Their production cost and their environmental footprint need also to be kept acceptable. Finally, only a very limited number of superconductors are produced industrially and commercially available. In this chapter, these superconductors will be briefly described.

### 1.2.1. Niobium Titanium

Niobium Titanium (NbTi) is the most common superconductor today. It stands for 80 % of the superconductors market in the world (6 billion dollars in 2017, about 3000 ton/y). It is a cubic centred metallic alloy, easy to produce and rather inexpensive. For production of NbTi wire, some NbTi billets are put in copper or copper alloy stabilizer (see part I-3.1.1) and everything is drawn together (extrusion), which is a classical process in metallurgy. By this mean, wires which are kilometres long with micrometrical filaments in a stabilizer matrix (copper or copper alloy) are obtained. Furthermore, NbTi has good mechanical properties. Its $T_C$ is 9.5 K and it is used in magnets which can provide B field until 10 T at 4.2 K and 12 T at 1.8 K. It is therefore classified as a LTS and is often used at 4.2 K (liquid helium at 1 bar) or 1.8 K (superfluid helium). NbTi is used for example in MRI and NMR magnets and has been used for the dipoles of the Tevatron and the LHC.

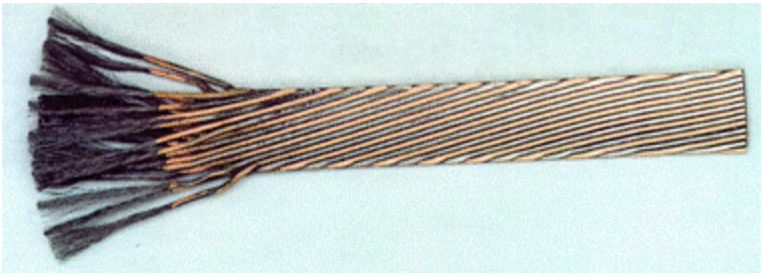

*Figure 4: A piece of Rutherford cable made of NbTi wires. On the left, the copper matrix has been removed by chemical attack and the NbTi strands are visible [Himb16].*

### 1.2.2. Niobium-Tin

Niobium-Tin ($Nb_3Sn$) is also a LTS but can be used to generate higher B field. Its $T_C$ is 18.3 K. As the NbTi, it has a simple crystallographic structure (A15 phase).

In order to achieve the manufacturing of coils with $Nb_3Sn$, two processes are possible. In both cases at the beginning the conductor contains unreacted precursors (Nb and Sn), but no $Nb_3Sn$. The conductor is produced by classical extrusion method, as NbTi. There are then two possibilities. Either the conductor is first submitted to a heat treatment to react the $Nb_3Sn$ precursors and to form $Nb_3Sn$

filaments, then the conductor is wound to make a coil. In this case, the process is called “react and wind”. The other possibility, which is used most often, is to wind the coil with the conductor first, then to heat the coil in order to produce the $Nb_3Sn$ filaments. This process is called “wind and react”. The react and wind process is difficult because the reacted $Nb_3Sn$ is very brittle. The react and wind process is also difficult because the performance of the coil depends a lot on the heat treatment quality and homogeneity, and because the conductor is shrinking during the reaction process. This shrinking requires to be compensated in advance by pre-stress in order to avoid loosening of the winding during the heat treatment.

Coils made of $Nb_3Sn$ are more expansive than ones made of NbTi. $Nb_3Sn$ is used to make high field magnets (until 23.5 T). It will be used for the central solenoid and toroidal coils of the ITER tokamak. $Nb_3Sn$ magnets are developed in the frame of the LHC “high-lumi” project.

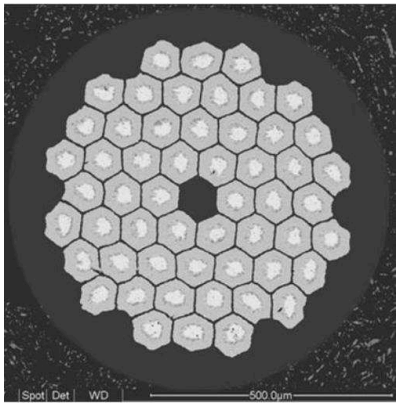


*Figure 5: Cross section view of a $Nb_3Sn$ wire [Hype00]*

### 1.2.3. $MgB_2$

$MgB_2$ (magnesium diboride) superconducting properties have been discovered quite recently, in 2001. It is more sensitive to magnetic field than $Nb_3Sn$ but it has a higher critical temperature, around 39 K (see Fig. 1). It is possible today to buy kilometre length of $MgB_2$ conductor, which are quite inexpensive. They are produced by PIT (Powder In Tube) process. In this process, some powder of $MgB_2$ or its precursors (Mg and B) is filled in metallic tubes, which are extruded then assembled together and re-extruded. The wire is reacted afterwards to form the superconducting $MgB_2$ filaments.

The performance of $MgB_2$ in term of current density is in constant progression. Similarly to $Nb_3Sn$, $MgB_2$ coils can be made by wind and react process or react and wind process. Using the “react and wind” process, some limitations in the radius of curvature are appearing [Pasq15]. Another drawback of the $MgB_2$, due to the PIT process, is that the filaments of superconductor are larger than filaments of NbTi or $Nb_3Sn$, which can lead to higher AC losses (see part I-3.4.2.3).

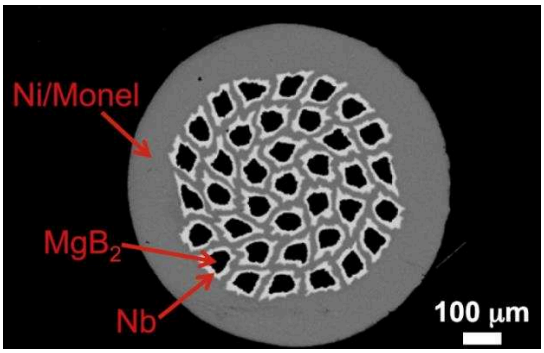


*Figure 6: Cross-section view of a MgB2 Wire [SBBB15]*

### 1.2.4. BSCCO

BSSCO (Bismuth Strontium Calcium copper oxide), which has to be pronounced “Bisco”, is the first HTS material, which has been implemented in a conductor, in 1990. For that reason, BSCCO conductors are generally called “first generation HTS conductors”. There is actually 2 different compounds in the BSSCO family which are used in commercialized conductors: BSSCO-2212 with formula $Bi_2Sr_2CaCu_2O_x$ and BSSCO- 2223 with formula $Bi_2Sr_2Ca_2Cu_3O_x$. The $T_C$ of BSSCO-2212 is 85 K and the $T_C$ of BSSCO-2223 is 110 K. The BSCCO-2212 conductors are either flat tapes or round wires. BSSCO-2223 is only elaborated under the form of flat tapes. The tapes have anisotropic properties: $I_C$ is depending on the B field orientation towards the tape surface. The BSCCO-2212 round wires have the advantage of isotropic properties and can be used to make cables with transposed wires (Rutherford cable for example, see part I-3.5), but with lower overall performances compared to tapes. BSCCO-2212 have made a lot of progresses due to the over pressure process [LJTK14].

The BSSCO conductors are produced by the PIT process. The matrix of the conductor is made of silver, which has 2 disadvantages:

- The silver is weak mechanically, which requires the conductor to be reinforced for applications with significant stress like high field magnets.
- Silver is expensive, which is limiting the use of BSSCO tapes in electrical engineering applications.

*Figure 7: Cross-section view of a BSCCO-2212 wire [BLTT11]*

Compared to REBCO conductors, BSSCO conductors have the advantage to be available in kilometric lengths, to be available in round wires and can be impregnated with epoxy resin. They are still in development, especially for very high field applications [JFAM16]. BSCCO tapes have been used for the first SMES developed at Grenoble.

### 1.2.5. REBCO

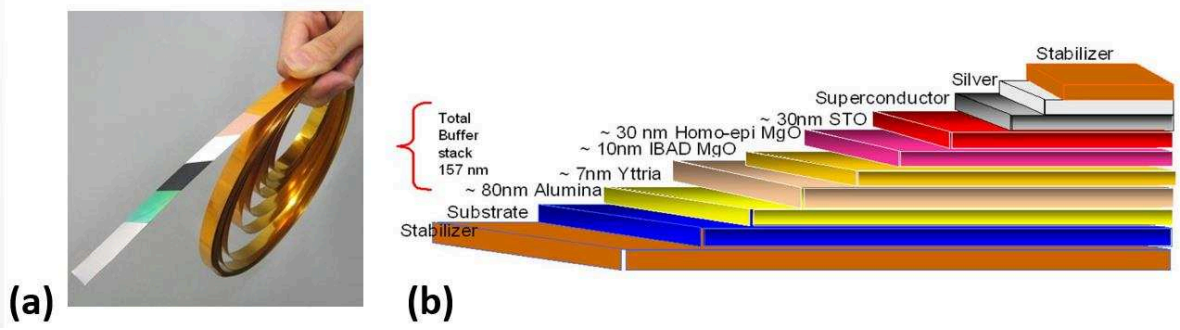


*Figure 8: (a) A REBCO tape from Fujikura® [Fuji00]. (b) Architecture of a REBCO tape from Superpower (not to scale) [MbSc08].*

REBCO (Rare Earth Barium Copper Oxide) conductors are also called 2nd generation HTS conductors. They are part of the cuprates family, as BSSCO. They are ceramics, organised in a 2D crystallographic structure. The "Rare Earth" element of the structure is either Yttrium or Gadolinium in commercial products. Yttrium being the first to be used, YBaCuO, YBCO or Y-123 are often used as a generic term for that family.

REBCO conductors can exhibit high critical current densities even under high field (see Fig. 9), which makes them very interesting to make high field superconducting magnets [SALT14]. The $T_C$ of YBaCuO is 93 K but show an irreversibility line much more favourable compared to BSCCO. They are elaborated as fine tapes. The basic idea is to deposit the SC layer on a textured layer. Two main routes are possible. The first one uses a Nickel alloy substrate which is textured by mechanical and thermal treatments. A buffer layer is however required to avoid reaction between the superconductor and the Ni. This route is known as RABiTS™ (Rolling Assisted Biaxially Textured Substrates). The second route (IBAD, ISD) uses a non-textured substrate, often Hastelloy® on which a textured layer is deposited (YSZ, MgO). The SC layer is then deposited either directly or through buffer layers. The layer of REBCO, which is generally 1 or 2 µm thick, is grown by epitaxy. It is then plated with silver to protect the REBCO layer and make possible to inject current. The Ag layer facilitates the oxidation. It may also be additionally copper-plated either by rolling or by electroplating for stabilization purpose (see part I-3.1).

Currently, REBCO conductors are produced by a tenth of companies in the world [Amsc00] [Bruk00] [Fuji00] [Suna00] [Supe00a] [Supe00b] [Thev00]. Their manufacturing process may differ, but they are mostly using some PVD (Physical Vapour Deposition) techniques. The price of REBCO tapes is relatively high and the lengths of conductors are short. The lengths of conductor which are sold are generally in the range of 100 m to 200 m and their price is in the order of 40 €/m or 30 €/m for a 4 mm wide tape in 2017.

Other drawbacks of REBCO tapes are the very low peel strength of the superconducting layer, the lack of performance homogeneity along the conductor and the lack of performance reproducibility. Properties of REBCO tapes will be detailed in part I-1.3). Despite all of these drawbacks, performances of REBCO tapes are extremely interesting and are still progressing. Their price is currently decreasing nearly by a factor 2 every 2 years and the worldwide production is growing.

Some new processes are under development for the growth of the REBCO layer, based on chemical method [ObPu14]. Even if the properties of the conductors obtained with these processes are not yet as good as the ones obtained with PVD, they are in quick progress. Above all, this deposition method has the potential to drastically reduce the manufacturing cost of REBCO conductors.

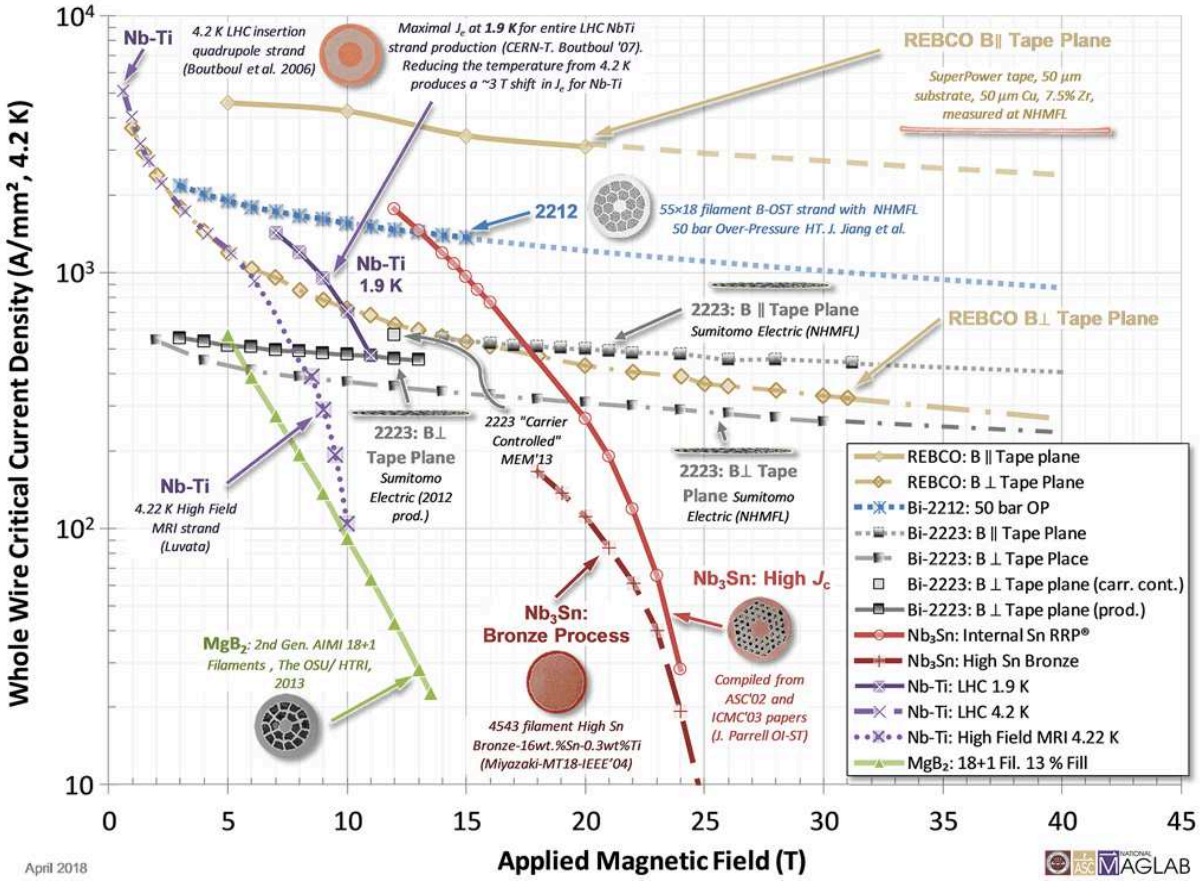


*Figure 9: World record critical current densities of several superconductors. If not specified, the data are given for 4.2 K [Nhmf00].*

### 1.2.6. Ferropnictides

Ferropnictides, also called Iron-based superconductors, is a family of HTS which is an association of iron and pnictogens. Their superconducting properties have been discovered quite recently, in 2006. Even if their critical field and temperature are lower that one's of REBCO or BSSCO, it seems that it will be easier and less expensive to produce conductors based on ferropnictides than 1st and 2nd generation HTS conductors. That is why they currently rise a very high interest. Already some lengths of ferropnictides coated conductors in the 100 m range can be produced [HYHM17].

| | NbTi | $Nb_3Sn$ | $MgB_2$ | YBaCuO | Bi-2223 | Bi-2212 | SmFeAsO |
|---|---|---|---|---|---|---|---|
| $T_C$ (K) | 9.5 | 18 | 39 | 93 | 110 | 85 | 55 |

*Table 1: Critical temperature of different superconductors.*

## 1.3. Properties of REBCO tapes

REBCO Conductors are quite different from other conductors because of their manufacturing process. Until now it has been only possible to produce thin layers of REBCO on flat tapes, attempts to create round wires of REBCO has not been successfully transposed to large scale production. The specificity of the production process of the REBCO leads to specific properties of REBCO compared to other superconductors. Properties and specificities of REBCO conductor are presented in this part.

### 1.3.1. Current Transport properties

As we have already said, REBCO layers are grown on flat tapes. The 2D cuprates plans are parallel to the tape (except for ISD route), which explains the strong anisotropy of the transport current properties: the critical current density depends on the orientation of the B field toward the tape

surface. In a (a,b,c) coordinate system, the surface of the tape is generally referred as the (a,b) plan and the axis perpendicular to the tape surface is referred as the c-axis. In REBCO tapes, the critical current is higher if the applied B field direction is in the (a,b) plan than in the c-axis direction. The ratio of $I_C$ between the case in which B is in the (a,b) plan (parallel configuration) or in the c-axis direction (transverse configuration) is depending on several parameters: temperature, B field value, manufacturing technique and doping. Some manufacturers are doping the REBCO layer for example with Zirconium nanotubes in order to "flatten" the anisotropy. The effect of the doping is to reduce the $I_C$ in parallel field condition but to increase the $I_C$ in transverse field condition.

$I_C$ can be measured in two different ways: either thanks to inductive probes like in the TAPESTAR™ device [Thev00], or by transport current (4 wires method). Quality control of the tapes is generally performed by manufacturers thanks to inductive probes as the measurement can be made continuously. Measurement of $I_C(B,\Theta)$ at low temperature requires high fields and is done by 4 wires method, which is more precise and provides the n-value of the power law of the sample.

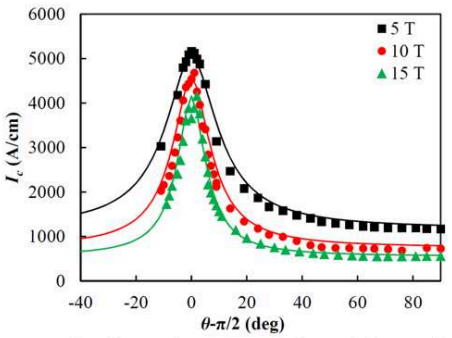


**Angular dependence towards B of the Ic** of Fujikura REBCO coated conductors at 4.2 K (Data by Tohoku Univ., fit by J. Fleiter, CERN)

(a)

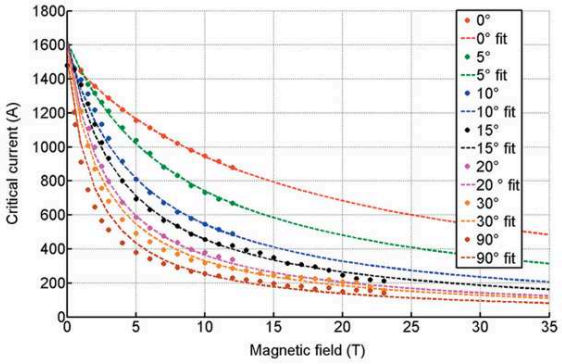


(b) Critical current of a 4 mm wide SuperOx REBCO tape depending on B and Θ. The fit (dotted lines) is based on the Kim's model.

*Figure 10: $I_C(B,\Theta)$ properties of REBCO tapes of 2 different manufacturers. Θ is the angle between B and the surface of the tape [FlBa00] [BMCB17].*

### 1.3.2. Lift factor

REBCO conductors are generally used in two ranges of applications: applications at high temperature (65 K to 77 K) with low B fields or applications with high fields at low temperature (4.2 K). Most of data about REBCO tapes performances is therefore available either at 4.2K or between 65 K and 77 K. For this reason, REBCO conductor manufacturers and characterization laboratories are often describing the tape performance at 4.2 thanks to the concept of lift factor. The lift factor is the ratio between the critical current at 4.2 K and the critical current at 77 K. It varies with the value of the applied field and its orientation. Two facts have to be highlighted:

- The manufacturers which obtain the best current transport properties at 77 K are not necessarily the same ones which obtain the best current transport properties at 4.2 K. Manufacturers are generally optimizing their process in order to improve the current transport property either at 77 K or 4.2 K but not both. The flux pinning phenomena depend on the temperature.
- During the manufacturing process, the feedback control of the process is based on $I_C$ inductive measurement at 77 K without field. The manufacturers are therefore able to guarantee the $I_C$ of a tape at 77K self-field. But they generally do not guarantee the lift factor, or they guarantee rather low values. There is a problem of reproducibility of performance at 4.2 K today. The complete process is difficult to master and strong variations of performance of the conductor at 4.2 K can be observed from a tape to another one from the same manufacturer.

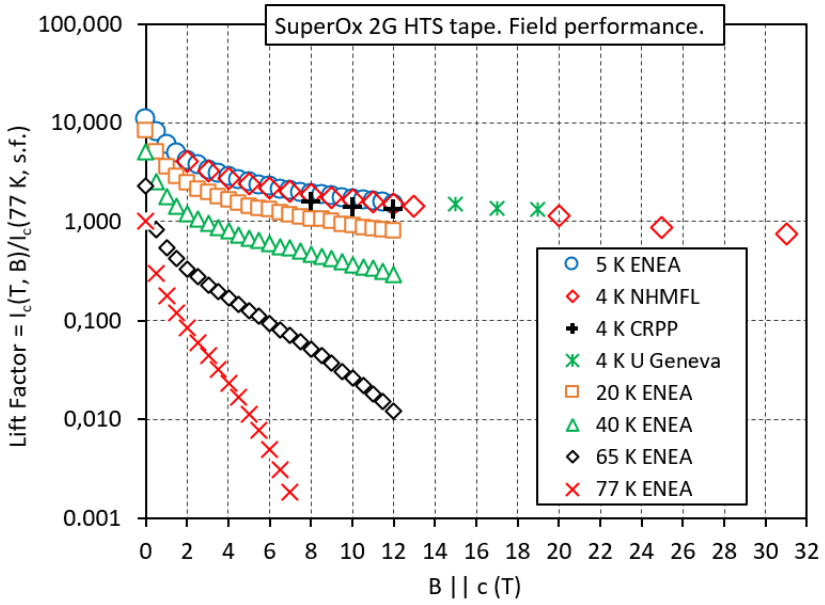


*Figure 11: Lift factors measured by different laboratories of SuperOx® samples [Supe00a]*

### 1.3.3. Critical Surface

Even if most of REBCO tapes characterization is done either at 4.2 K or 77 K, some data about the performance of REBCO tapes at intermediate temperatures is available today. For example, C. Senatore et al. [SBBK16] have led an extensive experimental work to determine the critical surface of REBCO tapes from several manufacturers for temperatures of between 4.2 K and 77 K, an external B field of between 0 T and 19 T and with orientation of the tape towards the B field of 0°, 45° and 90°.

### 1.3.4. Inhomogeneity

Thanks to inductive probe, it is possible to measure $I_C$ all along a piece of conductor. REBCO conductors are known to have $I_C$ variations along the length, generally in the order of 10 % to 20 % of average value. A high $I_C$ value is related to a homogenous crystalline growth of the REBCO layer, which is a difficult task. Control of the process is sometimes lost, which causes greater or lesser degradation of $I_C$. The difficulty to produce long length of conductor in a repetitive way is related to this problem. Systematic measurements of $I_C$ along and across several conductor lengths of different manufacturers have been performed by T. Kiss et al. [HKIK14] [KIHS16] with very fine spatial resolution. From these measurements, they can state that $I_C$ variations is obeying a statistic law, and more precisely a Weibull law, whatever the manufacturer is. One direct consequence is that the longer is the length of conductor, the higher is the probability that a short piece of this conductor will have a low $I_C$, nearly 30 % under what is likely to be measured on a randomly chosen piece of this same conductor. These measurements by T. Kiss et al. have been performed at 77 K without field. The determined statistic law is valid in these conditions. Measurements of inhomogeneity on long length of conductor but with a lower resolution have also been performed at 77 K under a 3 T background field [IKIF17].

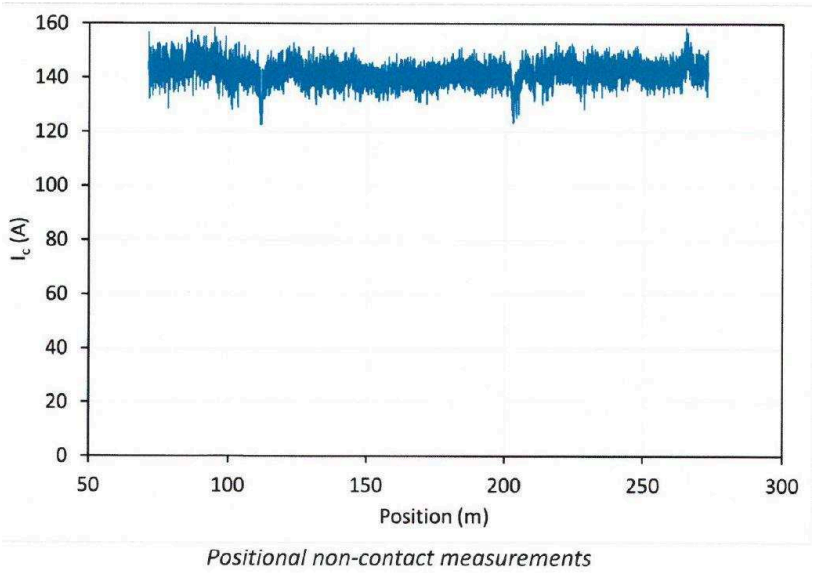


*Figure 12: An example of $I_C$ variations along a 4 mm wide REBCO tape, measured at 77 K thanks to an inductive probe.*

## 1.3.5. Mechanical properties

### 1.3.5.1. Longitudinal stress

Many manufacturers of REBCO tapes use Hastelloy® C-276 (Nickel based super-alloy) as substrate, with the exception of Brucker which is using stainless steel substrate. These materials have a very high yield stress and a very high Young Modulus. REBCO tapes are therefore able to withstand a high longitudinal stress, which makes them particularly suitable for high field magnets [AWOM17] [MBCB15] [MLWV12] [SALT14] [YKCL16]. The copper surrounding the tape has a much lower Young modulus, that is why most of the stress applied to the tape is supported by the Hastelloy® C-276 or stainless steel substrate (see part I-3.6.2).

Longitudinal mechanical properties of REBCO tapes of different manufacturers have been studied by C. Barth et al. [BaMS15]. It has been shown [AVVS06] that the irreversibility of the superconducting properties of the tape can be due to an overshoot of the yield strength of the substrate (Hastelloy® C-276). It is also clear that the delamination of the superconducting layer from the substrate plays a major role. In figure 13, we can see that the superconducting properties of Fujikura and SuperOx tapes are abruptly degraded at strains of 0.45 % and 0.57 %, respectively. This is likely due to a sudden partial delamination of the superconducting layer and is related to the fact that SuperOx® and Fujikura® tape processes at the time of study lead to weaker interface between superconducting layer and buffer layers compared to other manufacturers.

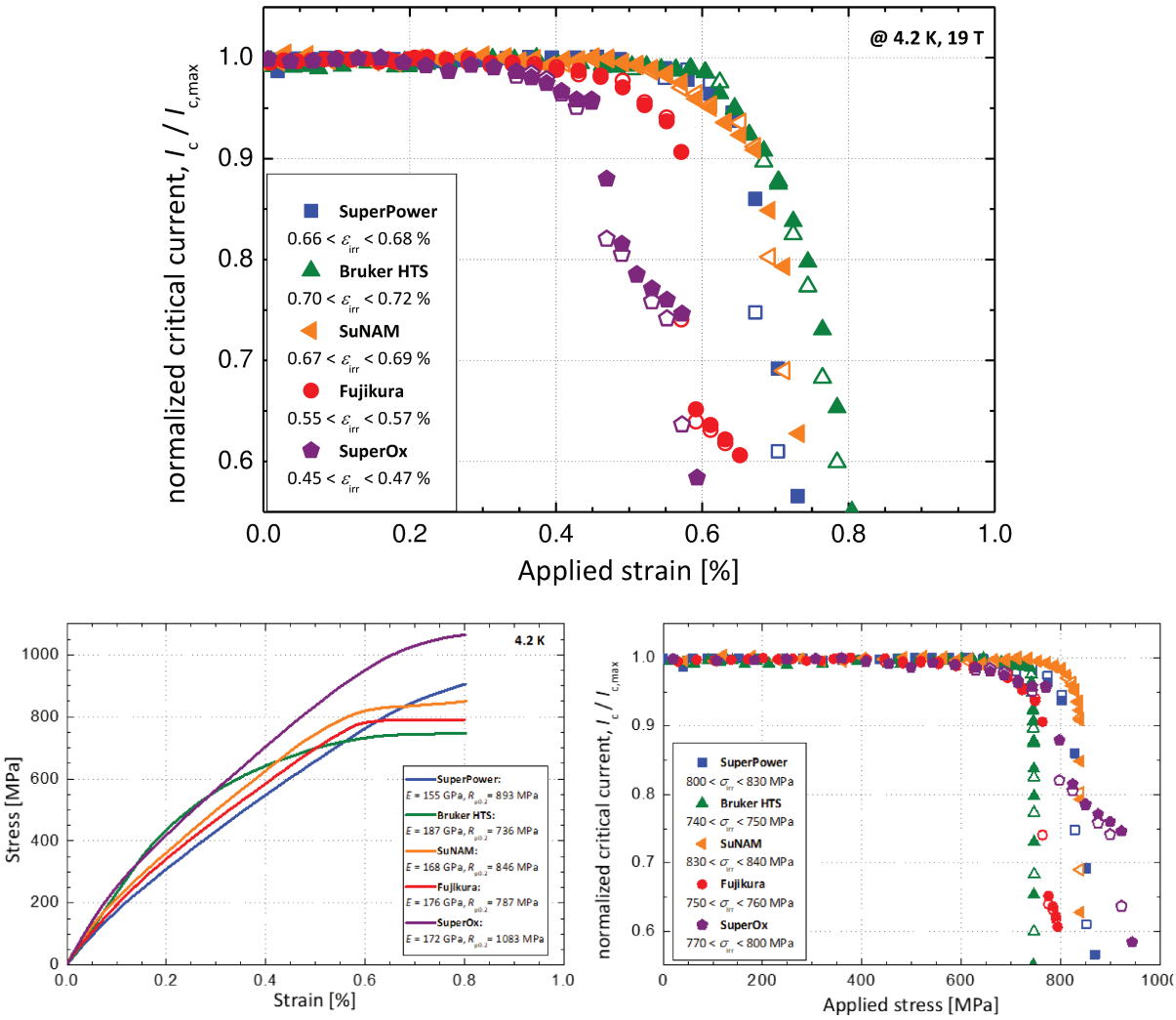


*Figure 13: Performances of REBCO tapes of several manufacturers [BaMS15]. The thicknesses of substrate and copper of the tested samples are presented in Fig. 14*

| *Manufacturer* | *Substrate thickness / Cu thickness* |
|---|---|
| AMSC | 75 µm/ 100 µm |
| BHTS | 100 µm / 100µm |
| FUJIKURA | 75 µm / 75 µm |
| SUNAM | 60 µm / 40 µm |
| SUPEROX | 60 µm/ 20 µm |
| SUPERPOWER | 50 µm / 40 µm |

*Figure 14: Thicknesses of substrate and copper of the samples tested by C. Barth et al. [BaMS15]*

Cycling effects of stress have been studied by several teams [CZCL18] [MbSc08] [SYHS08] on REBCO tapes. On figure 15, we can see that the level of strain applied to the conductor has a strong influence on the number of cycles, which can be applied before the conductor being irreversibly altered.

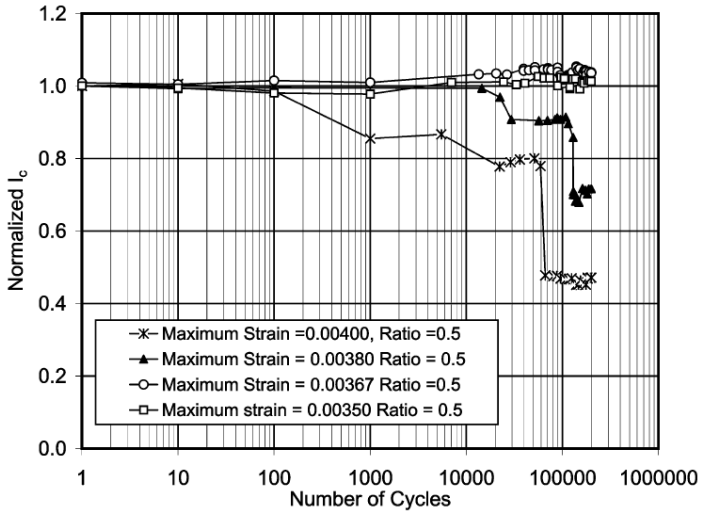


*Figure 15: Effect on the normalized critical current of strain cycles applied to REBCO tapes from SuperPower® [MbSc08].*

#### 1.3.5.2. Transverse stress, peeling and the problem of impregnating REBCO windings

Even if REBCO tapes can withstand high longitudinal tensile stress, they are very sensitive to transverse tensile stress, shear stress, cleavage and peeling, which can easily delaminate the conductor, i.e. to tear off the superconductor layer from its substrate [SALT14]. A consequence is that epoxy impregnation can damage REBCO windings [NZHH12] [SALT14]. This is due to the different thermal contraction between the epoxy resin and the conductor, which creates some tensile stress during the cooling down of the impregnated winding (see part I-4.3). Partial impregnation of REBCO windings has been studied by Takematsu et al. [THTY10] in order to mitigate this problem. Research is ongoing in order to develop an epoxy resin, which is suitable for REBCO windings impregnation [BBWB13] [NKBB18].

## 1.4. Applications of superconductivity and SMES (Superconducting Magnetic Energy Storage)

### 1.4.1. General applications

Superconductivity is used in a very wide range of applications such as detectors [MiMC16], electronics and electrical engineering.

Even within the electrical engineering field, the applications of superconductivity are numerous and very varied. Except for a few cases, such as superconducting radio frequency cavities for particle accelerators [Rode05] or magnetic bearings for levitation with bulk superconductors [CaCa97], most of the electrical engineering applications of superconductivity uses superconducting conductors (wires or tapes).

Today, the existing market for applications made of superconducting conductors relies mainly on MRI magnets, RMN magnets and magnets for scientific research (CERN, ITER, Tore-Supra, Jefferson Labs [BLSF17], etc…). Nevertheless, other applications are explored. Some are even exploited or at the point to be.

For example, some power transport cables have been exploited in Long Island (U.S.A.) [ScAl00] and Essen (Germany) [SMNH14]. Other power transport cables are currently in test or development [Ball13] [Tixa10].

The Japanese project SCMAGLEV (SuperConducting MAGnetic LEVitation) is a train using superconducting electromagnets made of NbTi for electrodynamic sustentation.

Electrical motors are under development for naval propulsion [LéBD18][SnGK05][YIUO17] or aeronautics [MBTL07][MISB18]. Wind generators are also under development [Poli11]. These systems are generally synchronous machines with superconducting field winding.
A high activity is currently led about Resistive Fault Current Limiters (RFCL) [Fast00] [RuZC15] made of 2nd generation HTS conductors since they are likely close of commercial applications.
Another application of superconductivity is the SMES (Superconducting Magnetic Energy Storage). The Superconducting Magnetic Energy Storage is the main topic of the present work. Its principle is detailed in the following part.
It has to be noticed that most of the proven and industrially used applications of superconductivity are using LTS while most of the applications under development are using HTS.

### 1.4.2. Principle of SMES

A SMES (Superconducting Magnetic Energy Storage) consists of a superconducting coil held at temperatures low enough to maintain its superconductivity. If a voltage is applied to the coil, the current in the coil is increasing (see eq. 5). A magnetic field B is generated, i.e. some energy is stored in the superconducting magnet (see eq. 2). When an opposite voltage is applied to the coil, the current is reduced, i.e. the energy is extracted from the coil. If the coil is perfectly short circuited by a superconducting connection, the current is kept indefinitely constant and magnetic energy is stored. Practically, as in the BOSSE project, the resistance of the coil can be nonzero because of the resistance of the current leads or the connections between the coil elements. In this case, the time constant of the SMES is not infinite, but has to be sufficiently long for the dedicated purpose.

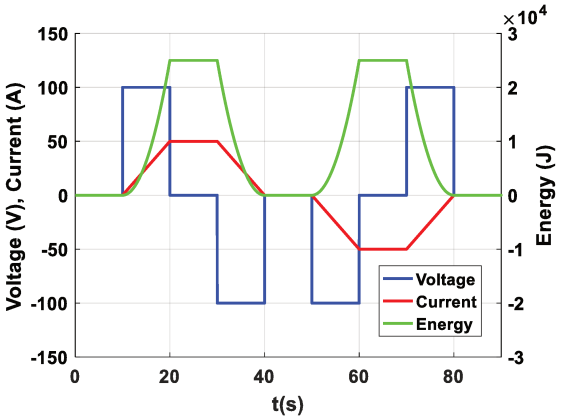


*Figure 16: Charge and discharge, then charge and discharge with reversed current, of a perfect inductance with L=20H.*

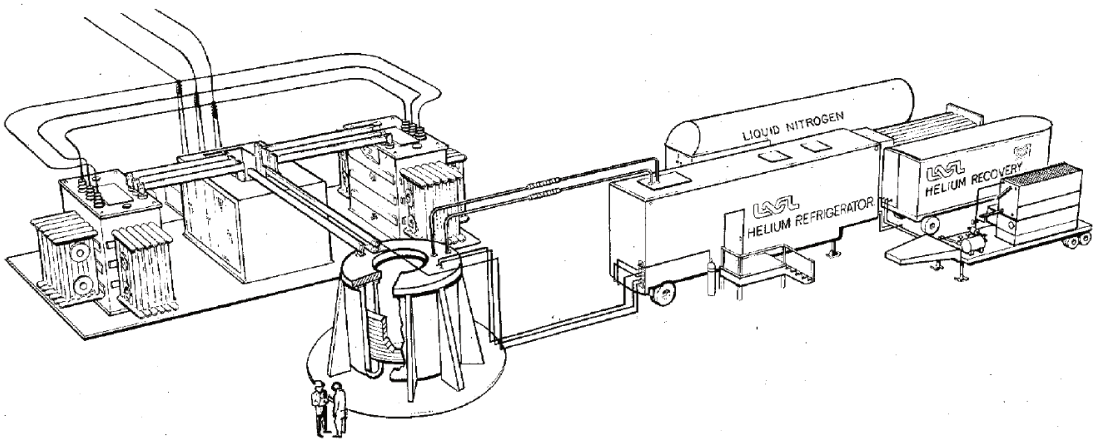


*Figure 17: 30 MJ SMES stabilizing system Tacoma Substation installation with superconducting coil in foreground, converter and transformers to the left, and refrigerator to the right [RBBC83]*

In some definitions, the term SMES stands for the whole plant, including the superconducting coil and its cooling system, but also the power conditioning system necessary to establish an appropriate interface with a power source and with the system being served. Of course, the term SMES also designates the very concept of superconducting magnetic energy storage.

### 1.4.3. History and applications

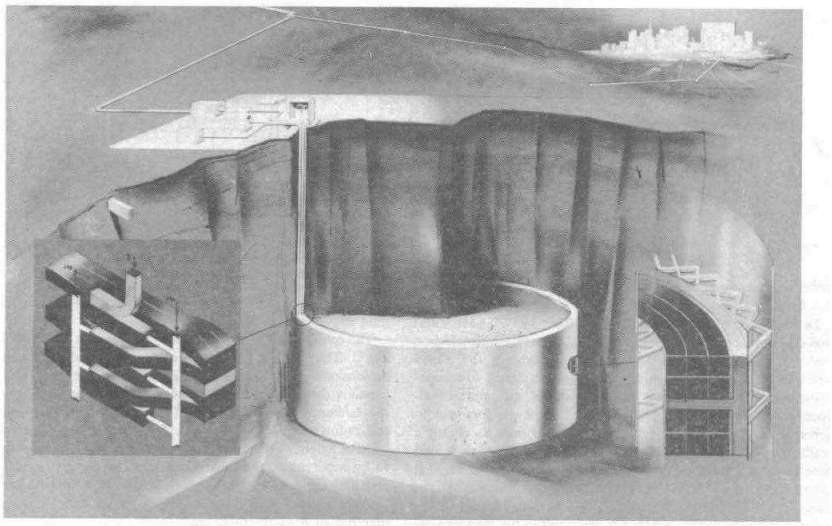

Fig. 2. An artist's rendition of the 1-GWh SMES unit designed by Los Alamos.

*Figure 18: Artist's view of A SMES plant for daily load levelling [Hass83].*

The principle of the SMES has been imagined by Ferrier in 1969 [Ferr69]. Originally, the idea was to build huge SMES plants in order to perform daily load levelling at a large scale. These SMES would have stored several thousands of MWh and their diameters would have been several hundreds of meters. The interest to build very big plants comes from the possible economies of scale. In this context was developed the concept of earth-supported SMES: the stress due to the magnetic load is transmitted to the bedrock thanks to a cold-to-warm interface, the aim being to reduce the cost of structural material [Luon96]. A development program for gigantic SMES (several thousands of MWh) has been lead in the USA until the beginning of the 1990's but such a real size plant has never been built [Ullr95]. Nevertheless since the 1990's, much smaller SMES systems have been developed and operated. SMES systems with an energy in the MJ range and made of NbTi conductor have been used as UPS (Uninterruptible Power Source) to protect critical equipment from voltage sags. Some SMES have also been used to improve the stability and capacity of the electric grid [Bade10] [RBBC83] [ScHa03] [ZiYo17].

One last application of SMES is to be used as a pulsed power source, for military applications such as directed-energy weapons [Ullr95] or to supply electromagnetic launchers [TBDV07] [PPAK99] [Luna88]. It can also be used in high energy physics [GJKB06] [JGKK02].

Since the 2000s, many projects have been undertaken to develop the HTS SMES technology [Bade10]. These SMES are mostly in the MJ range. Nevertheless, HTS SMES in the tenth of GJ (Gigajoule) range [SaGN13] or in the hundreds of MWh range [NCTS13] are still considered.

# 2. Fundamentals of SMES

## 2.1. Physics of magnetic energy storage

### 2.1.1. Magnetic energy

#### 2.1.1.1. Equations of the stored energy

According to the Biot-Savart law, an electrical current circulating in a wire generates a magnetic field. The magnetic energy of a circuit with an electrical current I is the half of the integral over the whole space of the B (Magnetic flux density) by H (Magnetic field) product (See eq. 2). In the absence of magnetic material (i.e. with $\mu_r \neq 1$) in the considered space, the eq. 2 can be simplified in eq. 3. The stored energy can also be expressed as a function of the current I and of the inductance L (eq. 4). If the circuit can be considered as purely inductive, which is in first approximation the case for a superconducting winding, then the voltage of the circuit, U, is the product of the inductance by the current variation (eq. 5)

$$E_{mag} = \frac{1}{2} \iiint_{Space} BH \, dx dy dz \tag{2}$$

$$E_{mag} = \frac{1}{2} \iiint_{Space} \frac{B^2}{\mu_0} dx dy dz \tag{3}$$

$$E_{mag} = \frac{1}{2} LI^2 \tag{4}$$

$$U = L \frac{dI}{dt} \tag{5}$$

#### 2.1.1.2. Approximation of windings with homogeneous current density

When we want to calculate the field distribution of a complete winding, we can in first approximation neglect the fact that the current is concentrated in the superconducting part of the conductor with a particular distribution and consider that the current density J, in A/mm$^2$, is homogeneous in the cross-section of the conductor. Furthermore, if we suppose that a winding is made of only one type of conductor, then the cross section of the conductor is the same in the whole winding and consequently the current density also is. That is why in the present work we will often use the simple case of windings with homogeneous current density.

#### 2.1.1.3. Relation between the operating current and the inductance.

The field distribution, and therefore the stored magnetic energy, of a winding with homogeneous current density J depends only on the geometry of the winding and on the value of J. It does not depend on the number of turns or the section of the conductor whose is made the winding. For example, a winding with a cross section of 10 cm by 1 cm can be a winding made of 10 turns of square conductor of 1 cm by 1 cm, or it can be a winding made of 1000 turns of square conductor of 1 mm by 1 mm. As J and the total magnetic energy are the same in both cases, the rated current I and by consequence the inductance L are different in these 2 cases. From eq. 4, the inductance is evolving inversely proportional to the square of the rated current for a given energy.

During the design phase of a magnet storing large energy, the choice of the rated current is of great importance when it comes to consider a fast discharge of the magnet. A fast discharge can be required in order to protect a superconducting magnet during a quench event (see part I-3.1.1) or in normal operation for a SMES used as a pulsed power source. As a superconducting magnet can be considered as a perfect inductance, the voltage at its terminals is given by eq. 5. The discharge speed is therefore

limited by the maximum voltage, which can be applied to the magnet. Taking into account eq. 4 and eq. 5, one can see that a magnet storing given energy and with given maximum voltage can be discharged faster if its rated current is higher, i.e. if its inductance is low.
On the other hand, the operating current I can be limited by the technical feasibility of a large multi-conductor cable, by the losses due to the current leads (see part I-3.4.1.3) and by the difficulty to make a high current source.

### 2.1.2. Laplace force

A piece of conductor of length dL, which carries a current I and submitted to a field B, is submitted to the Laplace force:

$$d\overrightarrow{F_L} = \vec{I} \wedge \vec{B}\, dL \tag{6}$$

The volume density of the Laplace force in a winding is given by the vector product of the current density J and the local field B:

$$\frac{d\overrightarrow{F_L}}{dV} = \vec{J} \wedge \vec{B} \tag{7}$$

### 2.1.3. The virial theorem

#### 2.1.3.1. The virial theorem applied to magnetic energy storage

A system, which generates a magnetic field is necessarily submitted to mechanical stress. This is the result of the virial theorem. In a nonferromagnetic system, the stress in the body of the system is related to the stored energy by the following equation [Moon82] [Boui92]:

$$\int_{Body} Tr(T_\sigma) dV = \int_{Space} \frac{B^2}{2\,\mu_0} dV = E_{mag} \tag{8}$$

In which $Tr(T_\sigma)$ is the trace of the stress tensor. According to this equation, the integral of the stress over the body of the system (conductor and structure) is proportional to the magnetic energy stored by the system (in the whole space). In order to understand the physical meaning of this equation, a simplified equation is often used. If only the compressive and tensile components of the stress tensor are taken into account, and if the absolute value of the stress is uniformly equal to σ, the equation 8 can be rewritten as

$$\sigma(V_T - V_C) = E_{mag} \tag{9}$$

In which $V_T$ is the volume of the body that is in tension and $V_C$ is the volume of the body that is in compression. This equation has the advantage to illustrate two facts:

- A system that stores energy has the majority of its body in traction.
- For a system whose body has a given volume, the stress of the body is proportional to the energy of the system.

If the density of the body of the system is ρ, the equation 9 can be written as:

$$\frac{\sigma}{\rho} = \frac{E_{mag}}{M_T - M_C} \tag{10}$$

In which $M_T$ is the mass of the body that is in tension and $M_C$ is the mass of the body that is in compression. As the stress distribution depends on the topology of the system, it is also possible to write:

$$k\frac{\sigma}{\rho} = \frac{E_{mag}}{M_{Total}} \tag{11}$$

In which k is a positive factor lower than 1, depending on the topology and $M_{Total}$ is the total mass of the body. If the whole body is uniformly under a tensile stress equal to σ, k is equal to 1. This is the ultimate limit in an ideal case, it is called the virial limit. This equation does not require simplifying assumptions, contrary to equations 9 and 10. In equation 11, we can see that the maximum specific energy that can be reached by the system depends on:

- The topology of the system
- The maximum allowable stress
- The average density of the body

It has been possible to calculate analytically the value of k for some topologies. For solenoids with thin walls, Sviatoslavsky [SvYo80] and Moon [Moon82], have shown that k is between 1/3 and 1/1.62. k approaches 1/3 for very long thin solenoids and approaches 1/1.62 for very short thin solenoids. For a torus with thin walls, Eyssa and Boom [EyBo81] have shown that k is lower or equal to 1/3. The consequence is that from a purely mechanical point of view, a solenoid is more adapted than a toroid to reach high specific energy.
Sviatoslavsky [SvYo80] has also shown that k is lower for solenoids with thick walls than for solenoids with thin walls. This is related to the fact that the stress is no more uniform across a thick wall. The structure is therefore not used at its full potential anymore.

#### 2.1.3.2. The Virial theorem applied to flywheels

The virial theorem also applies to flywheels (kinetic energy storage) [NoTs17].

$$\int_{Body} Tr(T_\sigma)dV = I\omega^2 = 2\,E_{kin} \tag{12}$$

$E_{kin}$ is the kinetic energy of the system. I is the moment of inertia and $\omega^2$ is the rotation speed. We have therefore a similar equation for flywheels and for SMESs even if the applied forces are completely different in nature.

#### 2.1.3.3. Precisions about the nature of the stored energy in SMES

The fact that the generation of a magnetic field induces a stress in the body of the system (virial theorem) may lead to question whether the energy stored by the system is magnetic energy or elastic (mechanical) energy. For an elastic system submitted to a given stress, the stored energy is inversely proportional to the stiffness of the material. This is because elastic energy is proportional to the square of the strain.
In an energised coil, the body of the coil is stiff and the strain of the conductor is only of a few tenth of percent. As a consequence, the stored elastic energy is very small. In the case of the high specific energy SMES of the BOSSE project for example, the stored elastic energy of the system is three orders of magnitude lower than the magnetic energy stored by the system. The elastic energy in a coil is therefore clearly negligible compared to the magnetic energy.

### 2.1.4. Advantages and drawbacks of SMES compared to other energy storage technologies

#### 2.1.4.1. General considerations about the advantages and drawbacks of SMES

The mass specific energy of a SMES is fundamentally limited by the virial theorem (see part I-2.1.3). Orders of magnitude of what have been achieved until now is given in Fig. 19. As a consequence, the SMES technology cannot compete with electrochemical energy storage (i.e. batteries) in terms of mass specific energy, or even volume specific energy. But similarly to capacitors and contrary to batteries, they can be considered as direct electricity storage since their stored energy does not need to be converted, for example from chemical energy to magnetic energy, to be delivered. Their output power is only limited by their rated current and voltage. That is why SMES systems can reach high specific power, both in terms of mass and volume. In addition to being able to deliver high power, the SMES has the advantage to be very reactive. Switching from the storage phase to a power exchange phase is only limited by the switching time of the solid-state components connecting the SMES to its power supply or to the load [Luon96]. According to Abdelsalam et al. [ABPH87] and Schoenung et al. [ScHa03], the cycling energy efficiency of SMES can be very high, around 98 % or 95 % respectively. But this energy balance does not take into account the energy required for cooling the system. The cycling efficiency is therefore degraded a lot for long time energy storage [NCTS13]. SMES better suits for "continuous" charge and discharge.

A general drawback for the SMES is its high investment and maintenance cost.

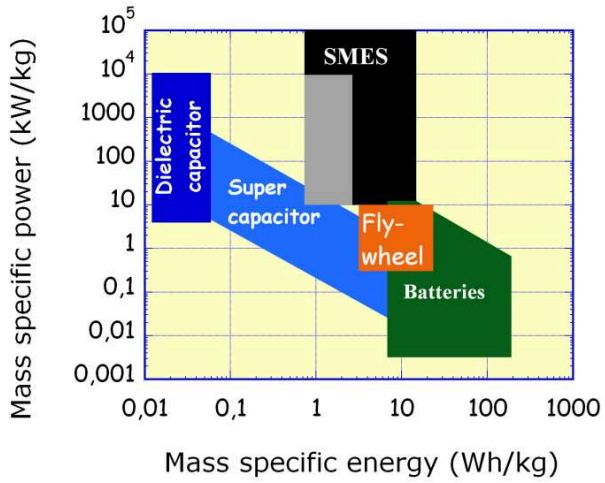


*Figure 19: Energy and Power densities for classical electric storage (Ragone chart). For SMES, the grey part is performances which have been achieved. The black part is potentially achievable performances. [Tixa95]*

#### 2.1.4.2. Comparison to high power capacitor banks

Compared to high power capacitor banks, they have the advantage to have higher mass and volume specific energy. The volume energy of a SMES can be roughly estimated if its B field is supposed to be homogeneous and that the thickness of the winding is neglected. In this case, the volume energy $E_v$ is given by equation 13:

$$E_v = \frac{B^2}{2\,\mu_0} \tag{13}$$

In Fig. 20, we can see that a SMES with a B field of 10 T already reaches a volume specific energy of 40 MJ/m$^3$. With HTS conductors, it is conceivable to make SMES coils with a field of 15 T or even 20 T

at low temperature, which corresponds to 90 MJ/m$^3$ and 160 MJ/m$^3$. These values have to be compared to the volume specific energy of high power capacitor banks, which is around 1 MJ/m$^3$.

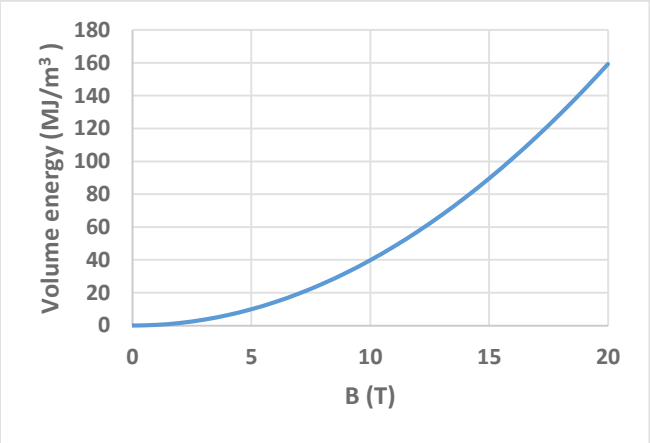


*Figure 20: Volume magnetic energy density in a volume with a homogeneous field B.*

Of course, a SMES is fundamentally different from a capacitor bank since the first one is inductive (current source) and the second one is capacitive (voltage source). Thus it has to be used for an appropriate purpose, for example to be used as a current source for electromagnetic launchers [BTAB12], or needs an adapted power conditioning system to deliver the stored energy [Hass83].

#### 2.1.4.3. Comparison to flywheels

SMES and flywheels both obey to the Virial theorem (see part I-2.1.3), so their specific energy should be in the same range. Nevertheless, a flywheel needs a generator to convert the stored mechanical energy into electrical power. The sizing of this generator depends on the required rated power. Furthermore, a flywheel needs a reinforced housing to ensure safety in case of breakage. The sizing of this housing depends on the total stored energy [AMBK07]. These two elements, the generator and the housing, add significant mass and volume to the system, degrading the overall power and energy densities. A SMES does not need a generator nor a housing and appears to be safer than a flywheel. Nevertheless, it requires a cryostat, a cooling system and eventually a power conditioning system, whose mass and volume can also be significant.

## 2.2. Geometry of superconducting coils for SMES

As we will see in part II-1.1, there is no simple answer to the question of the best geometry for a SMES coil. This geometry depends on the chosen conductor and on the constraints and objectives of the application, which are very different for each project. Nevertheless, SMES coils generally fall in two main families: solenoids and modular toroids. In this part, we will present specifically these two topologies since they appeared to be both interesting to satisfy the objective of the BOSSE project.

Other topologies exist or have been imagined for SMES coils. Generally, they are more difficult to design or to manufacture. Nevertheless, they offer interesting solutions to specific problems, and they are also briefly presented in this part.

The superconducting windings are often an assembly of modular elements. When these last ones are relatively flat, they are called “pancakes”. Theses pancakes are stacked to make a solenoid or spaced with a regular angle to make a toroid.

## 2.2.1. Classical topologies

### 2.2.1.1. Solenoids

#### 2.2.1.1.1. General description of solenoids

A solenoid is a cylinder made of wound conductor. It is a very classical topology not only for SMES but also for high field magnets, MRI (Magnetic Resonance Imaging) magnets and NMR (Nuclear Magnetic Resonance) magnets. From the mechanical point of view, a solenoid is a better option than a toroid to maximize the specific energy (see part I-2.1.3). Furthermore, this kind of topology is relatively easy to manufacture.

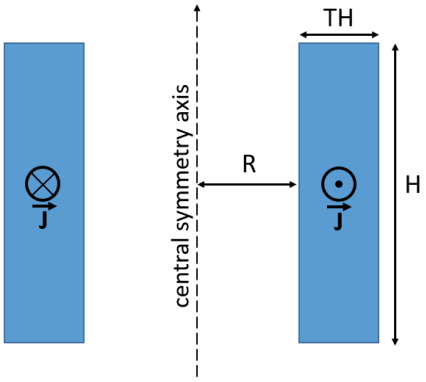


*Figure 21: Axial cross-section of a solenoid with rectangular cross section and homogeneous current density.*

In several parts of this work, a very simple model of solenoid will be used: a solenoid with rectangular cross-section and homogeneous current density. The geometry of such a solenoid is defined by only 3 parameters: R, H and TH (see Fig. 21).

In a free space (i.e. $\mu_r = 1$ in the considered space), the B field inside an infinite solenoid ($H = \infty$) in which the current density is J is given by:

$$B = \mu_0 J\, TH \qquad (14)$$

And there is no B field outside the solenoid. The evolution of B across the section is linear with the radius. Everywhere, B is collinear to the solenoid axis.

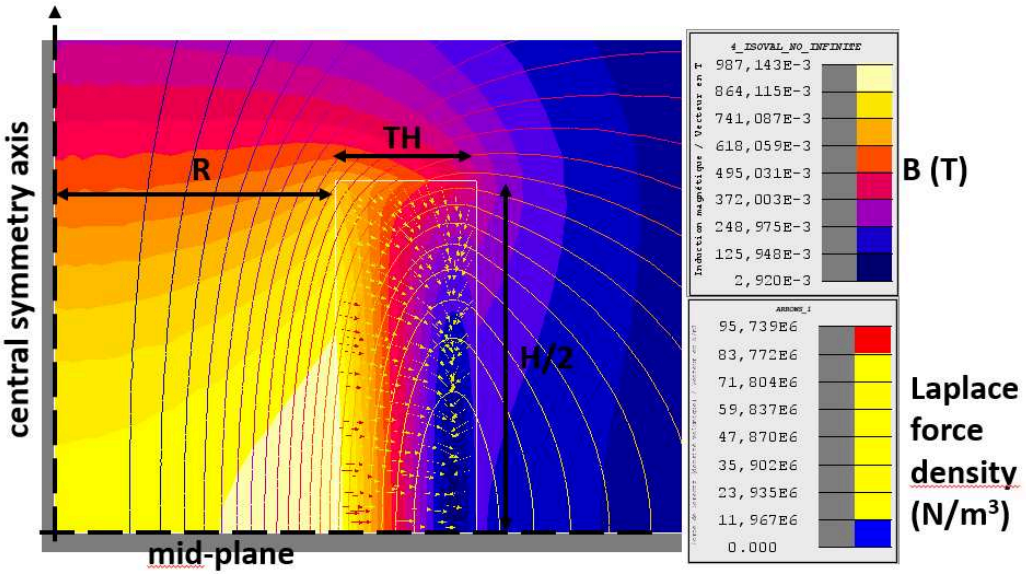


*Figure 22: B field value, B field lines and Laplace force density (arrows) of a solenoid with R = 20 mm, TH = 10 mm, H = 50 mm and J = 100 A/mm2.*

The field distribution of a long solenoid (H >> R) is similar to the one of an infinite solenoid. But the field inside the solenoid is lower and some leakage B field exists outside the solenoid, in opposite direction to the inner field. The magnetic field folds at the ends of winding section, i.e. the field is radial there. The shorter is the solenoid, the lower is the inner field and the higher is the external field. The longitudinal component of the B field, i.e. the component that is parallel to the solenoid axis, is maximum at the mid plan at the inner turn of the winding.

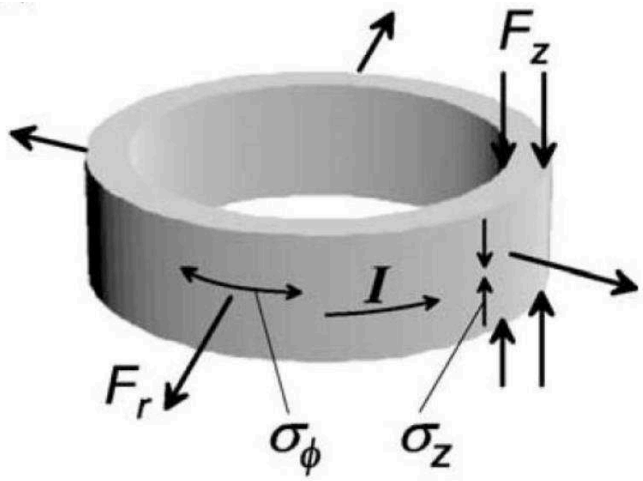


*Figure 23: Forces and stresses in a solenoid. The solenoid is submitted to compressive axial force and stress. It is also submitted to tensile azimuthal stress (i.e. "hoop stress") because of the radial centrifugal force.*

#### 2.2.1.1.2. Nested solenoids

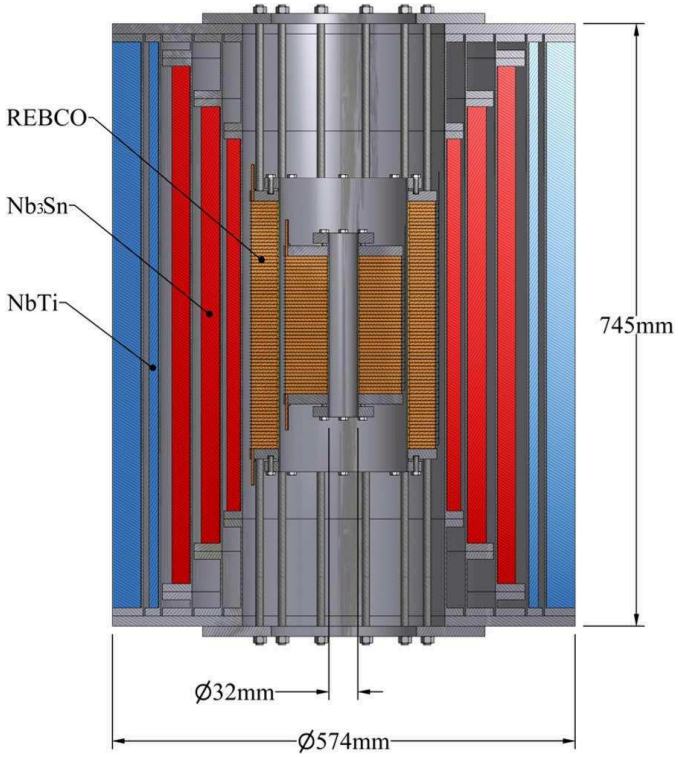


*Figure 24: Cross section view of an all superconductive magnet, designed to generate 32 T. The magnet is made of several nested solenoids made of different superconductors [MLWV12].*

Today, several all superconducting [SALT14] or hybrid (i.e. with bath resistive and superconducting parts) [FBBD12] high field magnets have been realised or are in project. In all of these projects, the

design is based on the use of nested solenoidal coils. Several solenoids made of different kinds of conductors are nested in each other (See Fig. 24). In this way, the field of each solenoid is adding to the field of other ones and the field is therefore maximum at the centre of the device. The current density can be different in each solenoid, which aims to optimize the use of conductor and to use superconducting conductor adapted to the local magnetic field. It can also bring benefit from the mechanical point of view (see part I-4.1.2). The idea of using several nested windings made of different types of superconductors could be applied to a SMES, even if it has not been the case in the BOSSE project.

#### 2.2.1.2. Toroids

##### 2.2.1.2.1. General description of toroids

The winding can also be arranged in a toroidal shape. In a modular toroid (see Fig. 25), a set of similar coils (modular elements) are arranged with regular angular interval around the central axis. In an ideal torus, the direction of the B field is purely azimuthal. This topology is therefore well adapted to the use of REBCO tapes, which are strongly anisotropic (see part I-1.3.1). The toroidal configuration aims to reduce the transverse field seen by REBCO pancakes. Another advantage of the toroidal configuration is that it has little fringe field. In an ideal torus, the field is zero outside the toroidal winding.

Inside an ideal torus, the field is perfectly azimuthal and is given by equation 15, in which N is the number of modular elements of the toroid, n is the number of turns in each module, I is the current, r is the distance to the main axis, J is the current density and S is the surface of the cross section of a modular coil. This equation is easily obtained thanks to the Ampère's law.

$$B = \frac{\mu_0 \, n \, N \, I}{2 \, \pi \, r} = \frac{\mu_0 \, J \, S \, N}{2 \, \pi \, r} \tag{15}$$

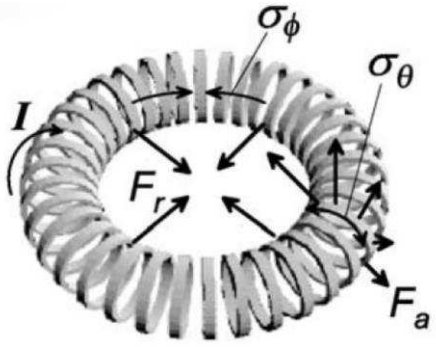


*Figure 25: An example of modular toroid. As the value of the azimuthal B field decreases with the radius, the coils are submitted to radial centring forces [Bade10]*

##### 2.2.1.2.2. D-shaped toroids

In the equation above, we can see that the value of the B field in the torus is decreasing with the radius. For this reason, the radius of curvature of the toroidal coils has to increase as the azimuthal field decreases in order to keep the tension regular along the conductor and to avoid bending moment. That is why, for mechanical reason, a "D-shape" section is sometimes preferred to a circular section (See Fig. 26) (See part II-3.3.3). This configuration is sometimes called Shafranov D-shape [Wils83].

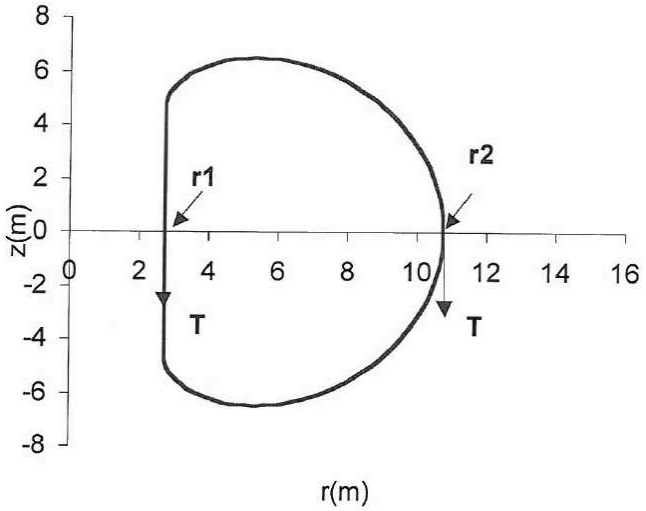


*Figure 26: D shaped toroidal form illustrated in ITER case (Courtesy Jean-Luc Duchateau).*

#### 2.2.1.2.3. Discharge with an XRAM system

Another advantage of the toroidal configuration is that in a modular toroid, all the coils constituting the toroid are geometrically equivalent. Thus it is easy to divide the toroid in several stages and to discharge the coils in parallel thanks to an XRAM system [DBBT11]. The XRAM principle consists in charging several inductances in serial then discharging them in parallel, thus multiplying the output current by the number of stages, which is interesting to supply an electromagnetic launcher [BTAB12] [PPAK99].

It is conceivable to discharge other SMES topologies than toroids thanks to an XRAM system. But care must be taken not to overcharge some stages during the discharge. For example in a solenoid that would be a stack of modular coils supplied in serial and discharged in parallel, the coils at the extremities of the solenoid would be overcharged during a fast discharge because of their low coupling with the other stages.

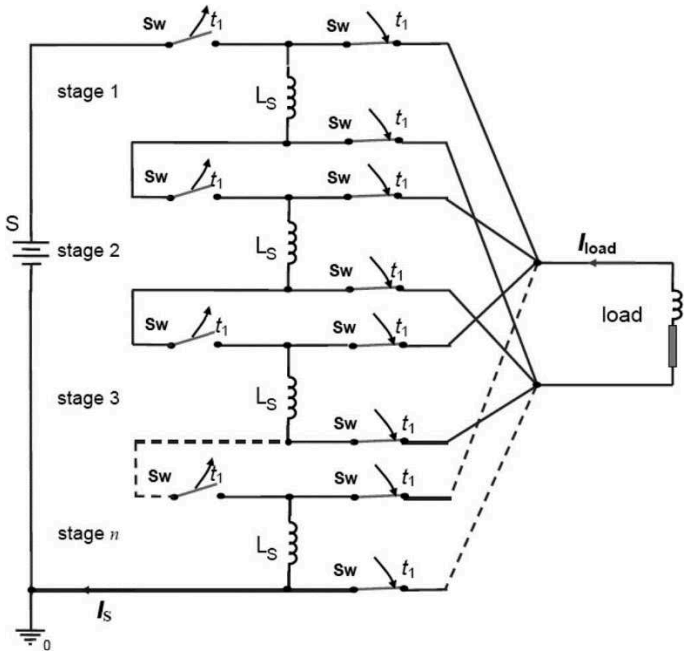


*Figure 27: Principle electrical diagram of the XRAM current multiplication circuit [DeBS11].*

## 2.2.2. Alternatives topologies

### 2.2.2.1. Dipoles

In the configuration called “Dipole”, the winding has long straight parts and short bended ends (see Fig. 28). The dipole configuration is very common in particle accelerators such as the LHC. They are generally not used for SMES, except in the S3EL concept. The S3EL (Superconducting Self-Supplied Electromagnetic Launcher) is an electromagnetic launcher powered by a dipole shaped SMES that is surrounding the rails. In this way, the magnetic induction generated by the SMES is increasing the propelling thrust and then the projectile output velocity [Bade10] [BaTA11]. Some of the undertaken about the S3EL in the frame of the BOSSE project is presented in [CiBT17] and [ACPV17].

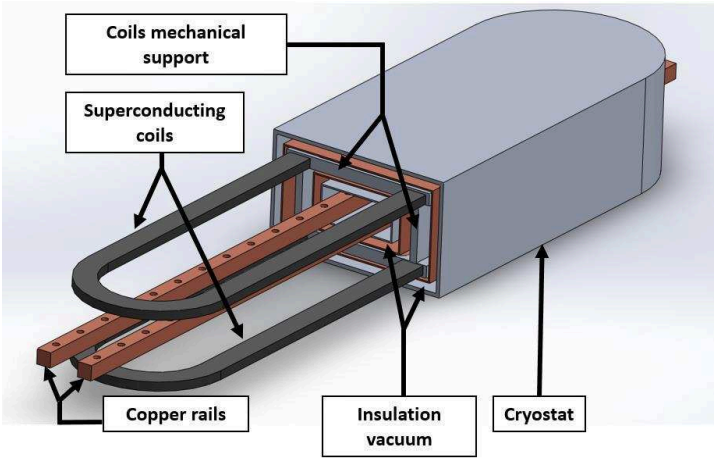


*Figure 28: CAO plan of the S3EL launcher of the BOSSE project (courtesy R.Pasquet, SigmaPhi®) [CiBT17]*

### 2.2.2.2. Force balanced coils

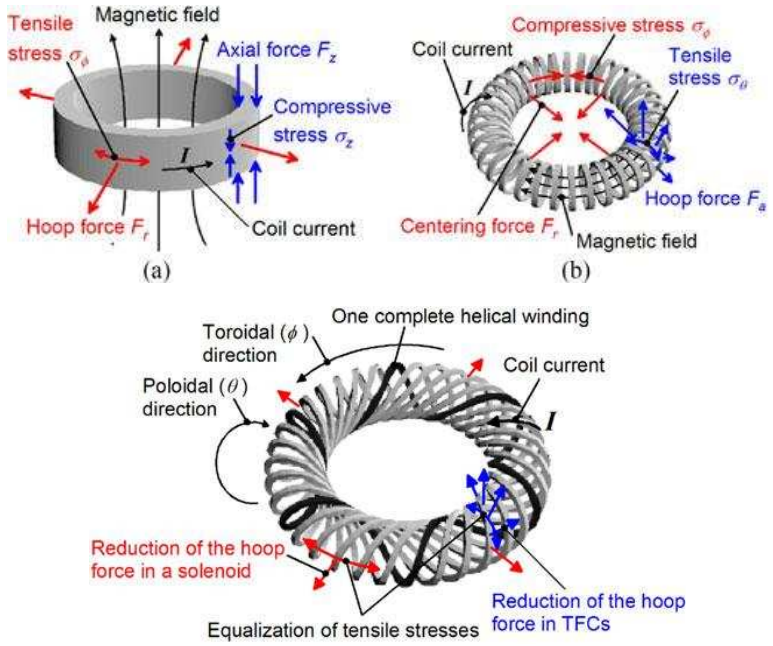


*Figure 29: Comparison of the forces and stresses in a solenoid, a toroid and a FBC [NoTs17]*

As a solenoid is submitted to a centrifugal force and that toroids are submitted to a centring force, the Force Balanced Coil (FBC) [NOKT99] [NoTs17] is a combination of a solenoid and a toroid in order to compensate these forces. In a FBC, the current direction has both a poloidal and a toroidal components.

Of course, even in a perfect FBC, the winding is still submitted to tensile stress, and the virial limit cannot be overtaken in any case (see I-2.1.3).

#### 2.2.2.3. Tilted toroidal coil

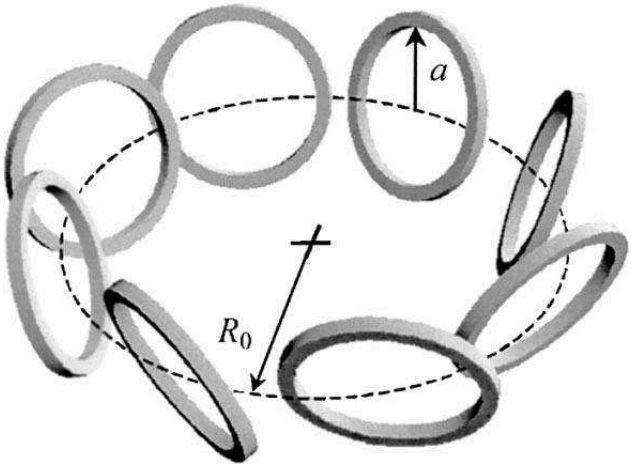


*Figure 30: Principle diagram of the Tilted Toroidal Coil [FANS03]*

Another solution to balance the centering force of a toroid is the Tilted Toroidal Coil (TTC), which is much simpler to manufacture than the FBC [FANS03]. At least one SMES of this type has been manufactured and operated [JGKP02]. Of course in this configuration, the magnetic field is no more purely azimuthal like in a perfect torus, which can be a problem if the winding is made of anisotropic conductor.

#### 2.2.2.4. Constant field toroid

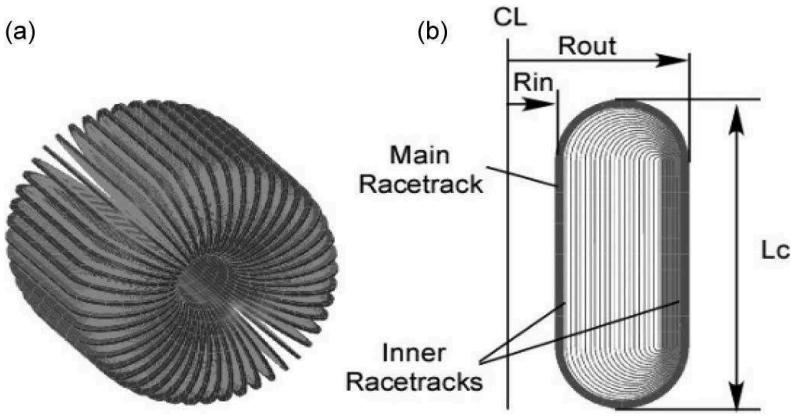


*Figure 31: Principle diagram of a Constant Field Toroid [RBMM16]*

The principle of the Constant Field Toroid is presented in Fig. 31. The inner halves of the turns are distributed along the main radius of the toroid. In this way, the B field is homogeneous inside the toroid, which optimizes the volume of the toroid for a given field [RBMM16]. This configuration is therefore interesting for isotropic superconductors. It has also the advantage to balance the centring force of the toroid.

### 2.2.2.5. Toroids with imbricated coils with different geometries

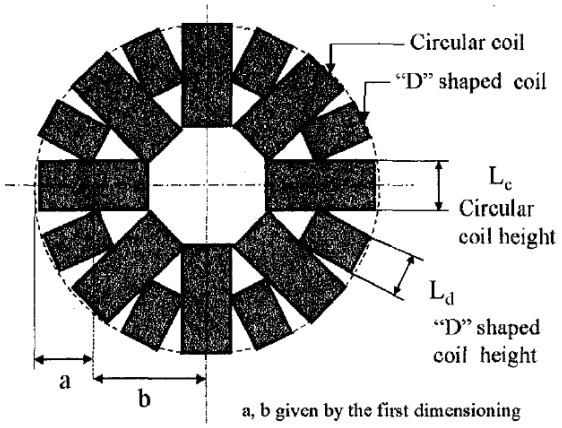


*Figure 32: Top-view of a toroid, which is a combination of circular coils and D-shaped coils [ViMT01]*

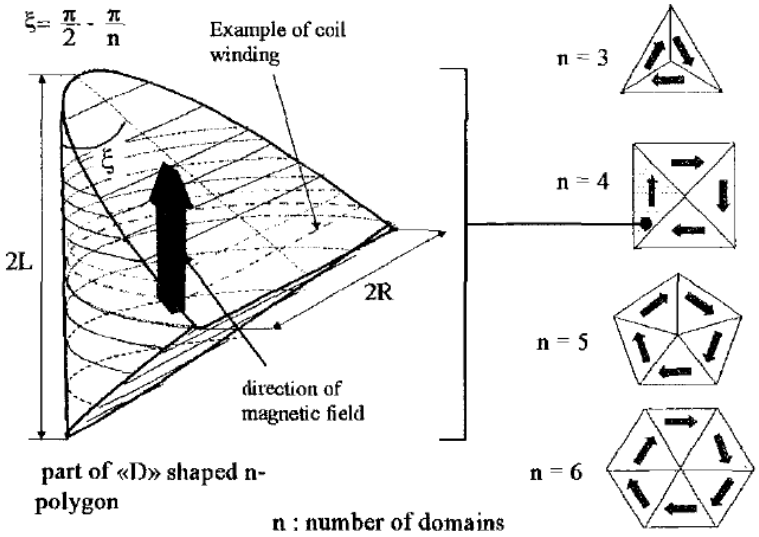


*Figure 33: A concept of polygonal SMES made of D-shaped coils [ViMT01]*

Vincent-Viry et al. [ViMT01] have proposed similar ideas. In Fig. 32, it is proposed to insert D-shaped coils between the circular coils of a toroid, which also homogenises the B field in the volume of the toroid. In Fig. 33 the SMES, which looks like a polygon when viewed from above, is made of n segments. No circular coils are used, but only D-shaped coils of different sizes.

### 2.2.2.6. Bunch of solenoids

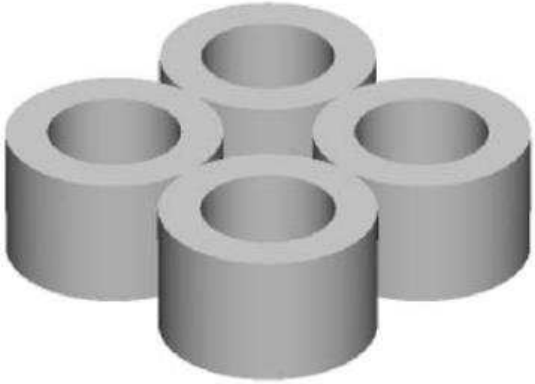

*Figure 34: A bunch of 4 solenoids for SMES.*

Rather than increasing the size of a solenoid to store more energy, it can be preferred to make several solenoids [NHKT04] [OgNT13]. Even if the use of conductor is not optimal in this solution, it has the advantage to be modular and can be easier to manage from a mechanical point of view. The fringe field is reduced if the B field of solenoids are in alternate directions [HSHW99].

#### 2.2.2.7. Association of solenoids connected with transition sections

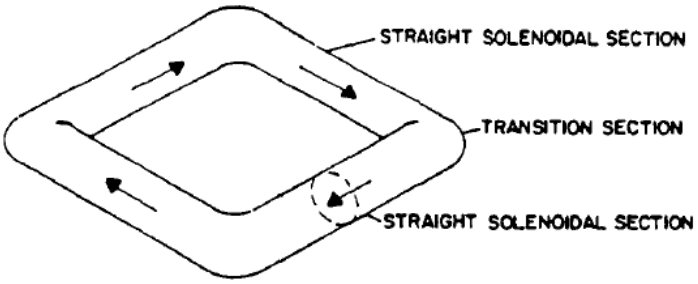


*Figure 35: A SMES made of long solenoidal sections and short curvy sections [Nasa88].*

In early studies of the NASA for a lunar station [Nasa88], the SMES of Fig. 35 was proposed. It is a combination of 4 solenoids connected with transition sections. This SMES is therefore a hybrid between a bunch of solenoids and a torus.

#### 2.2.2.8. Toroid with racetrack-shaped section and support structure

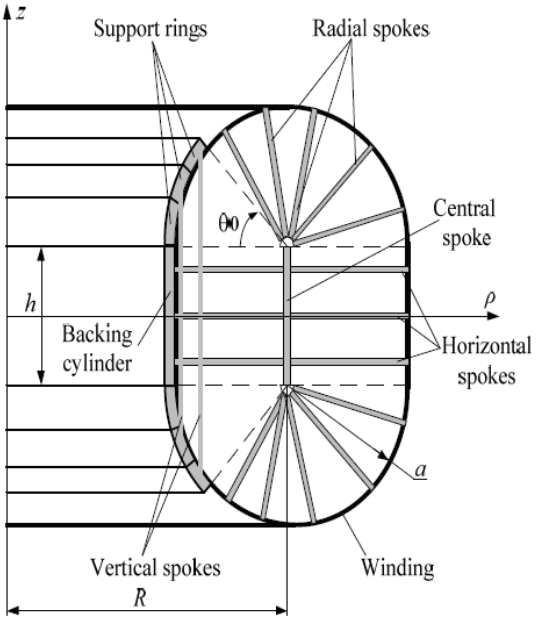


*Figure 36: Principle diagram of a Racetrack-shaped coils toroid, with spokes inside the coil [MaPV12].*

As an alternative to toroids with a D-shaped section, Mazurenko et al. [MaPV12] have proposed toroids with a racetrack-shaped section and a support structure placed inside the torus.

# 3. Operational aspects of superconducting windings

In this part are presented different technical and operational aspects, which apply not only to SMES but to superconducting magnets in general. Information is given about both LTS magnets and HTS magnets. First because the behaviour of LTS and HTS magnets is very different, which makes the protection of HTS windings specific. Second, to emphasize the opportunity offered by HTS conductors to widen the application and operating fields of SMES.

## 3.1. Thermal stability and protection

### 3.1.1. Stability of LTS magnets

LTS magnets are known to be subject to instability and can abruptly lose their superconducting state. In this event, called a quench, a part of the conductor or the entire winding is transiting from the superconducting state to the normal, resistive state. All sorts of initial perturbations can start a quench (see Fig. 37): an input of energy, limited into space and time, heats the superconductor. If the temperature of the conductor rises sufficiently, the critical temperature is reached and the superconducting state is lost. The difference between the normal operating temperature and the critical temperature at operating current density and magnetic field is referred as the temperature margin. As the conductor becomes resistive, the current generates heat by Joule effect then a thermal runaway generally occurs. The transition to normal state propagates from the hotspot (initial localized transited part) to the rest of the winding by thermal conduction.

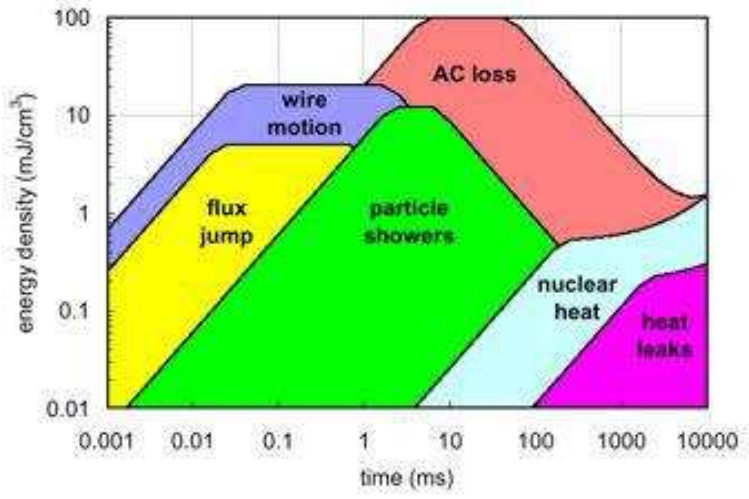


*Figure 37: All kinds of perturbations can bring a sufficient energy input in order to start a quench. This chart shows the order of magnitude of the energy density deposited with respect to the duration of the phenomenon. The data are compiled from existing LTS magnets (Courtesy Luca Bottura).*

LTS magnets are very sensitive to perturbations for two reasons:

- Their critical temperature is intrinsically low so their temperature margin is low, especially as their operating current is close to their critical current.
- Specific heat of materials are extremely low around 4.2 K. They can be 3 or 4 orders of magnitude lower at 4.2 K than at 90 K (see Fig. 38). For this reason, even a very small input of heat causes a significant rise of the temperature

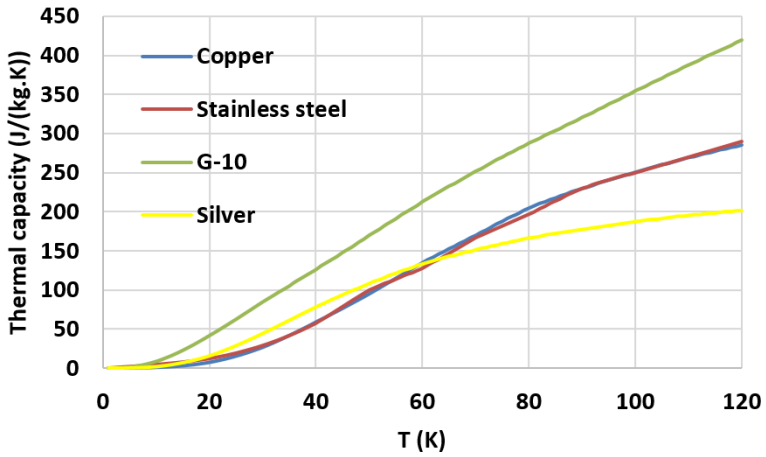


*Figure 38: Specific heat of several materials depending on the temperature. Data from CryoComp© [Cryo00]*

In order to limit the temperature rise of a conductor, several solutions are possible. First, it is possible to limit some heat input such as AC losses (see part I-3.4.2) by ramping the magnet slowly or improving the design of the conductor to reduce AC losses (see part I-3.5). One other obvious solution is to stabilise the superconductor with a classical conductor, such as copper or aluminium. This has two advantages:

- The heat capacity per unit length of the conductor is increased, which reduces the temperature excursion of the conductor.
- The resistivity per unit length of the conductor is decreased, hence a reduction of the heating by Joule effect.

The drawback of stabilizing the superconductor with copper or aluminium is to increase the mass and the volume of the winding.

The stability of LTS magnets is a mastered topic nowadays, even if precautions have still to be taken for their operation. LTS have to be submitted to a “training”, which means that they may quench several times before reaching their operating current. These quenches are due to microscopic displacement of the conductor. Once that the quench happened, the conductor is in place and the quench current for the next cycle is higher [Tixa95] [Iwas09]. Another precaution to take for operating LTS magnets is to limit AC losses, which entails slow charge and discharge of the magnet.

### 3.1.2. RRR and magneto-resistance

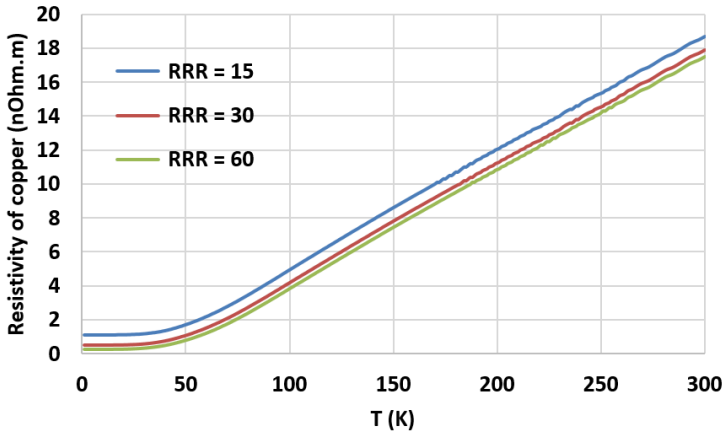


*Figure 39: Resistivity of copper, without B field, depending on the temperature and the RRR (data from CryoComp© [Cryo00])*

The resistivity of metals can be very dependent on the temperature. The ratio between the resistivity at 273 K and resistivity at 4.2 K is called the Residual Resistivity Ratio (RRR). The RRR is very dependent on the degree of purity of the metal, but also on its metallurgical state. For example, stainless steel has a very low RRR, close to 1.4 [Iwas09]. But the RRR of annealed copper or aluminium with a very high degree of purity can reach several hundreds or even several thousand [SMFS92] [WMSS00]. Nevertheless, annealed pure metals are very soft and mechanically weak, and the RRR of metals in practical conductors is generally lower. The RRR of the copper that is deposited on REBCO tapes is varying from 10 to 60 depending on the manufacturer [Sena14].
The resistivity of metals also depends on the value of the magnetic field B. This phenomenon is called magneto-resistance: the resistivity of a metal increases with the magnetic field. Metals with a high RRR are especially sensitive to magneto-resistance (see Fig. 40).

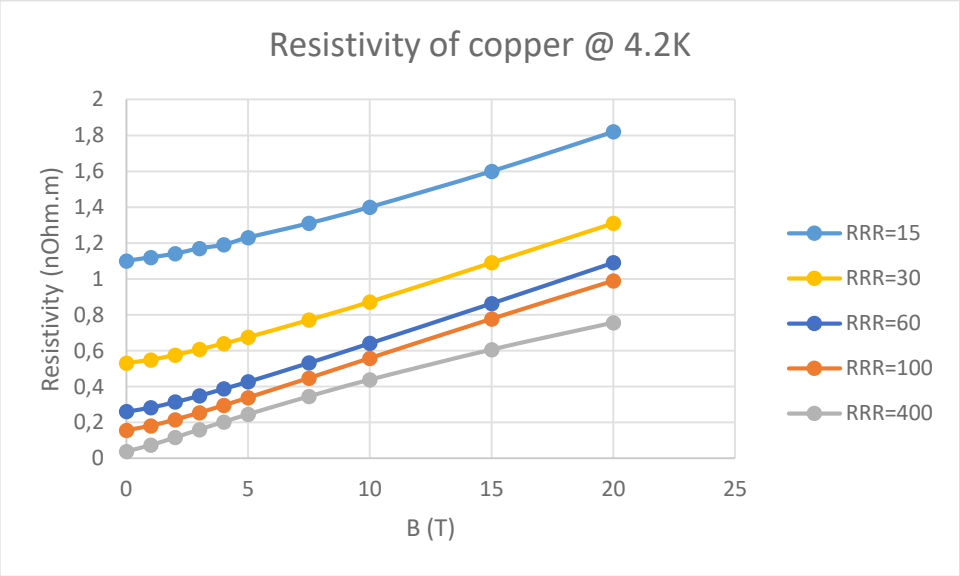


*Figure 40: Resistivity of copper at 4.2 K, depending on the RRR and the value of the B field (Data from CryoComp© [Cryo00]).*

### 3.1.3. Protection of LTS magnets

Superconducting magnets are operated at high current densities. The loss of the superconducting state causes heating of the conductor, hence a risk of damaging or destroying the coil. The classically used strategy consists in detecting the transition to normal state then to discharge quickly the coil in a load that is outside of the cryostat. The detection of the transition is generally performed thanks to voltage measurement, even if other methods are possible [GySG18] [MaGo17] [SIFS16].

Another strategy consists to accelerate by design the propagation of the quench in the whole coil. In this way, the energy stored in the coil is dissipated in the whole coil instead of being dissipated in one single hotspot. If the specific energy of the coil is sufficiently low, the temperature rise of the coil will be moderated. The fact to propagate quickly the transition to the whole coil aims to heat uniformly the coil, which avoids high localized stress due to localized thermal expansion. The propagation of the coil can be favoured by improving the thermal conduction between turns or by the insertion of heaters in the winding. These heaters are activated when the transition is detected [Iwas09].
Practically, the protection of LTS magnets can be a combination of these two concepts: a fast discharge of the coil in an external load and a fast propagation of the transition inside the coil.

### 3.1.4. Stability of HTS magnets

Contrary to LTS magnets, HTS magnets are very stable. Their critical temperature is higher as well as their temperature margin. Furthermore, as the heat capacity of materials is quickly rising above 4.2 K,

the energy margin is 3 or 4 orders of magnitude higher in a HTS magnet than in a LTS magnet. The energy margin is the maximum energy density that a conductor can absorb and still remain fully superconducting [Iwas09].
It makes them immune to most of perturbation sources listed in Fig. 37. Only a local (see part I-1.3.4) or widespread overshoot of the critical current or AC losses (see part I-3.4.2) can cause a loss of the superconducting state in a HTS magnet. It means that only the way the magnet is operated (value of the current and ramping speed) can cause the loss of the superconducting state, but no unpredictable phenomenon such as wire motion.

### 3.1.5. Protection of HTS magnets

Paradoxically, the high stability of HTS conductors causes a major issue for ensuring the protection of HTS coils cooled at low temperature (4.2 K). Several major projects based on HTS conductor have had to face a partial destruction of the winding because of a failure of the protection system [AWOM17] [GAJH16] [NZHH12] [Bade10]. In fact, when the destruction of an HTS tape, pancake or coil, happens because of uncontrolled overshoot of the critical current, it is often observed that the device is burned only on a very small part, a few millimetres long. A reason is that the normal zone propagation velocity, i.e. the speed at which the area which has lost its superconducting state propagates, is two orders of magnitude lower in HTS conductors than in LTS conductors [MBCB15] [VDWK15], which is related to the large temperature margin of HTS conductors. The non-propagation of the resistive part of the conductor is even worse in REBCO conductors because of the bad thermal conductivity of Ha®-C276 and because of the performance inhomogeneity of the superconducting layer (see part I-1.3.4). For these reasons, a loss of the superconducting state in a HTS conductor and especially in a REBCO conductor has a tendency not to spread. It is therefore possible to have a very high electric field E on a very localised part of the conductor but without, however, a significant variation of the voltage measured at the winding terminals. To detect the transition to normal state of the conductor on a very short length thanks to voltage measurement at the terminals of an HTS coil is therefore problematic. It requires to reject parasite effects such as inductive voltage and electromagnetic noise. Nevertheless, the measurement of the critical current of insulated REBCO pancakes cooled at 4.2 K has been achieved in the frame of this thesis (see part III-3.2.3). It has also been achieved recently by other teams [BJRC18] [VKBB18]. These achievements show that the detection and protection of insulated REBCO pancakes are possible. As for LTS magnets, REBCO windings are dumped in an external load when the transition is detected.

### 3.1.6. NI and MI coils

As the protection of insulated REBCO pancakes is an issue since several years, Non-Insulated (NI) [HPBI11] [YKCL16] or Metal-Insulated (MI) [LéIw16] coils have been developed these last years. In NI coils, some bare REBCO tape, i.e. without insulation, is used for the winding. There is therefore an electrical contact between each turn through the surface of the tape. It is nonetheless possible to charge the coil if the current ramp is very slow, so that the current can follow the superconducting path instead of short-circuiting the turns. The advantage is that if a part of the conductor transits from the superconducting state to the normal state, the current can escape to another turn and the burning of the tape is prevented. The MI coils are an evolution of the NI coil. In MI coil, the REBCO tape is co-wound with stainless steel tapes. The fact to add interfaces between the REBCO tapes increases the turn-to-turn resistance and reduces the time constant of the coil. Both NI coils and MI coils have proven their strong resilience to quench situations, even at high current densities. Their drawbacks are their low time constant, the required cooling power and the lack of precision in the current distribution and therefore in the field map. Furthermore induced currents in different parts of the coil are not controlled and lead to over stresses in the coil. Several mechanical damages have been recorded. This

principle cannot be used in a pulse SMES since NI and MI coils cannot be discharged quickly. The most part of the stored energy would be dissipated inside the coil by Joule effect.

## 3.2. Cooling methods

Several methods are used for cooling superconducting electromagnets. The coil can be immersed in a cryogenic bath. This method has the advantage to keep the operating temperature of the whole coil very stable and equal to the boiling temperature of the liquid. The liquids that can be used for HTS coils are liquid nitrogen, liquid Neon, liquid hydrogen and liquid helium. Only liquid helium can be used for LTS coils. Helium liquid bath cooling is used in the BOSSE project.

Another possibility to cool superconducting coils is to use cryocoolers [Rade09]. They are commercially available integrated cooling systems, which cold-head has to be placed in thermal contact with the superconducting coil. In this case, the cooling of the coil is made by thermal conduction and no handling of cryogenic fluids is required anymore. This is a great advantage for devices that have to be used in places where helium recovery is not possible. The first SMES developed at the Grenoble CNRS for the DGA [TBDV07] was cooled by cryocoolers. On the other hand the energy extraction is limited compared to a bath.

It is also possible to cool superconducting coils thanks to gaseous [VKBB18] or solid coolants [HLIO02].

## 3.3. Operating temperature

The operating temperature of a superconducting coil plays a major role in the sizing of the cooling system of the coil. Indeed, the efficiency of a cooling system cannot be better than the Carnot efficiency. The Carnot efficiency is given by eq. 16 in which $T_h$ is the temperatures of the hot reservoir and $T_c$ is the temperature of the cold reservoir, W is the minimum work done by the cooling system, $Q_c$ is the heat extracted at low temperature by the cooling system

$$\frac{Q_c}{W} = \frac{T_c}{T_h - T_c} \tag{16}$$

Practically, the efficiency of cooling systems is much lower than the Carnot efficiency. According to Strowbridge [Stro74], the ratio of the real efficiency and the Carnot one mainly depend on the power and increases with it, with an asymptotic value of about 0.3. In any case, the lower is the operating temperature, the more power is required to cool a coil with given losses.

| | Nitrogen | Neon | Hydrogen | Helium |
|---|---|---|---|---|
| Boiling temperature at 1 bar (K) | 77.4 | 27.1 | 20.4 | 4.2 |
| Inverse of Carnot efficiency (Room temperature = 293 K) | 2.8 | 9.8 | 13.4 | 68.8 |

*Table 2: Boiling temperatures of cryogenic fluids.*

## 3.4. Thermal losses

Several phenomena are prone to bring some heat to the superconducting coil. Apart from the random perturbations presented in Fig. 37 which can locally bring some energy to the magnet, the heat sources can be classified in two categories: the losses which occur even during the steady state operation of the winding and the losses which occur because of a field variation in the system, i.e. when the winding is charged or discharged.

### 3.4.1. Steady-state losses

#### 3.4.1.1. Radiative and conduction thermal leakage

The coils, cooled at cryogenic temperature, are insulated from the room temperature thanks to their cryostat. The cryostats are made of two walls separated by vacuum in order to prevent thermal conduction. Many layers of multi-foil insulation are added between the walls in order to lower the radiative heat transfer. If this is done correctly, the thermal insulation of the cryostat is excellent, and the cryostat thermal losses are very low. Nevertheless, there are necessary some mechanical junctions between the room temperature structure and the coil in order to support it. These junctions are generally tie rods made of stainless steel, glass fibre reinforced plastic or carbon fibre reinforced plastic, i.e. materials with high mechanical resistance but low thermal conductivity.

#### 3.4.1.2. Splices

Heat can also be directly generated inside the coil by Joule effect. Contrary to LTS, it is uneasy to make superconducting junctions between two HTS conductors, even if solutions exist [PLOL14]. In REBCO coils, welded splices are often used [Lecr12] [Flei13]. They have a low resistance but are not superconductive, hence heat dissipation at junctions between tapes. Welded junctions are used in the BOSSE project.

#### 3.4.1.3. Current leads

A major source of heating of the coil are the current leads. Contrary to mechanical supports, they have to carry current, so they are made of materials with a good electrical conductivity. Apart from superconductors, materials with a good electrical conductivity have also a good thermal conductivity. The current leads are therefore creating a thermal short circuit between the room temperature and the coil. Practically, HTS conductors can be used to carry the current from 4.2 K to 77 K, then copper or aluminium is used to carry the current from 77 K to room temperature. Thermalization of intermediate stages as well as optimization of the section and length of the current leads are used in order to reduce the heating of the coil. A balance has to be found between thermal conduction and Joule heating, depending on the operating current and operating temperature.
Current leads are generally designed to carry indefinitely the operating current of their magnet. However, for a SMES used as a pulsed power source, i.e. charged fast then discharged even faster, it is possible to play on the thermal inertia of the current leads. It is thus conceivable to undersize them compared to a normal steady-state operation.

### 3.4.2. AC losses

Other sources of heating of the coil are AC losses, i.e. losses due to a variation of the B field. Several phenomena can generate AC losses, which are listed hereinafter.

#### 3.4.2.1. Eddy losses

Eddy losses are due to the presence of a conductive material in a time varying B field. Electrical currents are induced by induction time variations, which result in Joule losses. Within some hypothesis, eddy losses are proportional to the conductivity of the material and to the square of the time variation of the field. Consequently, if the field variation is sinusoidal, the losses are proportional to the square of the amplitude of the B field and to the square of the frequency of the variation. The losses are also dependant on the shape of the piece of conductor submitted to a variable field. In order to limit eddy losses, current pathways for which the ratio of the integral of the Electro-Motive Force over the length is high have to be avoided. In other words, large plates or large loops perpendicular to the variable field have to be avoided. When the presence of copper plates is mandatory in a coil, for example in a conduction cooled coil such as the SMES developed at the Grenoble CNRS, it is preferable to split the plates to reduce eddy losses [Bade10].

#### 3.4.2.2. Magnetization losses

In a type II superconductor submitted to a variable field, losses are also existing. As the material is penetrated by the field, some electrical field E appears when the B field is varying, according to the Maxwell-Faraday equation. This electric field, combined with screening or transport current density, generates power dissipation in the superconductor [Tixa95]. Some analytical solutions are existing to calculate magnetization losses in a set of simple geometries submitted to a variable self-field, variable external field or submitted to in phase sinusoidal transport current and external field [Esca16]. Nevertheless, these analytical solutions are using the critical state model, which is an approximation. Losses and current distribution in a superconductor can be calculated by numerical means, but this kind of calculation is still challenging and time consuming today [Esca16] [Htsm00].

#### 3.4.2.3. Coupling losses

Coupling losses occur in a conductor or a cable that is a bundle of superconducting strands or layers, separated by conductive elements such as a resistive matrix. The conductor being submitted to a variable field, some current is looping between the filaments under the influence of the EMF. The current is passing through the resistive matrix and generates heat by Joule effect. A solution to limit the coupling losses is to twist the superconducting strands of the conductor [Tixa95] [Esca16] (see Fig. 4, 41 or 42).

#### 3.4.2.4. Magnetic losses

Magnetic materials, especially ferromagnetic materials, are subjected to magnetic losses. These losses come from the change of orientation, number and size of magnetic domains when the material is submitted to a variable field. Magnetic losses are not studied in this thesis since in the high density SMES of the BOSSE project, there is no ferromagnetic core and the used conductor has a non-magnetic substrate. But magnetic losses have to be taken into account for the design of motors, generators and transformers and superconductors with magnetic substrate [Esca16].

## 3.5. Cables

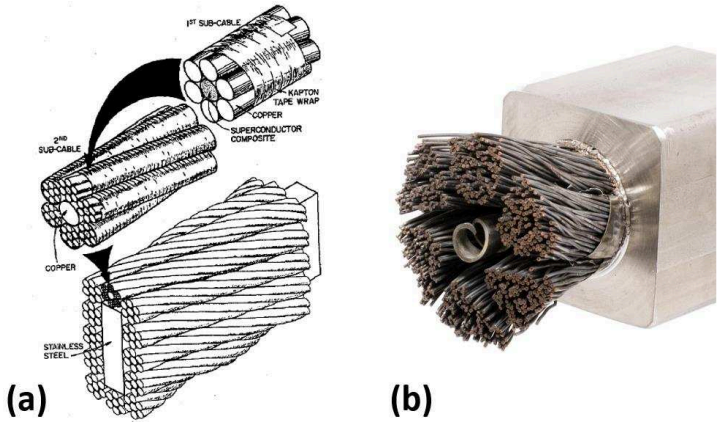


*Figure 41: Reinforced cables. (a) A Rutherford cable wrapped around a structural element, developed for a 30 MJ/10 MW SMES [RBBC79]. (b) A Nb3Sn Cable In Conduit Conductor (CICC) developed for ITER [Nhmf00].*

Superconducting cables are bundles of superconducting conductors. In large superconducting systems, it can be necessary to increase the rated current in order to lower the inductance and facilitate the protection of the system (see part I-2.1.1.3). The increase of the current is achieved by the association of several conductors in parallel in a cable. Most of the time, the conductors of the cable are transposed in order to guarantee the homogeneous distribution of the current in the cable cross-section and to limit the coupling losses. In cables, the superconducting conductors can be associated to structural material so as to improve mechanical properties. The reinforcement material can be

placed inside the cable (see Fig. 41.a) or around the cable (see Fig. 41.b). In this last case, the structure is referred to as Cable in Conduit Conductor.
A very common structure for LTS cables is the Rutherford cable (see Fig. 4 and Fig. 41.a). But for REBCO tapes, making Rutherford cables is inappropriate. Other cable structures are proposed for REBCO tapes: Roebel cable [RBBB15], CORC® (Conductor On Round Core) cable [Adva00] and the twisted stack cable [Himb16]. Among these 3 possibilities, the Roebel cable can reach the highest current density. But only half of the manufactured conductor is finally used in the cable, the rest being cut and wasted. The main disadvantage of the CORC® cable is certainly its low current density, due to the absence of conductor in its core. Finally, the twisted stack cable is probably the cheaper solution and can reach high current density but the tapes in this structure are only partially transposed.

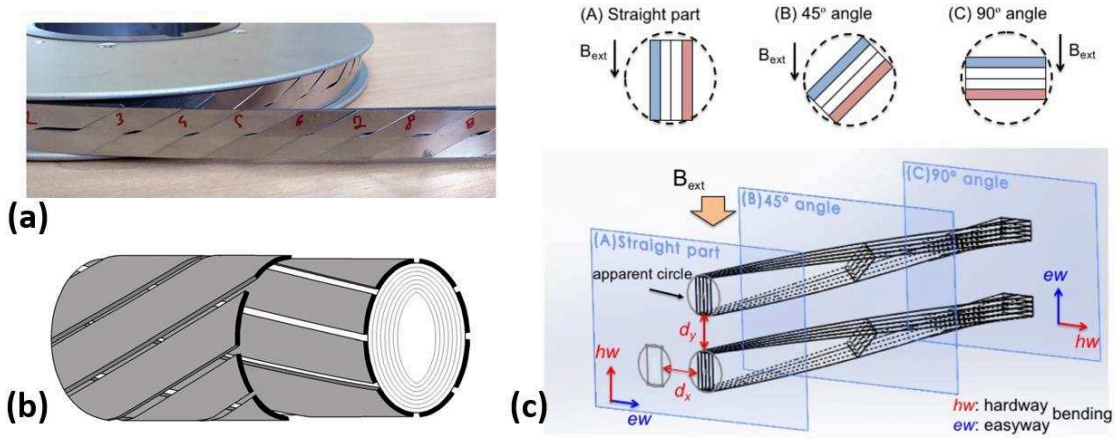


*Figure 42: (a) A Roebel cable [RBBB15]. (b) Principle of the CORC® cable [Laan09]. (c) Principle of the twisted stack-cable [Himb16].*

# 3.6. Mechanical reinforcement of the conductor

The reasoning presented in this paragraph can be applied indifferently to conductors or cables.

## 3.6.1. General considerations about the mechanical reinforcement of a superconductor

A superconducting conductor has to fulfil several functions. It has to be superconductive, but it also has to withstand high mechanical stress especially for high energy magnets. That is why there are several components in a superconducting conductor: a superconducting material of course, but also a material with a high electrical conductivity to ensure the stability of the superconducting state and the ability to protect the coil. Eventually, a material with high mechanical properties is added to reinforce the conductor. Nevertheless, in most of problems, the volume or the mass of the winding is constrained, for technical or cost issues. In our case, for the high energy density SMES, this is the mass of the winding which is constrained, since we want to reach a specific energy of 20 kJ/kg.

It is desirable that a same material plays a role both for stabilizing and reinforcing the conductor. But the materials with high electrical conductivity, i.e. pure copper, aluminium or silver with a high RRR, are soft. We can cite the notable exception of the Aluminium Nickel alloy (Al-0.1 wt%Ni) that has been developed for the Atlas detector at the CERN [WMSS00] [WMSY00] [LCSD13]. It has a RRR of 590 and a yield stress of 167 MPa at 4.2 K. This alloy has been used in the LTS coil that currently owns the world record for energy density [YMYO02]. Yet there is another difficulty which would prevent us to use this alloy to reinforce REBCO tapes. The fact is that this Al-Ni alloy has a low Young modulus and that Hastelloy®-C276 has a high Young modulus. But it is not efficient to reinforce a stiff material with a soft material.

### 3.6.2. Distribution of stress in two beams with different stiffnesses

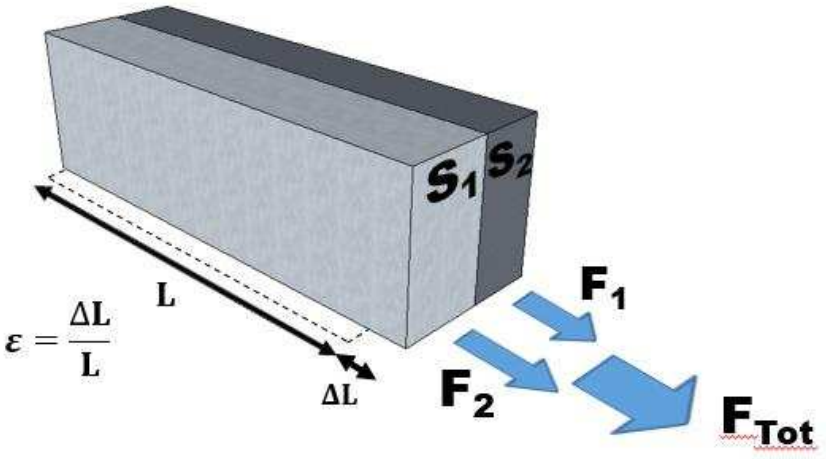


*Figure 43: Schematic diagram of 2 beams in parallel under tensile stress.*

To understand this, we can consider two beams in parallel, which represent the two elements of a conductor. As we will see in part II-2.2, the stress which limits the specific energy of a winding is generally the hoop stress, which is a traction stress, applied longitudinally to the conductor. In our example, we therefore consider a simplified case in which the conductor made of two parallel beams is only submitted to a longitudinal traction force F. As the two beams are the two parts of a same conductor, they are submitted to the same strain ε. The section of the beam n°1 is $S_1$, the section of the beam n°2 is $S_2$. The force applied to section 1 is $F_1$ and the force applied to section 2 is $F_2$. The stress of section 1 is $\sigma_1$, the stress of section 2 is $\sigma_2$, the Young modulus of material 1 is $E_1$ and the Young modulus of material 2 is $E_2$. The total force applied to the conductor is $F_{tot}$, the total section of the conductor is $S_{tot}$. The average stress on the conductor is $\sigma_{av}$ and the equivalent Young modulus of the conductor is $E_{eq}$. Thanks to following equations, we can then show that the beam with the higher Young modulus bear higher stress. From equation 28, the ratio between the stress of beam n°1 and beam n°2 is proportional to the ratio of their Young moduli.

$$\varepsilon_1 = \varepsilon_2 = \varepsilon \quad (17) \qquad F_{Tot} = F_1 + F_2 \quad (18) \qquad S_{Tot} = S_1 + S_2 \quad (19)$$

$$\sigma_{av} = \frac{F_{Tot}}{S_{Tot}} \quad (20) \qquad \sigma_1 = \frac{F_1}{S_1} \quad (21) \qquad \sigma_2 = \frac{F_2}{S_2} \quad (22)$$

$$\sigma_{av} = E_{eq}\,\varepsilon \quad (23) \qquad \sigma_1 = E_1\,\varepsilon \quad (24) \qquad \sigma_2 = E_2\,\varepsilon \quad (25)$$

$$\sigma_1 = E_1\,\frac{\sigma_{av}}{E_{eq}} \quad (26) \qquad \sigma_2 = E_1\,\frac{\sigma_{av}}{E_{eq}} \quad (27)$$

$$\frac{\sigma_1}{\sigma_2} = \frac{E_1}{E_2} \quad (28)$$

The value of the equivalent Young modulus is given by equation 29 (Rule of mixtures):

$$E_{eq} = \frac{E_1 S_1 + E_2 S_2}{(S_1 + S_2)} \tag{29}$$

The stress in the section of the beam n°1 is given by equation 30:

$$\sigma_1 = \frac{F_{\mathrm{Tot}}}{S_1 + S_2 \times \frac{E_2}{E_1}} \tag{30}$$

From equations 28 or 30, we can understand that reinforcing a stiff material with a soft material is inefficient. That is the reason why the copper stabilizer only plays a little role in the mechanical strength of REBCO conductors submitted to longitudinal stress. It is of course possible to reinforce a stiff material with a soft material, but the softer is the reinforcement material, the thicker will be the reinforcement to reduce the stress of the reinforced material to acceptable value. If the goal is to sustain a given tensile stress with a conductor which has to be as light as possible, reinforcing the original material with a softer material is interesting only if this reinforcement material is very light and that there is no constrain on the volume of the total conductor.

### 3.6.3. Proposition of materials to reinforce REBCO tapes

In the frame of the high energy density SMES of the BOSSE project, it would be interesting to have a conductor which could sustain high tensile stress while being light, i.e. which ratio between its maximum allowable tensile stress and its density is as high as possible. But in REBCO tapes available on the market, the substrate is made of Hastelloy® C-276, which has a density of 8900 kg/m$^3$ and a Young modulus of 217 GPa at 4.2 K. It is a very stiff material, but also heavy. It would therefore be interesting to reinforce it with a lighter material, but which Young modulus is in the same range or even higher than 217 GPa. Unfortunately, there are not many materials that satisfy these requirements. We can cite stiff stainless steels such as the Durnomag (E = 190 GPa at 30 K, 7900 kg/m$^3$). Nevertheless, the benefit compared to Hastelloy®C-276 is limited. So as to find more interesting reinforcement materials, we have to look at the family of synthetic fibres, such as glass fibres, carbon fibres or aramid fibres. Even if these materials have outstanding mechanical properties, they also have thermal contraction coefficients which are quite different of the ones of the Hastelloy®C-276 and copper, and make them difficult to associate to REBCO tapes. They are also difficult to handle and to associate to REBCO tapes for practical reasons, since they have to be used as epoxy impregnated composites. A last solution to explore and which could mitigate these problems is to use metallic matrix composites, in which fibres with high mechanical properties are included in a metallic matrix, such as the MetPreg®. The matrix of the MetPreg® is made of aluminium. It is available today as tapes which thickness is at least of 200 µm. Of course, the price of such a material is high, around 1000 $/kg.

In a general way, if a reinforced conductor or cable has to be designed for a specific winding with given requirements, the section of the reinforcement has to be determined, depending on the chosen materials. The compatibility between thermal expansions of the materials has to be verified. It is of course necessary to wonder if there is a practical way to associate the reinforcement material to the conductor, by brazing, lamination or gluing. Otherwise, a co-winding is conceivable, but can cause other practical issues (insulation, contacts…). Another possibility to reinforce a winding is the hoop reinforcement (see part III-2.2.1). In the frame of the high energy density SMES of the BOSSE project, no interesting reinforcement solution has been found. A standard tape without reinforcement has so been used.

| | Hastelloy® C-276 | 304L (Stainless steel) | G11-CR (warp) | Copper (OFHC, annealed) | Carbon /epoxy composite (66% fiber content) | Zylon® /epoxy composite (77% fiber content) | MetPreg® (50% fiber content) |
|---|---|---|---|---|---|---|---|
| Density (kg/m$^{3)}$ | 8940 | 7930 | 1900 | 8960 | 1600 | 1500 | 3300 |
| Young modulus (R.T.)(GPa) | 200 | 199 | 32 | 128 | 323 | 205 | 207 |
| Young modulus (4.2 K) (GPa) | 217 | 210 | 139 | 139 | 326 | 222 (77 K) | ? |
| Yield strength (R.T.)(MPa) | 500 | 1150 | 469 | 75 | 2358 | 3300 | 1407 |
| Yield strength (4.2 K)(MPa) | 1100 | 1300 | 872 | 90 | 2357 | 4300 (77 K) | ? |
| Electrical resistivity (R.T.) (nΩ.m) | 1230 | 720 | Insulator | 17 | ? | Insulator | 70 |
| Electrical resistivity (4.2 K) (nΩ.m) | 1230 | 490 | Insulator | 0.283 (RRR=60) | ? | Insulator | 7 |
| Thermal contraction (between R.T. and 4.2 K) (%) | 0.28 | 0.30 | 0.25 | 0.31 | -0.02 | -0.13 % (77 K) | ? |

*Table 3: Physical properties of possible reinforcement materials. These figures are indicative and can vary depending on the hardening, the manufacturer, the grade of the product, etc… G11-CR is a standardized Glass Fibre Reinforced Plastic (GFRP). Zylon® is a synthetic polymer. Its properties are given at 77 K instead of 4.2 K. MetPreg® is a metallic matrix composite with aluminium matrix. Its mechanical properties at low temperature are not available. Its electrical properties have been measured by us. R.T. stands for Room Temperature.*

# 4. Evaluation of the mechanical stress in solenoids

To determine precisely the mechanical stress distribution in a winding is not an obvious task. The appropriate calculation model depends on the structure of the conductor and the manufacturing technique of the winding. In the case of the high specific energy SMES of the BOSSE project, several difficulties have to be faced:

- As the insulation of the tape is polyimide, which is soft, and that the Hastelloy®-C276 is stiff, the winding is a stack of alternating soft and stiff materials. Because of that, the winding is anisotropic from the mechanical and the thermo-mechanical point of views. The Young equivalent moduli and the thermal contraction coefficients are different in the radial and circumferential directions in a solenoidal winding (see I-4.2).
- Contrary to most of LTS magnets, our REBCO windings are not impregnated with epoxy resin because of the risk of delamination of the conductor (see part I-1.3.5.2). The turns of the winding are rather independent from one another, and so they can separate from each other, for example under the influence of thermal contraction (see I-4.3). As it is difficult to simulate the mechanical behaviour of a winding with independent thin tapes thanks to a simulation software based on FEM (Finite Element Method), it is required to find adapted models to evaluate the mechanical behaviour of such a winding.

These points are developed below.

## 4.1. Analytical formulas to evaluate the hoop stress in solenoids

### 4.1.1. JBR formula

If we consider a single thin turn which carries a current density J and is submitted to an axial field B, the turn is submitted to a centrifugal force. As the turn is circular, this force results in circumferential stress, which is generally called “hoop stress”. The value of this stress, σ, is given by:

$$\sigma = \mathrm{JBR} \tag{31}$$

In which R is the radius of the turn. This formula is valid only for an independent turn, which is not in mechanical contact with other turns or structure

### 4.1.2. Wilson’s formula

Practically, the turns in a solenoid are not mechanically independent from one another. They will be pushed or pulled by other turns. Rather than using the “JBR” formula, it can be preferable to consider the body of the solenoid as a homogeneous material submitted to a volume density of the Laplace force. Arp [Arp77] has determined equations to calculate the hoop stress and radial stress in a solenoid with homogeneous current density. Wilson [Wils83] has also proposed an equation, known as the “Wilson’s formula”, which is currently used and valid under the following hypotheses:

- The material of the solenoid is mechanically isotropic
- The B field evolves linearly with the radius across the section of the solenoid, which is the case for long solenoids.
- The influence of the axial stress on the circumferential and radial stresses is neglected.

The input parameters are the inner radius, the thickness of the solenoid, the current density, the B field at the inner radius, the B field at the outer radius and the Poisson’s ratio of the material of the solenoid (but this last parameter has little influence). A Matlab® script which aims to calculate the stresses in a solenoid thanks to the Wilson’s formula is presented in appendix A-1.

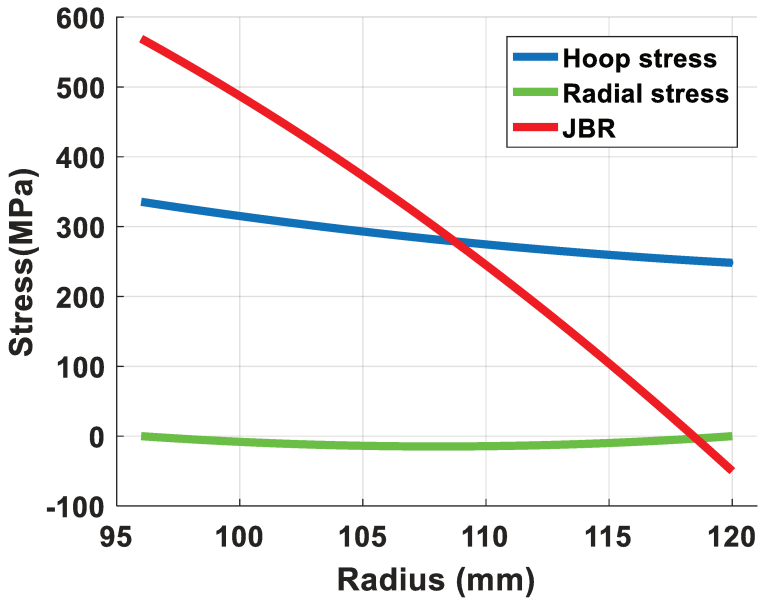


*Figure 44: Example 1. Stress distribution in a central pancake of the SMES of the BOSSE project, storing 1 MJ (see part II-3.3.5). The hoop stress and the radial stress are calculated with the Wilson’s formula.*

Fig. 44 shows the stress distribution, due to the magnetic load, in a central pancake of the SMES of the BOSSE project (see part II-3.3.5). The current density is 520 A/mm$^2$, the field $B_{INT}$ at the internal radius of the solenoid is 11.4 T and the field $B_{EXT}$ at the external radius of the solenoid is -0.8 T. We can see that the hoop stress is much smaller at inner turns with the Wilson's formula compared to the JBR formula, but it is higher at the outer turns. This is because the inner turns, which are submitted to a higher volume density of the Laplace force, are pressing the outer turns outward. We can see that the radial stress is negative due to the negative field (-0.8 T), which means that it is a compressive stress. The load of the Laplace force is spread from the inner turns to outer turns.

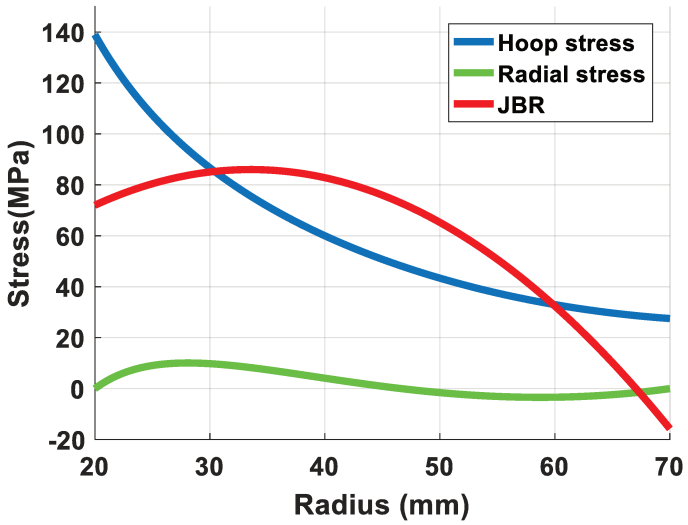


*Figure 45: Example 2. Stress distribution at the mid-plane of a solenoid with J = 250 A/mm2, H = 200 mm, R = 20 mm and TH = 50 mm.*

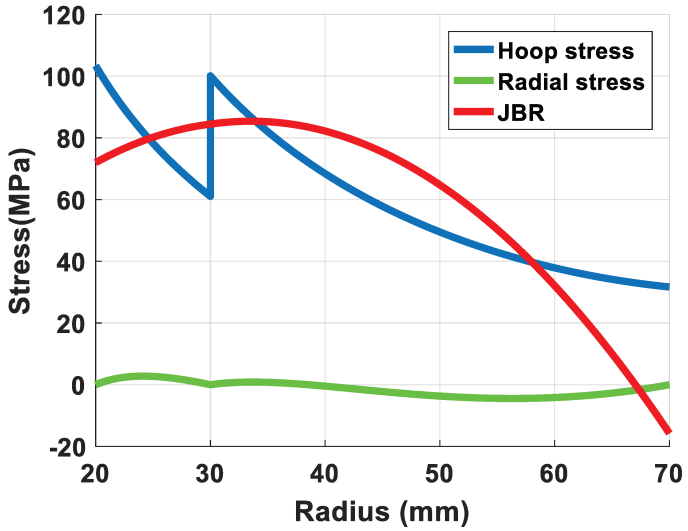


*Figure 46: Example 3. Same case than in Fig. 44, but with a split at r = 30 mm.*

Fig. 45 shows the stress distribution at the mid-plane of a solenoid with a rectangular cross section and a homogeneous current density of 250 A/mm$^2$. The height is H = 200 mm, the internal radius is R = 20 mm and the thickness is TH = 50 mm. Consequently, $B_{INT}$ is 14.3 T, $B_{EXT}$ is -0.9 T. In this configuration, we can see that that the maximum hoop stress calculated with the Wilson's formula is higher than the maximum of the JBR formula. At the inner part of the solenoid, the radial stress is positive, i.e. this is

tensile stress. The inner turns are pulled outward by the outer turns because of the epoxy impregnation, increasing their hoop stress.
In Fig. 46, almost the same case is considered. But instead of considering one single solenoid with a thickness of 50 mm, we consider that the solenoid is split in 2 mechanically independent coaxial solenoids, separated at a radius r = 30 mm. The field distribution is therefore the same as in the case presented above. But we can see that the maximum hoop stress is much lower than in the previous case.
From these examples, we can draw two conclusions:

- Depending on the configuration of the solenoid, it is possible that, according to the Wilson's formula, some parts of the solenoid are submitted to a radial tensile stress. Of course, this is valid only for impregnated magnets. For non-impregnated magnets, there cannot be tensile stress between the turns. The turns will separate instead and behave according to the JBR formula.
  The case the Wilson's formula can indicate that a part of the solenoid is submitted to a tensile radial stress is when the solenoid is thick (see the above examples) or if the solenoid is submitted to an external field (see part III-3.2.2).
- In an impregnated magnet, it can be interesting to split the solenoid in several coaxial solenoids or to make the turns independent [HTIW17] in order to limit the hoop stress. There are therefore mechanical reasons to the "nested coils" concept (see part I-2.2.1.1.2) in addition of optimizing the use of conductor.

# 4.2. Stress distribution in a mechanically anisotropic winding

A required hypothesis to use the Wilson's formula is that the body of the solenoid is mechanically isotropic, but this is not the case of a REBCO winding. This anisotropy has an influence on the stress distribution of a winding.

## 4.2.1. Equivalent Young moduli of anisotropic conductors

An insulated REBCO tape is a stack of thin layered materials with very different Young Modulus. As a consequence, the equivalent longitudinal (i.e. parallel to the length of the tape) Young Modulus $E_{//}$ is different from the equivalent transverse (i.e. parallel to the face of the tape) Young Modulus $E_{\perp}$.

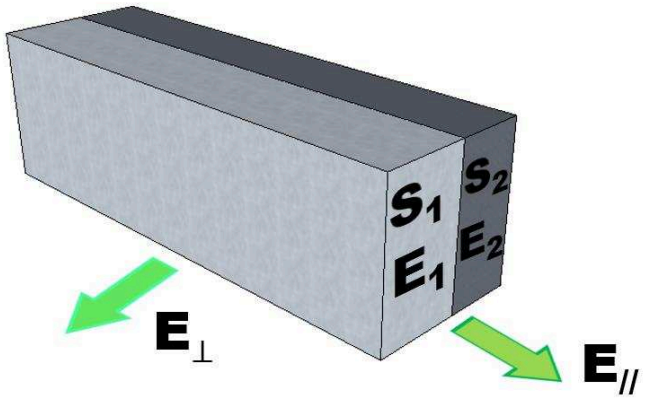


*Figure 47: Schematic diagram of two beams in parallel. The material 1 has a Young Modulus $E_1$ and a cross section $S_1$. The material 2 has a Young Modulus $E_2$, different from $E_1$, and a cross section $S_2$. Consequently, the equivalent longitudinal and transverse moduli are different.*

In order to evaluate $E_{//}$ and $E_{\perp}$ in the general case of an anisotropic conductor, we can use the rule of mixtures, which is for example used to determine the mechanical properties of composite materials. Let's consider two beams in parallel made of two different materials. According to the rule of mixtures, $E_{//}$ and $E_{\perp}$ are given by the following equations:

$$E_{//} = E_1\, vf_1 + E_2\, vf_2 \tag{31}$$

$$\frac{1}{E_{\perp}} = \frac{vf_1}{E_1} + \frac{vf_2}{E_2} \tag{32}$$

Equation 31 is the same as equation 29 (See part I-3.6.3). $E_1$ and $E_2$ are the Young moduli of materials 1 and 2. $vf_1$ and $vf_2$ are the volume fractions of materials 1 and 2. In our case, if $S_1$ is the section of material 1 and $S_2$ is the section of material 2:

$$vf_1 = \frac{S_1}{S_1 + S_2} \tag{33}$$

$$vf_2 = \frac{S_2}{S_1 + S_2} \tag{34}$$

### 4.2.2. Application to the conductor used for the high specific energy SMES

The REBCO conductor finally used for the high specific energy SMES of the BOSSE project (see part II-3) has a substrate made of Hastelloy-C276® which is 60 µm thick. Several buffer layers, the REBCO layer and a silver layer are deposited on it. This set of layers is nearly 5 µm thick in total. The whole of this is plated with copper, with 15 µm on each side so 30 µm in total. This stabilised conductor is then insulated with polyimide, with 20 µm on each side so 40 µm in total. The total thickness of the conductor is therefore 135 µm.

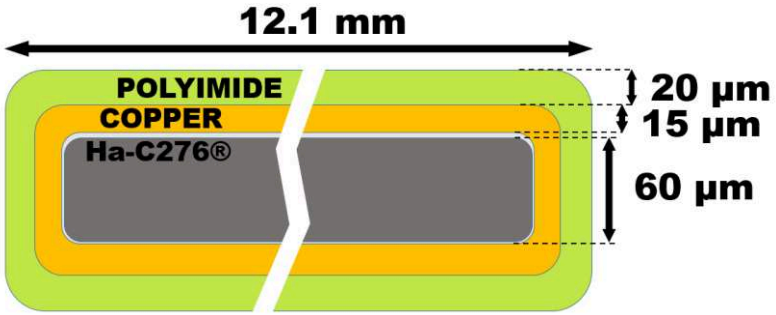


*Figure 48: Schematic diagram of the REBCO conductor used to manufacture the SMES of the BOSSE project.*

The Young moduli at 4.2 K of Hastelloy®C-276, copper, silver and polyimide are indicated in the table below. As polyimide is a wide chemical family, several values have been found for the Young modulus of the polyimide at low temperature [Fu13] [YaMY95], between 3 GPa and 12 GPa. Our supplier of REBCO tapes for the BOSSE project is the Russian company SuperOx, which is using P84® polyimide. The P84® polyimide has a Young modulus of 4 GPa at room temperature [High00]. We have not found data about the Young modulus of P84® polyimide at 4.2 K. But by analogy with the Upilex-R polyimide which has a Young modulus of 4 GPa at RT and a Young modulus of 5.5 GPa at 4.2 K [YaMY95], we can estimate that the Young modulus of the P84® polyimide insulation is around 5.5 GPa. Nevertheless, this value should be verified by proper measurements.

Based on the values in table 4, we can calculate the equivalent longitudinal Young Modulus $E_{//}$ and the equivalent transverse Young Modulus $E_{\perp}$ of the conductor used in the high specific energy SMES of the BOSSE project. As the buffers and REBCO layers are very thin, their influence is neglected. It is considered that they have the same Young modulus that silver. By adapting the rule of mixtures (equations 31 and 32) to a four components material instead of a two materials component, we can calculate $E_{//}$ and $E_{\perp}$: 132 GPa and 17 GPa respectively.

| | Ha®C-276 | Copper | Silver | Polyimide | Total | |
|---|---|---|---|---|---|---|
| Young modulus (4.2 K) (GPa) | 217 | 139 | 91 | 5.5 [3 – 12] | $E_{//}$ = 132 | $E_{\perp}$=17 |
| Thickness (µm) | 60 | 30 | 5 | 40 | 135 | |

*Table 4: Estimated stiffnesses of material mainly constituting the REBCO conductor and calculated equivalent transverse and longitudinal Young moduli.*

### 4.2.3. Effect of the mechanical anisotropy of the winding on the stress distribution in the solenoid

The mechanical anisotropy of a conductor has an influence on the stress distribution of the winding. In the case of the BOSSE SMES for example, $E_{//}$ is 132 GPa and $E_{\perp}$ is 17 GPa. The insulated REBCO tapes are therefore highly anisotropic from a mechanical point of view. Once the tapes are wound as pancakes, $E_{//}$ corresponds to the circumferential Young modulus and $E_{\perp}$ corresponds to the radial Young modulus. This anisotropy has an influence on the stress distribution in the solenoid.

We have seen that in a solenoid and according to the Wilson's formula, the load of the Laplace force is spread from the inner turns to outer turns. But if the turns are separated by a soft material such as polyimide, the load transfer is less effective. The radial stress is lower and so the inner hoop stress is higher compared to what is expected with the Wilson's formula.

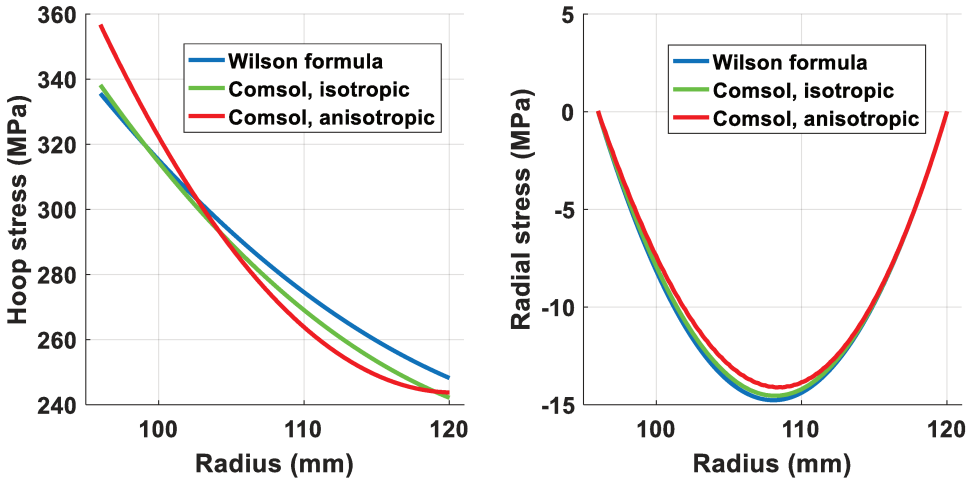


*Figure 49: Comparison between the results of the Wilson's formula and a FEM simulation software. In this last case, the material of the body of the solenoid is either isotropic or anisotropic.*

In figures 49, we suppose that the magnetic load is the same as in figure 44. We can compare the resulting stress distribution for 3 different cases: the first case is the result of the analytical Wilson's formula. The second case is the result of a simulation with the FEM software Comsol® for a long solenoid made of isotropic material. The third case is the result of a simulation with Comsol® for a long solenoid made of anisotropic (orthotropic) material ($E_{//}$ = 132 GPa and $E_{\perp}$ = 17 GPa). We can see that for the third case, the hoop stress at inner turns is higher than in other cases, in the order of 6 %. Of course, this value depends on the mechanical anisotropy of the winding and on the geometry of the considered system.

## 4.3. Mechanical effects of thermal contraction in a solenoid

The thermal contraction of insulated REBCO tapes is anisotropic, similarly to its stiffness. The thermal contraction of polyimide is much higher than the thermal contraction of Ha®-C276 or copper. In the same way as for the anisotropic Young Modulus, it is possible to define a longitudinal and a transverse thermal contraction. The transverse thermal contraction of the tape is the sum of the thermal contractions of the materials of the tape, which are weighted by the proportion of each material in the tape. In the longitudinal direction, the thermal contraction is dominated by the behaviour of stiffest materials, i.e. Ha®C-276 and copper [Bart13]. It is evaluated to 0.29 %.

| | Ha®C-276 | Copper | Silver | Polyimide | Total | |
|---|---|---|---|---|---|---|
| Thermal contraction (between R.T. and 4.2 K) (%) | 0.28 | 0.31 | 0.41 | 0.9 [0.5 – 0.9] | $\Delta L/L_{//}$ = 0.29 | $\Delta L/L_{\perp}$=0.48 |

*Table 5: Estimated thermal contraction of material mainly constituting the REBCO conductor and equivalent longitudinal and transverse thermal contractions. Data from [CoGn61]. Values of thermal contraction of different types of polyimide can be found between 0.5 and 0.9. In order to be conservative, the value of 0.9 is used for calculations.*

In order to calculate the stress generated in an impregnated solenoid during the cooling, it is possible to use the formula given by Arp [Arp77]. A Matlab® script which implements this formula is presented in appendix A-2. If we take the example of the solenoid of the BOSSE project and assuming that the turns of insulated REBCO tapes are bonded together by an impregnation, the resulting stress distribution is given in figure 50.

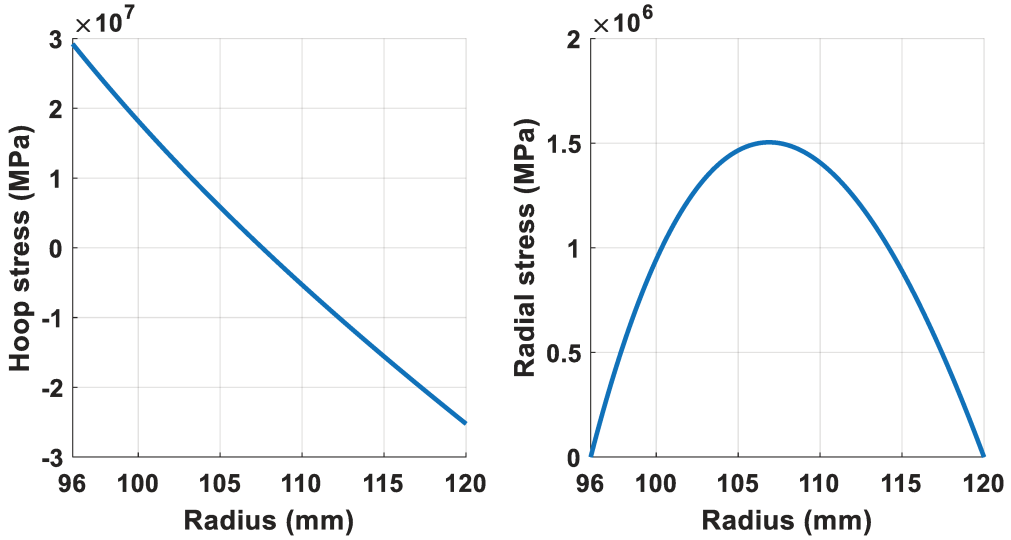


*Figure 50: Internal stresses resulting from the thermal contraction in a winding with the same dimensions and thermo-mechanical properties that a pancake of the SMES of the BOSSE project, but with bonded turns.*

This figure shows that the radial stress is positive, which means that it is tensile. The turns are pulled from each other. But in reality, the solenoid of the SMES project is not impregnated. During cooling down, the turns will therefore separate. The body of the coil is no more continuous and the Arp's formula cannot be applied. Instead, we can evaluate the behaviour of the coil during cooling down by geometrical considerations.

Let us consider an independent single turn of radius R made of REBCO tape. The longitudinal thermal contraction of the tape corresponds to the circumferential thermal contraction of the turn $\varepsilon_{//}$. Once

that the turn is cooled down, the length of its perimeter has been reduced of $2 \pi R \varepsilon_{//}$. As the perimeter is proportional to the radius, the radius has been reduced by $R \varepsilon_{//}$. Now, let's consider two adjacent turns with initial radii R1 and R2, then R2-R1=TH in which TH is the initial thickness of the tape. After the cooling down, the distance between the two turns has been reduced of $TH \varepsilon_{//}$. But during the cooling down, the thickness of the turns has also been reduced of $TH \varepsilon_{\perp}$, in which $\varepsilon_{\perp}$ is the transverse thermal contraction of the tape. As $\varepsilon_{\perp} > \varepsilon_{//}$, there is therefore a gap between each turns, which is equal to $TH (\varepsilon_{\perp} - \varepsilon_{//})$. According to the values of tables 4 and 5, a gap of 0.26 µm appears between each turn during the cooling down. It can appear to be very small. But as there are 178 turns in the pancakes of the coil, the sum of radial empty spaces in a pancake is equal to 46 µm. We will see in part II-3.4.2 what the consequence of such a gap is.

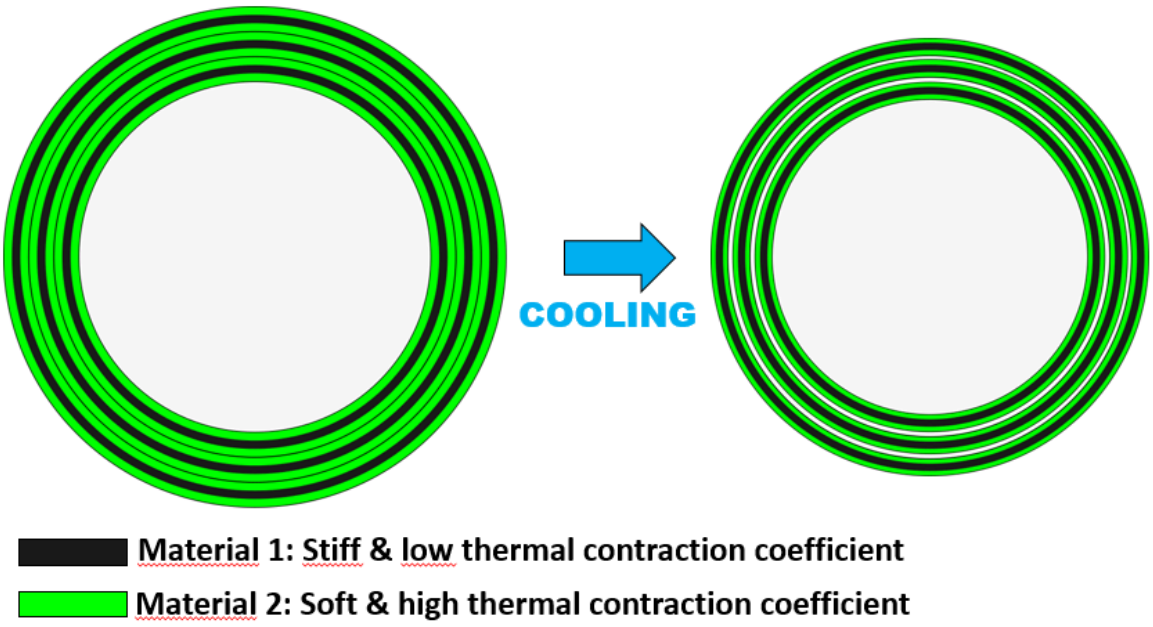


*Figure 51: Principle diagram of the evolution of dimensions during the cooling of a pancake made of thermo-mechanically anisotropic wire. If $E_{//} > E_{\perp}$ and $\varepsilon_{\perp} > \varepsilon_{//}$, and that the pancake is not impregnated, some gaps are appearing between the turns during the cooling down.*

## 4.4. Pre-stress and bracing

In order to improve the mechanical performance of a solenoid, it is possible to use pre-stress technique. It consists in winding the solenoid under tension. This will add some circumferential stress, which may seem counter-productive at first. What actually happens is that as the external turns are in tension, they will press the inner turns inward. So little by little, the inner turns are put into radial compression. If the inner mandrel is soft or can be compressed, this radial centripetal pressure is converted into inward radial displacement and compressive circumferential stress.
In order to convert the centripetal pressure into compressive circumferential stress, it is possible to soften the mandrel after the winding by partially removing it and making it thinner. It can even be totally removed if the coil is impregnated.

Following the equation given by Arp [Arp77], it is possible to calculate the stress distribution resulting from a winding under tension. A Matlab® script which implements this equation is presented in appendix A-3. Fig. 52 presents the stress distribution corresponding to the prestress of a pancake of the NOUGAT project [FBCD18]. It has been used to validate our implementation of the Arp's formula by comparison with the calculation made at the CEA Saclay.

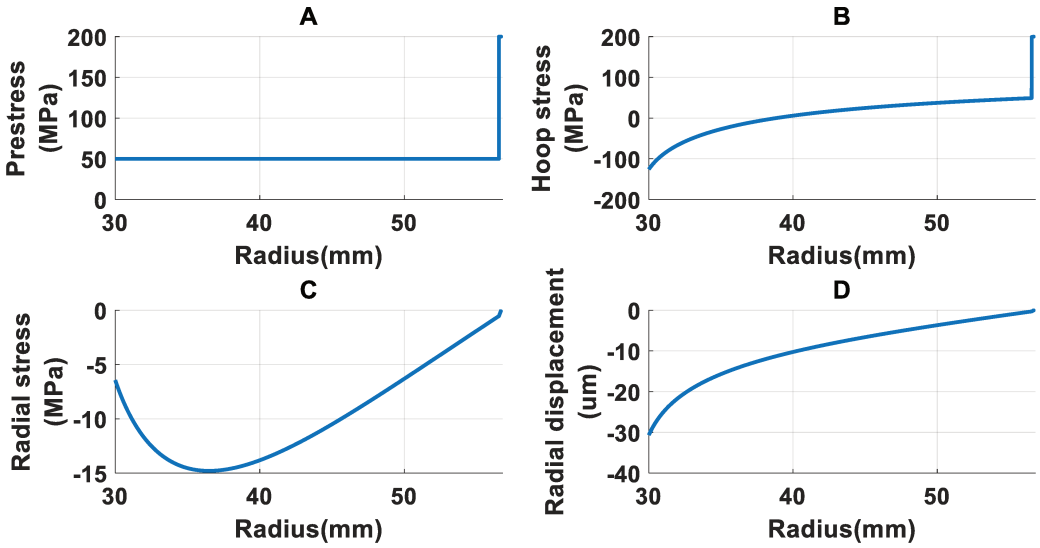


*Figure 52: Prestress and resulting stress distribution of a pancake of the NOUGAT project. The configuration is described in appendix A-3.*

The winding of the nougat project is a cowinding of a non-insulated REBCO tape and stainless steel tape. In this figure, part A, the winding has been made under a tension corresponding to a longitudinal stress of 50 MPa. After the electrical contact, the winding is continued only with the stainless steel tape. There are 5 additional turns, which are wound under a tension of 200 MPa. In B, we can see that the circumferential stress is compressive at inner turns, hence the term “prestress”. The inner turns are in circumferential compression. This compression has to be counterbalanced by the magnetic forces before the inner turns start to be submitted to a tensile stress.
We can also see that the external turns are in circumferential tension. It means that thanks to prestress technique, the inner turns are compressed but this is made at the expense of the external turns, which are submitted to additional tensile stress.

In order to improve the mechanical resistance of the solenoid, it is also possible to reinforce it by an external bracing, such as a ring [WNHA15], a tube or an external additional winding. This reinforcement is all the more efficient if it applies a centripetal radial stress to the solenoid. It can be achieved thanks to the prestress of an external additional winding, or by using the difference of thermal contraction. For example, it is conceivable to fit the solenoid inside a tube made of a material with high thermal contraction, such as aluminum. During the cooling down, the external tube is going to compress and prestress the solenoid, which has a lower thermal contraction. Nevertheless, this kind of solution can cause Eddy currents issues.
A limit of the external reinforcement is that it is mainly reducing the hoop stress of the external turns of the solenoid, while the inner turns are often those submitted to the highest hoop stress. Hence, the external reinforcement is efficient if the magnetic load applied to the inner turns can be transmitted, as radial stress, up to the external reinforcement. This transmission is more efficient if the winding is thin and stiff.

## 4.5. Stress due to bending

The fact of bending or winding a conductor also generates internal stress in the conductor. In a wound conductor, the local stress due to bending depends on the radius of curvature and the distance to the neutral axis. In a homogeneous or symmetrical conductor, the neutral axis is at the middle of the

conductor. A REBCO tape can be bent in two different ways: along the face or along the edge. The strain generated by these two kind of bending is given by equations 35 and 36. R is the radius of curvature. x and y are the distances to the face bending and edge bending neutral axes (see Fig. 53).

$$\varepsilon_{fb}(R) = \frac{y}{R} \tag{35}$$

$$\varepsilon_{eb}(R) = \frac{x}{R} \tag{36}$$

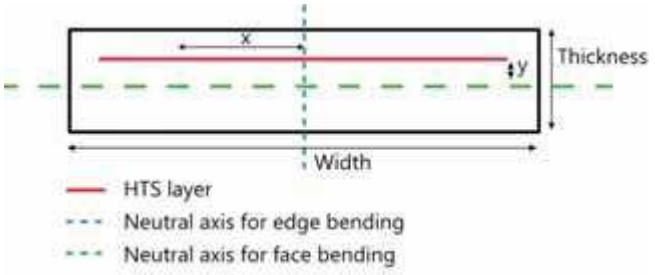


*Figure 53: Positioning of neutral axes in a REBCO conductor. The HTS layer is deposited on one side of the substrate and is therefore not place at the neutral axis for face bending.*

The two equations are similar, but as the tape is much wider than it is thick, the edge bending generates much higher internal stress than the face bending. There is therefore an “easy bending” (face bending) and a “hard bending” (edge bending).
These equations give us a first idea of what are the minimum “easy bending” and “hard bending” minimum radii of curvature of REBCO tapes. But as REBCO conductors have a complex architecture and that the stabilizer is not necessary homogeneously deposited, experimental measures are preferred. According to the measurements of J. Fleiter [Flei13], the minimum radius of curvature for the face bending of a REBCO tape before degradation of the critical current is in the centimetre range. The minimum radius of curvature of the edge bending is in the meter range for a 12 mm wide tape.
In the BOSSE project, the minimum radius of curvature of the solenoid is 96 mm. There is therefore no problem with the face bending of the tapes. Nevertheless, the internal stress due to bending can be significant in solenoids with low radius of curvature such as high field magnet inserts or in windings made of thick conductors.

As a side note, the twisting of a tape also generates internal stress. Formulas to calculate the stress resulting from the twisting of a conductor are also given in the thesis of J. Fleiter [Flei13]. But in the SMES of the BOSSE project, twisting of the conductor has been avoided.

# 5. Conclusion

In this first chapter are presented prerequisites and global considerations required for the design of SMES.

In the first part, the phenomenon of superconductivity is introduced and properties of different superconductors are described. A special focus is given on REBCO conductor since it is used in the BOSSE project. Nevertheless, other conductors are also presented because they can be interesting for SMES technology, depending on the specific purpose and objectives of a SMES.

In the second part, the physical principles and limits of SMES are presented. Advantages and drawbacks of SMES compared to other energy storage systems are also approached, as well as advantages and drawbacks of different kind of topologies for a SMES winding. It is shown that very different topologies are possible and existing and that the design of a SMES is a very open problem.

The third part is dedicated to different technical aspects of superconducting windings: stability and protection, operating temperature and cooling, losses, architecture and reinforcement of conductor. Rules and suggestions are given to efficiently reinforce and lighten the conductor, even if no easy solution was found in the case of the BOSSE project.

In the fourth part, a special attention is paid to the mechanical aspect since a high stress is required to reach a high specific energy. Solutions are proposed to estimate the stress in a solenoid, taking into account the fact that the winding is impregnated or not and the thermo-mechanical anisotropy of conductor.

# Chapter 2: Design and optimization of windings for energy storage

## 1. Development of an efficient calculation method for SMES optimization

### 1.1. Necessity to define a compromise between the objectives of the SMES.

As we have seen in part I-1.4.3, some SMES systems have been designed and/or manufactured for a wide range of applications and for a wide range of stored energy. Clearly, there is no possibility to give a simple answer to what the "best" choice for the shape and the engineering choices for a SMES coil is. This answer will be different as per the objectives and requirements of the SMES coil. This objectives can be numerous and varied depending on the purpose of the SMES coil. For example, a SMES considered to supply an electromagnetic launcher has to be an embedded system that can provide a very high current and power. Consequently, such a SMES has to have simultaneously a small volume, a low mass, a low fringe field, a high maximum power, and a high output current [CBTF17]. In addition, it is preferable if the investment and operating costs remain low.
Of course, all of these objectives are not mutually compatible. For example:

- A SMES with a low volume requires a high field. But a high field reduces the current carrying capability of a conductor, so it increases the cost of superconductor.
- A SMES that has a high operating current needs adequately sized current leads, which increases the thermal losses of the system. So it increases the size and the cost of the cooling system.
- A solution to limit the thermal losses is to increase the operating temperature of the coil. But it reduces the current carrying capability of a conductor, or requires to reduce the B field, which increases the volume of the coil.
- The use of a cable to increase the operating current can also increase the AC losses if it is not properly designed (see part I-3.4.2.3).
- A very high power is synonym of a fast discharge and so a fast flux variation, which can generates high AC losses and heating of the coil. The choice of the cooling method is therefore important (see part I-3.2).
- The use of a thick insulation to bear very high voltages can affect the mechanical properties of the coil (see part I-4).
- Etc...

Moreover, some criteria, like the volume of the coil, are not easy to define. Depending on the topology of the coil, the B field can be confined in a limited volume or radiates all over the space (see Fig. 55 and Table 6).

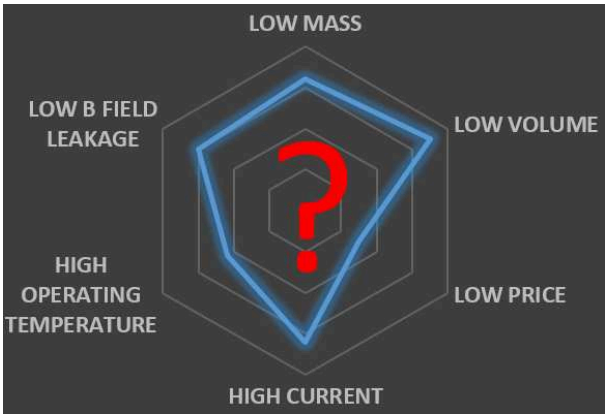


*Figure 54: A compromise between contradicting objectives has to be found to design a SMES.*

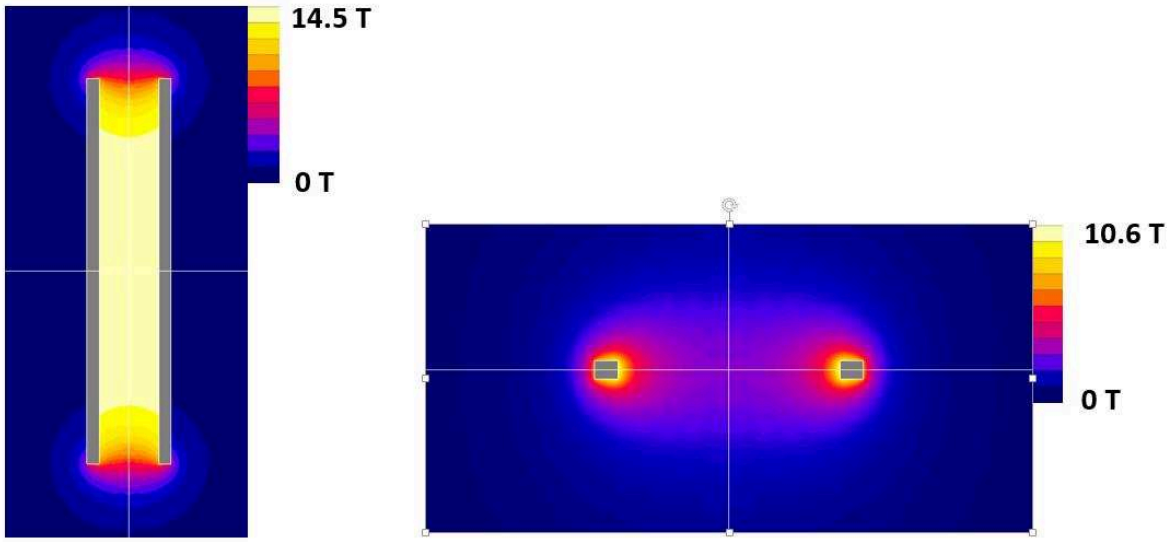


*Figure 55: Cross section views of 2 solenoids with similar energy, current density and hoop stress, but very different aspects. The volume of the body of the solenoid is smaller on the right side. But on the left, the field is confined inside the solenoid. On the right, it radiates all over the space. The characteristics of these solenoids are reported in table 6.*

| | **Left** | **Right** |
|---|---|---|
| **Energy (MJ)** | 100 | 100 |
| **Current density (A/mm$^2$)** | 100 | 100 |
| **Maximum hoop stress (Wilson) (MPa)** | 300 | 300 |
| **Height (m)** | 3.7 | 0.225 |
| **Outer diameter (m)** | 0.8 | 3.26 |
| **Thickness (m)** | 0.117 | 0.282 |
| **Volume of the body of the solenoid (m$^3$)** | 0.93 | 0.59 |

*Table 6: Characteristics of the 2 solenoids presented in Fig. 52.*

## 1.2. Reflection about the problem of SMES optimization

As we have just explained, there are many related and counteracting parameters to define during the design stage of a SMES. That is why optimization algorithms are often used to determine the most adapted geometry of the coil. An optimization function is defined, which assigns weighting coefficients to specific objectives such as the target energy, minimizing the volume of conductor, minimizing the stray field, etc…There can be several criticisms to this approach.

- The algorithm gives the optimal solution to the defined problem, but this will not be the best solution if the problem is not properly defined. Actually, given the high number of parameters, objectives and engineering issues involved in the design of a SMES coil, defining the weighting coefficients or the appropriate simplifying assumptions of the optimization problem has nothing obvious. It requires to have a good understanding of the physics of the problem and a good estimation of what will be the main limitations. In other words, we need to have a fairly accurate idea of what is the expected solution to define correctly the optimization problem.
- The optimizations are generally based on the combination of an iterative optimization algorithm and a simulation software. Genetic algorithms [HNSH07] [KKLC06] [XRTX17] or simulated annealing [SoII08] [ChJi14] [NoYI02] are often used in association with a FEM (Finite Element Method) software. Software for electromagnetic simulation based on the Biot-Savart law can be used instead of FEM software [MoHF11] [DZSC15]. Other algorithms can also be used [SSSW09] [ABFJ08]. The problem of all of these methods is that a query is send to the simulation software at each step of the optimization, and that the number of steps in the whole optimization process is very large. Furthermore, as we will see later (see part II-2.4.1), the optimal geometry of the problem can be a very "flat" optimum, which can disturb some maximum-seeking algorithms and requires uselessly long calculation time [CBTF17]. As a result, the optimization process is time consuming or requires high computational power.
  To solve this issue, it is possible to use analytical formula in order to evaluate the relevant quantities of the tested sets of parameters, such as the inductance or the energy for instance [CJXZ09] [Iwas09] [Lieu97] [MoWe69] [SMPP95] [TsNS02]. Nevertheless, analytical formulas are not available for any topology, and for a given topology they are not valid on a wide range of aspect ratios. Furthermore, to our knowledge, there are no analytical formulas to calculate quantities such as the transverse field, the external field or the axial stress in solenoids, which can be essential quantities in the design of a HTS SMES.
  In conclusion, either a numerical method is used and the process is time consuming, or analytical formulas are used and the result can be inaccurate.
- In any case, an optimization process is valid only for a given set of objectives. If the set of objectives is changed, for example if the target energy is changed, the whole process has to be repeated.

For all of these reasons, we have developed new tools and approach for the pre-design of SMES coils. They are focused on understanding the trends in the variations of the objectives with the input parameters, rather than optimal solutions.

## 1.3. Evolution of quantities for a homothetic transformation or variation of current density

The essential quantities for a given winding with a given current density, such as the total energy, the maximum B field, the force distribution, etc… can be calculated thanks to a FEM simulation software for example. One important observation is that, thanks to simple equations presented in this part, it is possible to calculate these same quantities for another winding which is a homothetic transformation of the original winding. It is also very easy to calculate these same quantities for the same winding with another current density.
In this part, we will take the example of a solenoid with a rectangular cross section and homogeneous current density (see part I-2.1.1.2). Nevertheless, the reasoning and the equations are valid for all types of windings, even if more geometrical parameters may be necessary to describe more complex geometries.

Because of the non-linear behaviour of magnetic materials, these scaling laws are not strictly valid if there is some magnetic material in the system, such as a ferromagnetic core for instance, unless the magnetic material being completely saturated.

### 1.3.1. Definition of aspect ratio parameters α and β

The geometry of a solenoid can be defined by the 3 following parameters (see Fig. 21, 22 or 58):

- The inner radius R
- The height H
- The thickness TH

or it can be defined by the 3 following parameters:

- The inner radius R
- The parameter α=H/(2R)
- The parameter β=TH/R

This description of the geometry has the advantage that in a homothetic transformation, only R is changing, and α and β are held constant. The factor $\lambda=R/R_0$, in which $R_0$ is the original radius of the solenoid, is the ratio of the homotethy. Then the new height is $H=\lambda H_0$ and the new thickness is $TH=\lambda TH_0$, with $H_0$ the original height of the solenoid and $TH_0$ the original thickness of the solenoid.

Using aspect ratio parameters, such as α and β, reduces by one the number of geometrical variables of the topological combinations which have to be tested. For the solenoid for example, the space of topological solutions which are explored is characterized by 2 parameters, α and β (see part II-1.3.5). If the optimization is performed by systematically testing solutions directly in a simulation software, as usually done in an optimization process, three parameters have to be explored (R, H, TH) and the current density is also a variable parameter.
Aspect ratio parameters are commonly used for the design of superconducting magnets [Iwas09] [MoWe69] [RBCD11]. But from our knowledge, they have been only used for the calculation of the B field, but not to calculate the energy or the forces and stresses.

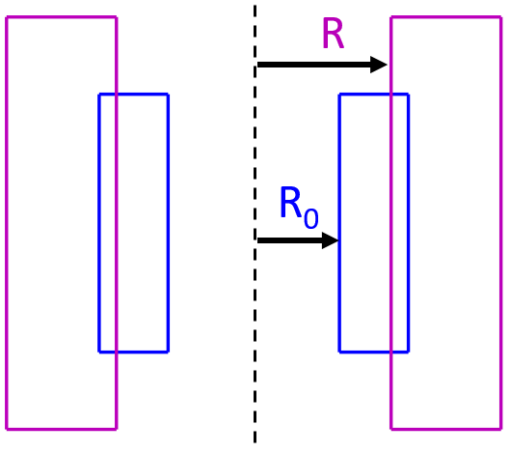


*Figure 56: Homothetic transformation from a solenoid with an inner radius R0 to a solenoid with an inner radius R. The factor $\lambda=R/R_0$ is the ratio of the homothety.*

### 1.3.2. Evolution of quantities for a homothetic transformation with constant current density

If a winding generates a magnetic field $\vec{B}_0$ at a point of space, then the homothetic transformation with a ratio λ of this winding generates a field $\lambda\vec{B}_0$ at the point of space that is the homothetic

transformation of the original point. In other words, the B field map generated by a winding is dilated according to the homothety of the solenoid, and the value of the B field evolves proportionnally to λ. This property is expressed mathematically by eq 37. It can be demonstrated from the Biot-Savart Law. This is valid if the current density J is homogeneous in the winding and if J is constant during the transformation.

$$\vec{B}(\lambda x_0, \lambda y_0, \lambda z_0) = \lambda \, \vec{B}_{0(}x_0, y_0, z_{0)} \tag{37}$$

The magnetic energy of the system is the integral over space of the square of the B field, in the absence of magnetic material (see part I-2.1.1.1). On the other hand, the volume of the system evolves with the third power of the ratio of an homothetic transformation. As a consequence, the energy stored by the system evolves with the fifth power of the ratio of an homothetic transformation (see Eq. 38). As the mass also evolves with the third power of the ratio λ, the specific energy evolves as the square of λ (see Eq. 39 ).

$$E = \lambda^5 \, E_0 \tag{38}$$

$$E_{mass} = \lambda^2 \, E_{mass\_0} \tag{39}$$

The volume force density of the Lorentz force is $\vec{J} \wedge \vec{B}$. As $\vec{B}$ evolves linearly with λ and the volume evolves with the third power of λ, the resulting forces integrated on a volume, such as the total axial force (see Fig. 58), evolve with the fourth power of λ (see eq. 40). As the cross sections evolve as the square of λ, the resulting stresses (hoop stress, axial stress) evolve as the square of λ (see Eq. 41), at least as far as the strain of the material is considered linear with the stress.

$$\vec{F} = \lambda^4 \, \vec{F}_0 \tag{40}$$

$$\vec{\sigma}(\lambda x_0, \lambda y_0, \lambda z_0) = \lambda^2 \, \vec{\sigma}_0(x_0, y_0, z_0) \tag{41}$$

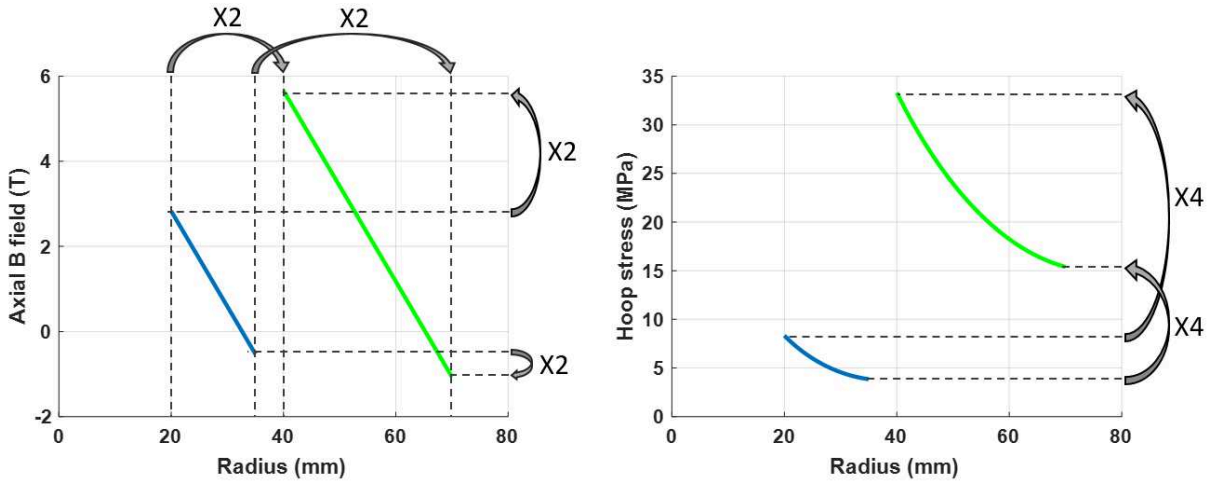


*Figure 57: Comparison at mid-plane of the axial B field and the hoop stress calculated by the Wilson's formula of two solenoids. The second solenoid is the homothetic transformation of the first solenoid, with a ratio λ = 2. For the first solenoid: R = 20 mm, TH = 15 mm, H = 50 mm. For the second solenoid, R = 40 mm, TH = 30 mm, H = 100 mm. In both cases, the current density is 200 A/mm². We can see that the B field evolves linearly with λ. The hoop stress evolves with the square of λ.*

### 1.3.3. Evolution of quantities with the current density

Once the essential quantities of a winding with a current density $J_0$ are calculated, it is also possible to get these same quantities for a winding which has the same shape but a different current density J. If the winding with a current density $J_0$ generates a magnetic field $\vec{B}_0$ at a point of space, then the field $\vec{B}$ generated at the same point when its current density J is proportionnal to the ratio ζ=J/ $J_0$ (see Eq. 42). It is also a consequence of the Biot-Savart Law.

$$\vec{B} = \zeta \vec{B}_0 \tag{42}$$

As the magnetic energy of the system is the integral over space of the square of the B field, then the total magnetic energy stored by the system evolves as the square of ζ (see Eq. 43), as well as the specific energy (see Eq. 44):

$$E = \zeta^2 E_0 \tag{43}$$

$$E_{mass} = \zeta^2 E_{mass\_0} \tag{44}$$

As the volume force density of the Lorentz force is $\vec{J} \wedge \vec{B}$, and that both $\vec{J}$ and $\vec{B}$ are proportional to ζ, then the resulting forces and stresses evolve as the square of ζ (see Eq. 45 and 46):

$$\vec{F} = \zeta^2 \vec{F}_0 \tag{45}$$

$$\vec{\sigma} = \zeta^2 \vec{\sigma}_0 \tag{46}$$

### 1.3.4. Evolution of quantities with a combination of a homothetic transformation and variation of the current density

It is of course possible to combine the evolutions of the quantities due to a homothetic transformation and a variation of the current density. By consequence, if the essential quantities of a given winding with a given current density are known, it is very easy to calculate these same quantities for a winding which is a homothetic transformation of the original one, whatever its current density is. If λ is the ratio of the homothetic transformation and ζ is the ratio of the current densities, then the evolution of the B field, the energy, the specific energy, the resulting forces and stresses are given by the following equations:

$$\vec{B}(\lambda x_0, \lambda y_0, \lambda z_0) = \lambda \zeta \vec{B}_0(x_0, y_0, z_0) \tag{47}$$

$$E = \lambda^5 \zeta^2 E_0 \tag{48}$$

$$E_{mass} = \lambda^2 \zeta^2 E_{mass\_0} \tag{49}$$

$$\vec{F} = \lambda^4 \zeta^2 \vec{F}_0 \tag{50}$$

$$\vec{\sigma}(\lambda x_0, \lambda y_0, \lambda z_0) = \lambda^2 \zeta^2 \vec{\sigma}_0(x_0, y_0, z_0) \tag{51}$$

### 1.3.5. Application to a solenoid with rectangular cross section and homogeneous current density

In order to use the equations above, we need reference values. In the case of the solenoid, we have calculated these quantities on a set of reference topologies, entirely characterized by their parameters

$R_0$, α and β. For all of these reference topologies, the internal radius $R_0$ is always the same, and has been arbitrarily fixed at 100 mm. The current density $J_0$ is also always the same, and has been arbitrarily fixed at 100 A/mm$^2$. α and β are both varying between 0.02 and 51. Both of them take 51 arbitrary different discrete values between 0.02 and 51. There are therefore 51 x 51 = 2601 reference topologies for which the essential quantities have been calculated. They have been calculated thanks to the FEM software Flux®, which is dedicated to electromagnetic simulation. The set of reference topologies is displayed in figure 59. We then obtain matrices of 2601 elements each which store the data about the essential quantities : energy, internal axial field ($B_{INT}$), external axial field ($B_{EXT}$), radial field ($B_R$) and the total axial force $F_Z$ (see Fig. 58). $B_{INT}$ and $B_{EXT}$ are necessary to calculate the hoop stress of the coil thanks to the Wilson's formula. $F_Z$ is the integration on the upper half coil of the axial force.

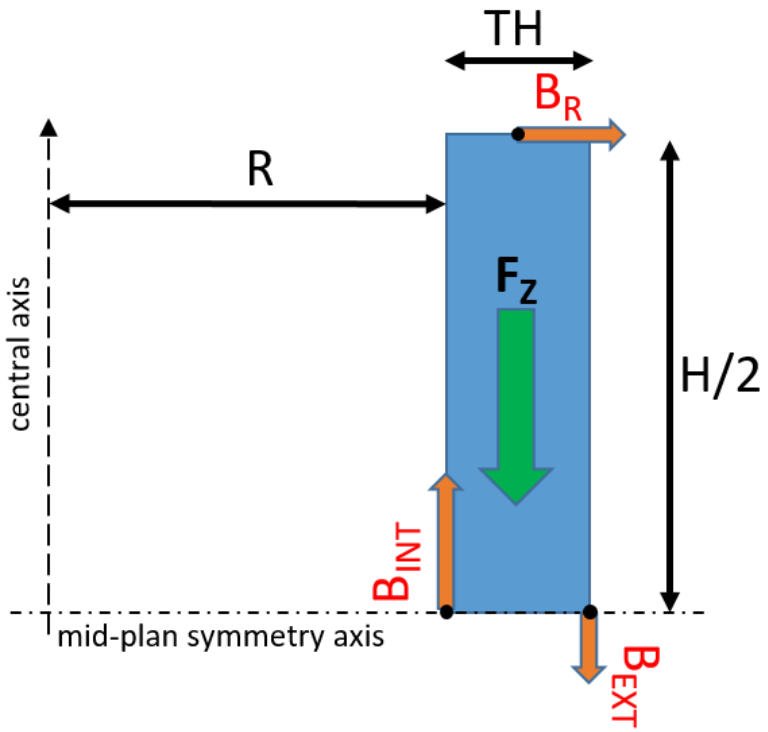


*Figure 58: Diagram of the half-solenoid which is simulated in the FEM softawre Flux®. TH and H are varying. The points where $B_{INT}$, $B_{EXT}$ and $B_R$ are measured are visible.*

$F_Z$ can be used to estimate the compressive axial stress at the mid-plane of the solenoid, i.e. where this stress is maximum. If we suppose that the axial force is homogeneously distributed on the mid-plane cross-section of the solenoid, then the maximum compressive axial stress $\sigma_Z$ is given by Eq. 52, where R is the inner radius and TH is the thickness of the winding (see Fig. 58).

$$\sigma_z = \frac{F_z}{\pi\left((R + TH)^2 - R^2\right)} \tag{52}$$

From the matrices which store the data of the 2601 reference points, it is possible to create interpolation functions to get the desired quantities for other values. In our case a piecewise cubic interpolation was used in Matlab® environment.
The aspect ratio of the (α,β) couples which are spotted in Fig. 59 are displayed in Fig. 60. We can see that the studied space of solutions covers a range of solenoids with very different aspect ratios.

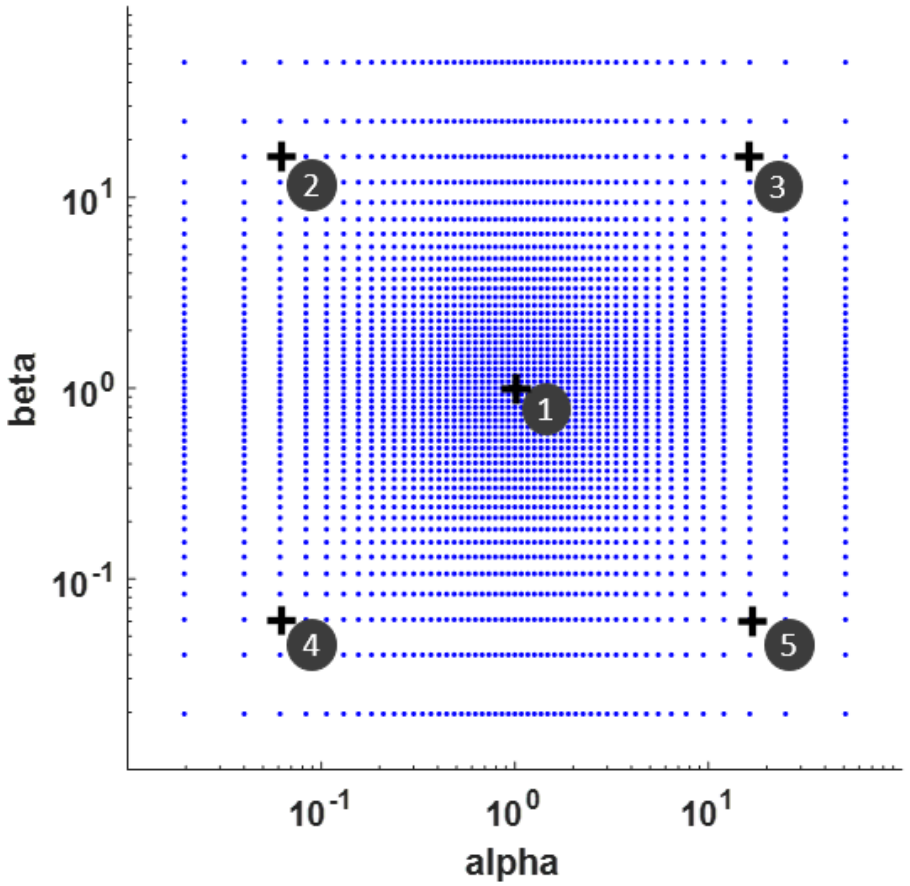


*Figure 59: For the solenoid with rectangular cross-section, the aspect ratio is characterized by the parameters α and β, with α=H/(2R) and β=TH/R. The coordonates in the (α,β) space of the topologies wich have been simulated in the simulation software Fux® are represented here. α and β each take 51 different values, varying between 0.02 and 51.*

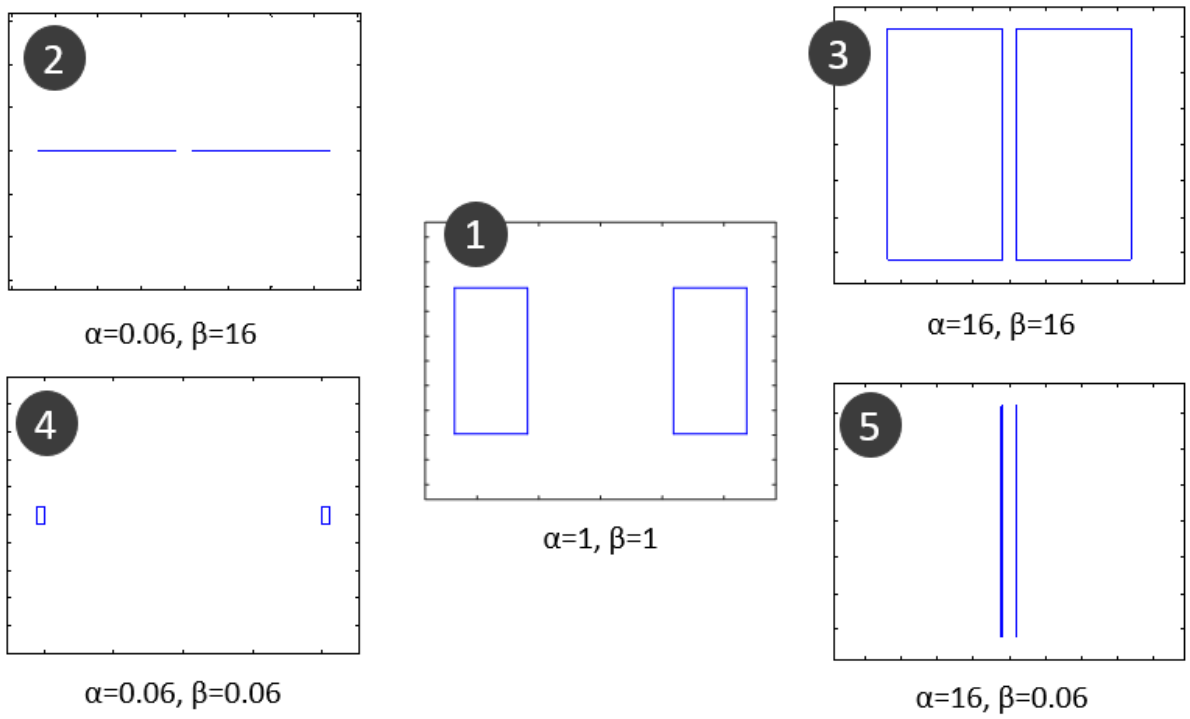


*Figure 60: Aspect ratio of the (α,β) couples which are spotted in Fig. 56.*

Thanks to these interpolated functions, it is possible to calculate the essentials quantities for solenoids with any set of R, J, α, β parameters, α and β being in the range [0.02; 51], thanks to the following equations:

$$E(R, J, \alpha, \beta) = \lambda^5 \zeta^2 \text{ function\_}E_0(\alpha, \beta) \quad (52)$$

$$E_{mass}(R, J, \alpha, \beta) = \lambda^2 \zeta^2 \text{ function\_}E_{mass\_0}(\alpha, \beta) \quad (53)$$

$$B_{INT}(R, J, \alpha, \beta) = \lambda \zeta \text{ function\_}B_{INT\_0}(\alpha, \beta) \quad (54)$$

$$B_{EXT}(R, J, \alpha, \beta) = \lambda \zeta \text{ function\_}B_{EXT\_0}(\alpha, \beta) \quad (55)$$

$$B_R(R, J, \alpha, \beta) = \lambda \zeta \text{ function\_}B_{R\_0}(\alpha, \beta) \quad (56)$$

$$F_z(R, J, \alpha, \beta) = \lambda^4 \zeta^2 \text{ function\_}F_{z\_0}(\alpha, \beta) \quad (57)$$

### 1.3.6. Discussion about the calculation method

First of all, this method aims to quickly explore a wide domain of topological solutions (i.e. with very different aspect ratios) and of stored energy (see part. II-2). The goal is to be able to visualize the evolution of the essential quantities with the topology, to gain an understanding of the governing laws of the problem and not only an optimal solution for a given case.

It also has several advantages:

- The aspect ratio parameters are used, reducing by 1 the number of geometrical variables of the topological combinations which have to be tested.
- The calculation of the quantities for the reference points is very accurate thanks to the use of detailed FEM simulation, and these simulations are only conducted once, in order to establish the interpolation function. Then, getting the results for a given set of parameters using the interpolation function is nearly 30 times faster than with a FEM simulation. It could likely be even faster by using other computer language than Matlab®, such as C/C++. So the method is fast and gives precise results simultaneously. In the case of the solenoid (See part II-1.3.5), some tests performed on the studied domain show that the error on the energy and the magnetic field is always less than 1 %.

# 2. Exploitation of the calculation model

This part is subdivided in 4 subparts and gives essential and quantitative elements about the physics that underlies the design of SMES windings.
The first part concerns the maximization of the specific energy of a winding without taking into account the mechanical constraints or the current carrying capabilities of the conductor. In the second part are considered the mechanical limits of magnetic energy storage. The third part gives information about the B field distribution depending on the topology. The fourth part takes into account the mechanical and current carrying capability constraints to determine the limits and the adequate solutions to the target of the BOSSE project, i.e. to maximize the specific energy of a 1 MJ SMES made of REBCO tape.

The data presented here have been obtained with the calculation model presented in the previous part (II-1.3.5), describing solenoids with rectangular cross section and homogeneous current density. It can be used to estimate roughly the feasibility and/or the topology of any solenoidal SMES, whatever the stored energy is.

## 2.1. Maximisation of the specific energy of a winding, made of a given volume of perfect conductor

In this part, we consider that the winding is made of a conductor that is insensitive to the mechanical stress and to the magnetic field B. The question we want to answer is, for a given mass M of a material that can carry a current density J, to determine the best way to shape this material in order to maximize the total magnetic energy.

### 2.1.1. Case of a solenoid

If we consider a solenoid with rectangular cross section and homogeneous current density, the maximum specific energy is reached for H=TH=R, i.e. α=0.5 and β=1. This configuration is called the Brooks inductor [Murg89]. The specific energy of a solenoid with circular cross section (as a single turn) is even higher [VRRK99], but is difficult to manufacture.

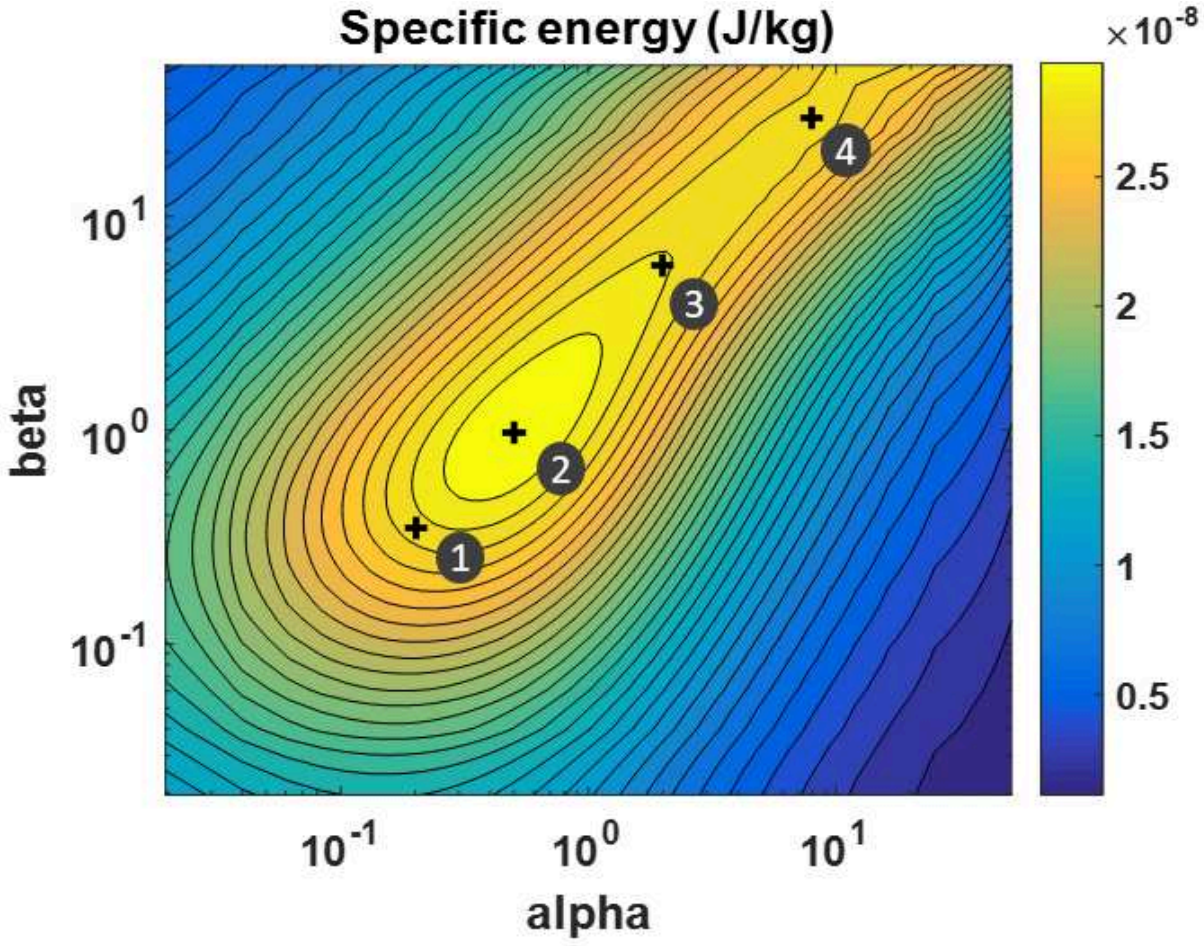


*Figure 61: Specific energy of a solenoid with a rectangular cross section, a homogeneous current density equal to 1 A/m², a mass of 1 kg and a density of 1 kg/m³, depending on its aspect ratio.*

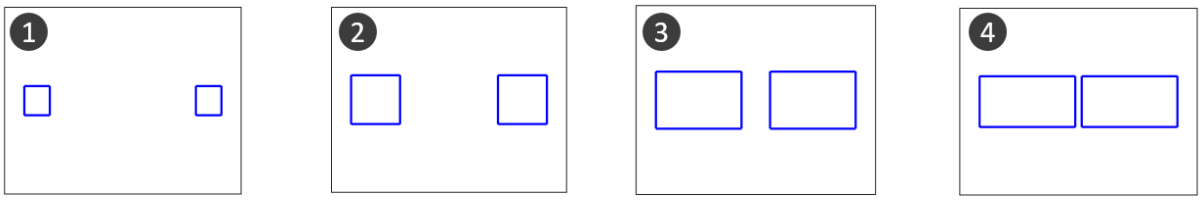


*Figure 62: Aspect ratios of the solenoids 1 to 4, whose the (α, β) coordinates are marked in Fig. 58.*

In Fig. 61 has been plotted the specific energy of a solenoid with a rectangular cross section, a homogeneous current density equal to 1 A/m$^2$, a mass of 1 kg and a density of 1 kg/m$^3$, depending on its aspect ratio. Of course, the volume of the body of the solenoid is 1 m$^3$. The aspect ratio of the solenoid is characterized by α and β, as defined in part II-1.3.1. Several points corresponding to specific (α, β) couples are marked in Fig. 61. The aspect ratios of the corresponding solenoids are shown in Fig. 62. The Brooks inductor corresponds to the point n°2 (α = 0.5, β = 1). We can see that in the (α, β) space of solutions, there is a kind of "ridge line" from point 1 to point 4 in which the specific energy is high. We can see that the solenoids with a high specific energy are rather compact ones. These configurations are maximizing the sum of the self magnetic energy of each turn with the sum of the mutual energy of all turns with all other turns.

In Fig. 62, only the aspect ratio of the solenoids are shown. Of course, the internal radius R differs according to the chosen (α, β) couple. The value of the internal radius of the solenoids whose specific energy is presented in Fig. 61 is shown in Fig. 63.

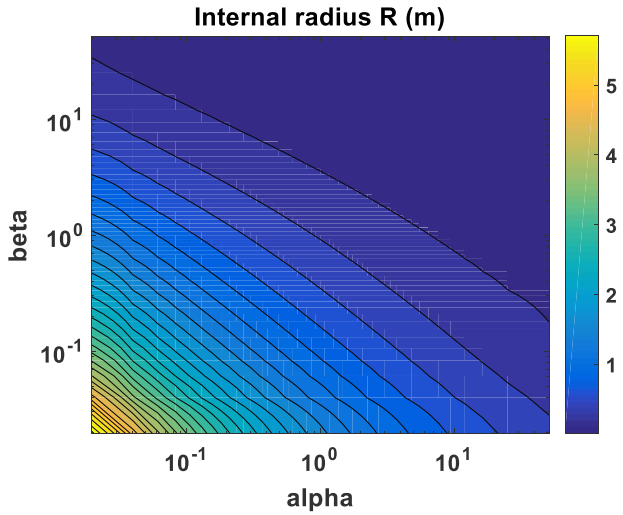


*Figure 63: Internal radius R of a solenoid whose volume of the body is 1 m³, depending on the aspect ratio factors α and β.*

Of course, the chosen example of a solenoid whose mass is 1 kg, with a density of 1 kg/m$^3$ and a current density of 1 A/mm$^2$ is arbitrary but the results presented in Fig. 61 can be easily extrapolated to solenoids with other mass, densities and current densities thank to the equations given in part II-1.3.5. In any case, the aspect ratio that is maximizing the specific energy is always the same, since this is purely a geometrical problem. In other words, whatever are the mass, the density and the current density of a solenoid, the plot of its specific energy depending on α and β always follows the plot in Fig. 61. The ratio of the specific energies between two solenoids with the same mass, density and current density only depends on their aspect ratio. It is therefore possible to display the specific energy as a function of α and β, normalised by the specific energy of the Brooks inductor (see Fig. 64). The specific energy of the Brooks inductor is a function of the current density and the volume and density of the body of the solenoid. It can be calculated by the following equation in which ρ is the density of the body of the solenoid (in kg/m$^3$), R is the internal radius (in meters) of the Brooks Inductor and J is the current density (in A/m$^2$).

$$\mathrm{E_{mass}}(\mathrm{R}, \mathrm{J}, \rho, \alpha = 0.5, \beta = 1) = \frac{\mathrm{R}^2\,\mathrm{J}^2\,1.3529\,10^{-7}}{\rho} \qquad (58)$$

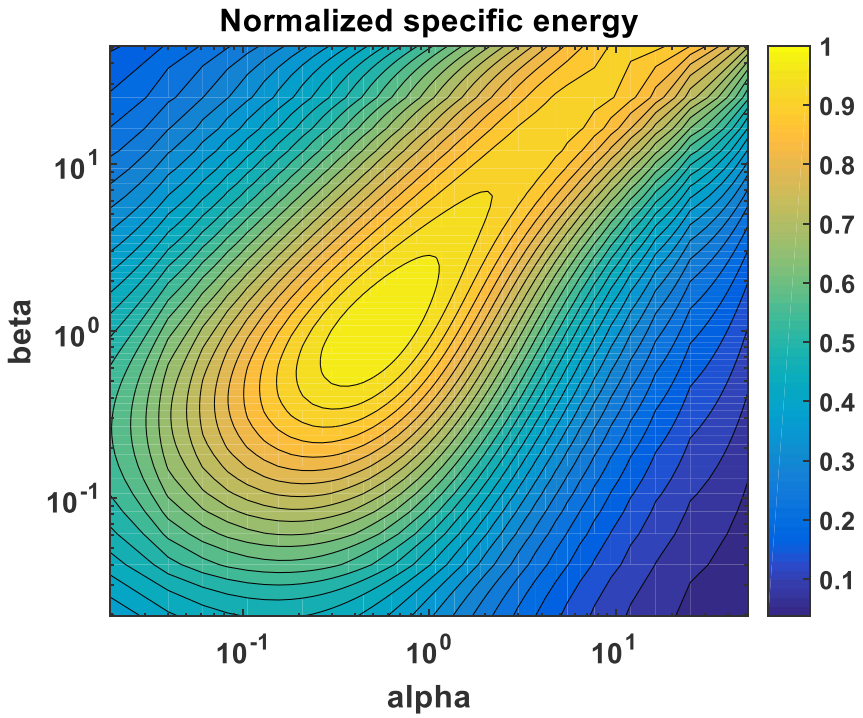


*Figure 64: Specific energy of solenoids with similar body volume and current density depending on α and β, normalised by the value of the specific energy of the Brooks inductor (R=H=TH). The specific energy of the Brooks inductor is given by Eq. 58.*

### 2.1.2. Case of a toroid

The same question about the best usage of a conductor to maximize the energy can be raised about a toroidal coil. The information presented in this paragraph only comes from bibliographic sources but ads complementary information to the one presented in the previous paragraph.

For a thin continuous torus with circular cross section, the specific energy is maximized for a ratio equal to 0.55 between the minor radius and the major radius of the torus [Hass89]. Nevertheless, this value can be significantly different for toroids with thick windings [Ştef00] or for modular toroids (i.e. discontinuous toroids). In the same way, there is a specific aspect ratio that maximizes the specific energy of a thin torus with a Shafranov D-shaped section (see part I-2.2.1.2.2). The maximum specific energy is reached for a ratio equal to 5.3 between the outer radius and the inner radius of a thin torus with a D-shaped section [Murg89].

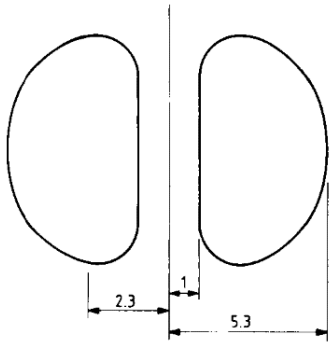


*Figure 65: Cross section view of a thin torus with a D-shaped section. The ratio between the inner and outer diameters of the torus has been chosen to maximize the specific energy.*

Murgatroyd [Murg88] suggests that for a toroid with a circular cross section, the specific energy is maximised if the inner halves of the turns that are close to the central axis are continuously distributed

and respecting the aspect ratio shown in Fig. 66. Similar ideas are exploited in the design of the SMES presented in Fig 31, 32 and 33.

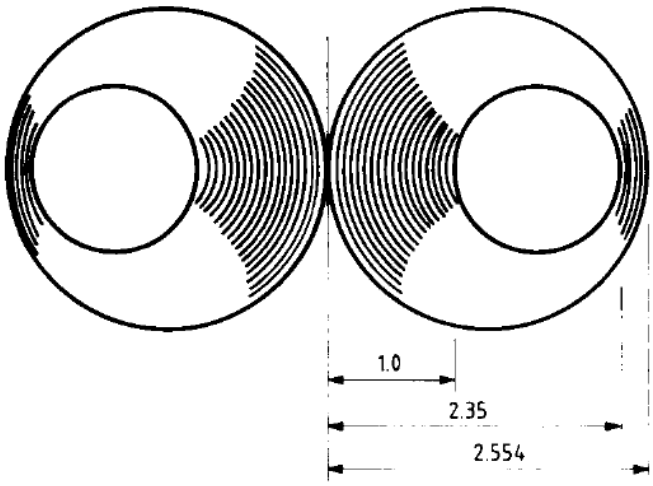


*Figure 66: Cross section of a toroid with continuous variation of the minor radius, maximizing the specific energy [Murg88].*

Globally, for a similar volume of conductor and a similar current density, a solenoid has a higher specific energy than a toroid. The specific energy of a Brooks inductor is 2.6 times higher than the specific energy of the winding shown in Fig. 66. So it is the same conclusion that with the comparison of maximum specific energy of thin solenoids and toruses with the virial theorem (see end of part I-2.1.3.1). Nevertheless this result is not of the same nature since the virial theorem takes into account mechanical considerations.

## 2.2. Maximization of the specific energy with respect to mechanical considerations

As we have seen in part I-2.1.3.1, a system which stores magnetic energy is necessary submitted to mechanical stress (Virial theorem). To design such a system, mechanical considerations have therefore to be taken into account. As we will see, the maximal specific energy of magnetic energy storage systems is mainly limited by the current density if the system stores little energy and is mainly limited by mechanical considerations if the system stores high energy.

In this part, we focus on the mechanical considerations of magnetic energy storage. Considerations about the current density dependence of superconductors with the B field are not taken into account and are tackled in the next part (see part II-2.3). The considerations presented in this part therefore apply both to resistive coils [Lieb17] and SMES. We will focus on the simple case of solenoids with rectangular cross section and homogeneous current density. If not specified, the hoop stress is calculated using the Wilson's formula (see part I-4.1.2), at the central mid-plane of the solenoid (i.e. where the hoop stress is maximum). First, we consider that the hoop stress is the main stress in the solenoid and thus that this is the most pertinent quantity to determine the mechanical limit of the structure. We then give complementary information and this assumption is called into question (see part II-2.2.3).

From the previous part, we know that the optimal shape to maximize the specific energy of a solenoid with rectangular cross section is the Brooks inductor, with R=H=TH. But for mechanical reason, this topology is not adapted to high current density or high energy.

We can easily understand it by increasing little by little the current density of a Brooks inductor. According to the equations presented in part II-1.3, the specific energy is going to increase with the

square of the current density, and the stress increases proportionally to the specific energy. At some point, the stress will be too high to be withstood by the body of the winding. It is nevertheless possible to continue to increase the specific energy, but it will be necessary to tend to topologies, which are more adapted to withstand the magnetic pressure.
In the same way, the value of the total magnetic energy stored by the system influences its topology. For example, we can increase little by little the size of a Brooks inductor with a constant current density. The energy and the specific energy are increased, but also the stress, proportionally to the specific energy. Once again, at some point the stress will be too high to be withstood by the body of the winding, and an evolution of the topology is required.

In the next two parts, we will quantify the evolution of the topology due to mechanical constraints. The case where the total energy is fixed to 1 MJ, which is the objective of the SMES of the BOSSE project, is considered first. We then give an insight into how evolves the topology when the total stored energy is varied.

### 2.2.1. Maximization of the specific energy with respect to the current density and maximum allowable hoop stress for a fixed value of energy.

Fig. 67 shows the specific energy of a solenoid with rectangular cross section, as a function of the current density and the maximum hoop stress. The density of the body of the solenoid is supposed to be 8900 kg/m$^3$, which is nearly the density of copper or Hastelloy®C-276. The total energy stored by the system is always 1 MJ. We can see that the specific energy increases with the maximum allowable hoop stress. But this is true only if the current density is sufficient to reach this allowable hoop stress. This is illustrated by Fig. 68 and 69. In these figures, we can see the specific energy of a solenoid that stores an energy of 1 MJ as a function of α and β. In Fig. 68, the current density is 400 A/mm$^2$ and in Fig. 69, the current density is 600 A/mm$^2$. In this figures, information about the maximal hoop stress is superimposed to the specific energy. Borders corresponding to solenoids with a hoop stress of 600 MPa, 500 MPa and 400 MPa are showed. These borders separate the set of solutions in two groups: all the solenoids above the border have a higher hoop stress than the value at the border. All the solenoids below the border have a lower hoop stress than the value at the border.

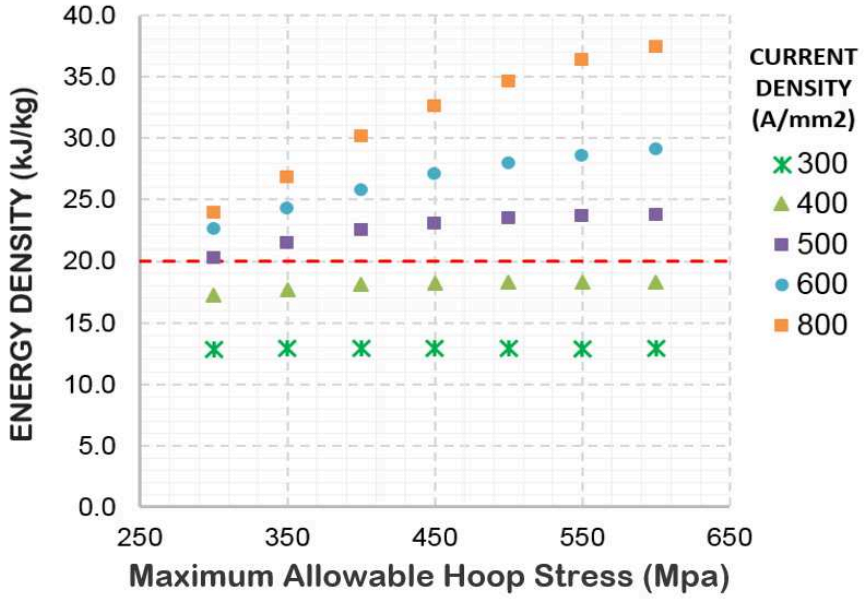


*Figure 67: Maximum possible specific energy of a solenoid with the maximum stress and engineering current (ρ = 8900 kg/m$^3$, Energy = 1 MJ).*

In Fig. 68, we can see that if the current density is 400 A/mm$^2$, the maximal hoop stress of the Brooks inductor ($\alpha = 0.5$, $\beta = 1$) is between 500 MPa and 400 MPa. If the stress has to be limited to 400 MPa, the topology has to evolve slightly. The new optimal solution is the point of the line corresponding to a maximal hoop stress of 400 MPa at which the energy density is maximal. This point has the coordinates $\alpha = 0.37$ and $\beta = 0.62$. Its specific energy is almost the same that the one of the Brooks inductor, i.e. 18.15 kJ/kg, compared to 18.29 kJ/kg for the Brooks inductor. This slight evolution is visible in Fig. 67.

But the evolution of the topology and the specific energy is much more visible if the current density is 600 A/mm$^2$. In Fig. 69, we can see that the maximal hoop stress of the Brooks inductor is higher than 600 MPa. The values of the $\alpha$ and $\beta$ coordinates of the solutions maximizing the specific energy decrease when the maximum allowable hoops stress is reduced.

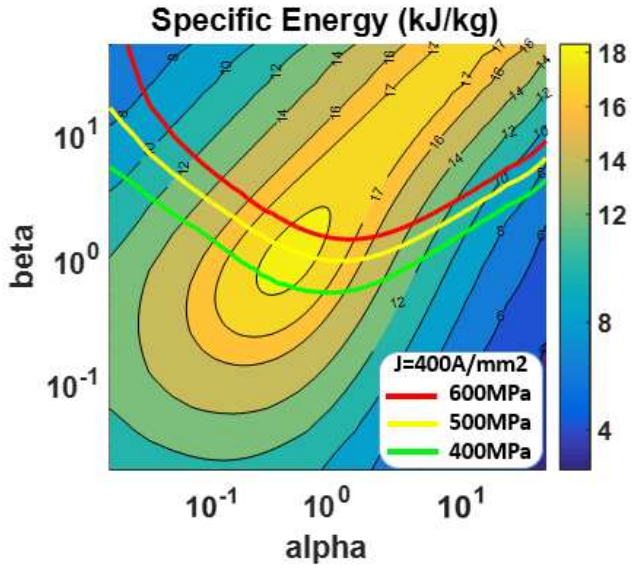


*Figure 68: Specific Energy of a solenoid with rectangular cross section and a current density of 400 A/mm$^2$. The energy is 1 MJ and the density is 8900 kg/m$^3$. Borders corresponding to solenoids with a maximal hoop stress of 600 MPa, 500 MPa and 400 MPa are displayed.*

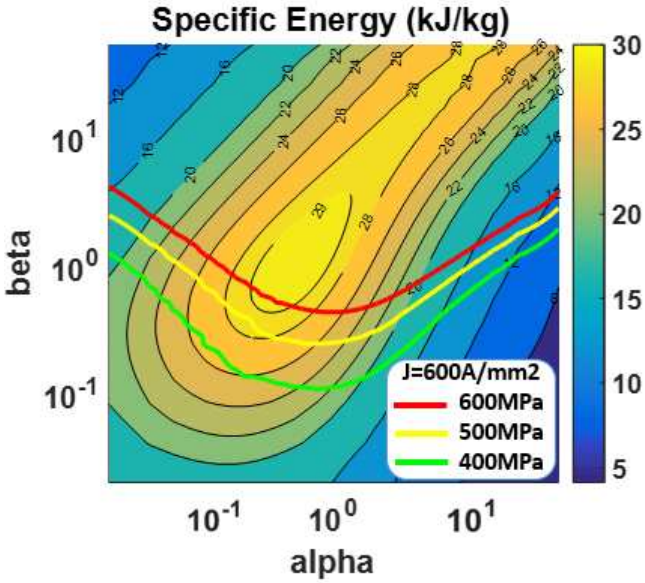


*Figure 69: Specific Energy of a solenoid with rectangular cross section and a current density of 600 A/mm$^2$. The scale is not the same that in Fig. 65. The energy is 1 MJ and the density is 8900 kg/m$^3$. Borders corresponding to solenoids with a maximal*

*hoop stress of 600 MPa, 500 MPa and 400 MPa are displayed. The colour scale of the value of the specific energy is not the same than in Fig. 68.*

### 2.2.2. Evolution of the optimal topologies with the range of energy

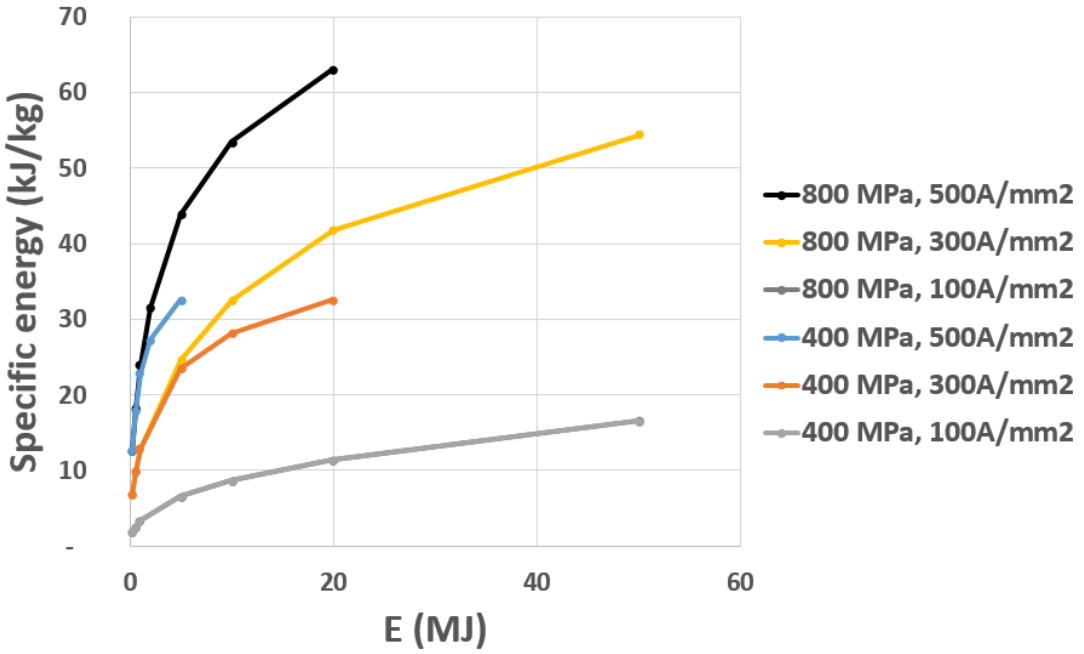


*Figure 70: Evolution of the specific energy as a function of the stored energy, for a solenoid with rectangular cross section. The maximum allowable hoop stress is either 400 MPa or 800 MPa. The current density is 100, 300 or 500 A/mm$^2$. The density is 8900 kg/m$^3$. The curves corresponding to 400 MPa, 100 A/mm$^2$ and 800 MPa, 100 A/mm$^2$ are superimposed. More data about the B field, the radius, and the value of the JBR formula of the topologies presented in this figure are available in appendix B-1.*

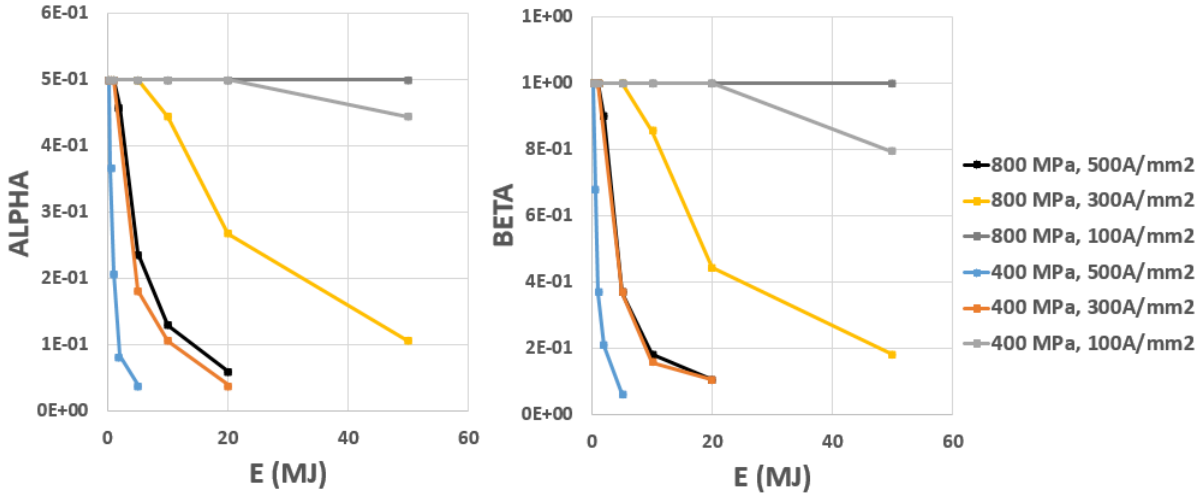


*Figure 71: Evolution of the aspect ratio parameters α and β, corresponding to the previous figure.*

In figures 68 and 69, the evolution of the specific energy as a function of the current density and the maximum allowable hoop stress are displayed for a fixed value of stored energy (1 MJ). But it is also interesting to see what happen when the target stored energy is varied. In Fig. 70, the specific energy is shown with respect to the stored energy. This is done for two different maximum allowable hoop stress values, 400 MPa and 800 MPa. The current density is 100, 300 or 500 A/mm$^2$. The stored energy is comprised between 0.2 MJ and 50 MJ. The considered density remains 8900 kg/m$^3$.

At low energy, the Brooks inductor is an acceptable solution from the mechanical point of view. So at the left side of the curves, the specific energy evolves as the power 2/5 of the stored energy (according to Eq. 38 and 39). But when the energy is large enough, the stress in the Brooks inductor is too high and another topology has to be preferred. The evolution of the aspect ratio parameters α and β is shown in Fig. 71. We can see that α = 0.5 and β = 1 as far as the hoop stress of the Brooks inductor is smaller than the maximum allowable hoop stress of the solenoid. For higher energies, α and β are decreasing, which means that the height and thickness of the solenoid are both small compared to the radius.

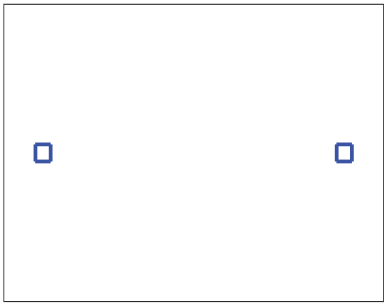

*Figure 72: Aspect ratio of a solenoid with α=0.06 and β=0.106. This topology maximizes the specific energy of a solenoid with J = 500 A/mm², E = 20 MJ and having a hoop stress (calculated by the Wilson formula) lower than 800 MPa.*

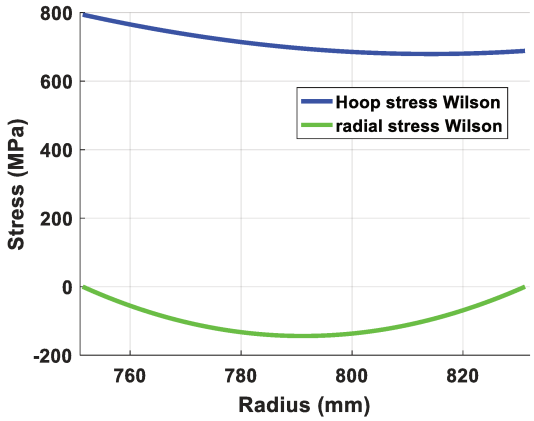


*Figure 73: Hoop stress and radial stress, calculated by the Wilson formula, of a solenoid with α=0.06, β=0.106, J = 500 A/mm² and E=20 MJ.*

An example of a solenoid with low α and β is showed in Fig. 72. This solenoid has α = 0.06 and β = 0.106. This topology maximizes the specific energy of a solenoid with a current density of 500 A/mm$^2$ and an energy of 20 MJ while having a hoop stress lower or equal to 800 MPa. The hoop stress and the radial stress of this solenoid, are showed in Fig. 73. Fig. 74 also shows the value of the JBR formula (see part I-4.1.1), across the solenoid. We can see that the value of the JBR product is much higher than the hoop stress calculated by the Wilson formula at the inner radius of the solenoid and is much higher but negative at the outer radius of the solenoid. This is because in a topology with α=0.06 and β=0.106, the value of the external B field has the same order of magnitude than the value of the internal B field. In the particular case where J=500 A/mm$^2$ and E= 20 MJ, $B_{INT}$= 16.7 T and $B_{EXT}$ = 12.6 T. As a consequence, the outer part of the solenoid is submitted to strong centripetal forces that counterbalance the strong centrifugal forces at the inner part of the solenoid. The result is that the solenoid is submitted to a strong compressive radial stress, which reaches 144 MPa at the middle of the cross-section. It means that in this topology, the radial stress is not negligible compared to the hoop stress. In this case, it is more pertinent to determine the mechanical integrity of the solenoid thanks to yield surfaces, such as the Tresca yield surface or the Von Mises yield surface, rather than

independent 1-dimensional stress components such as the hoop stress, the radial stress or the axial stress.

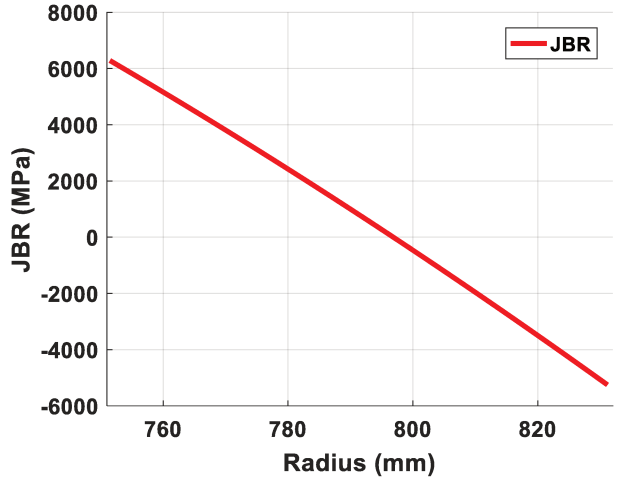


*Figure 74: Value of the JBR formula (product of the current density by the B field by the radius) across a solenoid with α = 0.06, β = 0.106, J = 500 A/mm2 and E = 20 MJ.*

### 2.2.3. Evolution of the stress distribution with the topology

As we have seen in part II-1.3, some simple equations aim to extrapolate the stress distribution of a winding from the stress of its homothetic transformation, or from the stress of a similar winding with a different current density. The result is that it is possible to draw some general laws, which only depend on the topology of the winding and apply whatever are the current density or the size of the winding.

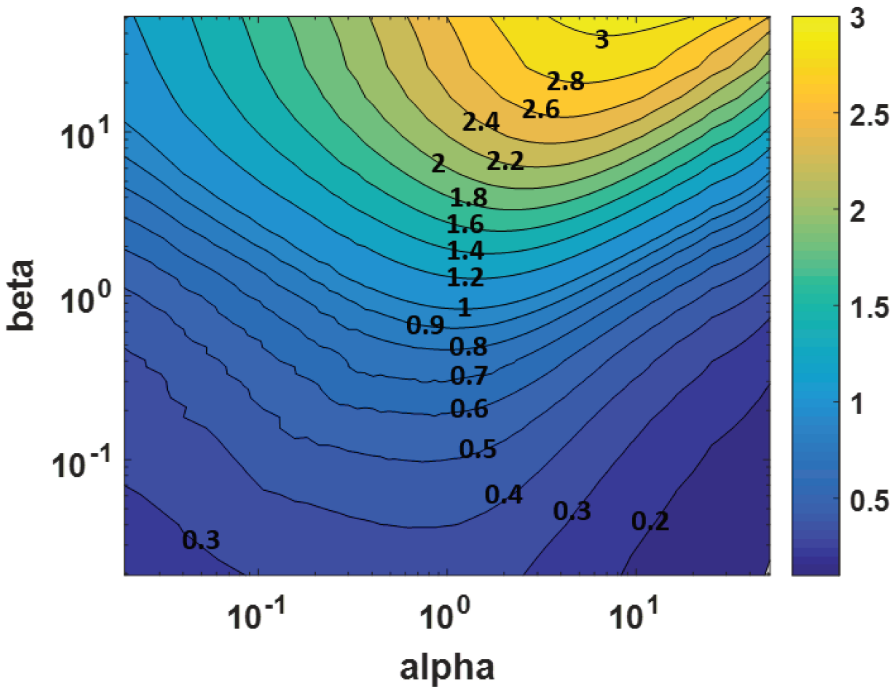


*Figure 75: Value of the hoop stress normalised by the hoop stress of the Brooks inductor. Here, all the topological solutions have the same energy and current density that the Brooks inductor, which is used as a reference, so their body do not have the same volume.*

For example Fig. 75 shows the hoop stress calculated by the Wilson formula. This hoop stress has been arbitrarily normalised by the hoop stress of the Brooks inductor. The value of the stored energy is

constant. The hoop stress of the Brooks inductor is given by Eq. 59. The stress $\sigma_{hoop\_Brooks}$ is in Pa, the energy E is in J and the current density J is in A/m$^2$.

$$\sigma_{hoop\_Brooks} = 9.1188\ 10^{-5} \left(\frac{E}{J^2}\right)^{\frac{2}{5}} J^2 \tag{59}$$

Another example in that for a solenoid with rectangular cross section, the ratio between the maximum hoop stress and the axial stress only depends on α and β. This ratio is showed in Fig. 76. We can see that for long and thin solenoids, which can be an attractive solution for low energy with high energy density SMES [YMYO02], the axial stress is not at all negligible compared to the hoop stress. The axial stress can be 45 % of the hoop stress or more. In this case again, it is more pertinent to determine the mechanical integrity of the solenoid thanks to yield surfaces, such as the Tresca yield surface or the Von Mises yield surface, rather than independent 1-dimensional stress components. Nevertheless, these yield criteria are pertinent only for mechanically isotropic material and can be inappropriate for a solenoid made of mechanically anisotropic conductor.

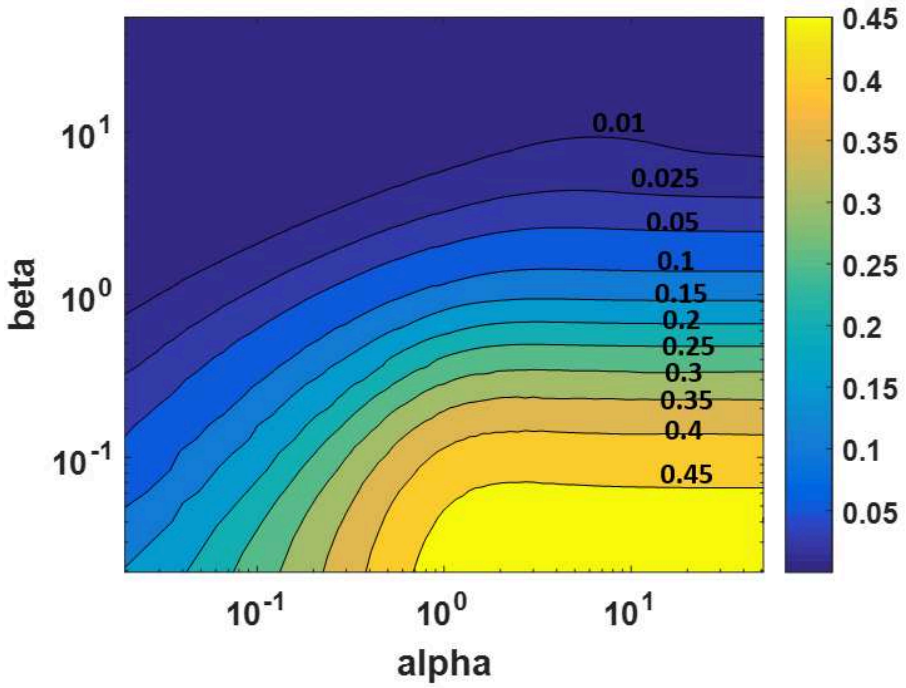


*Figure 76: Ratio between the axial stress at mid-plane and maximum hoop stress at mid-plane calculated by the Wilson's formula, depending on α and β. In the described space of solutions, limited by β ≥ 0.02, the maximum is reached at α = 2.25 and β = 0.02.*

In Fig. 77 is displayed the ratio between the value of JBR at the inner radius and the hoop stress calculated by the Wilson's formula. We can see that for solenoids with low α and low β, the fact that the hoop stress is much lower than the value of JBR, which means that the magnetic force is efficiently distributed and homogenised in the whole structure thanks to radial stress. On the contrary for thick solenoids (i.e. when β is high), the JBR is lower than the hoop stress. In this case, it is preferable to split the solenoid in several independent nested solenoids (see part. I-4.1.2) to lower the mechanical stress.

More information about the stress distribution in solenoids is given in appendix B-2.

The laws and relations presented in these parts are valid as far as the stress/strain relation of the material of the solenoid is linear and isotropic, which is not necessary the case for a SMES winding.

As a conclusion, the solenoids with low alpha and beta aspect ratios appear to be an attractive solution for magnetic energy storage, from the mechanical point of view. This is consistent with the results obtained by Sviatoslavsky [SvYo80] and Moon [Moon82] (see part I-2.1.3.1). Nevertheless, these topologies can generate relatively high magnetic fields (see appendix B-1), which is an issue for SMES.

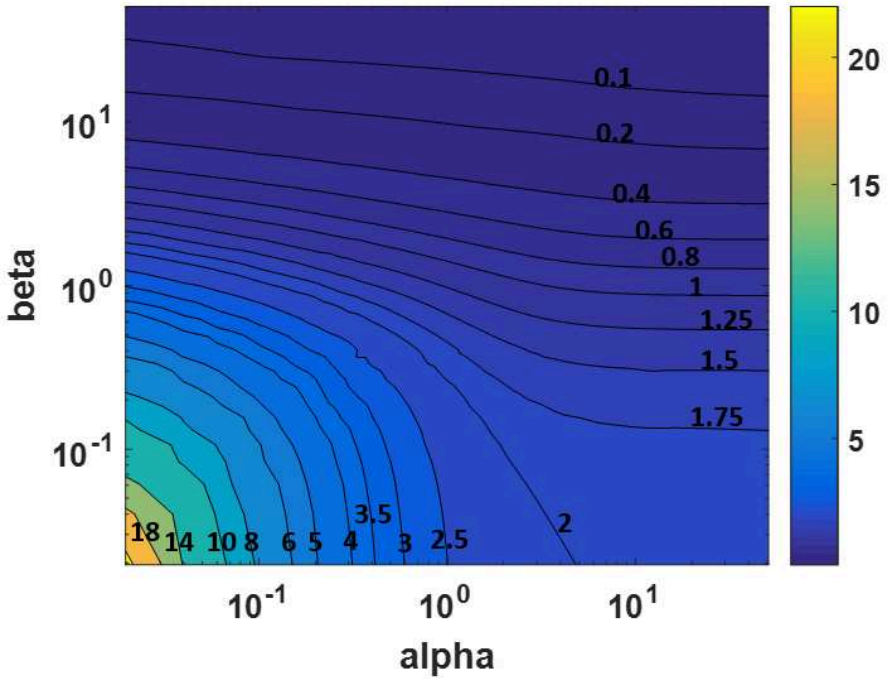


*Figure 77: Ratio between the value of JBR at the inner radius and mid-plane and the maximum hoop stress at mid-plane calculated by the Wilson formula, depending on α and β.*

## 2.3. Effect of the topology on the B field

In the previous part, we have seen that it is necessary to take into account the magnetic forces to design a magnetic storage system. Of course, it is also necessary to take into account the current carrying capability of the superconducting conductor to design a SMES. This current carrying capability depends on the temperature and on the field amplitude and orientation (see part I-1.1.1, I-1.2 or I-1.3.1). Nevertheless, proper operation of a superconducting winding requires the temperature to be kept stable or at least under a given maximum value. In first approach, it is therefore possible to design a SMES considering that the temperature is constant and homogeneous. This approximation is valid if the winding is cooled by a cryogenic bath, which is the case for the prototypes pancakes and the SMES of the BOSSE project (see part III).

In this frame, the current carrying capability $J_C$ only depends on the field value and orientation towards the tape. In a winding, the current in the conductor will be limited by the point where the B field value and orientation leads to the lowest $J_C(B,\Theta)$ (see part I-1.3.1).

If we suppose that the conductor is isotropic and that only one type of conductor is used in the winding of the SMES, then $J_C(B)$ is limited by the point of the winding where the B field is maximum. In a solenoid, this maximum field is often reached at the inner radius and mid-plane of the solenoid, i.e. the maximum field is $B_{INT}$ (see Fig. 58).

### 2.3.1. $B_{INT}$ depending on the topology

In Fig. 78, the value of $B_{INT}$ depending on α and β is displayed. This value is normalised by the value $B_{INT}$ (α=0.5, β=1), which is the value for the Brooks inductor. In this figure, the energy and current density are held constant. The value of B for the brooks inductor is given by Eq. 60 or 61 in which the energy E is in joule, J is in $A/m^2$, R is in meter and $B_{INT\_Brooks}$ is in Tesla. In this figure, we can see that the topologies that correspond to high specific energy (see Fig. 64) have also a high $B_{INT}$. But a high value of $B_{INT}$ reduces the current carrying capability of the conductor. The geometry of a SMES coil is therefore the result of a compromise between the desired specific energy and the current carrying capability of the conductor, as well as being a compromise between the desired specific energy and the mechanical properties of the conductor (see the previous part II-2.2).
Finally, Fig. 75 and 78 show why relatively thin solenoids are preferred to thick solenoids for SMES with a high current density or a high total energy. This is due, independently, both to mechanical and electrical reasons.

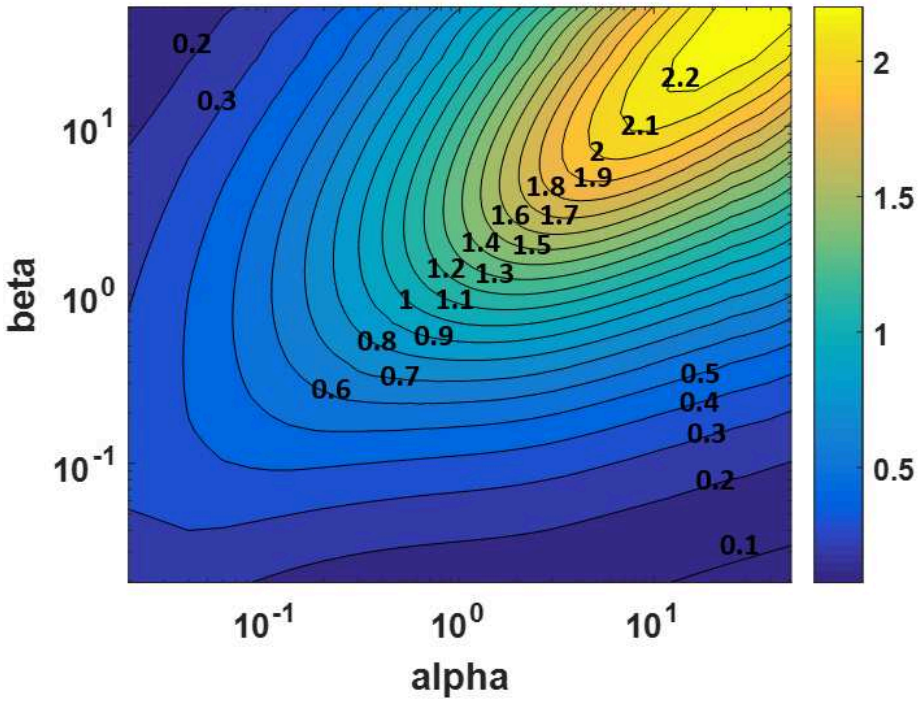


*Figure 78: Value of $B_{INT}$ normalised by $B_{INT}$ of the Brooks inductor. Here, all the topological solutions have the same energy and current density than the Brooks inductor, which is used as a reference, so their body do not have the same volume.*

$$B_{INT\_Brooks} = 8.701\ 10^{-6} \left(\frac{E}{J^2}\right)^{\frac{1}{5}}\ J \tag{60}$$

$$B_{INT\_Brooks} = 5.763\ 10^{-7}\ R\ J \tag{61}$$

### 2.3.2. Ratio between $B_R$ and $B_{INT}$

Similarly to what have been explained for the ratio between the axial or radial stress and the hoop stress in part II-2.2.3, the ratio between $B_R$ and $B_{INT}$ only depends on the topology of the solenoid. This ratio is shown in Fig. 79. We can see that for some topologies, interesting for Superconducting Magnetic Energy Storage, $B_R$ is higher than $B_{INT}$, i.e. $B_{INT}$ is not always the maximum field in the solenoid. We can see that relatively thin solenoids have a high transverse field, which can be a problem for windings made of anisotropic tapes such as REBCO.

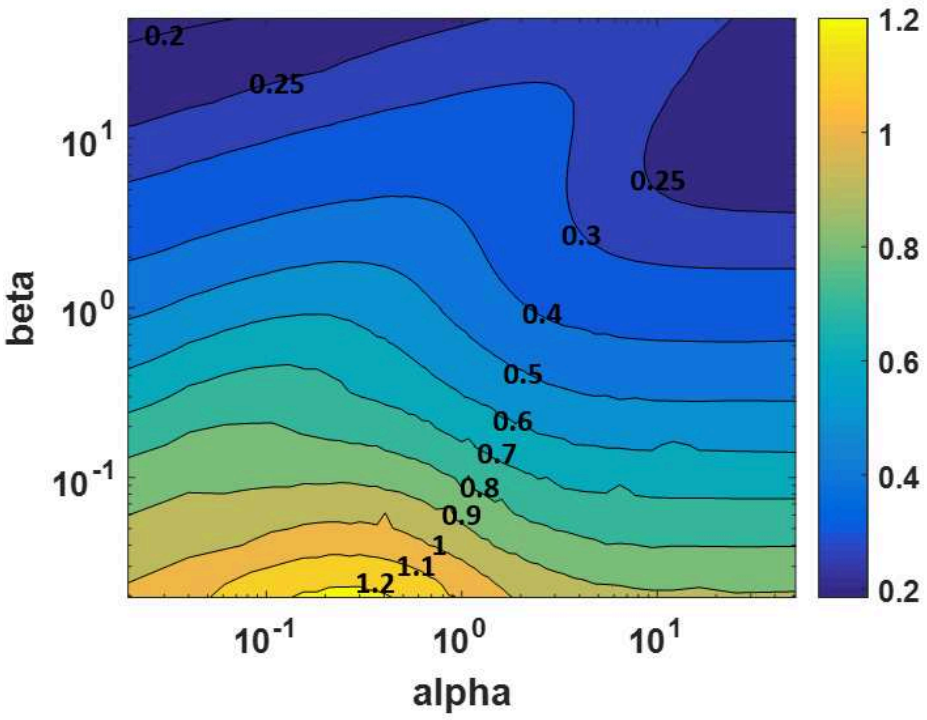


*Figure 79: Ratio between the radial field $B_R$ and the internal field $B_{INT}$ (see Fig. 58), depending on α and β.*

# 2.4. Considerations about the design of a SMES made of REBCO tapes, taking into account multiple constraints

## 2.4.1. Exploration of the space of solutions, with the energy, the stress being fixed and the current carrying capability being defined

In this part, we are going to focus on the case of magnets built using REBCO conductor, defining first the limits of the problem. Both mechanical and transport current properties, under a constant temperature of 4.2 K, are taken into account. According to the specifications of the BOSSE project, we consider solenoids with a total energy of 1 MJ. As we want to maximize the specific energy and that the specific energy is proportional to the stress (See part I-2.1.3.1), we search for the solutions in which the maximal stress is close to the ultimate stress of the conductor. C. Barth et al. [Barth2015] have shown that the standard commercially available REBCO tapes can bear a longitudinal tensile stress of 600 MPa (See part I-1.3.5.1), even if this value can be varied by modifying the ratio between copper and substrate in the conductor. That is why in this part, we consider solutions with a constant energy E = 1 MJ and a constant maximum hoop stress equal to 600 MPa. As in the previous parts, the hoop stress is calculated by the Wilson's formula, at the mid-plane of the solenoid. As a first approach, we consider a bare conductor without insulation, so the density of the body of the solenoids is 8900 kg/m$^3$. The method to obtain data with constant energy and constant maximum hoop stress is described in appendix B-3. It is also possible to obtain data with constant energy and constant current margin (See also appendix B-3).

In the following charts (in which the energy is 1 MJ and the maximum hoop stress is 600 MPa), we can see that the highest specific energies are reached for solenoids with low beta (i.e. relatively thin solenoids). This is because in thin solenoids, the hoop stress across the section is more homogeneous

than in thick solenoids. The conductor is therefore used almost at its ultimate tensile stress in the most part of the solenoid, which is beneficial to the specific energy according to the virial theorem.
The value $J/J_C(B_{INT})$ is the ratio between the current density of the topology and the critical current density calculated with the value of $B_{INT}$, the field being considered parallel to the tape. The value $J/J_C(B_R)$ is the ratio between the current density and the critical current density calculated with the value of $B_R$, the transverse field to the tape. The current carrying capability of the REBCO tapes comes from the data of T. Benkel et al. (See part I-1.3.1). The bare tapes are supposed to have a thickness of 95 µm, which is the thickness of the tapes used in the BOSSE project (see part III-3.1.2).

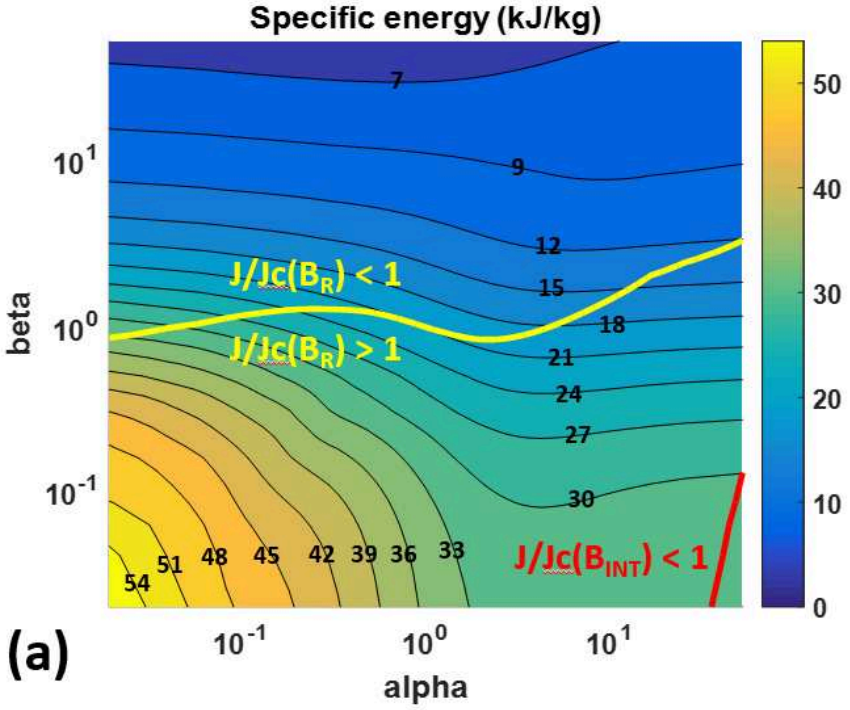


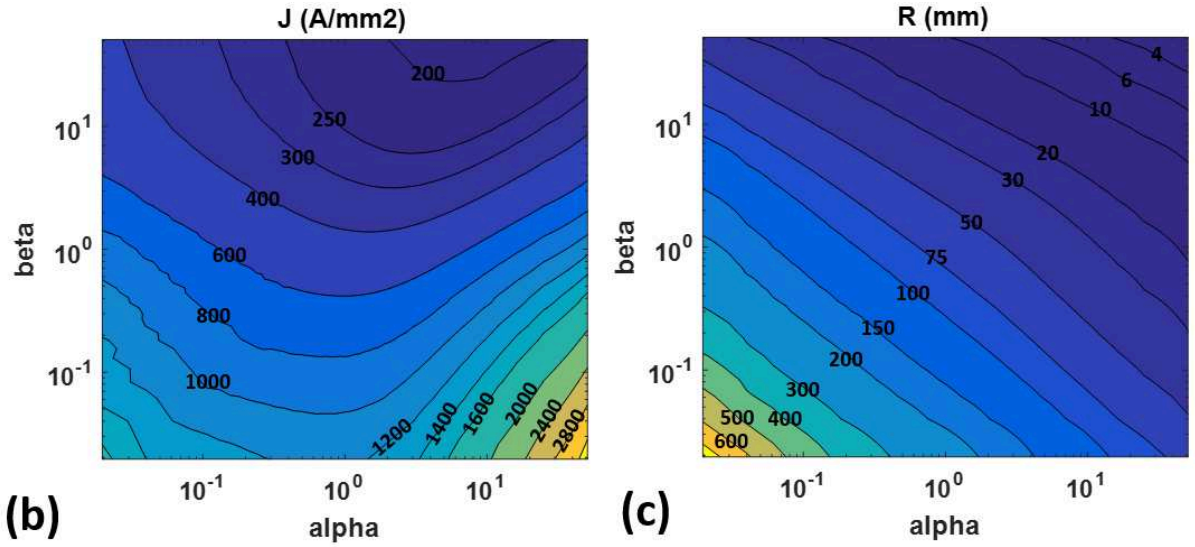

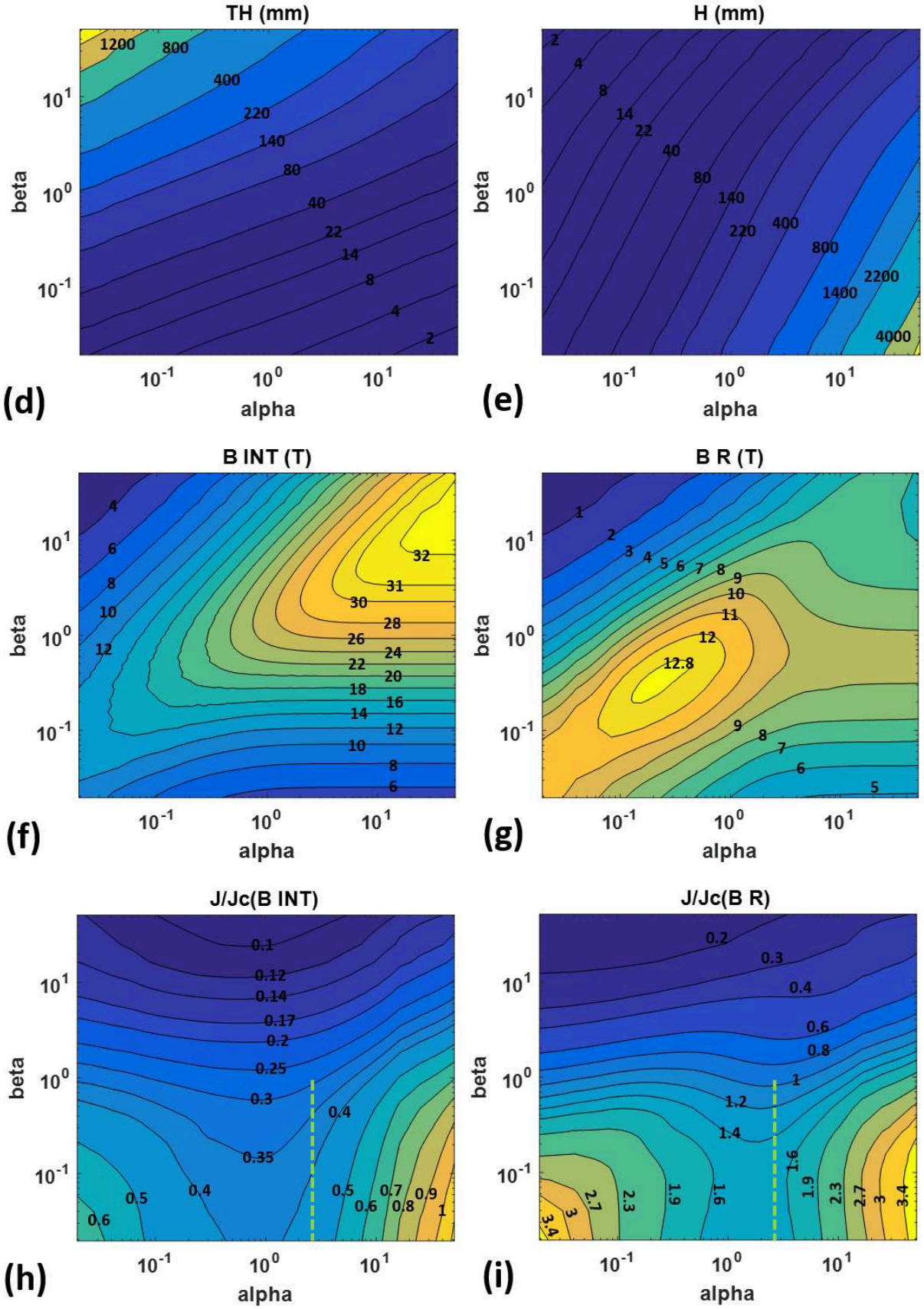


*Figure 80: Physical parameters, depending on aspect ratios α and β, of solenoids with rectangular cross section and homogeneous current density with a total energy of 1 MJ and a maximum hoop stress (calculated by the Wilson formula) equal to 600 MPa. The density of the body of the solenoids is 8900 kJ/kg, which is the density of bare REBCO tapes.*

In Fig. 80 (a) and (h), we can see that almost in the whole studied domain, $J/J_C(B_{INT})$ is significantly lower than 1. The reduction of the current density due to the longitudinal field is therefore not a major problem in our case. On the other hand, we can see in Fig. 80(a) and (i) that $J/J_C(B_R)$ is higher than 1 for most of the topologies which have a specific energy higher than 20 kJ/kg. There is a small part of the domain for which the specific energy is higher than 20 kJ/kg and $J/J_C(B_R)$ is lower than 1, but these topologies are very flat solenoids (see Fig. 81). Such solutions would be very uneasy and uncommon to manufacture for several reasons: the cryostat would be huge or would have an unusual shape, the unit lengths of conductor should be very long, there would be a risk of collapse of the coil if it was not reinforced by an external structure, etc...That is why these topologies have not been considered as acceptable solutions. For several reasons which are detailed in part II-3.1.1, we have preferred more classical configurations. For this to be possible, it is necessary to adapt the extremities of the solenoid to reduce the value of $J/J_C(B_R)$. The proposed solutions are presented in part II-3.2.

Note that if an optimization was conducted on the studied space of topologies with criterions about the specific energy, the maximum hoop stress and sufficient current margin, the algorithm would determine that the optimal solution is a very flat solenoid, as shown in Fig. 81. The process would be very long since the studied space of solutions is large, however the result would be useless. So this is an example of the limits of the optimization approach (see part II-1.2).

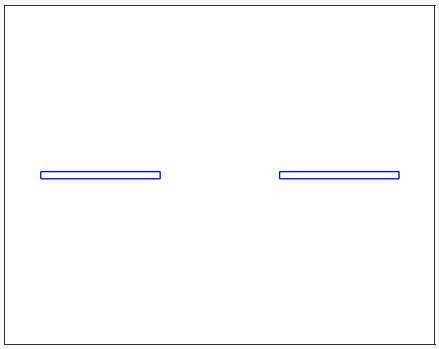

*Figure 81: Aspect ratio of a solenoid with α=0.06 and β=2, which is theoretically a solution to store 1 MJ with a specific energy of 20 kJ/kg with REBCO tapes. This kind of solution has not been seriously considered for practical reasons.*

### 2.4.2. Additionnal constraint about fixed current density

In Fig. 80 (h) and (i) is shown the pathway which has been used to plot the Fig. 82 and 83. This pathway is the green dotted line defined by $\alpha = 2.5$ and $0.02 < \beta < 1$. In Fig. 82 and 83, we can see that when R increases, $B_{INT}$ and the thickness of the coil decrease. The specific energy increases but in counterpart the current density J also increases. Having a solenoid with a very thin wall is the strategy that has been followed by the designers of the solenoid which currently owns the world record of specific energy [YMYO02]. This solenoid, which reaches a specific energy of 13 kJ/kg, has $\alpha = 1.63$ and $\beta = 0.007$, and a current density in the bare conductor equal to 650 A/mm$^2$. From Fig. 82 (a) and (c), we can see that for $\alpha = 2.5$, we need a current density of 530 A/mm$^2$ to reach a specific energy 20 kJ/kg. Actually, as the specific energy is degraded by the modification of the extremities of the solenoid (see part II-3.2), an even higher current density is required.

The specific energy is therefore not only limited by the current carrying capability of the superconductor and its mechanical properties, but also by the maximum current density which seems reasonable in order to be able to ensure the safety of the winding.

As we will see (see part II-3.1.1.2), in the case of the BOSSE project, a high specific energy is searched but a high volume energy density is required as well. The constraints are the weight but the footprint as well.

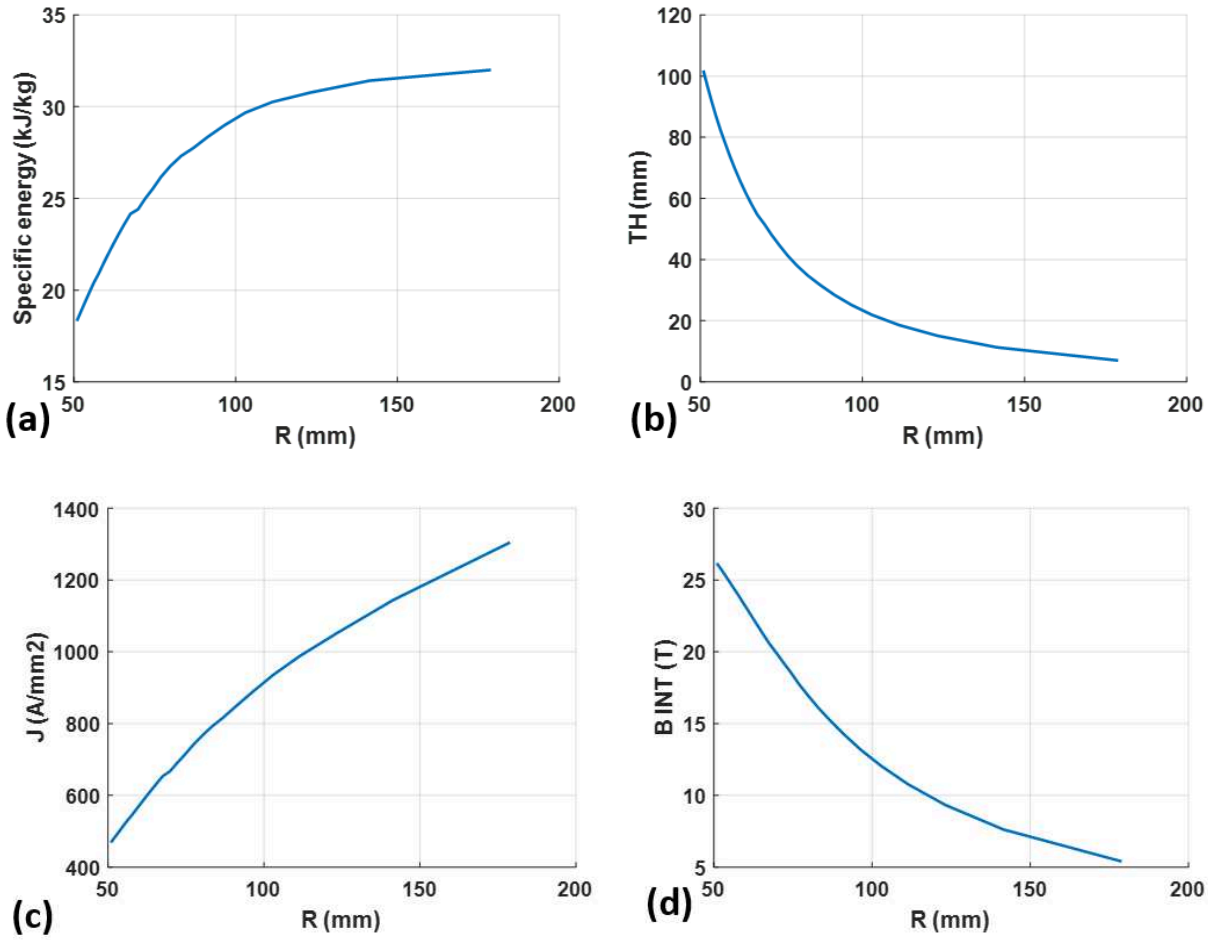


*Figure 82: Evolution of physical parameters along the pathway displayed in Fig. 80 (h) or (i) (green dotted line). α = 2.5 and 0.02 < β < 1. The evolution of other physical parameters is shown in appendix B-4.*

If the current density is identified as major issue in the design of a SMES, it is relevant to define a maximum current density that should not be overstep. This criterion has to be added to other criterions such as the target energy and the maximum hoop stress. As there is an additional constraint, solutions are no more existing for the whole studied domain but only for a set of (α, β) couples describing a line in the studied space of topological solutions. So the properties of the solutions can be described by curves rather than surfaces. For example Fig. 83 (a) shows the physical parameters of solenoids with an energy of 1 MJ, a maximum hoop stress of 500 MPa and a current density of 600 A/mm$^2$. In Fig. 83 (b) are displayed the two topologies spotted in Fig. 83 (a). The topology 1 has the highest specific energy (28 kJ/kg). So if the specific energy was the only design criterion, this topology should be chosen. But this topology is very thick and would be difficult to manufacture. Furthermore, it shows a high transvers field at extremities which reduces the current margin. For these reasons, solenoids which look like the topology 2 rather than the topology 1 have been chosen for the high specific energy SMES of the BOSSE project. The specific energy of the topology 2 is lower (21 kJ/kg), but is still over 20 kJ/kg. The topology 2 has the advantage to have a lower $B_R$. What is more, it is a rather long solenoid compared to the topology 1. It is therefore possible to modify its extremities without degrading too much its specific energy, as will be shown in part III-3.2.

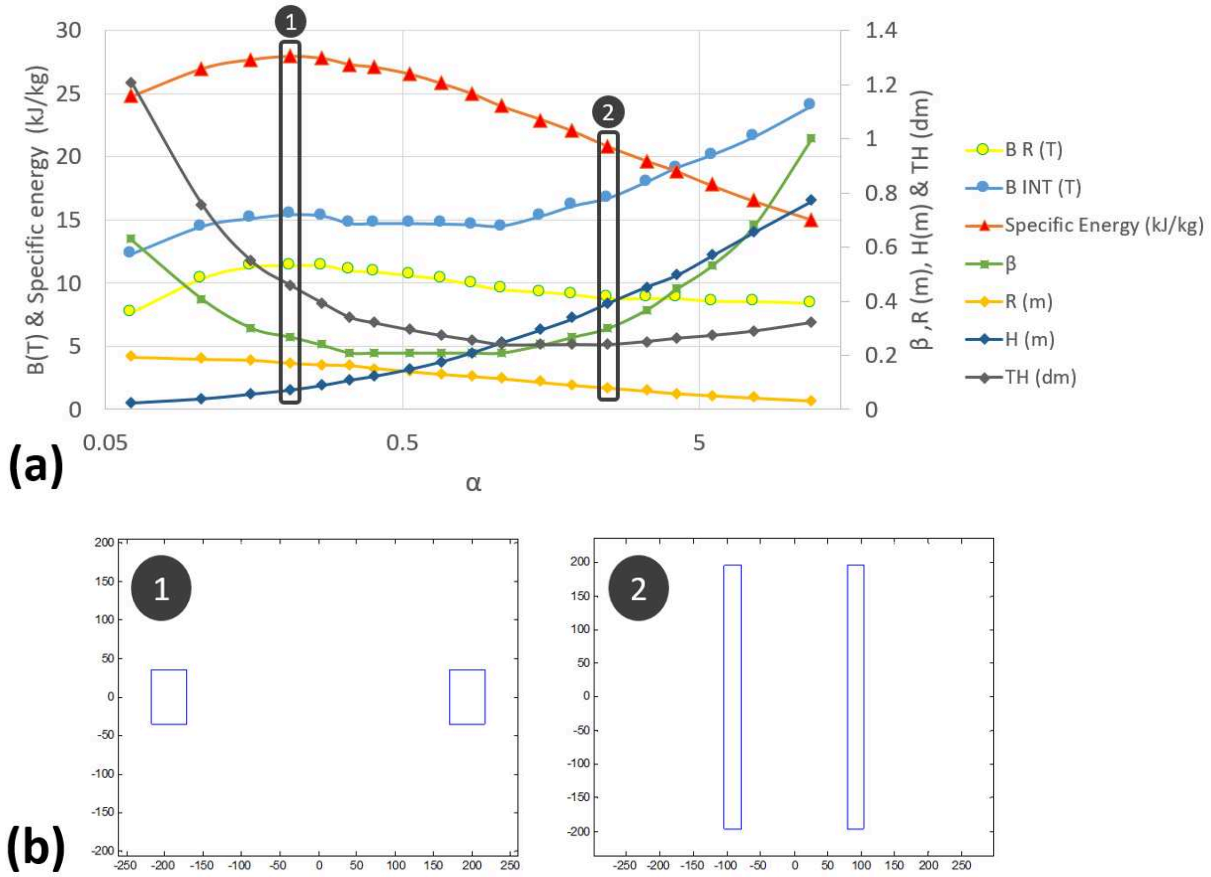


*Figure 83: (a) Physical parameters of solenoids with an energy of 1 MJ, a maximum hoop stress of 500 MPa and a current density of 600 A/mm². ρ=8900 kg/m³. The pathway which is followed to plot these curves is the yellow border visible in Fig. 80. (b) Aspect ratios of the solutions 1 and 2, which are spotted in Fig. 83 (a).*

# 3. Design of the SMES of the BOSSE project

## 3.1. Introduction to the design of the high specific energy SMES of the BOSSE project.

### 3.1.1. Objectives and constraints of the high specific energy SMES of the BOSSE project

The goal for the high specific energy SMES of the BOSSE project is to reach an energy of 1 MJ and a specific energy of 20 kJ/kg thanks to the performance of new generation superconductors at 4.2 K. For comparison, the BESS project, which currently owns the world record of specific energy for a superconducting winding, has an energy of 550 kJ and a specific energy of 13.4 kJ/kg and is based on NbTi conductor [YMYO02].

REBCO tapes have outstanding properties but they also have several drawbacks which are unsolved until now (see part I-1.3) and which make REBCO devices difficult to protect. This problem has to be considered in the design of the SMES and adds some practical design constraints. During the BOSSE project, it quickly appeared than the objective of 20 kJ/kg with REBCO tapes was very challenging.

### 3.1.1.1. Comparison of the viral limits between REBCO tapes and the conductor of the BESS project

The conductor of this coil is made of NbTi stabilized with a specific aluminium-nickel alloy. As explained in part I-2.1.3.1, we know that the maximum specific energy of a SMES is limited by the ratio of the maximum allowable stress and the density of the body of the system, and also depends on the topology of the system. In the coil of the BESS project, the maximum stress is 174 MPa. Even if we do not know the respective proportions of NbTi and copper in the core of the used conductor, we can calculate that its density is lower than 4600 kg/m$^3$. In this case, the ratio between the stress and the density is 38 kJ/kg. For the record, the ratio between the ultimate tensile strength of a conductor and its density is called the virial limit.

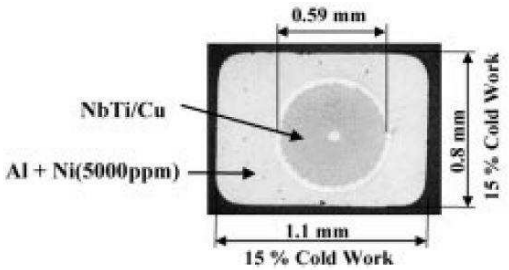


*Figure 84: Cross-section of the BESS coil conductor [YMYO02].*

In the case of standard REBCO tapes, the maximum reasonable longitudinal tensile stress at 4.2 K is around 600 MPa (see part I-1.3.5.1) and the density is around 8900 kg/m$^3$, hence the ratio is about 67 kJ/kg. REBCO tapes can therefore be considered as a better conductor than the conductor of the BESS experiment from the mechanical point of view. Nevertheless, this advantage does not give a large margin to increase the world record of specific energy from 13.4 to 20 kJ/kg. The ratio between 67 kJ/kg and 38 kJ/kg is 1.76 while the ratio between 20 kJ/kg and 13 kJ/kg is 1.49. Besides other constraints about the conductor, this is one of the reasons which make difficult the goal to reach a specific energy of 20 kJ/kg.

### 3.1.1.2. Trade-off between high specific energy and high volume energy

As we have seen in part II-1.1, the objective to have a SMES with a high volume energy is not the same and is even contradicting with the objective to have a high specific energy. The Large and thin solenoids are adapted to reach a high specific energy, but in counterpart the field that they generate is low and so their volume density is also low. Nonetheless, REBCO tapes have good current transport properties under high field at low temperature, so they can be used to develop very compact SMES. It seemed interesting to us to find a compromise between both objectives. We have therefore tried to find a topology with a maximum B field higher than 10 T while still respecting the objective of a specific energy of 20 kJ/kg. In comparison, the maximum field in the BESS coils is only 1.7 T.

### 3.1.1.3. Protectability of the SMES

At the beginning of the BOSSE project, the protection of a relatively large system made of REBCO tape was perceived as a very challenging task, since several REBCO magnets had been destroyed (see part I-3.1.5). To limit the risks of degradation of the device, three strategies have been adopted:

- To have a large current margin.
- To limit the current density.
- To have a winding made of modular elements.

Another strategy could have been to assemble several REBCO tapes together to make a cable (see part I-3.5), or at least a face-to-face conductor. This strategy has not been followed, because of its

additional cost and because the maximum voltage is not the parameter that limits the discharge speed of the BOSSE SMES (see part II-3.4.3).

#### 3.1.1.3.1. Current margin

In the designs A, B, C and D presented in the following parts, there is a large current margin, higher than 40 %. There are at least two reasons for that.

- At the beginning of the project, we were not sure to be able to protect the SMES. As a matter of fact, some major projects based on insulated REBCO tapes had been recently degraded (see part I-3.1.5). The classical models that aim to determine if a LTS magnet can be protected or not do not apply to HTS magnets and specific models are required, which take into account the performance inhomogeneity (see part I-1.3.4) of REBCO tapes [BRRM00]. Nevertheless, as the variation of performance along the length of the tapes is not known at 4.2 K, there is no mean to know with certainty if REBCO windings can be protected or not at 4.2 K.
- The second reason is that the samples that are used as reference to determine the current margins (see part I-1.3.1) have good performances and are not necessarily representative of the performances on long tapes. In addition, the manufacturers guarantee the performances at 77 K, but not at 4.2 K, and there can be large variations in the lift factor (see part I-1.3.2). It is therefore necessary to have a large current margin in the SMES design.

As the project progressed, we became more confident in the reproducibility of the performances of the tapes. So it appeared to us acceptable to partially reduce the current margin in the last designs.

#### 3.1.1.3.2. Limitation of the current density

As we have seen in part II-2.4, very thin solenoids are an interesting option for high specific energy windings. As we explained before, these solutions show the disadvantage to have low volume energy (see part II-3.1.1.2). But another disadvantage is related to their very high current density. A high current density makes the protection of the device more difficult (see part I-3.1). As the protection of REBCO windings is an issue, we have preferred to limit the current density rather than maximizing the specific energy in order to facilitate the protection of the system.

#### 3.1.1.3.3. Modularity of the design

Given the fact that REBCO conductors are burned only on a small part when damage occurs, we thought it was important for the system to be modular, i.e. that it would be easily possible to remove or replace a part of the winding and continue to operate it. That is why the solutions involving layer wound magnets have been withdrawn and solutions with pancakes have been preferred. A modular design has also the advantage that it is possible to test the performance of modular elements of the magnets before testing the whole magnet.

### 3.1.1.4. Other practical constraints

#### 3.1.1.4.1. Testability of the modules

Another aspect which has been taken into account in the design was the testability of the modular elements of the SMES. The external diameter of the SMES had to be sufficiently small for the pancakes to fit in an available cryostat and to be tested in external background field (see part III). Practically in the final versions, the external diameter of the active winding was voluntarily limited to 240 mm.

#### 3.1.1.4.2. Budget

During the BOSSE project and given the high price of REBCO conductor, it appeared that the budget dedicated to the acquisition of conductor will be a limiting element of the project. This budget was dedicated to the purchase of conductor for both the S3EL (See Introduction) [ACPV17] and the high

specific energy SMES and it has been necessary to work on the design of both devices in order to know how to allocate and share the budget between each of them. In any case, the cost of the conductor is another constraint of the design.

#### 3.1.1.4.3. Limitation in the choice of the unit length of conductor.

A drawback of REBCO tapes is that the produced lengths are anyway rather short (generally less than 200 m for a standard purchase). The price increases very rapidly with the length. Nervethess it is preferable to avoid to use too short lengths of REBCO tapes, which require many connections. These are generally weak points in the winding and generate heat since they are no superconducting welded connections.

The thickness of the winding is related to its radius and to the length of conductor. If the length of conductor is fixed, the radius and the thickness of a winding are no more independent parameters, which has to be taken into account in the design of the SMES.

### 3.1.1.5. Details about the evolution of the criterion of the specific energy (20 kJ/kg for the winding)

As explained before, it appeared difficult to reach a specific energy of 20 kJ/kg with REBCO tapes in the megajoule range within the constraints of the BOSSE project. It has been decided that the objective of the design is a specific energy of 20 kJ/kg for the winding, i.e. that only the mass of the conductor would be taken into account. The mass of the structure pieces (flanges, mandrel, tie rods, screws …) and the mass of the copper contacts are not taken into account. Of course, the mass of the instrumentation, pick-up coils and cryostat is neither taken into account. So in the data presented in the following parts, the specific energy is the ratio between the total magnetic energy of the system and the total mass of the insulated REBCO tapes.

It would have been possible to optimise the structure and to reduce its mass, but this was not done in this project because of limited time and human means. We could also have envisaged to replace for example the screwed copper contacts (see part II-3.4.1.1) by soldered REBCO tapes but in this case the SMES would have not been easily demountable and repairable.

For all of the reasons presented above, the successive designs which are presented in part II-3.3 are the result of a compromise between the initial goal to reach 1 MJ and 20 kJ/kg and other considerations, which aims to guarantee the safety or resilience of the system and the project to be achieved in time.

## 3.1.2. Considerations about the conductor

The manufacturer which have been selected is SuperOx®, since they offer a good compromise between the price and the transport current properties at low temperature. Their standard production is using a substrate of 60 µm made of Hastelloy-C276®. The total thickness of the buffer texturing layers, the REBCO layer and the silver platting can be estimated to 5 µm. With this architecture and given the budget of the project, it appeared that the thickness of stabilizer (copper) had to be limited to 30 µm in order to reach a specific energy of 20 kJ/kg. The total thickness of the bare conductor is therefore 95 µm.

As we have seen in part I-4, a thick insulation can degrade the mechanical strength of the coil. The insulation of superconductors is often made of wrapped polyimide. Another option, which aims to obtain thinner insulation, consists in depositing the polyimide on the conductor. SuperOx® has developed such a process to insulate REBCO tapes [Supe00a]. In order to guarantee the dielectric withstand strength, a thickness of at least 20 µm on each face is required. This solution has been selected for the BOSSE project. Other thin insulation technologies exist such as thin films of UV cured epoxy [LKHS12]. It is possible to obtain even thinner insulations, based on sol-gel process, but this kind of process requires a high temperature treatment, which is not applicable to REBCO conductor. It is

nevertheless possible to deposit the insulator on a stainless steel tape co-wound with bare REBCO tapes [KLJH12].
With 20 µm of polyimide deposited around the Bosse conductor its total thickness reaches 135 µm. Fig. 45 (part I-4.2.2) showed the theoretical cross section of the tape. In reality, REBCO tapes are not flat: they may show a “bone” shape cross-section, because of excess thickness of stabilizer and deposited insulation on its sides (Fig. 85).
The fact that the tapes are not flat is likely to have a negative influence on the mechanical behaviour of pancakes, but this influence is difficult to evaluate and to quantify.

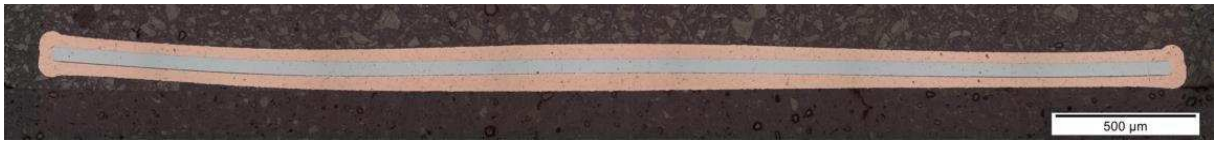


*Figure 85: Cross section of a REBCO tape with irregular copper deposition (Courtesy H.W. Weijers).*

For comparison reasons, the designs presented in the following parts are all supposed to be made of such a conductor, with a substrate thickness of 60 µm and a total thickness for the insulated conductor of 135 µm. The current carrying capabilities are supposed to correspond to the ones measured on SuperOx® samples (see Fig. 10.b in part I-1.3.1) unless otherwise specified.
If another tape manufacturer had been selected, the thickness of the tapes and especially of its substrate would have been different. So the selected designs would have been different.

## 3.2. Solutions to deal with the transverse field at extremities of solenoids

As we have seen in part II-2.4, the value of the radial field at the extremities of solenoids is a major issue in our case. If a solenoid is made of REBCO tape pancakes, the radial field is perpendicular to the surface of the tapes. In this case, the radial field is called “transverse field”. The axial field, which is parallel to the tape surface, is called longitudinal. From the characterisations presented in Fig. 10.a and 10.b, we can see that at 4.2 K, the transverse field reduces much more the critical current than the longitudinal field. According to the results presented in part II-2.4, even thin solenoids would not be a solution to reach a specific energy of 20 kJ/kg if the solenoid is compact and with rectangular cross section. Fortunately, it is possible to adapt the solenoid in order to reduce the maximum value of the transverse field. Different strategies can be adopted to mitigate the problem of the transverse field. These strategies are presented in Fig. 86. In this figure, 4 solenoids are compared. The last one (solenoid 4) corresponds to the design A of the SMES of the BOSSE project (see part II-3.3.2). For comparison reason, the operating current is kept the same in these four solenoids. The current density is 700 A/mm$^2$ in solenoids 1, 2, 3 and in the central pancakes of the solenoid 4. The values of current density and hoop stress are average values in insulated tapes. The values in bare tapes are therefore even higher. The average density of insulated tapes is around 6700 kg/m$^3$. The value of the critical current is based on the performance of Fujikura® tapes (See Fig. 10.a) because it was the only manufacturer for which precise $I_C(B,\Theta)$ measurements at 4.2 K were available at the beginning of the project. Precise measurements of the performances of SuperOx® tapes have been achieved nearly six months after the beginning of the project and these data are used in the following next parts. The critical current is determined by the turn of the solenoid where the local critical current density is minimum. In this part, the maximum transverse field on a turn is used to determine its critical current. As the transverse field can significantly vary along a turn, its critical current can be underestimated. Other evaluation method have been used in the following parts.

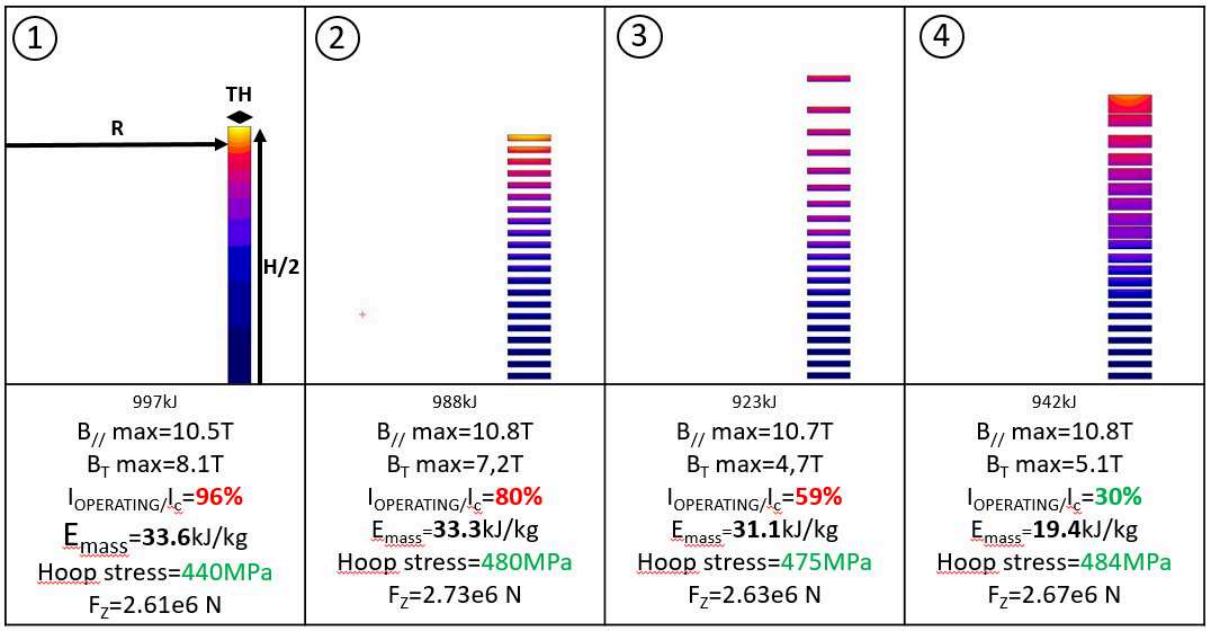


*Figure 86: Evolution of the topology of a solenoid, starting from a solenoid with rectangular cross section and homogeneous current density. More complex solutions aims to obtain a better compromise between the current margin and the specific energy. In each of the 4 cases, the operating current is 380 A.*

From solenoid 1 to solenoid 2, their thickness is multiplied by two, but regular gaps are added between the pancakes. The pancakes are 4 mm wide and the gaps are also 4 mm wide. The average radius, which is R + TH/2, is kept constant in the 4 solutions. Consequently, there is little difference between solenoids 1 and 2. The hoop stress is a bit higher because as the thickness is higher, the inner radial forces are less efficiently reported on the whole structure. The transverse field is lower because the average current density in the cross section is divided by 2, hence an increase of the current margin. Here we can notice that if the objective of the design was to minimize the amount of used conductor rather than maximizing the specific energy, it would be interesting to increase TH by adding some material between the turns. For example, co-winding the REBCO tapes with stainless steel tapes, even if it was useless from the mechanical point of view, would lower the radial field and increase the current margin without changing significantly the longitudinal field nor the total energy if the average radius was kept constant. But of course, as the mass of the winding would be increased, the specific energy would be degraded.

Compared to the solenoid 1 and because of the increase of TH, the solenoid 2 has the advantage that the length of the tapes used to wind the pancakes is 200 m, which was the initial target of the design (see part II-3.3).

From solenoid 2 to 3, the gaps between the pancakes are increased little by little towards the extremities. It aims to significantly reduce the maximum radial field, even more pancakes are submitted to a high radial field. The specific energy is slightly degraded, because the external pancakes are less coupled with other pancakes than in the solutions number 2, so the total energy is a bit lower.

In the solenoid 4, pancakes of different width are used. The gaps between the pancakes are also adapted to increase the current margin. The pancakes are made of tapes with width of 4 mm, 6 mm, 8 mm and 12 mm. They are connected in serial, so the current density is 700 A/mm$^2$ only in the 4 mm wide pancakes. The specific energy is degraded because wider and thus heavier tapes are used at the extremities. The extremities are therefore oversized to sustain their hoop stress, but the fact that the tapes are wider increases the critical current of these pancakes and largely increases the current margin.

We can see that for each of the four solenoids, the axial force is nearly constant.

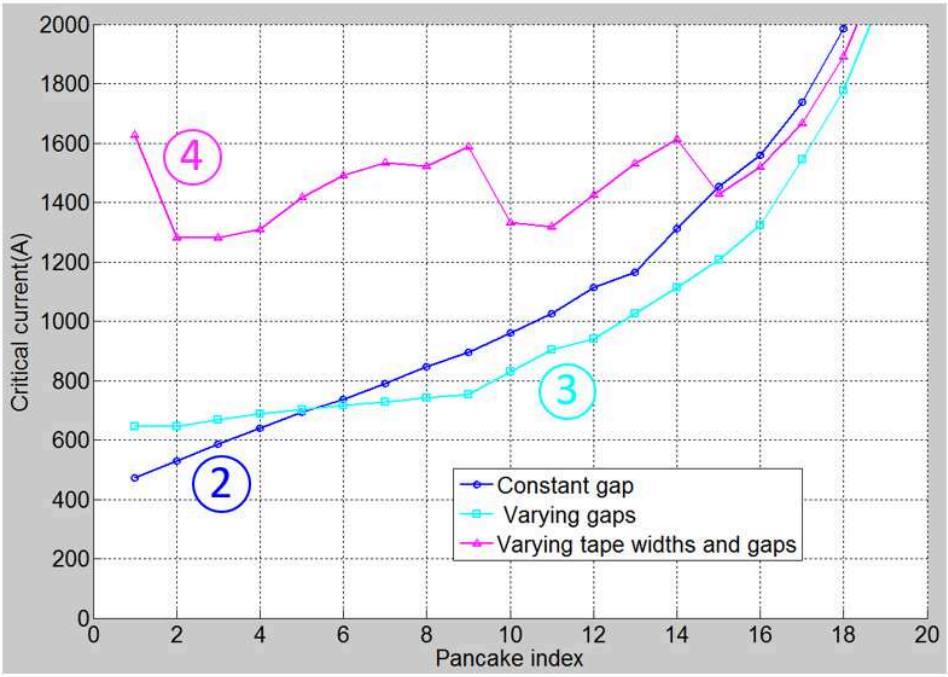


*Figure 87: Critical current depending on the index of the pancake in solenoids 2, 3 and 4. The pancake n°1 is at the extremity of the solenoid and the pancake n° 18 is at the middle of the solenoid. The critical current is evaluated according to the performance of Fujikura® tapes [FlBa00].*

# 3.3. Evolution of the design of the SMES

## 3.3.1. Introduction to the presented designs

### 3.3.1.1. Evaluation of stress

During the project, several designs have been considered for the high specific energy SMES of the BOSSE project. These designs are presented in this part.

To calculate the hoop stress, the Wilson formula is used. Additional stress due to anisotropic Young modulus and anisotropic thermal contraction of REBCO tapes is not taken into account, except for the last design. The hoop stress is always calculated on the central pancakes of the solenoid. These pancakes are the ones submitted to the highest hoop stress since they are exposed to the highest internal B field $B_{INT}$ and to the lowest external B field $B_{EXT}$ (see Fig. 58).

In order to evaluate the strain in accordance with the calculated stress, it is possible to use the data from C. Barth et al. (See part I-1.3.5.1). The data of their measure of the stress/strain relation of a SuperOx® tape at 4.2 K is reported in the 2 first columns of table 7. The measure has been done on a tape with 60 µm of Ha-C276® substrate and 20 µm of copper, which is different of the architecture of the tape used for our SMES. It is then necessary to adapt this data to our case. To do this, we suppose that the copper does not play a role in the mechanical strength of the conductor, and that all the hoop stress is supported by the Hastelloy® substrate. We are therefore a bit conservative in our calculation, but we are nevertheless close to reality since at strains above 0.3 %, the yield strength of copper is overtaken. The polyimide insulation neither plays a role in the longitudinal mechanical strength of the conductor. Since we neglect the copper and the polyimide, only the ratio of the sections matters to calculate the average stress on the conductor, based on the stress on the Hastelloy® substrate. The average stress on the insulated conductor is 135/60 times lower than the stress on the Hastelloy® substrate.

| Strain (%) | Average stress, measured by C. Barth et al. (SuperOx® sample) (MPa) | Average stress on Ha-C276® substrate (60 µm) (MPa) | Average stress on bare conductor (95 µm) (MPa) | Average stress on insulated conductor (135 µm) (MPa) |
|---|---|---|---|---|
| 0.05 | 145 | 193 | 122 | 86 |
| 0.1 | 255 | 339 | 215 | 151 |
| 0.2 | 420 | 560 | 355 | 250 |
| 0.3 | 570 | 760 | 483 | 340 |
| 0.35 | 640 | 853 | 539 | 379 |
| 0.4 | 700 | 933 | 590 | 415 |
| 0.45 | 770 | 1027 | 648 | 456 |
| 0.5 | 840 | 1120 | 708 | 498 |
| 0.55 | 900 | 1200 | 759 | 534 |

*Table 7: Relation between the longitudinal strain and stress of SuperOx® tapes, depending on their architecture. In the column n°2, the tape has 60 µm of substrate and 20 µm of copper. In columns n°3, 4 and 5, the tape is the one which is used for the SMES of the BOSSE project.*

#### 3.3.1.2. Evaluation of the current margin

At the very beginning of the project, a precise $J_C(B,\Theta)$ characterisation of REBCO tapes at 4.2 K under high field was available only for Fujikura® tapes. A few months after the beginning of the BOSSE project a complete $J_C(B,\Theta)$ characterisation at 4.2 K of SuperOx® tapes had been performed by T. Benkel et al. [BMCB17] at the LNCMI Grenoble. That is why these 2 sets of data have been used to determine the current margins of the SMES. At some time, it appeared that Fujikura was no more selling products abroad, because of the reorganisation of their production. What is more, their offer would have probably be outside of our budget. The estimation of current margin with Fujikura tapes has therefore been abandoned and is not done for the last two designs.

To make a simulation of the complete SMES taking into account the superconducting behaviour of the tape is a huge task and requires a high calculation power [Htsm00]. It is therefore not adapted to a predesign stage, and a simplified method has been used to evaluate the current margin. First, the distribution of current is supposed to be homogeneous in the tapes, and therefore in the pancake cross-section. According to this hypothesis, the field map is calculated. For the solenoidal designs, the critical current of each tape is evaluated based on the field value and orientation measured at the middle of the tape. Of course, the width of the tape is also taken into account. The critical current of the SMES is equal to the critical current of the tape that has the lowest critical current, since all tapes and pancakes are in serial.

For the toroidal design, the value of the field at the middle of the tape is not pertinent since the field is purely longitudinal at this point. The critical current is therefore calculated by integration of the local critical current density along the width of the tape. Otherwise, the method remains unchanged.

### 3.3.2. Design A

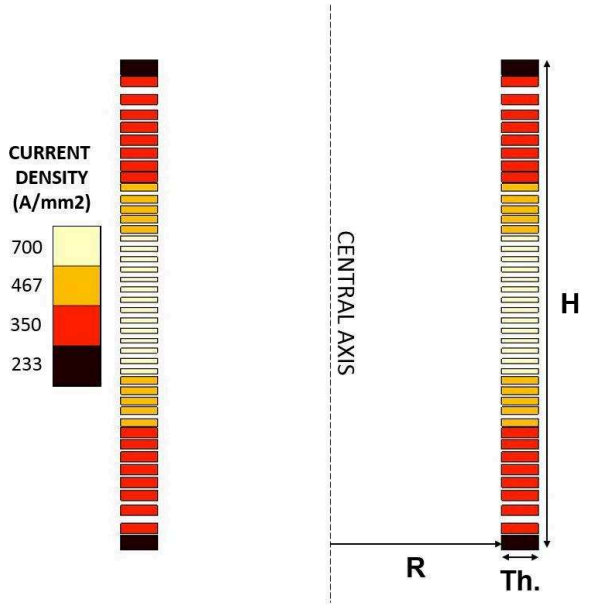


*Figure 88: Cross section of the winding of the design A.*

| | Unit | Value |
|---|---|---|
| Energy | kJ | 950 |
| R | mm | 135 |
| H | mm | 380 |
| TH | mm | 29 |
| $B_{INT}$ | T | 10.8 |
| $B_R$ | T | 5.1 |
| $I_{OPERATING}$ | A | 380 |
| $I_{OPERATING}/I_C$ (SuperOx®) | % | 37.5 |
| $I_{OPERATING}/I_C$ (Fujikura®) | % | 30 |
| Maximum current density (insulated conductor) | $A/mm^2$ | 700 |
| Maximum current density (bare conductor) | $A/mm^2$ | 995 |
| Maximum hoop stress (Wilson) (insulated conductor) | MPa | 500 |
| Maximum hoop stress (Wilson) (bare conductor) | MPa | 710 |
| Inductance | H | 13.3 |
| Length of the tapes | m | 200 |
| Number of turns | | 215 |
| Mass of the winding | kg | 49 |
| Specific energy | kJ/kg | 19.4 |

*Table 8: Characteristics of the design A.*

The design A is a solenoid, which is a stack of pancakes made of tapes with different width. The pancakes at the middle of the solenoid are made of 4 mm wide tapes. These pancakes are surrounded by pancakes made of 6 mm wide tapes, then 8 mm wide tapes and finally 12 mm wide tapes at the

extremities of the solenoid. The gaps between the pancakes are varied in order to improve the current margin. Its characteristics are presented in table 8. This design has the advantage to have a large current margin. But the current density and the hoop stress in the 4 mm wide pancakes is very high. Too reach a specific energy of 20 kJ/kg would require to be very close to the mechanical limit of the REBCO tapes. The use of an external reinforcement made of impregnated glass-fibre or prestress of the winding (see part I-4.4) could have decreased the maximum hoop stress. These solutions have been approached, but their execution turned out to be difficult (see part III-2.2.1.5).

### 3.3.3. Design B

Even if REBCO tapes have amazing current transport properties under high longitudinal field, their critical current is much lower if exposed to a transverse field.

Globally, the critical current of a Fujikura® tape submitted to a transverse field is divided by 5 compared to the case where the tape is submitted to a longitudinal field of same amplitude. For SuperOx® tapes, this ratio is rather close of 3 or 4. Note that this ratio depends on the field and on the temperature. It is lower at higher temperature, such as 77 K, so we can say that REBCO tapes have a particularly anisotropic behaviour at 4.2 K.

In any case, this anisotropic behaviour forces us to adapt the extremities of a solenoid, by reducing gradually the average current density towards the extremities of the solenoid. This adaptation has a detrimental effect on the specific energy, since some conductor used in these extremities is not really useful to store energy but only to increase the current margin.

To avoid this problem, a toroidal solution has been studied. If only mechanical considerations are taken into account, the toroids have clearly a lower specific energy than solenoids (see part I-2.1.3.1). But for a SMES made of a conductor with anisotropic current transport properties, it is not necessary the case.

The characteristics of the proposed toroidal design are presented in table 9 and in Fig. 89. It is a modular toroid with a D-shaped section. It is not a real Shafranov D-shaped toroid (see part I-2.2.1.2.2), because in the 3D finite element software that we have used [Flux00], it is not possible to define some curves with a continuously changing radius of curvature. The section is therefore a coarse approximation of a Shafranov D-shaped section. The half-section (see Fig. 89.b) is made of a vertical part of height H, then 3 eighth of circle with a radius of curvature RC1. The rest of the section, which is one eighth of circle, has a radius of curvature RC2 which is defined by TH and RC1.

The toroid is made of 112 single pancakes with unit lengths of conductor of 95 m, or it can be made of 56 double pancakes with unit lengths of conductor of 190 m. One advantage of a modular toroid is that each module is similar to the other ones, facilitating the manufacturing. As each module is equivalent, the torus can be easily divided in parallel stages in order to increase the discharge speed thanks to an XRAM system (see part I-2.2.1.2.3). With 56 double pancakes, the toroid can be divided in 2, 4 or 8 stages.

In a toroid made of REBCO tapes pancakes, the longitudinal field is the azimuthal field and the transverse field is the radial field. As the pancakes are regularly disposed and very close from each other, the transverse field is very low. The maximum local transverse field is 1.6 T, which aims to obtain a very high current density.

As this toroid has not a real Shafranov D-shaped section, there is a stress concentration at the change of radius of curvature, and it is difficult to determine what the real stress is in a non-impregnated winding with such a shape.

Anyway, this solution has not been pushed further for at least 3 reasons:

- The small angles between the pancakes would have made the structure pieces difficult and expensive to manufacture with the required tolerance.

- The current density in this configuration is quite high, which increases the difficulty to protect the coil. Furthermore, if one pancake is destroyed, it has to be replaced, otherwise the toroid is unbalanced and the operating conditions have to be degraded. In contrast, removing a pancake of a solenoid doesn't have such a detrimental impact.
- The toroidal solution would have been interesting with Fujikura® tapes, but the current margin would have been much lower with SuperOx® tapes. This is because Fujikura® tapes are especially anisotropic REBCO tapes. But Fujikura® was no more selling abroad its products during the beginning of the BOSSE project. In this situation, the toroidal solution does not seem to be the most adapted.

The toroidal solution has not been selected, but it is nevertheless interesting to see that this option is competing with the solenoidal version. It shows that REBCO tapes are well adapted to toroidal designs, which can be mandatory for pulsed power applications because of their near-absence of fringe field (see part I-2.2.1.2.1).

| | **Unit** | **Value** |
|---|---|---|
| Energy | kJ | 950 |
| RIN | mm | 106 |
| H | mm | 111 |
| TH | mm | 15 |
| RC1 | mm | 54 |
| $B_{//}$ | T | 10.3 |
| $B_{Tr}$ | T | 1.6 |
| $I_{OPERATING}$ | A | 494 |
| $I_{OPERATING}/I_C$ (SuperOx®) | % | 66 |
| $I_{OPERATING}/I_C$ (Fujikura®) | % | 35 |
| Maximum current density (insulated conductor) | $A/mm^2$ | 915 |
| Maximum current density (bare conductor) | $A/mm^2$ | 1300 |
| Total axial force on a half section | N | 26409 |
| Total radial (centering) force on a half section | N | 25 247 |
| Inductance | H | 7.8 |
| Length of the tapes | m | 95 |
| Number of turns | | 111 |
| Number of pancakes | | 112 |
| Width of the tapes | mm | 4 |
| Mass of the winding | kg | 40 |
| Specific energy | kJ/kg | 24 |

*Table 9: Characteristics of the design B.*

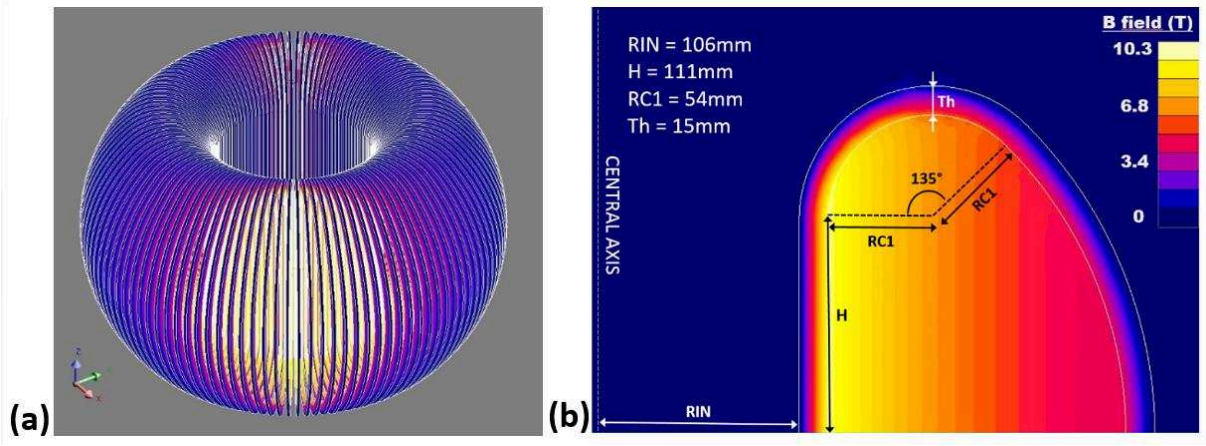


*Figure 89: (a) Overview of the toroid (b) Half cross-section of a pancake of the toroid.*

### 3.3.4. Design C

When discussing with the tape manufacturers, it was found that the price per meter of 4 mm wide tapes was higher than one third of the price per meter of 12 mm wide tapes. This is because the 4 mm wide tapes are actually 12 mm wide tapes which are divided in 3 tapes. The splitting operation can cause some damage to the tapes and a degradation of their performance. What is more, it appeared that our initial expectation for the length of the tapes, 200 m, was too high and that the price could be significantly reduced if the length of the tapes was reduced. For these reasons, a new solenoidal design has been proposed, without 4 mm wide tapes and with unit lengths of conductor of 150 m instead of 200 m. Compared to design A, the radius is smaller, the B field is higher, the height is higher. The current density has been reduced but the current margin has also been reduced. The hoop stress is somewhat lower.

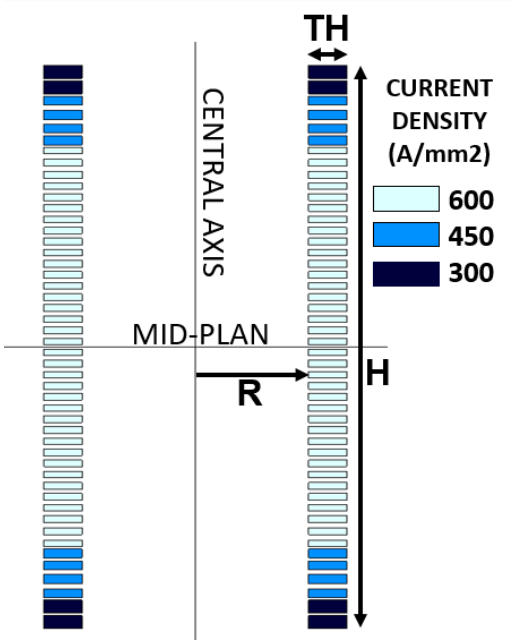


*Figure 90: Cross section of the winding of the design C.*

As the radius is reduced and that the current density is also reduced, it is necessary to increase the longitudinal field to increase the hoop stress and by consequence the specific energy. Except near the extremities of the solenoid, the gaps between the 6 mm wide pancake are 4 mm wide, while in the design A, the gaps are 4 mm wide between 4 mm wide pancakes. So the proportion of void gaps in the section is reduced, which increases the longitudinal field. The fact to reduce the radius also increases the longitudinal field.

| | Unit | Value |
|---|---|---|
| Energy | kJ | 942 |
| R | mm | 90 |
| H | mm | 508 |
| TH | mm | 30.5 |
| $B_{INT}$ | T | 13.1 |
| $B_R$ | T | 5.5 |
| $I_{OPERATING}$ | A | 486 |
| $I_{OPERATING}/I_C$ | % | 55 |
| Maximum current density (insulated conductor) | $A/mm^2$ | 600 |
| Maximum current density (bare conductor) | $A/mm^2$ | 853 |
| Maximum hoop stress (Wilson) (insulated conductor) | MPa | 440 |
| Maximum hoop stress (Wilson) (bare conductor) | MPa | 625 |
| Inductance | H | 8 |
| Length of the tapes | m | 150 |
| Number of turns | | 226 |
| Mass of the winding | kg | 44.9 |
| Specific energy | kJ/kg | 21 |

*Table 10: Characteristics of the design C.*

### 3.3.5. Design D (final design)

Once that the tape manufacturer was chosen and that a first contract was signed, it was decided in agreement with us and the tape manufacturer to use only 12 mm wide tape, with a continuous length of 120 m.

As several prototype pancakes have already been tested at this time, we preferred to keep the design of the pancakes of the version D similar to the design of the version C. Compared to the design C, the external diameter is kept the same and the thickness is reduced from 30 mm to 24 mm since the length of conductor is reduced of 20 %. The gap between the pancakes at the middle of the solenoid is 4 mm wide while the pancakes are 12 mm wide. In this way, the proportion of void gaps is reduced of 20 % compared to the design C. So the longitudinal field is the same as in design C if the current density in pancakes is kept the same.

There are in total 42 single pancakes, arranged in 21 double pancakes.

Since only 12 mm wide tapes are used in this design, the gaps between the pancakes are increased little by little towards the extremities. This is the same strategy that the one used in the design 3 of Fig. 86. The radial field is distributed on more pancakes but the maximum value of the radial field is reduced.

The fact that the quantity of delivered tapes has been increased aims to gain some current margin and mechanical margin. In the design D, the SMES is relatively similar to the design C but is longer. In a way, we can say that the pancakes at the middle of the solenoid are more useful to store energy that the pancakes at its extremities. It can be seen from a mechanical point of view, since the central pancakes are submitted to a higher longitudinal field and then to a higher hoop stress. According to the virial theorem, the stored energy is related to the tensile stress, such as the hoop stress. It can also be seen from an electromagnetic point of view, since the central pancakes are the ones with the maximum

coupling with the other pancakes of the solenoid. Increasing the length of the solenoid aims to increase the number of “useful” pancake compared to the pancakes at the extremities of the solenoid, which are oversized to sustain their hoop stress.

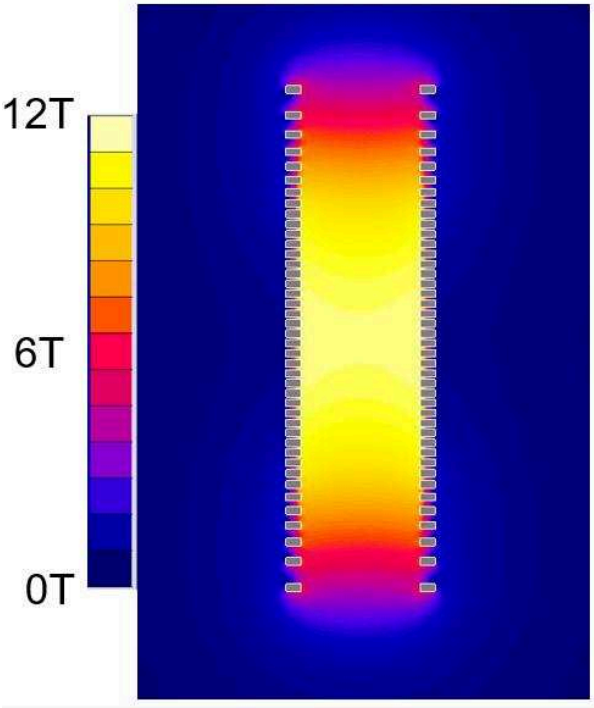


*Figure 91: Cross section of the winding of the definitive design of the high specific energy SMES of the BOSSE project. The amplitude of the B field is shown. I=880 A.*

*Figure 92: Representation of the SMES in its cryostat [Courtesy SigmaPhi®].*

Consequently, it is possible to reach a specific energy of 20 kJ/kg with a lower current density than in the design C. The characteristics of the design D are given in the table 11. These characteristics are given for an operating current of 972 A for comparison with the design C, but also for a current of

880 A which aims to reach a specific energy of 20 kJ/kg and for a current of 839 A which aims to reach an energy of 1 MJ.
As only 12 mm wide tapes are used, the operating current is largely increased compared to design C. The consequence is that the inductance is much reduced, even if the total energy has been increased. The voltage between the extremities of the SMES is therefore reduced for a similar discharge speed.
The current leads which will be used are able to withstand a voltage of 2.5 kV between the current lead itself and the cryostat. If the ground of the electrical circuit is fixed at the middle of the SMES, i.e. if the central pancake is connected to the cryostat, it is possible to discharge the SMES under a total voltage of 5 kV. In this case, the SMES with a current of 880 A could be discharged with a time constant of 0.45 s. As we will see in part II-3.4.3, it will probably not be possible to achieve such a fast discharge because of the eddy losses in the inner contacts of the double pancakes.

| | **Unit** | **Value (J=600 A/mm$^2$)** | **Value ($E_{MASS}$= 20 kJ/kg)** | **Value (E = 1 MJ)** |
|---|---|---|---|---|
| Energy | kJ | 1343 | 1101 | 1000 |
| R | mm | 96 | | |
| H | mm | 814 | | |
| TH | mm | 24 | | |
| $B_{INT}$ | T | 13.2 | 12 | 11.4 |
| $B_R$ | T | 5 | 4.5 | 4.3 |
| $I_{OPERATING}$ | A | 972 | 880 | 839 |
| $I_{OPERATING}/I_C$ | % | 61 | 49 | 45 |
| Current density (insulated conductor) | A/mm$^2$ | 600 | 543 | 518 |
| Current density (bare conductor) | A/mm$^2$ | 853 | 772 | 736 |
| Maximum hoop stress (Wilson) (insulated conductor) | MPa | 446 | 370 | 335 |
| Maximum hoop stress (Wilson) (bare conductor) | MPa | 640 | 525 | 477 |
| Maximum hoop stress, taking into account thermomechanical anisotropy (insulated conductor) | MPa | 507 | 421 | 386 |
| Maximum hoop stress, taking into account thermomechanical anisotropy (bare conductor) | MPa | 720 | 598 | 548 |
| Maximum strain, taking into account thermomechanical anisotropy | % | 0.51 | 0.41 | 0.36 |
| Inductance | H | 2.84 | | |
| Length of the tapes (single pancake) | m | 120.7 | | |
| Number of turns per single pancake | | 178 | | |
| Number of single pancakes | | 42 | | |
| Mass of the winding | kg | 55.1 | | |
| Specific energy | kJ/kg | 24.4 | 20 | 18.2 |

*Table 11: Characteristics of the final design.*

# 3.4. Details about the final design

## 3.4.1. Design of a double pancake

### 3.4.1.1. Description of a double pancake

The SMES is a stack of double pancakes made of a tape with a width of 12 mm and two tape lengths of 120 m. The tapes are wounded on a mandrel and separated with flanges which are 4 mm thick. Both the mandrel and the flanges are made of G-11 (glass fibre reinforced plastic). The two tapes of a double pancake are soldered on an inner contact made of CuC1 copper. At the external diameter, they are soldered on a crescent moon shaped contact, also made of CuC1 copper. The length of conductor between the inner and the external contact is around 120 m. After the external contact, the winding is continued for 6 turns. The last three turns are glued together with little drops of Stycast®. These additional turns aim to balance the hoop stress on the external contact and to report the local stress due to mechanical blockage from the soldered contact to the outer turns, which are not conducting electrical current.

When the double pancakes will be stacked together to form the SMES, the external contacts will be screwed together on their flat surface, in order to ensure the electrical serial connexion of all the double pancakes.

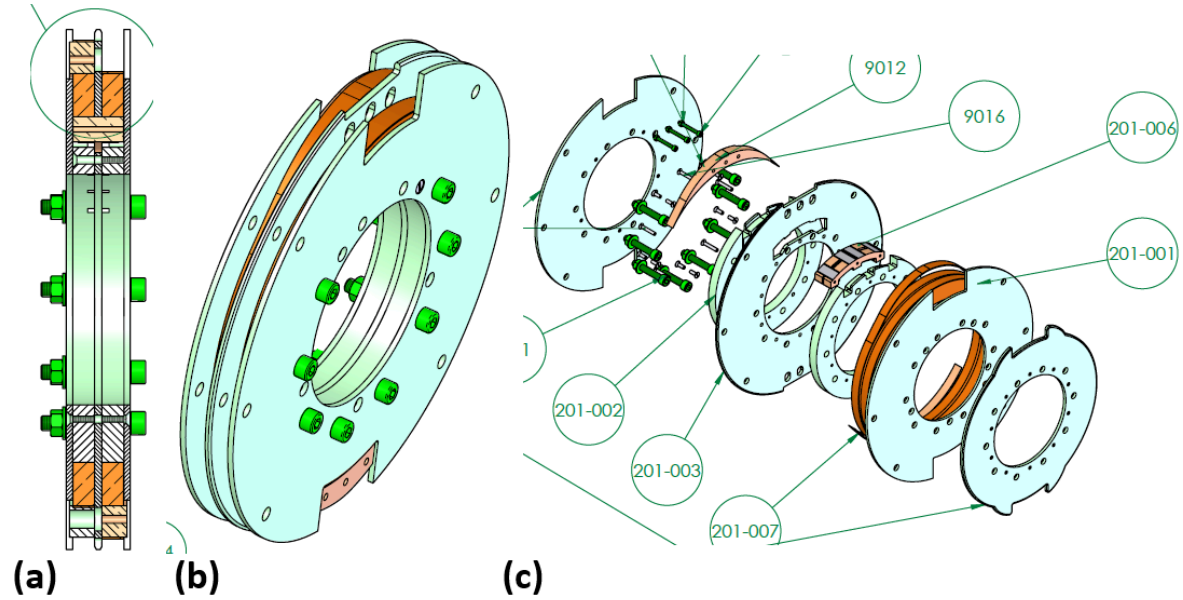


*Figure 93: a) Sectional view of a double pancake. b) Drawing view of a double pancake. c) Exploded view of a double pancake. The internal contact (201-006) is fitted in the slot of the central flange (201-003) and blocked by the 2 mandrels (201-002). When the double pancake is stacked with other ones to make the SMES, one of the two external flanges (201-001) is removed. The flange at the forefront is only used during the winding of the double pancake.*

The extremities of the REBCO tapes are soldered on massive copper pieces, which are the inner and external contacts. This has be done to have a low contact resistance and good reliability of the contacts, both from the mechanical and thermal points of view. Massive pieces of copper are indeed mechanically strong and they enable to distribute the heat due to non-superconducting joints.

The external contact has a crescent moon shape because the REBCO tape is soldered on the external side of this contact and that there are several additional reinforcement turns around it. This crescent moon shape was also originally required because we had the project, finally abandoned (see part III-2.2.1.6), to reinforce the pancakes with collars made of glass-fibre tapes. It is anyhow necessary for the beginning and the end of the contact to be very thin and smooth, for the conductor not to suffer from stress concentration. Despite these precautions, the edge of the external contact is, all the same,

a vulnerable point of the pancake. The single pancake prototype was damaged at this point when submitted to high mechanical stress, higher than what is required in the design of the SMES (see part III-3.2.2.2). According to simulations performed by Loïc Jean, the problem comes from the rigidity of the contact compared to the winding, and to the slight difference of thermal contraction between the copper and the conductor.
In order to support the axial forces, some spacers are placed all around the pancakes. Some space is left between the outer turns of the pancakes and the spacers, in order to let the pancakes to move freely during the charge of the SMES and to avoid pinching and/or stress concentration.
There is a pair of voltage taps on each double pancake, which are soldered at the external end of both tapes, after that the last turns are glued with Stycast®.
A double pancake is shown in Fig. 93 and 94. The detailed plans of a double pancake and the SMES are shown in annexes B-5 and B-6. The plans have been drawn by C. Lecrenn from SigmaPhi [Sigm00].

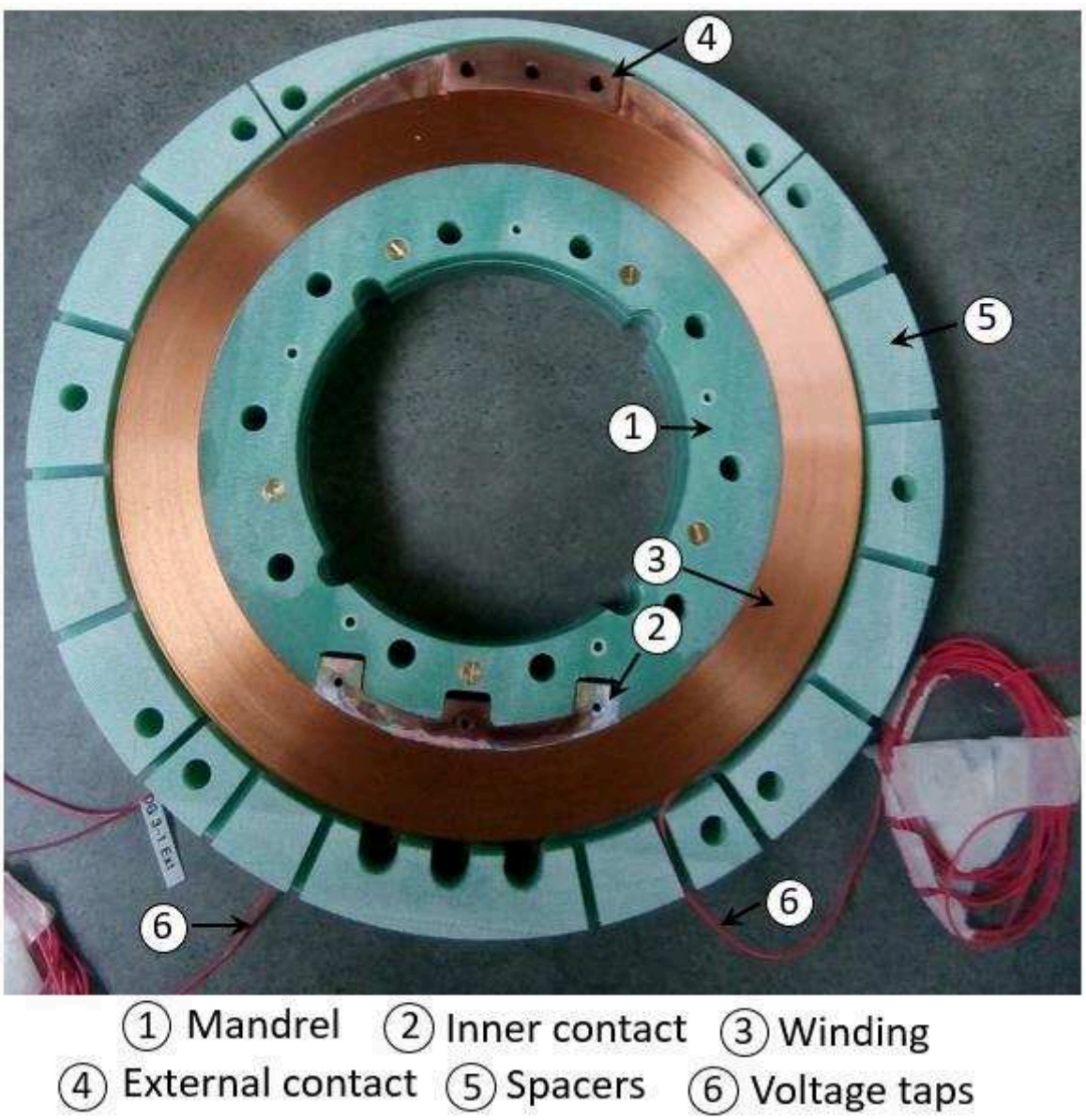


*Figure 94: Top view of a double pancake of the SMES.*

#### 3.4.1.2. Manufacturing of the pancakes.

The prototype pancakes and the first double pancake of the SMES have been wounded at the Neel Institute. The other double pancakes of the SMES are wounded by SigmaPhi [Sigm00] at Vannes. The winding of a pancake made at the Neel Institute is visible in Fig. 95. The REBCO tape is unwound from the spool delivered by SuperOx®. Thanks to an electrical motor and a controlled brake, a tension is applied to the tape during the winding. The brake applies a constant torque of 0.70 N.m to the spool. The tension of the REBCO varies then from 0.7 kg when the spool is full (beginning of the winding) to 1.4 kg when the spool is almost empty (end of the winding).
Before to start the winding, the 2 tapes are soldered on the inner contact of the double pancake. This contact is blocked by a flange and two mandrels. The preparation of the inner contact is shown in Fig. 96. Some short lengths of REBCO tapes are put in grooves perpendicular to the main REBCO tapes. This lowers the resistivity of the contact. Each time a tape is soldered to a copper contact, it is necessary to heat this contact to achieve the soldering. This is performed by a resistor inside a copper piece screwed to the contact. Thermal paste improves the thermal exchanges. The two pieces are heated up, a little bit below 180 °C, which is nearly the fusion temperature of the Indium alloy (In Pb (15) Ag (5)) used to solder the REBCO tapes. Once that the contact is hot enough, the REBCO tapes are soldered with Indium alloy using a soldering iron at 180 °C. Alloys with low fusion temperature are required to solder REBCO tapes not to degrade them. It is recommended not to expose REBCO tapes to temperatures higher than 180 °C, even if this value varies with the exposure time and depends on the manufacturer.

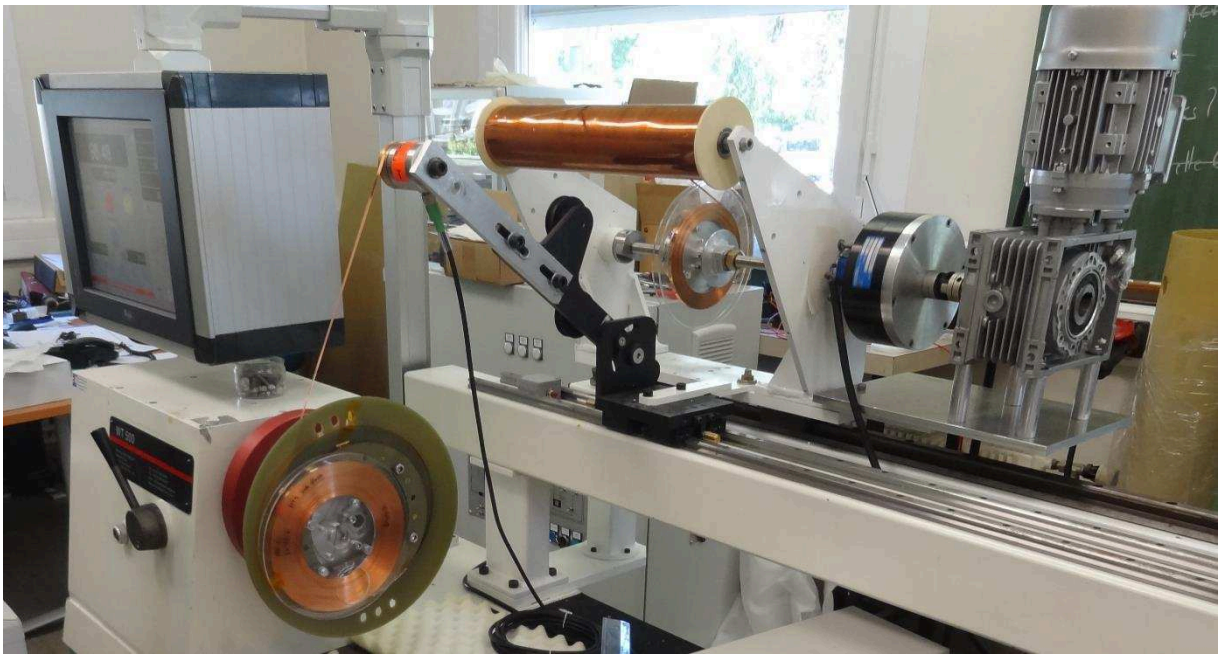

*Figure 95: Winding of a pancake.*

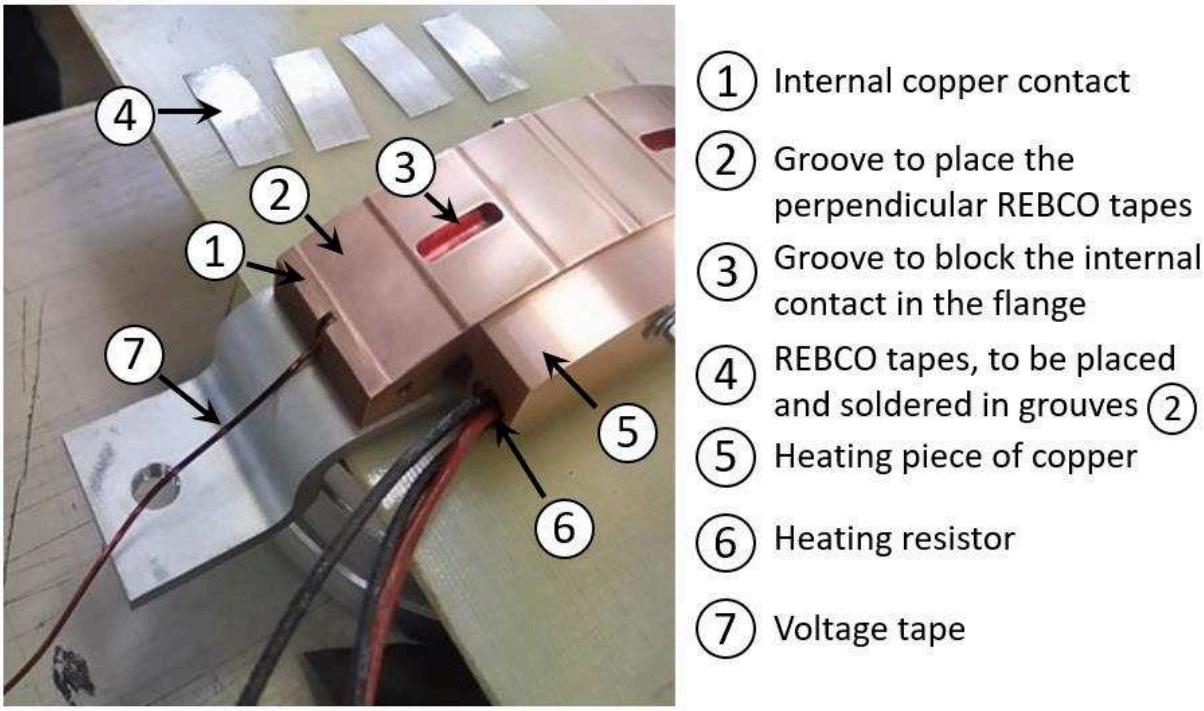


*Figure 96: An inner contact, just before the soldering of perpendicular REBCO tapes.*

In Fig. 97, we can see the operation to remove the insulation from the tape. The tapes received from SuperOx® are completely insulated, and it is necessary to remove the polyimide where the tape has to be soldered. The polyimide is removed thanks to a chemical attack during 1 minute.

*Figure 97: Operation to remove the insulation from the tape, in order to solder the tape to the external contact.*

To finish the pancake, the last three reinforcement turns are glued with some Stycast®. This product is a bi-component black glue, able to keep its properties in helium liquid bath. Some small drops of this product are deposited between the last turns of the pancake. The amount of deposited product is voluntarily small, to prevent the Stycast® from dripping to other turns or between the turns and the flange, which can be harmful for the winding (see part III-2.2.1.5).

*Figure 98: Gluing of the last turns of the pancake with Stycast®*

## 3.4.2. Details about the mechanical design of the SMES

### 3.4.2.1. Precisions about the hoop stress and the mechanical limitations of the SMES

In our design, the stress which limits the stored energy of the SMES is the hoop stress. More precisely, the most sensitive points of the SMES are the inner turns of the mid-plane double pancake where the hoop stress is maximum. The hoop stress can be estimated thanks to the Wilson formula. But as we have seen in part I-4, the Wilson formula does not take into account the influence of the stiffness and thermal contraction anisotropy of the conductor. It is therefore necessary to rectify the value of the hoop stress calculated with the Wilson formula by taking into account these phenomena.

#### 3.4.2.1.1. Stiffness anisotropy:

On the one hand, we have seen in part I-4.2 that the value of hoop stress depends on the geometry of the pancakes and the relative stiffness of the deposited polyimide and bare tape at low temperature. From the results obtained in part I-4.2.3, we can estimate that in the case of our SMES, the hoop stress at the inner turn is 6 % higher than the one calculated with the Wilson formula.

#### 3.4.2.1.2. Thermal contraction anisotropy:

On the other hand, as we have seen in part I-4.3, the anisotropic thermal contraction of the conductor creates small voids between the turns of the pancakes. In the design of our SMES and given the relative thermal contractions of the deposited polyimide and the bare REBCO tape, the cumulated distance of the gaps along the radius is 46 µm. When the SMES is going to be charged, the inner turns will be pushed outward by the magnetic forces, until they touch the other turns again. As the inner turns are pushed outward by a high B field and that the outer turns are pushed inward by a low B field, we can suppose that in the worst case, the inner turns have to expand radially of 46 µm until all the turns are touching each other. A radial expansion of 46 µm for the inner turn (radius of 96 mm) corresponds to a strain of 0.048 %. It means that until the inner turns is expanded of 0.048 %, it is pushed outward

without pressing on other turns, i.e. without radial stress. The other turns start to touch each other earlier, starting with the outer one. During the first phase, i.e. when the strain of the inner turn is lower than 0.048 %, the behaviour of the inner turn is ruled by the JBR formula since there is no radial stress. Once that all the turns are in contact, the behaviour of this same turn follows the Wilson formula corrected according to the effect of the stiffness anisotropy.

#### 3.4.2.1.3. Combination of the corrections due to the stiffness anisotropy and the thermal contraction anisotropy:

This change in the relevant model to estimate the hoop stress is shown in Fig. 99. This figure shows the hoop stress of the inner turn according to several models. We are interested in the first turn since this is the one submitted to the highest hoop stress. The hoop stress calculated by the Wilson formula is in blue, the Wilson formula increased by 6 % is in green and the JBR formula is in red. At low current, the inner turn is ruled by the JBR formula. A strain of 0.48 %, which is equivalent to an average hoop stress of 86 MPa on the insulated conductor, is reached at a current of 330 A. At this point, the inner turn starts to behave according to the same model that the green curve. Finally, the hoop stress of the inner turn is described by the black curve. It starts to behave like a free turn then behaves like a turn in a mechanically anisotropic winding. The black curve is similar to the green curve, but with an offset determined by the point where the behaviour of the turn has changed.

We can conclude that the inner turn is submitted to a stress of 386 MPa at I = 839 A (E = 1 MJ) and 421 MPa at I = 880 A ($E_{MASS}$ = 20 kJ/kg). These stresses are averaged values on the insulated tape. The corresponding strains are respectively 0.36 % and 0.41 % (see table 7 or 12). According to the data presented in Fig. 13, such values of strain are acceptable. Nevertheless, they are high and close to the delamination limit of the tapes. It will therefore be necessary to act with caution when we will try to reach a specific energy of 20 kJ/kg. During the testing programme, high currents around 880 A will likely be reached only at the last experiments.

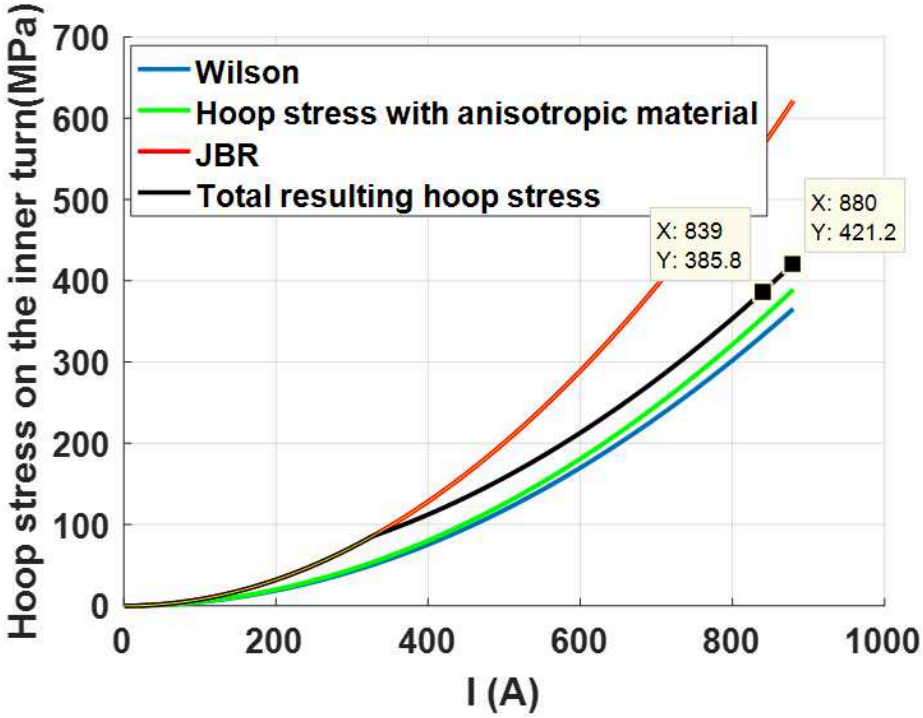


*Figure 99: Hoop stress of the inner turn according to several models, depending on the current. The values are average values on the insulated conductor. The pertinent model to determine the real hoop stress of the inner turn changes at I = 327 A (strain = 0.048%). The real hoop stress reaches 386 MPa when the stored energy is 1 MJ and 421 MPa when the specific energy is 20 kJ/kg for the winding.*

According to the data presented in Fig. 15, to reach repeatedly such level of strain would cause a premature aging of the tapes. Our design is therefore satisfying to reach a specific energy of 20 kJ/kg for the winding, but it could not be used in a very repetitive way.
It is also important to remind that the evaluation of the ratios of the transverse and longitudinal stiffnesses or thermal contractions are based on bibliographical documentation. The real properties of the components of the tapes, especially the polyimide, could be different from the ones used for the calculation. An experimental evaluation of the transverse Young modulus and thermal contraction of the REBCO tapes used in the BOSSE project would be useful to enhance the reliability of the presented calculations.

#### 3.4.2.2. Details about the axial stress

The SMES is submitted to a very high hoop stress but is also submitted to a high axial forces. The pancakes which are submitted to the highest self axial force are the ones which are at the extremities of the SMES since they are the ones submitted to the highest radial field. But as the axial compressive forces are cumulated from the extremities until the mid-plane of the solenoid, the highest compressive axial stress is reached at the mid-plane of the solenoid. When I = 880 A (i.e. when $E_{MASS}$ = 20 kJ/kg), the maximum axial force applied to an extremity pancake is 186 kN. The total compressive axial force of a half solenoid is 1 840 kN. If this total force was applied on the edge of the mid-plane pancake, this pancake would be submitted to an axial stress of 113 MPa. It is highly questionable that a pancake made of insulated but non impregnated REBCO tape could withstand such a compressive stress on its edge. But it is not the case in our design since the compressive axial forces are reported to the mandrel and the spacers by the flanges. In this way, the central pancakes are not submitted to a high axial stress (See Fig. 100). The central mandrel and spacers are submitted to an axial stress of 90 MPa for I = 880 A, which is well below the compressive strength of the G-11 [Good01].

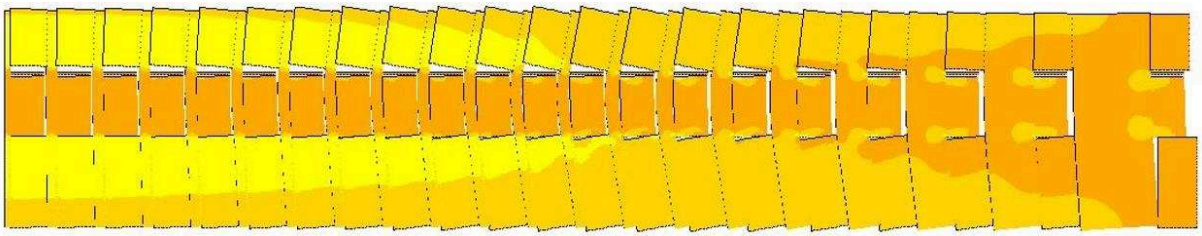

*Figure 100: Axial stress in the cross section of the half SMES, including the REBCO pancakes, the mandrels (below) and the spacers (above). The mid plane of the SMES is on the left and the extremity of the SMES is on the right. The pancakes are considered to be homogeneous blocks. The axial compressive stress goes from 0 MPa (dark orange) to 90 MPa (yellow) for I = 880 A. This simulation has been done by Loïc Jean.*

Even if the problem of the cumulated axial stress is avoided by the spread of the magnetic load from the pancakes to the mandrels and spacers thanks to the flanges, we can wonder if the pancakes can endure their own axial force. This aspect has not been simulated, but the double pancakes which have been tested in self field were submitted to a compressive axial stress partly similar to the one endured by the external pancakes of the SMES. The average radial field is indeed 2 T in both cases (see part III-3.1.2). No problem related to this axial stress was observed during the tests of the double pancakes.

### 3.4.3. Heating of the inner contacts during fast discharge of the SMES

The inner and external contacts of the double pancakes are massive pieces of copper. In that respect, they are submitted to eddy losses when the SMES is charged or discharged. In steady state, assuming no skin effect, eddy losses are proportional to the electrical conductivity of the material and to the

square of the time variation of the field (see part I-3.4.2.1). In other words, they globally increase with the square of the current ramp. They are therefore not a problem when the SMES is charged or discharged slowly, at a rate of a few Amps per seconds. They are neither a problem in the external contact, where the local field (less than 1 T) is much lower than the field of the inner contact (12 T). But if the SMES is discharged too quickly, there is a risk that the temperature of the inner contact rises to dangerous values. This heating could be conducted to the inner REBCO turns, endangering the winding of the SMES.

The heating of the inner contact has been evaluated by simulations whose results are presented in Fig. 101 and table 12. In these finite element simulations, the inner contact is submitted to a field of 12 T which follows an exponential decay. This situation corresponds to the case where the SMES is discharged in an external resistor. The eddy losses are calculated, taking into account the RRR and the magneto-resistance of copper (see part I-3.1.2). These simulations have been performed with Flux®. For the eddy losses calculation, the temperature of the contact is supposed to be homogeneous and the temperature rise is calculated taking into account only the thermal capacity of the copper (adiabatic conditions). The cooling by the helium bath is not considered. The variation of the resistivity with the temperature is not taken into account, but it remains very low in the studied range of temperature anyway (see part I-3.1.2). Of course, this simulation is quite simple and should be improved, using a more detailed model and a multi-physical approach. Nevertheless, it gives us a first insight of the problem.

The simulations have been performed for 2 different time constants and 2 different values of RRR. The time constants are 1 s and 10 s. The value of the RRR are 64 and 200. The value of 64 has been measured in the inner contact of a prototype double pancake (see part III-2.2). This value seems rather low compared to what can be classically expected from a massive piece of CuC1 copper, that is why simulations are also performed with a higher value of RRR, equal or higher than 200.

But no big difference occurs between the results of the simulations with a RRR of 64 and with a RRR of 200. This is due to the magneto-resistance. At 4.2 K and under 12 T, the resistivity of copper with a RRR of 64 is only 25 % higher than the resistivity of copper with a RRR of 200 [Cryo00].

We can see that in all the simulations, the temperature quickly rises at the beginning. This is because the thermal capacity of copper is very small at 4.2 K (see part I-3.1.1), and also because the deposited power is higher at the beginning.

In Fig. 101, the discharges with a time constant of 1 s are on the left and the discharges with a time constant of 10 s are on the right. We can see that multiplying the time constant by 10, the maximum power of the dissipated eddy losses is nearly divided by 90 and the energy deposited in the contacts during the discharge is nearly divided by 12 (see table 12). The difference on the final temperature is not so significant, since the temperature increase is only divided by 2, which is due to the sharp increase of the thermal capacity of copper in this temperature range.

As already mentioned, the inner contact is supposed not to be cooled by liquid helium (adiabatic conditions) in the simulations presented here. Of course, this hypothesis is pessimistic, since the SMES will be immersed in a liquid helium bath. For slow discharge, the helium bath should be able to limit the temperature excursion. But in this case, the maximum temperature of the contact and of the attached REBCO tape is difficult to simulate and calculate. It depends on the heat exchange between the helium bath and the copper piece but also of the geometry of this piece and of its surroundings (G-11 mandrel and flanges). In order to improve the cooling of the contact, some void spaces between the copper contact and the mandrel as well as helium channels in the mandrel have intentionally been prepared.

The problem of the heating of the inner contacts by eddy losses appears to be a critical point of the design and limits the discharge speed of the system. For this reason, it would merit further study. A Cernox® temperature probe will be inserted in the inner contact of the central pancake in order to

monitor its temperature. Iterative discharge tests with increasing currents and/or decreasing decay time constants will be performed to determine what seem to be an acceptable discharge speed for the SMES.

A fast discharge of the SMES is desirable to demonstrate the ability of the SMES to deliver high power, but also to ensure the safety of the coil if a local loss of superconductivity is detected (see part I-3.1). But as we have seen in this part, a too fast discharge of the SMES may heat the inner REBCO tapes and endanger the safety of the SMES. A compromise between these two aspects has therefore to be found to determine the preferable discharge speed of the SMES. In the absence of more precise simulations or experimental data of the complete SMES, a decay time constant of 10 s seems to be a good target. With this time constant, the initial slope would be -88 A/s, which should be sufficient to protect a pancake according to the experiments performed on prototype pancakes (see part III-3). And the maximum heating power (around 0.6 W) of the eddy losses could likely be counterbalanced by the cooling power of the helium bath.

Obviously, if the SMES has had to be a pulsed power source with a time constant of a few milliseconds, it would have not been possible to use massive pieces of copper as inner contacts. It would be mandatory to make real double pancakes (no inner connexion between the two pancakes) or to design the junction in a completely different way.

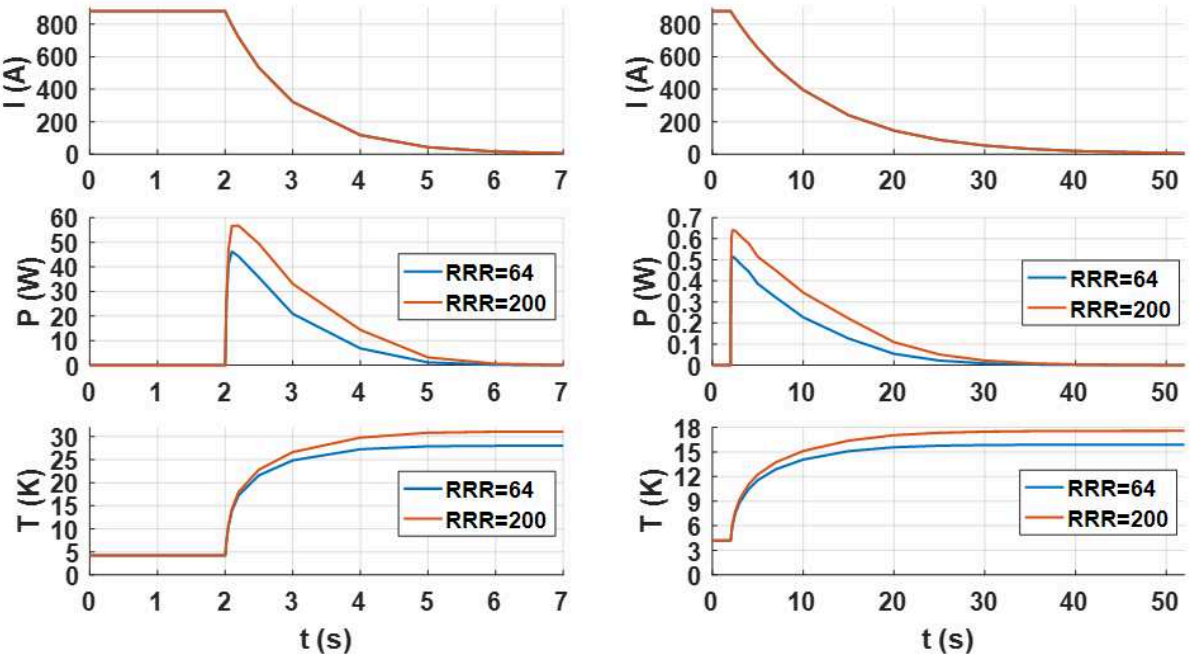


*Figure 101: Comparison of the discharge of the SMES with a time constant of 1 s (on the left) and a time constant of 10 s (on the right). I is the current in the SMES, P is the power dissipated by eddy losses in the inner contact and T is the temperature of the inner contact, which is considered to be adiabatic. The discharge starts at t = 2 s.*

| RRR | Decay time constant (s) | Total deposited energy per contact (J) | Volume of vaporized liquid helium per contact ($cm^3$) |
|---|---|---|---|
| 64 | 1 | 53 | 20 |
| 200 | 1 | 81 | 31 |
| 64 | 10 | 4.6 | 1.8 |
| 200 | 10 | 6.9 | 2.7 |

*Table 12: Energy deposited in an inner contact by an exponential decay of the B field from 12 T to 0 T. The volume of vaporized liquid helium is calculated using its latent heat of vaporization (at 4.2 K and 1 bar): 20.3 kJ/kg.*

### 3.4.4. Protection system

The protection system of the SMES will be based on a voltage detection of a transition to normal state. Instead of having only one voltage measurement at the extremities of the SMES, there will be 21 voltage measurements, i.e. one for each double pancake of the SMES. The voltage of each double pancake will be combined with the voltage of an associated compensation coil to compensate its inductive voltage. The interest to use multiple differential measurements and to use compensation coils is explained in part III-1.2.

#### 3.4.4.1. Compensation coils

To simplify the manufacture of the compensation coils, the compensation coils all will have the same geometry and the same number of turns. The number of turns will be oversized and only a portion of the voltage of each compensation coil is subtracted to the voltage of its corresponding double pancake thanks to a resistive dividers. The design of the compensation coils and/or the calculation of the ratio of the voltage dividers can be achieved thanks to the equations given in part III-1.2.5. On one half of the SMES, the ratio of each voltage divider will be different since each pancake has a different position in the SMES and that its compensation coil has a different position compared to the SMES.

Practically, the compensation coils will be placed inside the SMES to limit the size of the cryostat, but they could have been placed around the SMES. They will have an inner radius of 56 mm, an outer radius around 63 mm and a height of 28 mm. They will have 1200 series turns, made of standard insulated copper wire with a diameter of 0.36 mm. There are two reasons why their number of turns is much higher than the number of turns of a double pancake. First, the compensation coils are relatively far away from the superconducting winding because of the thickness of the mandrel of the SMES, which decreases the coupling between the compensation coils and the SMES. Secondly, as they are smaller than the REBCO pancakes, they need more series turns for the same magnetic flux.

The wire used to wind the compensation coil is relatively large. We could use wire with smaller diameter if we wanted to reduce the size and/or the mass of the compensation coils. In addition to the fact that there is higher risk to damage the wire if it is very thin, it is preferable to have a resistance of the compensation coil negligible compared to the resistance of the voltage divider. Otherwise, it is necessary to know the resistance of the compensation coil at low temperature and to take it into account to calculate correctly the ratio of the voltage divider.

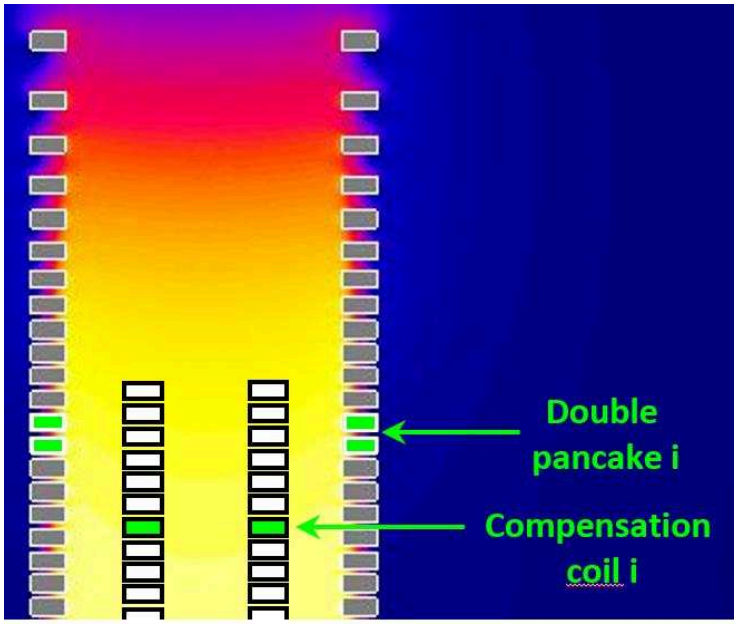


*Figure 102: Cross-section of the upper half of the SMES with its compensations coils.*

### 3.4.4.2. Detection of a transition to normal state and discharge

The 21 independent compensated signals will be treated by an analogue-to-digital acquisition card then transmitted to a computer. During the tests of the prototype pancakes (see part III-3.2), we identified transitions by visualizing the signal with an oscilloscope. But as there would be 21 independent signals to observe during the tests of the SMES, an automation of the signals analysis is necessary. Each signal will therefore be independently treated by an algorithm which should recognize a transition of a pancake to the normal state. This algorithm has not been realised yet. The criterions which will be used to identify a loss of superconductivity will be determined thanks to the experimental work presented in part III-3.2. As we will see, a simple voltage threshold detection is far from being sufficient, and several kinds of events are likely to trigger false positives if the algorithm is not properly designed.

If a transition to normal state is detected, the SMES is discharged in an external resistor. As we have seen above (see part II-3.4.3), the discharge speed, i.e. the discharge resistor, will be limited by the heating of inner contacts due to eddy losses. The inductance of the SMES is 2.84 H, so a dump load resistor of 0.28 Ω is required to have a discharge time constant around 10 s. In this case, the maximum voltage of the SMES is only 250 V (± 125 V) during the discharge.
When the SMES is discharged, the acquisition electronics and the current source have to be disconnected from the SMES to avoid overvoltages. The current source is protected and the acquisition electronics are protected by switches. In case one of the switches would fail to open, the inputs of the acquisition card and the current source should also be protected by ZnO varistors.

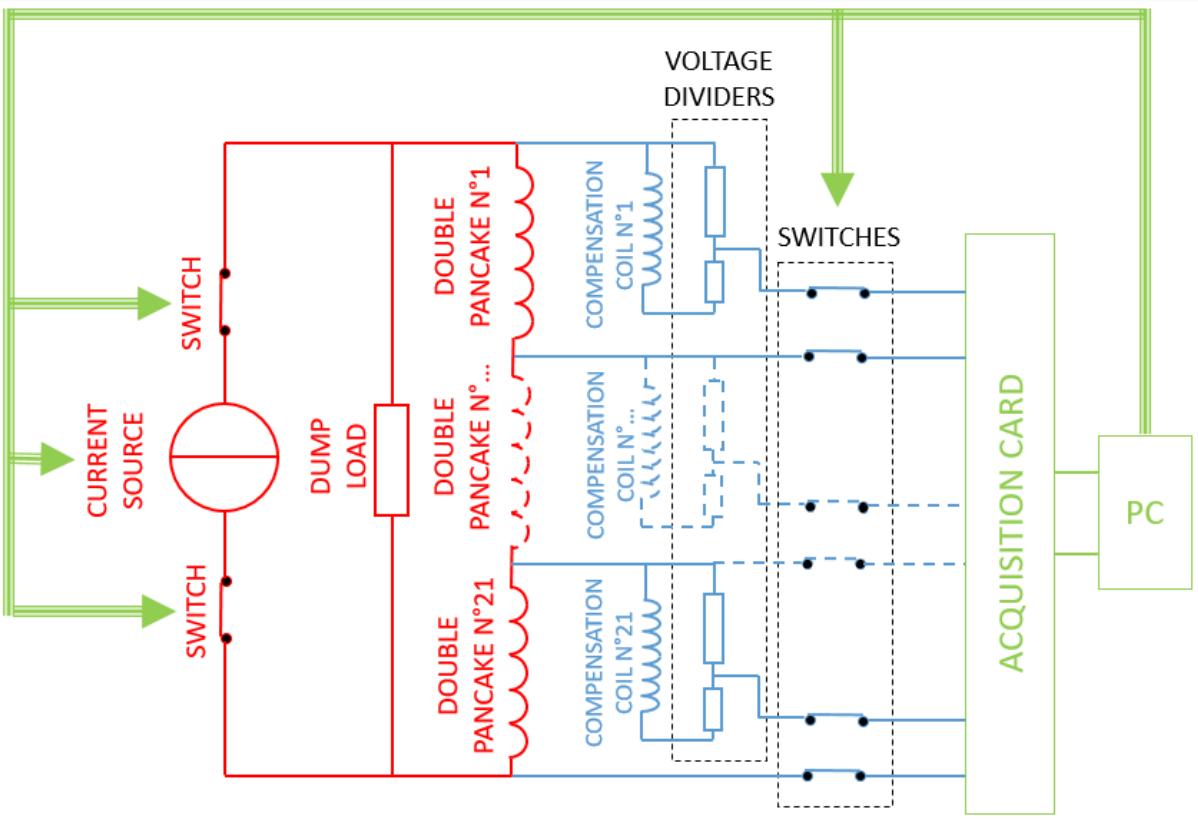


*Figure 103: Diagram of the detection and protection system of the SMES. The power circuit is in red. The analogical compensation circuits are in blue. The numerical treatment and control command elements are in green. The ground is at the middle of the winding of the SMES, i.e. the central pancake of the SMES is connected to the cryostat. In this way, the maximum voltage between the current leads and the cryostat during the discharge is minimized.*

#### 3.4.4.3. Possible alternatives to the detection system

Other solutions could have been chosen to protect the SMES. The voltages of all the compensation coils are proportional to the variation of the same current I, so they are all proportional to each other. It could therefore appear logical to use only one compensation coil and to multiply its signal by electronic or numerical means to compensate the inductive voltage of all the superconducting pancakes. Nevertheless, an electronic treatment of the signal of a compensation coil would delay its comparison to the signal of the pancake and would also degrade its fidelity, hence degrading the effective compensation of the inductive voltage. On the other side, a numerical compensation has also drawbacks which are explained in part III-1.2. That is why we prefer to compensate the signal by fully analogical means before acquisition of the signal by the analogue-to-digital acquisition card.

Satisfying results could also probably be obtained using electronic multiplication of one compensation coil or using numerical compensation. Both of these solutions have the advantage that only one compensation coil is needed. Nevertheless, we preferred to base the detection system of the SMES on a fully analogical compensation of each independent signal since we have feedback about this method and that it has proven its effectiveness during the tests of the prototype pancakes (see part III-3).

# 4. Conclusion

The optimisation of the design of a SMES can be a complex task, depending on its objectives and specifications. It is advantageous to lead a reflection about the optimisation method prior to start it in order to choose the adapted one.

Contrary to numerous devices used in electrical engineering, there is generally no ferromagnetic materials in SMES systems. It makes it possible to extrapolate the field distribution of a SMES winding and the ensuing quantities (stored energy, stress distribution,…) from another SMES winding with the same aspect ratio but a different size and/or current density.

Thanks to the approach based on the aspect ratios and extrapolation equations, it is possible to quickly explore a large set of solutions with varied geometry and/or stored energy. It is then possible to evaluate the limits of the performances of SMES, for example in term of specific energy and according to the stored energy.

The very simple case of a solenoid with rectangular cross section and homogeneous current density is presented in details in order to demonstrate the advantages of the proposed method. It shows that very different geometries can be interesting solutions to the same problem. It also shows the limits of the appropriateness of some formulas and evaluation methods for some designs. For example, the Wilson formula is less relevant if the winding is thick and the conductor is mechanically anisotropic.

This study has been used to determine what the possible topological solutions were for the SMES of the BOSSE project. The geometry is determined by the mechanical and electrical properties of the conductor, but also by our will to limit the current density and to compact the SMES and other practical problems.

In the fourth part of the chapter, some methods are proposed to deal with the problem of the high transverse field at the extremities of the solenoid. Several releases of the design of the BOSSE project are presented. The final version of the design of the SMES, which can reach a specific energy of 20 kJ/kg for the winding, is presented in details. It is shown that the discharge speed of the SMES will be limited by the heating of internal contacts due to eddy losses rather than by the voltage at the extremities of the SMES. The manufacturing method of the first pancakes is also presented.

# Chapter 3: Development of prototype pancakes

# 5. Introduction to the experimental work

## 5.1. Presentation of the elements of the experimental set-up

In the experiments presented in chapter III, the same equipment has often been used. The essential elements of these experiments are presented here.

For the tests of the pancakes (see parts III-2 and III-3) the experimental setup is always more or less the same. The pancake and its compensation coils are mounted at the lower extremity of a probe. The probe has two current leads connected to the extremities of the pancake. It also has many signal wires, which are used to transmit information about voltage of the pancake and compensation coils, temperature and value of the magnetic field.

We have used a probe which was developed during the Eucard project. This probe is able to carry 3 kA, which is much more than what is required in our case. But this probe has the advantage to have a large cryostat, with an inner diameter of 298 mm, which is large enough for the pancakes to fit inside. The plan of the probe is showed in appendix C-1.

The voltage signals, which come from the voltage taps at the extremities of the pancakes and compensation coils are send directly to an oscilloscope, which is a Yokogawa®-DL 850. Real time data processing is performed by the oscilloscope. The digital filters which have been used are the average mean filters and/or low pass filters proposed by the oscilloscope. The cut-off frequency of the low pass filters is quite low, it is generally 6 Hz.

At least in the first experiments, the voltage measurements are simultaneously performed by nanovoltmeters 2182A from Keithley®, in order to guarantee the measured values. The nanovoltmeters are interfaced with a computer and the signal is treated by a LabVIEW® program.

Depending on the experiments, the current source is either a current source from Sorensen®, either the “Bertha” current source. Bertha is a homemade DC power source, developed at the LNCMI Grenoble. The Bertha has lead-acid batteries and is operated disconnected from the grid, which aims to supress the 50 Hz parasitic component.

The current source is controlled thanks to a LabVIEW® program. It aims to control the current ramps during the charge and the discharge but also to maintain current plateaus. Depending on the experiments, the discharge can be controlled by the current source or the current source is disconnected and the pancake is discharged in a resistor. In the first case, the discharge is done more or less at a constant rate. In the second case, the current follows an exponential discharge. As the evolutions of the transitions were quite slow and progressive, the discharge was manually triggered based on the observation of the oscilloscope. It is of course possible to trigger the discharge automatically when the compensated voltage (see part. III-1.2) oversteps a given value. But given the observed inductive voltage drifts (see part III-3.2.3), this method has showed little relevance.

The temperature of the pancakes and their copper contacts was measured thanks to Cernox® sensors, which were placed at the surface of the copper contacts or directly inside a drilling in the copper

contact. To improve the thermal contact between the copper contacts and the Cernox® sensors, some Apiezon® grease was used.
The magnetic field developed by the pancakes or due to the background field as measured by a Hall sensor from Arepoc®. The sensor was placed at the central axis and mid-plane of the single or double pancake.
The resistive voltage dividers, used for the compensation of the inductive voltage (see part III-1.2), have been implemented thanks to classical resistive decade boxes (See Fig. 104.d).

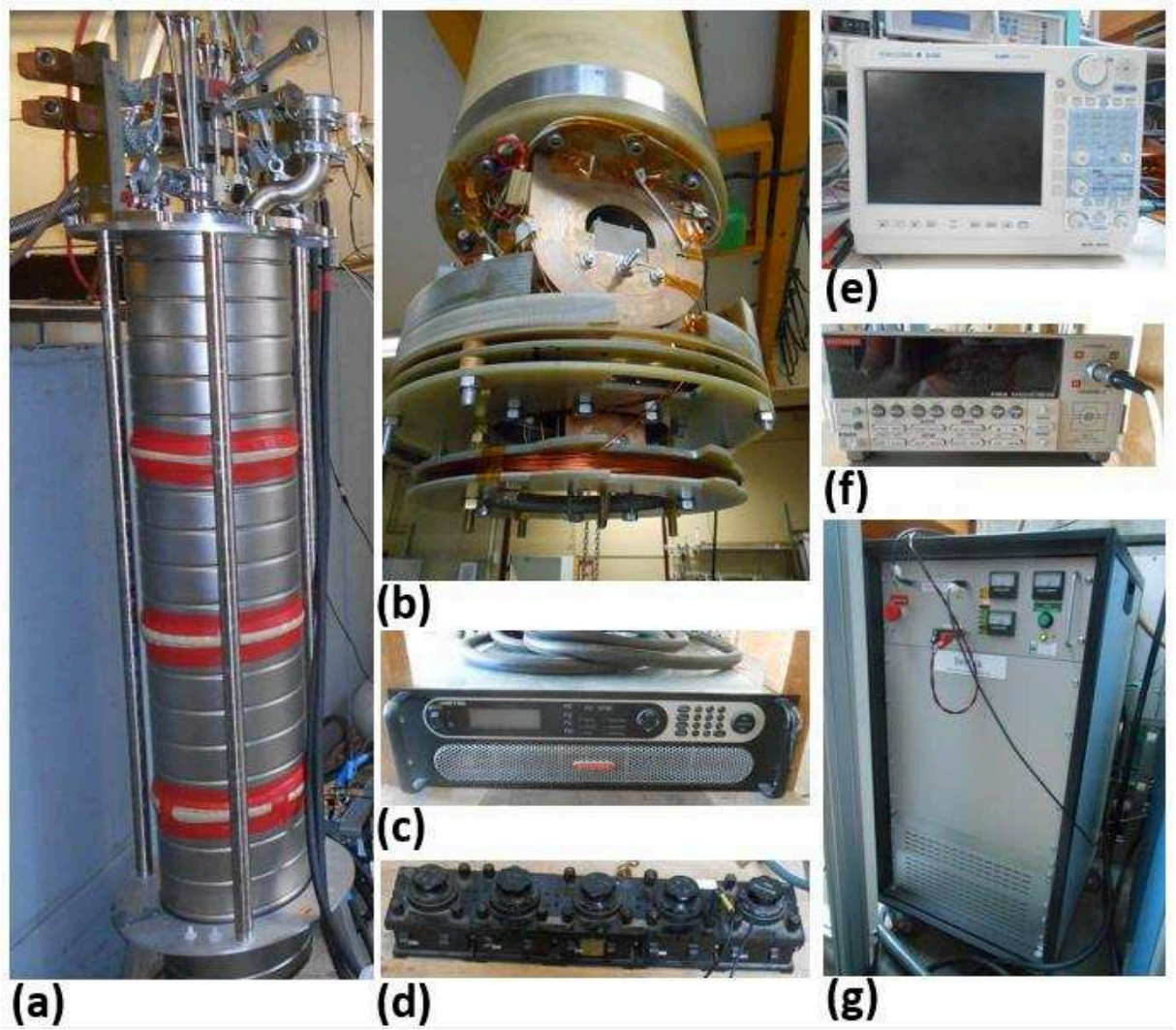


*Figure 104: (a) The probe developed for the EuCARD program, inside its cryostat and placed on its support. (b) A pancake and its compensation coils mounted at the lower end of the probe (see part III-1.2 and III-3). (c) A DC power source, 10 V / 1200 A, from Sorensen. (d) Resistive decade boxes. (e) An oscilloscope DL850 from Yokogawa. (f) A nanovoltmeter from Keithley. (g) The "Bertha" DC power source.*

## 5.2. Considerations about the compensation of inductive voltage and the detection of transitions

In all our experiments, the voltage of the pancakes is measured in order to detect a transition of the superconductor to the normal state. But the measured voltage has two different origins, which are of

a different nature. The voltage can come from the variation of the flux embraced by the winding. We call it the “inductive” voltage. This phenomenon is described by the Faraday's law. But the voltage can also come from a dissipation of electrical energy into thermal energy in the conductor. This can be due to a partially resistive state of the superconductor, for example when the critical current is overtaken (see part I-1.1.3). But even in the superconducting state without resistivity a superconducting coil shows losses as soon as its electromagnetic environment (current and/or magnetic field) varies. These AC losses (see part I-3.4.2) also lead to a “dissipative” voltage. The voltage of a superconducting coil is therefore the combination of an inductive voltage and a dissipative voltage. The inductive voltage is absolutely normal since it is related to the fact that the coil is charged or discharged. A dissipative voltage can be a problem since it is related to the fact that heat is dissipated in the coil, which destabilizes the superconducting state of the conductor.

In the voltage measured at the extremities of the pancake, it is therefore necessary to distinguish the part due to the inductive voltage and the part due to the dissipative voltage. This can be achieved thanks to pick up lossless no load coils, coupled to the pancake. Their voltage is proportional to the variation of the magnetic flux shared with the pancake and consequently proportional to the inductive voltage of the pancake. But the voltage of the pick-up coil has no dissipative component since they are supposed to be lossless. By subtracting a voltage fraction of the pick-up coil to the voltage of the pancake, it is therefore possible to extract information about the dissipative voltage of the pancake.

This is completely true if the dissipative voltage is due to the resistivity of the superconductor, described by a power law or a percolation law (see part I-1.1.3). But if the dissipative voltage is due to magnetisation losses, these losses are by definition related to the fact that the magnetic field is penetrating in the superconductor. It means that the position of the current layers drift along the width of the conductor when the coil is charged (see part III-1.2.6). This drift of current changes the distribution of the magnetic field, which can have an influence on the voltage of the compensation coils. For this reason, it is difficult to quantify the magnetisation losses with a system based on compensation coils. In the equations presented in parts III-1.2.1 to III-1.2.5, the inductances of the pancakes and their couplings with the compensation coils are supposed to be constant. So this problem is neglected in first approach.

The compensation aims to cancel the inductive voltage due to the current variations in the superconductive coil. These variations can be either due to the fact that the coil is charged or discharged (current ramps) but also to the small amplitude current variations due to the non-perfect regulation of the current source. As we will see in part III-1.2.3, the variation of the voltage can also be due to the variation of an external background field.

The compensation can be made either by numerical means, such as the mathematical functions of an oscilloscope for example, but it can also be made analogically, thanks to a resistive voltage divider. Both solutions have been tried experimentally, but the analogical compensation appeared to give better results. This is likely due to the fact that when the compensation is done analogically, the signal recorded by the oscilloscope is low and can be recorded with high sensitivity. On the contrary, if the signals of the pancake and the compensation coil are recorded independently, both values are large and same order of magnitude, a lot of sensitivity is lost. An analogical compensation has been used to obtain the results presented in part III-3.3.2. As we can see in Fig. 108, the ratio between the amplitudes of the non-compensated signal and the compensated signal is around 2 or 3 orders of magnitude.

### 5.2.1. Simple case of an active coil with one compensation coil.

The simplest case is when a winding is supplied by a current source without other perturbation source. The power source is the only source of flux variation, and only one compensation coil is necessary to achieve, theoretically, a perfect compensation.

The voltage of the tested superconducting pancake, $V_p$, is given by eq. 62 where $L_P$ is the inductance of the pancake, I is the current in the pancake and $V_{Dissip}$ is the dissipative voltage in the coil. The voltage of the compensation coil $V_c$ is given by eq. 63, where $M_{pc}$ is the mutual inductance between the pancake and the compensation coil. $M_{pc}$ is given by eq. 64, where k is the coupling coefficient between the pancake and the compensation coil and $L_c$ is the inductance of the compensation coil.

From equations 63 and 63, we obtain eq. 65, in which the dependence to the current variation has been eliminated.

$$V_p = L_p \frac{dI}{dt} + V_{Dissip} \tag{62}$$

$$V_c = M_{pc} \frac{dI}{dt} \tag{63}$$

$$M_{pc} = k \sqrt{L_p L_c} \tag{64}$$

$$V_{Dissip} = V_p - \frac{L_p}{M_{pc}} V_c \tag{65}$$

It is difficult to design the position, the geometry and the number of turns of the compensation coil in order to obtain $M_{pc} = L_p$ within some tenths even hundredths of percent required to get the useful dissipative voltage. It is easier to oversize the number of turns of the compensation coil. In this case, $M_{pc}$ is higher than $L_p$ and only a portion of $V_c$ has to be subtracted to $V_p$. This can be easily achieved thanks to a resistive voltage divider. Furthermore, the voltage divider has the advantage to be adjustable during the experiment, which of course not the case for the number of turns of the compensation coil.

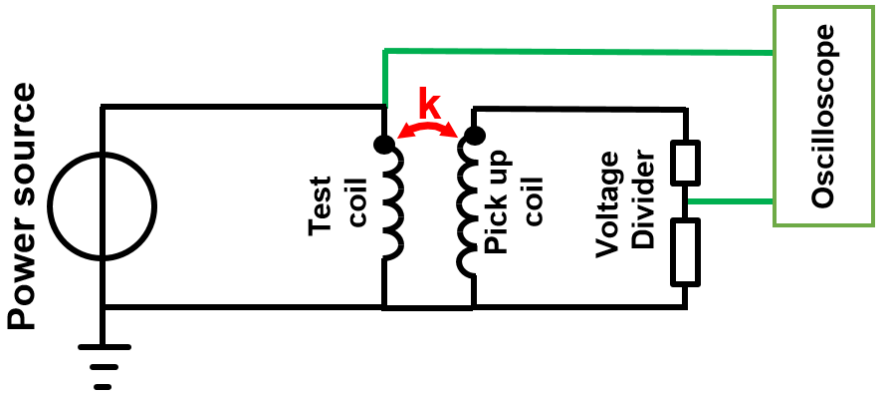


*Figure 105: Principle electrical diagram of the analogical compensation of the inductive voltage of a test coil thanks to a compensation coil.*

The principle of the acquisition of an analogically compensated signal is shown in Fig. 105. In this figure, we can see that it is necessary for the resistors of the voltage divider to have a significant resistance value, in order to prevent some current to circulate in the circuit of the compensation coil. In our

experiments, the resistance of the voltage divider was in the order of 1 kΩ. During the charge of our prototype pancakes, the voltage of the compensation coils is never more than 1 V, so the induced current is not more than 1 mA and its influence on the magnetic field is negligible.

### 5.2.2. Case of an active coil in a noisy homogeneous background field

In our experiments, the prototype pancakes have sometimes been tested under a background field, in a large bore magnet of the Grenoble LNCMI [Lncm00] (see part III-3.2). This solenoidal magnet has an aperture of 376 mm, in which fits the cryostat of the probe described in part III-1.1. It is a resistive magnet which uses up to 12 MW to produce a field of 10 T. So its electrical power is very high compared to a superconducting magnet. But there is no equivalent superconducting magnet available in Grenoble. An advantage of resistive magnets is that they have no risk to quench. Nevertheless, such a resistive magnet is supplied by a noisy current and consequently produces an also rather noisy magnetic field. These flux variations generate a parasitic voltage, whose amplitude is much higher than the dissipative voltage we want to observe (see Fig. 108). In consequence, that parasitic voltage has also to be compensated to be have the possibility to protect the superconducting pancake.

In the present case, the inductive voltage of the pancake has therefore two different origins: The variation of its current, and the background electromagnetic noise, due to the resistive magnet. These two perturbation sources have no correlation, and it is therefore mandatory to have information about each of these noise sources in order to compensate them correctly.

In this part, we propose a solution, based on the use of two different pick up coils. These pick-up coils have different positions and eventually different geometries or number of turns. In this way, their voltages have a different sensitivity to each of the two inductive perturbation sources. Thanks to a suitable combination of the voltages of the pancake and the two pick-up coil, it is theoretically possible to achieve a perfect compensation of the inductive voltage and to extract information about the dissipative voltage.

This solution is described by the following equations. The voltage of the tested pancake is given by eq. 66. $V_p$, $L_p$, I and $V_{Dissip}$ have the same meaning that in the previous subsection. $B_{ext}$ is the value of the background field. $A_p$ is a factor which gives the relation between the variation of the background B field and the voltage of the pancake.

The field generated by the resistive magnet is perpendicular to the planes of the pancake and the pick-up coils. Furthermore, it is well homogeneous in the volume of the aperture of the magnet, or at least in the volume of the experimental set-up. In these conditions, it is easy to calculate $A_p$ thanks to geometrical considerations. It is just the sum of the electromotive force of each turn of the pancake, submitted to the variation of a homogeneous B field (perpendicular to the turn) at a rate of 1 T per second.

In eq. 67, $V_1$ is the voltage of the compensation coil 1, $M_1$ is the mutual inductance between the tested pancake and the compensation coil 1. $A_1$ is the same as $A_p$ but for the compensation coil 1 instead of the pancake.

Eq. 68 is the same as eq. 67 but for the compensation coil 2.

$$V_p = L_p \frac{dI}{dt} + A_p \frac{dB_{ext}}{dt} + V_{Dissip} \tag{66}$$

$$V_1 = M_1 \frac{dI}{dt} + A_1 \frac{dB_{ext}}{dt} \tag{67}$$

$$V_2 = M_2 \frac{dI}{dt} + A_2 \frac{dB_{ext}}{dt} \tag{68}$$

From equations 67 and 68, we can obtain equations 69 and 70.

$$\frac{\mathrm{dI}}{\mathrm{dt}} = \frac{V_1 A_2 - V_2 A_1}{M_1 A_2 - M_2 A_1} \tag{69}$$

$$\frac{\mathrm{dB_{ext}}}{\mathrm{dt}} = \frac{V_1 M_2 - V_2 M_1}{M_2 A_1 - M_1 A_2} \tag{70}$$

These equations are then combined with eq. 66 to obtain equations 71 and 72. $C_{V1}$ and $C_{V2}$ are constant coefficients given by equations 73 and 74. In these equations, $\alpha_1$ is the division of $A_1$ by $A_p$ and $\alpha_2$ is the division of $A_2$ by $A_p$. $\lambda_1$ is the division of $M_1$ by $L_p$ and $\lambda_2$ is the division of $M_2$ by $L_p$. Contrary to $L_p$, $M_1$, $M_2$, $A_p$, $A_1$ and $A_2$, the coefficients $\alpha_1$, $\alpha_2$, $\lambda_1$ and $\lambda_2$ are easily measurable during the experiment. $\alpha_1$ and $\alpha_2$ are measured when the power source of the pancake is off and $\lambda_1$ and $\lambda_2$ are measured when the background resistive magnet is off.

The coefficients $L_p$, $M_1$, $M_2$, $A_p$, $A_1$ and $A_2$ are of course calculated when the compensation coils are designed. Nevertheless, given that the manufactured compensation coils can be slightly different of what was designed and given the uncertainty about the current distribution in the width of the REBCO tape (see part III-1.2.6.1), it is preferable to measure the coefficients $\alpha_1$, $\alpha_2$, $\lambda_1$ and $\lambda_2$ once that everything is in place. This aims to precisely adjust the two voltage dividers and to optimize the compensation.

$$\mathrm{V_p} = \mathrm{L_p}\left(\frac{\mathrm{V_1 A_2 - V_2 A_1}}{\mathrm{M_1 A_2 - M_2 A_1}}\right) + \mathrm{A_p}\left(\frac{\mathrm{V_1 M_2 - V_2 M_1}}{\mathrm{M_2 A_1 - M_1 A_2}}\right) + \mathrm{V_{Dissip}} \tag{71}$$

$$\mathrm{V_{Dissip}} = \mathrm{V_p} + \mathrm{V_1\ C_{V1} - V_2\ C_{V2}} \tag{72}$$

$$\mathrm{C_{V1}} = \frac{\mathrm{L_p A_2 - A_p M_2}}{\mathrm{M_2 A_1 - M_1 A_2}} = \frac{\alpha_2 - \lambda_2}{\lambda_2 \alpha_1 - \lambda_1 \alpha_2} \tag{73}$$

$$\mathrm{C_{V2}} = \frac{\mathrm{L_p A_1 - A_p M_1}}{\mathrm{M_2 A_1 - M_1 A_2}} = \frac{\alpha_1 - \lambda_1}{\lambda_2 \alpha_1 - \lambda_1 \alpha_2} \tag{74}$$

$$\alpha_1 = \frac{\mathrm{A_1}}{\mathrm{A_p}} \quad (75) \qquad \alpha_2 = \frac{\mathrm{A_2}}{\mathrm{A_p}} \quad (76) \qquad \lambda_1 = \frac{\mathrm{M_1}}{\mathrm{L_p}} \quad (77) \qquad \lambda_2 = \frac{\mathrm{M_2}}{\mathrm{L_p}} \quad (78)$$

### 5.2.3. First implementation of the double pick-up coil compensation

We have implemented for the first time the double pick-up coil compensation during the tests of the single pancake prototype made of 6 mm wide tape (see part III-3.2.1.1). The principle of the experimental setup is shown in Fig. 106. The REBCO pancake was centred in the resistive magnet. A pick-up coil made of copper wire, with the same geometrical dimensions and the same number of turns, was positioned under the REBCO pancake. A second compensation coil, with also the same geometrical dimensions and the same number of turns, is positioned even lower.

As the three coils have the same inner and outer radii as well as the same number of turns, we can write that:

$$\mathrm{A_p} \approx \mathrm{A_1} \approx \mathrm{A_2} \quad (79) \qquad \text{or} \qquad \alpha_1 \approx \alpha_2 \approx 1 \quad (80)$$

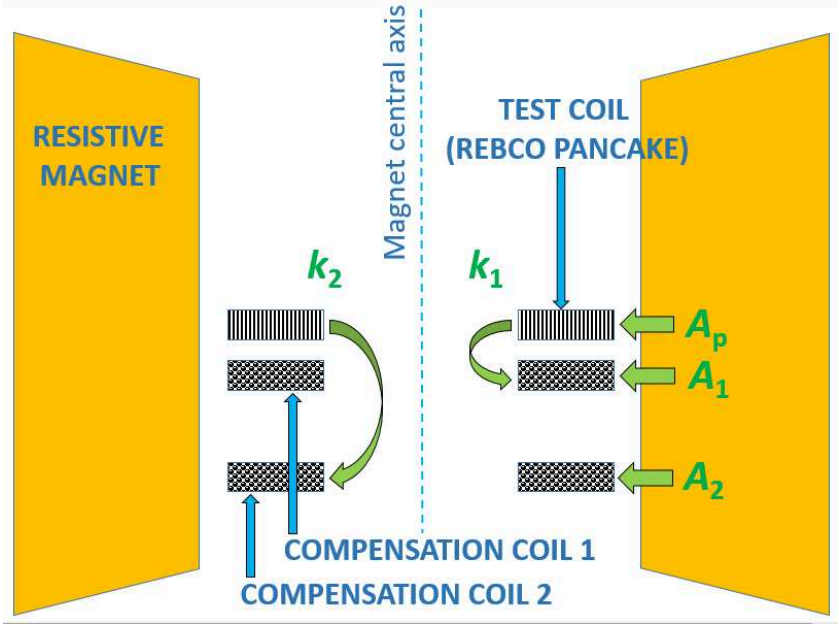


*Figure 106: Cross section of the experimental setup (not to scale). First implementation of the double pick-up coil compensation.*

The values of $k_1$ and $k_2$ were calculated with Flux®. As the three coils have the same geometrical dimensions and the same number of turns, they have nearly the same self-inductance, even if the pancake is made of tapes and the compensation coils are made of round wires. Consequently, $\lambda_1$ and $\lambda_2$ are respectively equal to $k_1$ and $k_2$:

$$\lambda_1 \approx k_1 \approx 0.8 \quad (81) \qquad \lambda_2 \approx k_2 \approx 0.3 \quad (82)$$

From equation 72, we can then conclude that in this configuration:

$$V_{Dissip} = V_p - 1.4\,V_1 + 0.4\,V_2 \quad (83)$$

We can see that the coefficient $C_{V1}$, equal to 1.4, is higher than 1. We have therefore two solutions:

- To multiply $V_1$ by 1.4 thanks to an amplifier.
- To divide all the coefficients of the equation by a value equal or higher than 1.4.

This second solution has been chosen, because using an amplification system on one signal before combining the three signals would have resulted in a poor efficiency of the compensation. The compensation equation then becomes:

$$\frac{1}{1.5}V_{Dissip} = \frac{1}{1.5}V_p - \frac{1.4}{1.5}\,V_1 + \frac{0.4}{1.5}\,V_2 \quad (84)$$

In this equation, the amplitudes of all the coefficients are smaller than one. It can therefore be analogically implemented thanks to passive elements, such as resistive voltage dividers. The coefficients have been divided by 1.5 rather than 1.4 in order to keep some margin on the adjustment of the voltage dividers. The principle diagram of the analogical implementation of this equation is shown in Fig. 107. The only disadvantage with this solution is that the amplitude of the signal of the pancake is divided by 1.5, which slightly reduces the sensitivity of the system and complicates the implementation of the system.

Fig. 108 shows the benefit of the double coil compensation on the signal to noise ratio. The presented signals have been recorded during a current ramp under a background field of 1 T (see part III-3.2.1.1). The interpretation of such signals is given later (see part III-3.2.3).

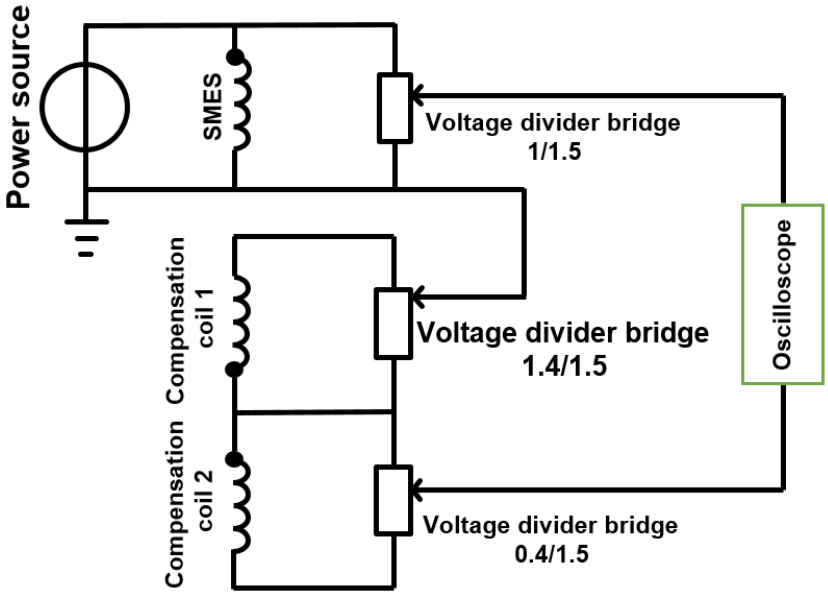


*Figure 107: Principle electrical diagram of the first implementation of the double pick-up coil compensation.*

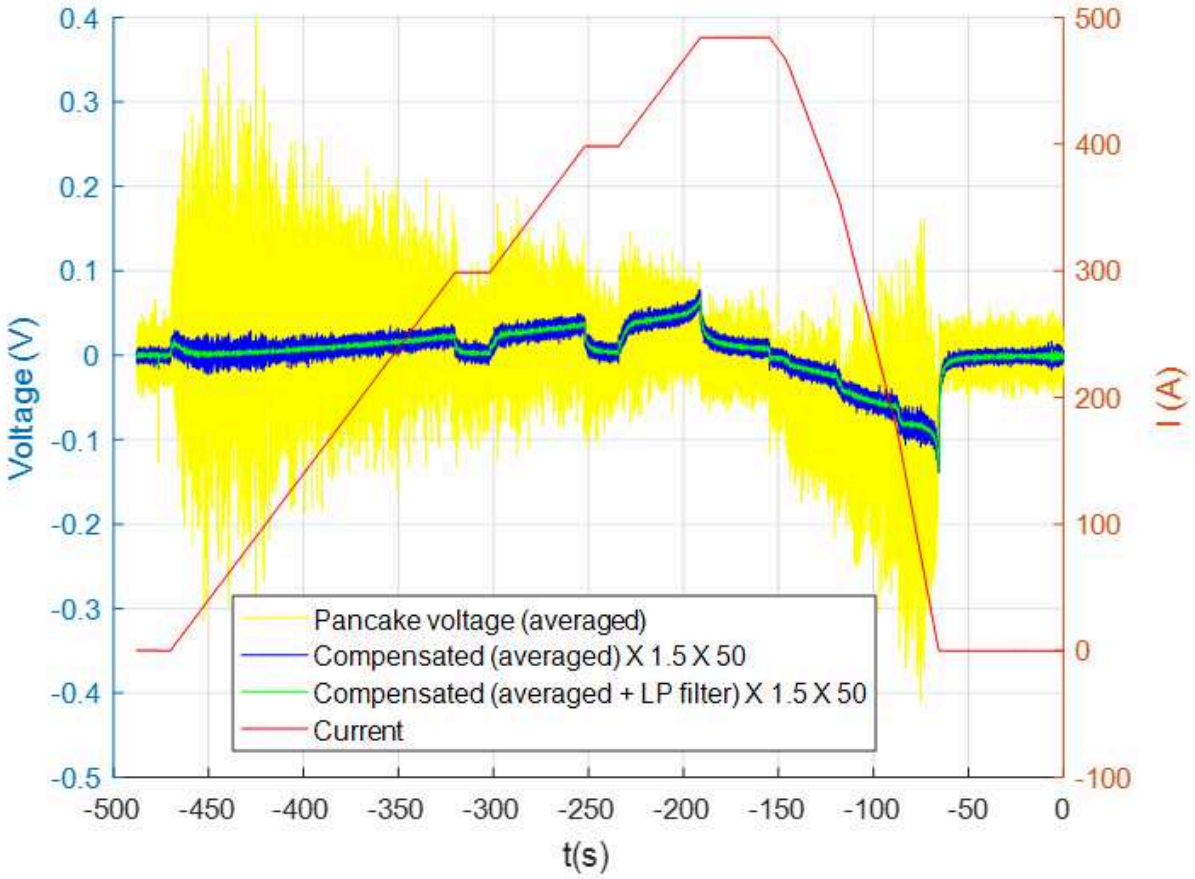


*Figure 108: Comparison of the compensated and non-compensated signals of a test in background field.*

The yellow signal is the voltage of the pancake, without compensation but with a sliding mean value filter. The blue signal is the compensated signal with the same sliding mean value filter being applied. The measured signal has been multiplied by 1.5 to compensate the reduction of $V_{Dissip}$ by the voltage dividers, then it has been multiplied by 50 just to be visible compared to the voltage of the pancake. In other words, the blue curve is 75 times the original measured signal. The green signal is the same as the blue signal, but an additional 6 Hz low pass filter is applied. We can see that the amplitude of the

noise on the pancake voltage is in the order of 100 mV or more, while the amplitude of the noise of the blue signal, without being multiplied by 50, is in the order of 0.300 mV. The amplitude of the noise of the green signal, without being multiplied by 50, is in the order of 0.100 mV. The gain in term of noise reaches two to three orders of magnitude.

### 5.2.4. Case of 2 active coils independently compensated in a noisy homogeneous background field

The last prototype which has been tested is a double pancake made of 12 mm wide tape (see part III-3.1.2). As it is a double pancake, we wanted to observe the voltage of each single pancake independently, and to have the possibility to do it in the noisy background of the resistive magnet of the Grenoble LNCMI. The problem is then quite similar to what has been presented in the previous paragraph but with the difference that there is a mutual inductance between the two pancakes and that pick-up coils have different mutual inductances with the two pancakes. Of course, the two pancakes are in series, so the current as well as the current variation are the same in the two single pancakes.

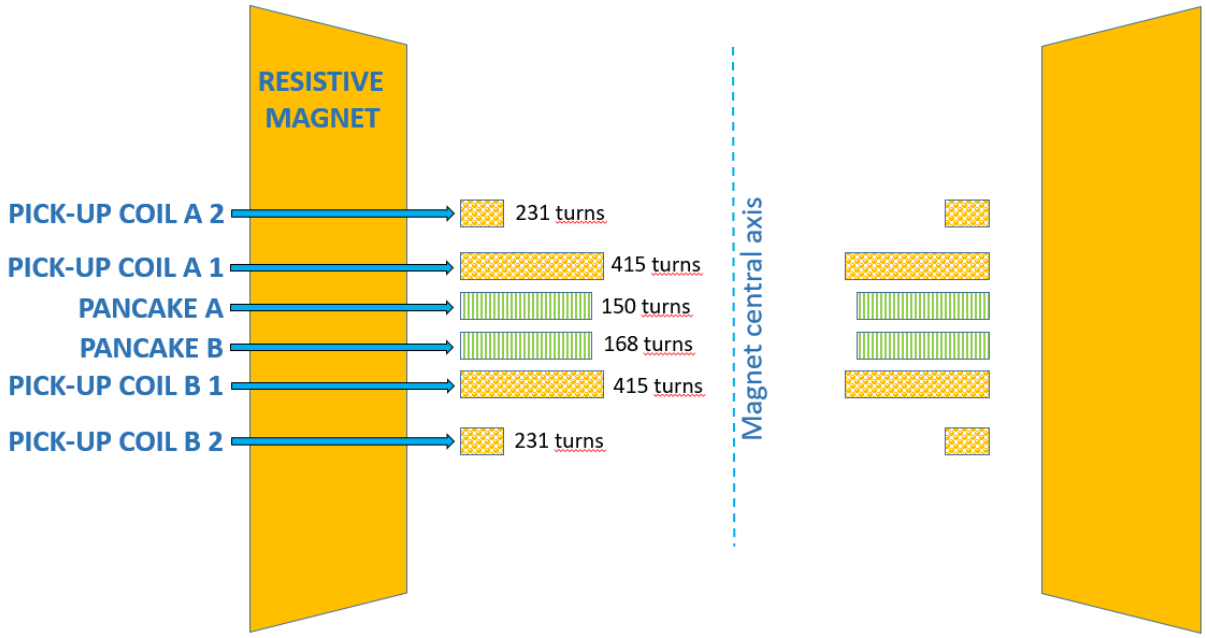


*Figure 109: Cross section of the experimental setup (not to scale) for independent double compensation of each single pancake.*

The implementation of the experimental setup is shown in Fig. 109. There are two pick-up coils for each single pancake, so 4 pick-up coils in total. In this way, the signals of each single pancake can be independently observed and compensated. Here, we are going to present the equations for the compensation of the inductive voltages of the pancake a. The equations are exactly the same for the pancake b, but the subscripts "a" and "b" just have to be inverted.

$V_a$ is the voltage of the pancake a, $V_{a1}$ and $V_{a2}$ are the voltages of pick-up coils a1 and a2. $L_a$ is the self-inductance of the pancake a, $M_{a/b}$ is the mutual inductance between pancakes a and b, $M_{a/a1}$ is the mutual inductance between the pancake a and the compensation coil a1, $M_{b/a1}$ is the mutual inductance between the pancake b and the compensation coil a1, etc…It is then possible to define the equivalent inductances $L_{a\_eq}$, $M_{a1\_eq}$ and $M_{a2\_eq}$ (see eq. 88 to 90).

$$V_a = (L_a + M_{a/b})\frac{dI}{dt} + A_a\frac{dB_{ext}}{dt} + V_{Dissip} \qquad (85)$$

$$V_{a1} = (M_{a/a1} + M_{b/a1})\frac{dI}{dt} + A_{a1}\frac{dB_{ext}}{dt} \quad (86)$$

$$V_{a2} = (M_{a/a2} + M_{b/a2})\frac{dI}{dt} + A_{a2}\frac{dB_{ext}}{dt} \quad (87)$$

$$L_{a\_eq} = L_a + M_{a/b} \quad (88)$$

$$M_{a1\_eq} = M_{a/a1} + M_{b/a1} \quad (89)$$

$$M_{a2\_eq} = M_{a/a2} + M_{b/a2} \quad (90)$$

The problem then becomes the same that in part III-1.2.2, and the compensation of the inductive voltages of the pancake a is determined by eq. 91 in which $C_{Va1}$ and $C_{Va2}$ are given by eq. 92 and 93.

$$V_{Dissip\_a} = V_a + V_{a1}\,C_{Va1} - V_{a2}\,C_{Va2} \quad (91)$$

$$C_{Va1} = \frac{L_{a\_eq}A_{a2} - A_a M_{a2\_eq}}{M_{a2\_eq}A_{a1} - M_{a1\_eq}A_{a2}} = \frac{\alpha_{a2} - \lambda_{a2}}{\lambda_{a2}\alpha_{a1} - \lambda_{a1}\alpha_{a2}} \quad (92)$$

$$C_{Va2} = \frac{L_{a\_eq}A_{a1} - A_a M_{a1\_eq}}{M_{a2\_eq}A_{a1} - M_{a1\_eq}A_{a2}} = \frac{\alpha_{a1} - \lambda_{a1}}{\lambda_{a2}\alpha_{a1} - \lambda_{a1}\alpha_{a2}} \quad (93)$$

The coefficients $\alpha_{a1}$, $\alpha_{a2}$, $\lambda_{a1}$ and $\lambda_{a2}$ are defined below. They can be easily measured during the experiment, which aims to adjust the voltage dividers and to optimize the compensation.

$$\alpha_{a1} = \frac{A_{a1}}{A_a} \quad (94) \qquad \alpha_{a2} = \frac{A_{a2}}{A_a} \quad (95) \qquad \lambda_{a1} = \frac{M_{a1_{eq}}}{L_{a_{eq}}} \quad (96) \qquad \lambda_{a2} = \frac{M_{a2_{eq}}}{L_{a_{eq}}} \quad (97)$$

In Fig. 109, we can see that all the compensation coils do not have the same number of turns neither the same geometry. Thanks to that, the coefficients $C_{Va1}$, $C_{Va2}$, $C_{Vb1}$ and $C_{Vb2}$ are all smaller than 1. It is therefore not necessary to divide the amplitude of the voltage of the pancake, like what was done in the first implementation of the double pick-up coil compensation (see part III-1.2.3).

### 5.2.5. Application of the compensation principle to the high energy density SMES

The SMES will be made of 42 single pancakes, i.e. 21 double pancakes. It is possible to imagine only two voltage taps at the extremities of the SMES and try to ensure the protection of the SMES based on that signal. Nevertheless, this seems to us to be a wrong protection strategy. As we have seen in part I-3.1.5, the transition to normal state of REBCO tapes is highly localised, and the discharge of the SMES has to be triggered when the dissipative voltage is still very low. So early detection of a transition is required, wherever it is in the full SMES. To this end, the inductive voltage will have to be compensated. As during the tests of the prototype, the compensation has two goals:

- To cancel the small amplitude noisy voltage due to the imperfection of the current source
- To cancel the inductive voltage signal due to the current ramps in the SMES. In this way, the amplitude of the measured signal is much smaller, and the signal acquisition can be made by more sensitive electronics.

In order to achieve this compensation, pick-up coils will be used.
But the length of the winding between two voltage taps also matters. The amplitude of the residual voltage noise increases with the length of the circuit. But the amplitude of the dissipative voltage due to a local transition does not depends of this length. It is therefore interesting to reduce the distance between two voltage taps to increase the ratio of the dissipative voltage over the envelope of the noise of the signal or in other word, to increase the signal to noise ratio.
In the SMES, there will be voltage taps at the extremities of each double pancake. There will therefore be 21 voltage measurements. Each of these voltage signals will be combined with the signal of a compensation coil. So there will be 21 compensation coils. There is no need for a double compensation as in the previous paragraphs, since the power source of the SMES is the only major source of perturbation.
In this situation, each pancake is submitted to the voltage due to its self-inductance but also to the mutual inductance of the rest of the coil. Similarly, the voltage of the compensation coil is due to its mutual inductance with the compensated pancake but also with the rest of the coil. So we can write that its voltage is due to its mutual inductance with the SMES.
It is possible to adapt the equations of part III-1.2.4 to this case, with the compensated coil being the coil a and the rest of the coil being coil b. As there is no external field, the term with $B_{ext}$ disappears. We then obtain the equations below. $V_{p\_i}$ is the voltage of the double pancake with index number i. $L_{p\_i}$ is the self-inductance of the considered double pancake. $M_{p\_i/rest\_SMES}$ is the mutual inductance between this double pancake and the rest of the SMES. $V_{c\_i}$ is the voltage of the corresponding compensation coil. $M_{c\_i/SMES}$ is the mutual inductance between this compensation coil and the complete SMES. From equations 98 and 99, we obtain equation 100.

$$V_{p\_i} = (L_{p\_i} + M_{p\_i/rest\_SMES})\frac{dI}{dt} + V_{Dissip} \tag{98}$$

$$V_{c\_i} = (M_{c\_i/SMES})\frac{dI}{dt} \tag{99}$$

$$V_{Dissip} = V_{p\_i} - \frac{L_{p\_i} + M_{p\_i/rest\_SMES}}{M_{c\_i/SMES}} V_{c\_i} \tag{100}$$

To simplify the manufacture of the compensation coils, they all will have the same geometry and the same number of turns. The number of turns will be oversized and the compensation voltage will be attenuated thanks to resistive voltage dividers, in order to implement the compensation defined by eq. 100. On one half of the SMES, the ratio of each voltage divider will be different since each pancake has a different position in the SMES and that its compensation coil has a different position compared to the SMES.

Practically, the compensation coils will be placed inside the SMES to limit the size of the cryostat, but they could have been placed also around the SMES. They will have an inner radius of 56 mm, an outer radius of 63 mm and a height of 28 mm. They will have around 1200 series-turns. There are two reasons why their number of turns is much higher than the number of turns of a double pancake (178 turns). First, the compensation coils are relatively far away from the superconducting winding because of the mandrel thickness of the SMES, which decreases the coupling between the compensation coils and the SMES. Secondly, as they are smaller than the REBCO pancakes, they need more turns to embrace a sufficient magnetic flux.

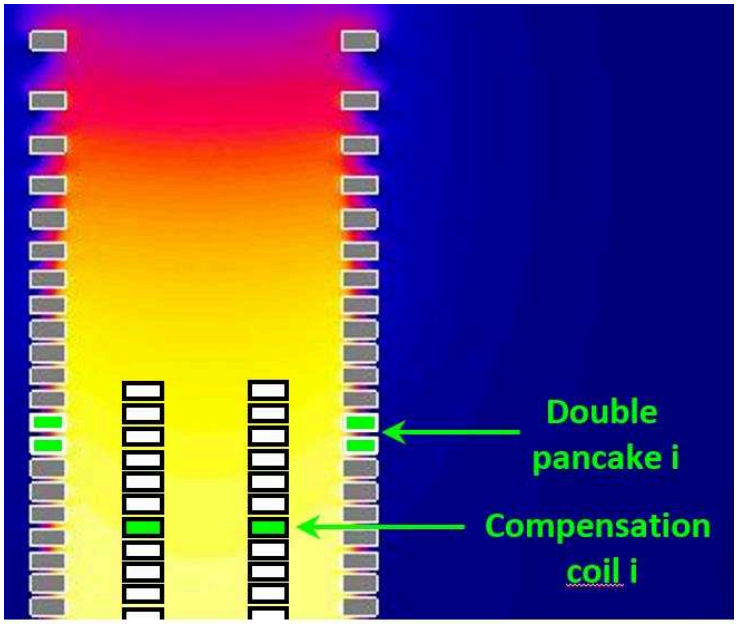


*Figure 110: Cross-section of the upper half of the SMES with its compensations coils.*

## 5.2.6. Gradual imbalance of the compensation

### 5.2.6.1. Drift of the current in the width of the conductor

In all the paragraphs above, it is supposed that the inductances and couplings are known and that they can be calculated or measured. If they were constant during the experiments, we could theoretically achieve a perfect compensation thanks to passive voltage dividers. But practically, we have to face several difficulties. The inductances of the pancakes and the couplings between the pancakes and the compensation coils change when the pancakes are charged.

There are several reasons for that (see also part III-1.2.6.2), but this is mainly due to the fact that the current does not penetrate homogeneously in the REBCO conductor. The current first penetrates by the sides of a superconductor. The consequence is that when a single pancake starts to be charged, the current will be concentrated along the edges of the pancake.

When the current penetrates the pancake, the transverse field at the edges of the pancake is progressively increases. As the critical current is strongly dependent on the transverse field, the current density decreases at the edges of the pancake and the electrical current concentrates itself towards the centre of the pancake. Fig. 111 shows in an extremely simplified way what happens when the pancake is charged. In Fig. 111.a, the current, in blue, is penetrating the pancake by its sides. In Fig. 111.b, the current, in orange, is concentrated to the middle of the pancake. In both cases, the current density is homogeneous or null. This schematic representation aims to show in a qualitative way how the inductance and the couplings are evolving during the charge of the pancake. In this simplified frame, the evolution of the self-inductance and coupling coefficients $k_1$ and $k_2$ have been calculated for the case of the first implementation of the double pick-up coil compensation (see part III-1.2.3). The results are shown in Fig. 111.c. We can see that these values are changing of several percent when the pancake is charged, which influences the coefficients $C_{V1}$ and $C_{V2}$. Because of this evolution, the compensation bridge becomes incorrectly adjusted during the charge of the pancake. We will see in part III-3.2.3.1.1 that the observed compensated signal has a residual inductive behaviour because of this imbalance.

Of course, the schematization presented here is very coarse, and is not really representative of what really happens during the charge of the pancake. Chiefly, the current is not going to concentrate that much towards the centre of the pancake.
In order to know exactly where the current is flowing in the tapes of the pancakes, it is necessary to perform a simulation which takes into account the power law electric field versus current density and the $J_c$ (B,Θ) properties (see part I-1.1.3 and I-1.3.1) of the conductor. Such simulations have been performed for example by X. Deng et al. [DTZR15] who have shown the variation of the self-inductance during the charge of pancakes. B. Rozier [RBRM00] in our laboratory develops a simulation model for that purpose.

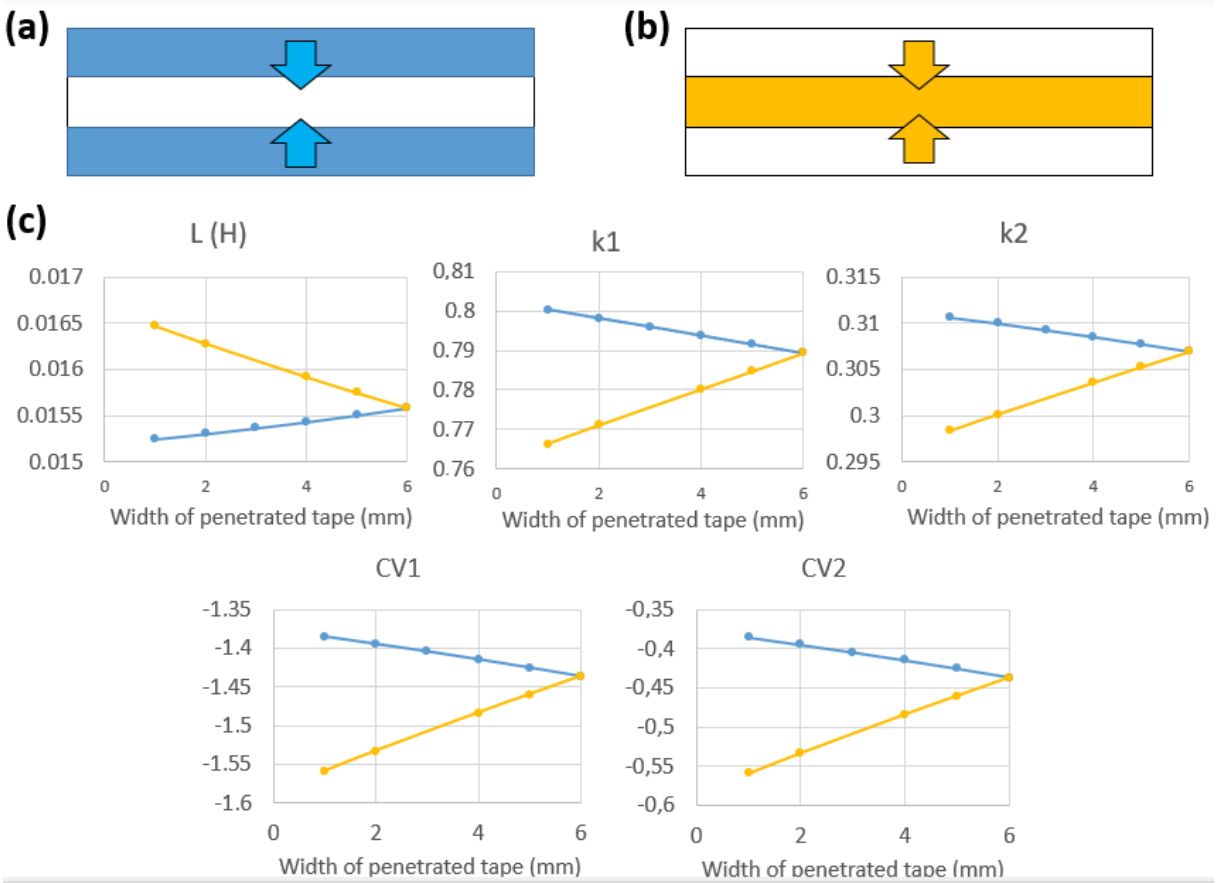


*Figure 111: a & b) Hypothesis of current distribution in the cross section of the pancake calculated for the prototype n°3 (see part III-3.2). The current density is supposed to be homogeneous in the coloured sections and null in the white sections. c) Evolution of L, $k_1$, $k_2$, $C_{V1}$ and $C_{V2}$ (See part III-1.2.2) depending on the position of the current in the 6 mm wide pancake. The blue part of the curve corresponds to the situation where the current fills only the top and the bottom of the pancake. The orange part of the curve corresponds to the situation where the current fills only the centre of the pancake. The values are calculated in a magneto-static situation.*

### 5.2.6.2. Outward expansion and contraction of the pancake

The fact that the electrical current drifts into the REBCO conductor is not the only reason why the inductance and the couplings are varying during the experiment. They also vary because the shape of the pancake is modified by the Lorentz Force. First, because of the inner magnetic pressure, the pancake is going to slightly expand outward. Secondly, due to the thermal contraction (see part I-4.3) and the elasticity of the insulation (see part I-4.2), the pancake can also contract: the inner turn goes closer to the outer turn during the charge of the coil. This is because the longitudinal self-field is in opposite directions to the inner turn and the external turn (see part I-2.2.1.1.1).

In an experiment under a background field, the outward expansion and the contraction depend on the values of the current density (and consequently the self-field) but also the value of the background field. We will therefore not make an extensive study of the problem here, but we can evaluate the order of magnitude of the effects of each phenomenon for given values of outward extension or contraction. An outward expansion of 0.45 % corresponds to a strain that is the order of magnitude for the critical strain for tapes from SuperOx (see part I-1.3.5.1). The contraction of the pancakes in the 1 MJ SMES can be estimated around 0.25 %. These two values are reported in the table below, with their respective influence on the variations of the inductance and the couplings.
In this table, we can see that the effect which has the most influence is the drift of the current in the width of the tape. The influence of the outward expansion on the variation of inductance is lower but significant, though. In contrast, the influence of the contraction is clearly negligible compared to the penetration of the tape.

| | ΔL (%) | $\Delta k_1$ (%) | $\Delta k_2$ (%) |
|---|---|---|---|
| Penetration of the tape | + 2.6 | - 1.7 | - 1.3 |
| Outward expansion (0.45 %) | + 0.53 | - 0.0007 | + 0.11 |
| Contraction (0.25 %) | + 0.08 | - 0.02 | - 0.04 |

*Table 13: Comparison of the influence of the current penetration and deformations on the inductance and couplings of the prototype n°3.*

### 5.2.7. Precisions about the term of transition

We have seen in part I-1.1.3 that the overstepping of the critical current generates an electric field and consequently a voltage at the terminals of a superconducting winding. The electrical field strongly depends of the current, following a power law with a relatively high exponent. So the overstepping of the critical current is characterised by a quick rise of the voltage. The transition from a superconducting state to a non-superconducting state therefore goes with a transition of the voltage signal.
Nevertheless, as we will see in part III-3.2.3, a transition of the voltage signal is not necessarily due to the overstepping of the critical current. Other phenomena can cause such a quick variation of the voltage. As it can be difficult to identify the reason of the voltage variation in some of the results presented beyond, the general term of “transition” is used in the following parts. So in what follows, the term “transition” is systematically used to describe a relatively fast and visible change in the dynamics of the measured voltage, which cannot be explained by the variation of the current ramp rate.

# 6. Preliminary experimental work

## 6.1. Characterization of the electrical contacts

One of the first tests performed was the characterization of the welded contacts. In the final design of the SMES, there are 21 inner contacts with 2 REBCO tapes soldered on each of them and 42 outer contacts with 1 REBCO tape soldered on each of them. The ultra-low resistance and the reliability of these solderings is therefore required to prevent the system to over-consume liquid helium or even to avoid a degradation of the performances because of an overheating of the contacts.

### 6.1.1. Measurement of the resistance of the inner contact

The REBCO tapes have been soldered according to the process described in part II-3.4.1.2. Fig. 112 shows the resistance measurement of an inner contact with two tapes soldered, immersed in a liquid nitrogen bath (77 K). The inner contact which has been used is the one of the first double pancake with 6 mm tapes (see part III-2.2). The face of the tape with the REBCO layer is oriented toward the soldering.

In these conditions, the total resistance of the contact, which includes the 2 soldered interfaces and the piece of copper is 85 nOhm.

*Figure 112: Measure of resistivity of an inner contact, immersed in liquid nitrogen.*

### 6.1.2. Estimation of the respective resistivities of the welded interfaces and of the copper piece

With this measurement, it is of course not possible to determine if the resistance is due to the soldered interfaces or to the piece of copper. According to a simulation with Flux®, the resistance of the copper piece is 55 nOhm at 77 K if its RRR is equal to 64. This value of RRR has been measured a posteriori on a small piece of this inner contact, carefully cut with electro-erosion techniques. At the same time, the characterizations of a tape-to-tape soldering have been performed. A surface resistance of 60 nOhm.cm$^2$ have been measured. This value is in agreement with other references [Lecr12] [Flei13]. According to this value, the resistance of each interface of the inner contact should be around 10 nOhm since the length of the interface is 10 cm and its width 6 mm. According to this value, the total resistance of the contact should therefore be 75 nOhm. This value is coherent with the measured value of 85 nOhm for the complete contact.

### 6.1.3. Additional considerations about the resistance of the soldered contacts

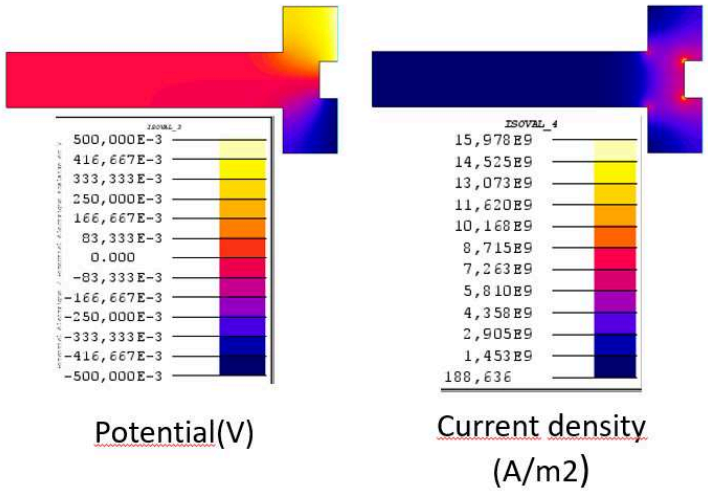


*Figure 113: Cross-section of the model used to evaluate the resistance of the copper of the contact.*

The SMES will be operated at 4.2 K, and not at 77 K. The resistance of the contacts will therefore be reduced compared to what have been measured in these tests, even if the magneto-resistivity also maters. The objective of these tests was to train to make good solderings and to have a first value

about the heat generated by the numerous resistive contacts of the SMES. It has also been verified that the soldering does not delaminate the REBCO layer and that the resistance of the contact is not affected after 4 cooling and heating cycles.
The resistance under background magnetic field of the inner contact is difficult to measure due to its small value, to the noisy background and to the long transitions of the voltage on current plateaus. With the prototype n°3 (see part III-3.1.1) at 433 A under a background field of 7 T, the resistance is lower than 300 nOhm. In the SMES, superconducting tapes will be added perpendicularly to the main REBCO tapes in order to lower this resistance (see part II-3.4.1.2).

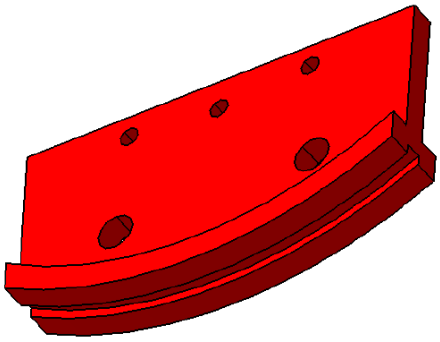

*Figure 114: Geometry of the inner contact used in the first prototype of double pancake (see part. III-2.2).*

### 6.1.4. Resistance of the pressed contact

The resistance of the pressed contact between the outer contact and a copper bloc has been measured during the tests of the prototype n°2 (see part III-2.3). Its value has been measured around 26 nOhm without background field, which correspond to a surface resistance around 234 nOhm.cm$^2$. In the SMES, the external field is low, so in first approximation this resistance value is appropriate.
One side of the pressed contact had been manually plated with indium to ensure a low resistance of the contact. The two blocs were pressed by stainless steel screws passing through them. It is considered to replace the indium plating, which is a relatively long process, by the insertion of a foil of indium alloy (In Pb (15) Ag (5)). The resistance of the pressed contact with this alternative solution has not been measured yet.
For 22 contacts with a resistance of 26 nOhm, the dissipated power is 443 mW at 880 A. It corresponds to a consumption of 0.6 L of helium per hour, which is acceptable for a demonstrator. But the resistance of the inner contacts (with perpendicular superconducting strips) should be added to this calculation.

## 6.2. First prototype of double pancake

This part presents the manufacture, the tests and the analysis of the results of the first double-pancake prototype of the BOSSE project. This prototype has been used to qualify several techniques, especially the pre-stress. Clearly, this was very useful to improve the design and its manufacturing process. The measured critical current was indeed quite low compared to the expectations. Some likely explanations to this poor critical current are presented in part III-2.2.1.5.

### 6.2.1. Manufacture of the double pancake

#### 6.2.1.1. Geometry of the double pancake

This prototype has been manufactured when the design of the project was the design C (see part II-3.3.4). It was therefore initially supposed to be a double pancake made of 6 mm wide and 150 m long tapes, with an inner radius of 90 mm and an external radius of 120 mm. Nevertheless, the two

unit length available for the project at this time were only 120 m long. The inner radius has therefore been increased to 96 mm. globally, the manufacturing process is the same than the one presented in part II-3.4.1.2, which is now used for the final pancakes of the SMES. For this reason, only the differences and additions to this process are presented here.

The geometry of the inner contact of the pancakes has already been shown in Fig. 114. The plate of the inner contact can be connected to a current lead. In this way, it is possible to supply only one pancake of the double pancake.

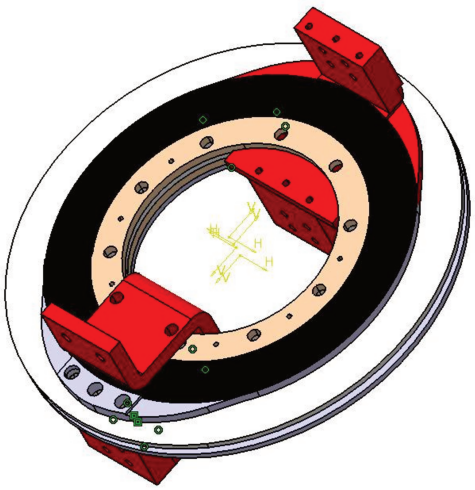

*Figure 115: A Computer Assisted Design view of the prototype double-pancake. The top flange is missing. The winding is represented in black. The copper pieces are in red. Other pieces are made of G-11.*

### 6.2.1.2. Objective of the pre-stress

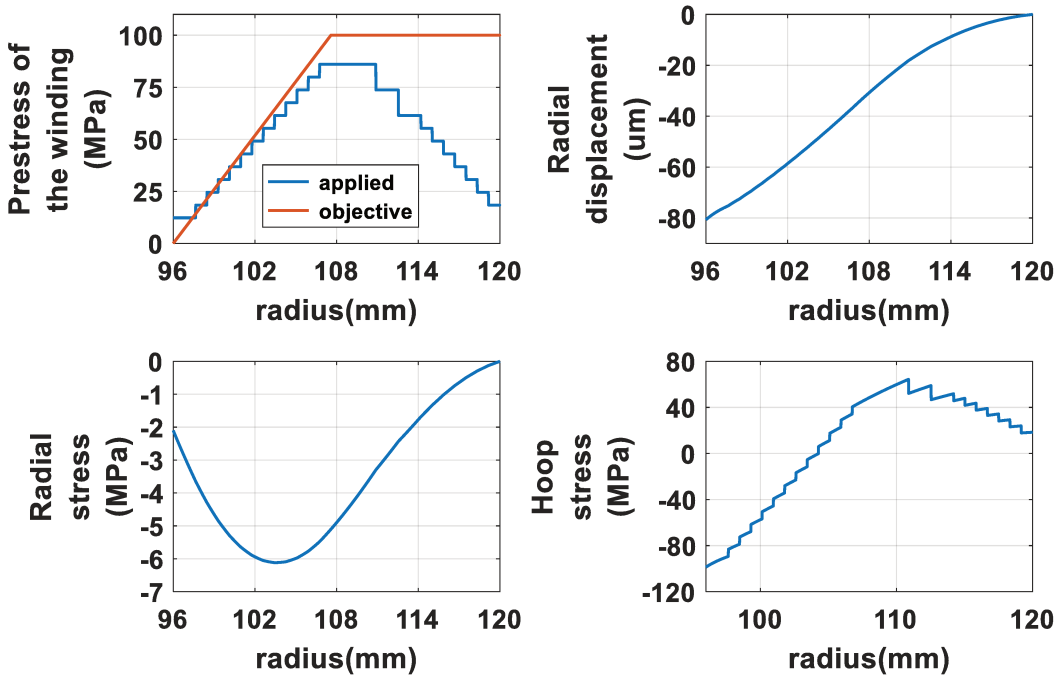


*Figure 116: Effects of the pre-stress of the REBCO tapes, which has been applied to the second manufactured pancake, before the external reinforcement and the cooling. In the first chart (top left corner) are showed what the initial objective of the winding tension (in red) was and what finally was applied (in blue).*

One objective was to apply a pre-stress to the winding and also to pre-stress an external reinforcement, made of glass fibre tissue, which would shrink the pancakes, including the moon-shaped external contacts. Simulations had shown that in order to compensate the loosening of the coil due to the thermal contraction of the polyimide and to obtain a significant pre-stress of the inner turns of the coil, a strong pre-stress was required. The initial goal was to have a negative hoop stress (i.e. pre-stress) of 100 MPa at the inner turns of the pancakes at the end of the cooling phase before charging the pancakes. This pre-stress would have been achieved by the combination of the winding under tension, until 100 MPa (81 N) of the REBCO tapes and by the winding under tension of the glass fibre tissue. Nevertheless, several problems occurred during the winding, forcing us to reduce the tension of the winding.

The benefit of the pre-stress is optimal if the tension of the tape is increased gradually during the winding (See Fig. 116, top left corner). For the sake of convenience, the tension of the winding has been increased step by step, with increments of 5 N, which was maybe a mistake (see part III-2.2.1.5).

For the pre-stress to be effective, it is necessary for the radial pressure to be converted in radial displacement (see part I-4.4). As we had no time to develop an adapted soft mandrel, the G-11 mandrel has been covered by a 1 mm thick layer of Kapton, whose Young Modulus is 2.5 GPa at room temperature. This value has been used for the simulation presented in Fig. 116.

#### 6.2.1.3. Manufacturing operation

Once that the two tapes were soldered on the inner contact, the winding of the first pancake started. The tension of the winding was gradually increased in order to reach a tension of 81 N (i.e. 100 MPa), then this tension was maintained. But at the 108$^{th}$ series turn, the pancake deviated from the plan which was perpendicular to the winding axis because the flange was pushed aside. The G-11 flange, which was 4 mm thick, was deviated of several millimetres at one point of its external circumference. In these conditions, it was not possible to continue the winding. The REBCO tape was unwound, then the winding started again. This time, the tension was only increased until 40 N.
Once that the winding of the REBCO tape was finished and the REBCO tape soldered on the external contact, the winding of the second pancake was started. The tension of the winding was increased until a maximum value of 70 N (86 MPa) (See Fig. 116).

The first pancake was then reinforced with a tape of glass fibre tissue, progressively impregnated. This tape was wound under tension, under a maximum stress of 50 MPa. The total thickness of the glass fibre strapping was 10 mm. But during the phase of drying of the epoxy impregnation, some of the turns of the glass fibre strapping slipped between the REBCO pancake and the flange. It has therefore been necessary to remove a part of the external turns of the glass fibre reinforcement.
Consequently, it has been preferred not to brace the second pancake with such a thick strapping. Nevertheless, the second pancake has been wrapped with a few turns of impregnated glass fibre tissue, just to maintain the external contact in position.
As the tapes were supposed to be 135 µm thick, each pancake should have had 178 series turns. But the 24 mm thickness of the pancakes was reached with only 155 turns for the 1$^{st}$ pancake and 166 series turns for the second pancake. The lengths of conductor were therefore cut at 100 m and 112 m respectively. We realised that there could be a significant uncertainty about the thickness of the tapes, mostly due to the excess thickness of the polyimide insulation.

#### 6.2.1.4. Tests of the first prototype

Our original will was to test the double pancake under background field in order to reach the critical current at a lower value of current than in self-field. In this way, the current density is lower at the

transition and the protection of the device is easier. Another advantage is that the background field increases the hoop stress.
At this time, the resistive high field magnets of the Grenoble LNCMI were not available because of the upgrade and change of their current source. But the opportunity has been offered to test some prototypes of our team in the high field large bore superconducting magnet at the HFLSM of Tohoku University [Hfls00]. The double pancake has therefore been moved to Japan to be tested.
This test has been the opportunity to develop our methods and knowhow for the detection of transitions. The double pancake has been tested under a 6 T background field. A transition was observed and the pancake was discharged slowly when the current reached 180 A. It corresponds to a maximum hoop stress around 140 MPa (average value on insulated conductor).
In self field, a current of 215 A has been reached. In both cases, the limitation of the current was mainly due to the lower pancake.
Thanks to the design of the internal contact, it was possible to supply and test only one of the two single pancakes of the prototype. We did not have had enough time to change the configuration of the connections and to test only the other pancake in Japan. But in the following weeks, we finally had the opportunity to have access to the 376 mm diameter bore resistive magnet of the Grenoble LNCMI [Lncm00]. We therefore tested only the upper pancake. A current of 185 A has been reached under a background field of 9 T, which corresponds to a maximum hoop stress around 190 MPa (average value on insulated conductor). A current of 200 A has been reached under 6 T of background field and a current of 250 A has been reached in self field.
For all of these tests, the current was limited at values which were much lower than what was expected according to the performance of the tapes.

| | Pancake A | Pancake B |
|---|---|---|
| $I_C$ in self field (A) | 215 | 250 |
| $I_C$ under 6 T background field (A) | 180 | 200 |
| $I_C$ under 9 T background field (A) | | 185 |

*Table 14: List of the observed transitions observed for the prototype n°1 (at 4.2 K).*

#### 6.2.1.5. Unwinding

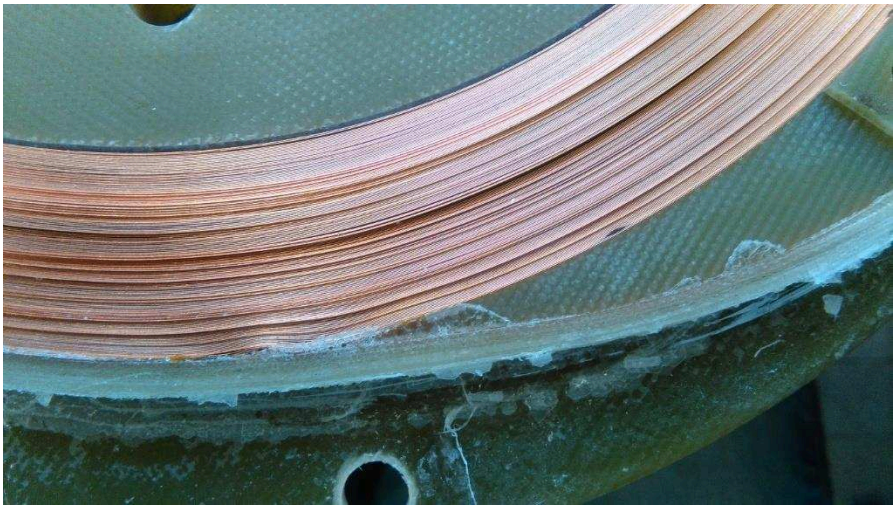

*Figure 117: View of the first pancake after dismounting of the external flange. The deformation of the pancake due to the centripetal pressure of the bracing is clearly visible.*

After the experiments, the flanges were dismounted and the pancakes were unwound. Two problems were observed:

- The first pancake had been deformed by the centripetal pressure of the bracing (see Fig. 117).
- Some epoxy resin had dripped from the glass fibre tissue until the last turns of the pancake, between the tapes and the flanges. This led to a partial delamination of the external turns of the REBCO tapes of (see Fig. 118), which probably occurred during the cooling of the prototype.

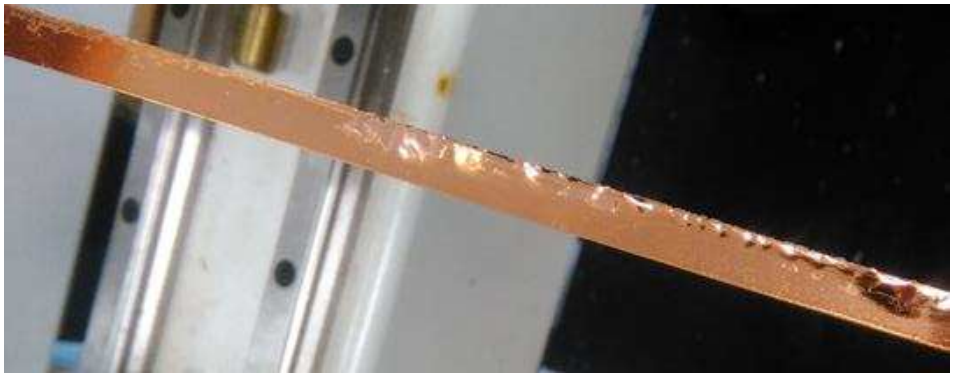

*Figure 118: A REBCO tape during the unwinding of a pancake. The delamination of the tape is clearly visible on the side were there was drips of epoxy.*

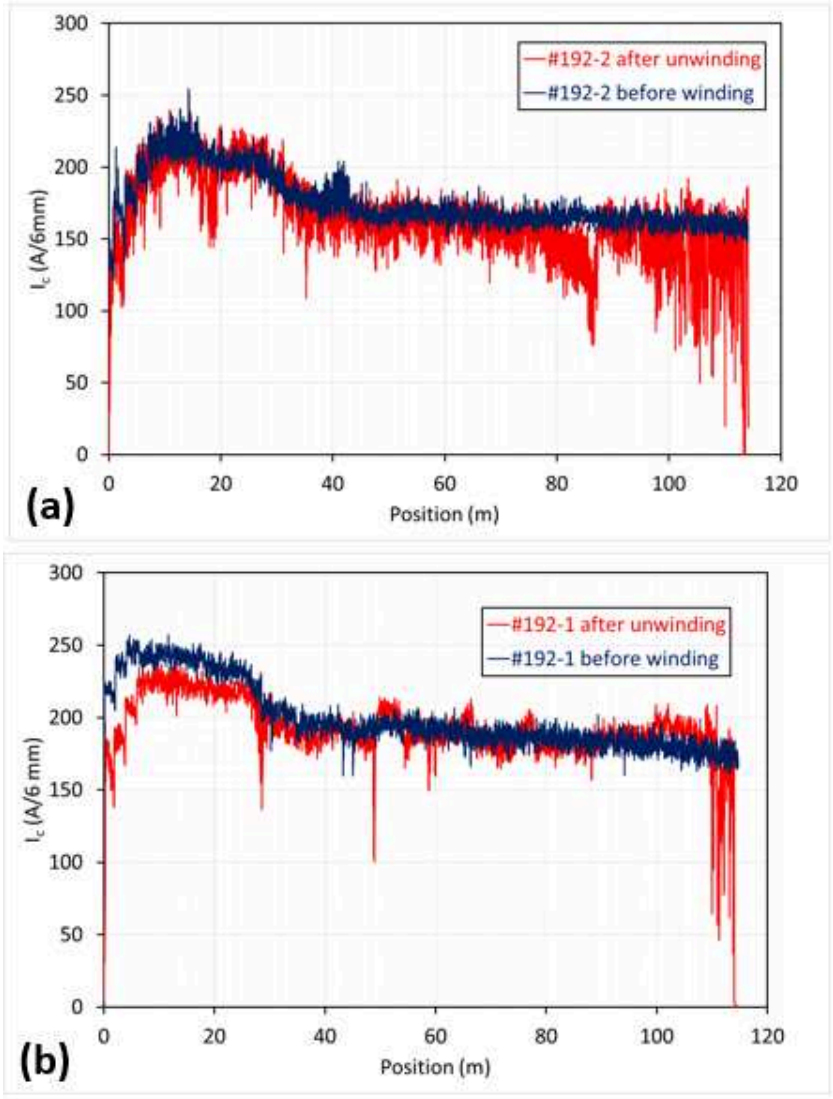


*Figure 119: Measurements of the critical current of the tapes with an inductive probe (Tapestar®), before their winding and after their unwinding. (a) Data of the tape used for the first pancake (b) Data of the tape used for the second pancake.*

The two unwound tapes have then been sent back to the manufacturer, which measured again the critical current along the length of the tapes with an inductive probe (Tapestar®). The superimposition of the measurement of $I_C$ of each tape before and after the winding is showed in Fig. 119. The fact that the calibration of the probe has changed can explain the uncertainty on the measurement and the fact that the post-winding measurement is sometimes higher than the original measurement. Nevertheless, we can clearly see that some degradations occurred between the first and the second measurement.
The degradation is especially visible at the outer turns, were the tapes delaminated because of the epoxy. But we can also see sharp degradations of at several points of the tapes. These degradations could be due to the irregular variation of the mechanical tension of the tapes during the pre-stress which could cause stress concentrations. Another hypothesis is that the tape on the spool was not pre-stressed before the winding operation. According to the team of the CEA Saclay, a good practice to pre-stress a pancake is to transfer several times the tape between two spools, increasing each time little by little the tension of the tape. In this way, the winding of the pancake is done with a tape which is already pre-stressed on its spool. There is therefore no risk of distortion or slipping of the tape wound on the spool.

#### 6.2.1.6. Lessons learned from this first prototype

The poor results obtained with this first prototype have shown the difficulty to pre-stress the winding without degrading it. Even if the pre-stress of REBCO pancakes has already been achieved with success for Non Insulated or Metal Insulated coils (See part I-3.1.6), it requires to develop the process as well as expendable spare lengths of conductor. As we had no time neither budget to develop this technique in the context of the BOSSE project, we gave up the idea to pre-stress the pancakes of the SMES. However this technique remains attractive since it theoretically improves the mechanical strength and therefore the specific energy of the coil.
Consequently, we simplified the manufacturing process of the pancakes without pre-stress neither glass fibre reinforcement.

## 6.3. Second prototype: coil made of short length conductor.

As the first double pancake prototype was far from reaching the operating current of the SMES, it was decided to make a simplified prototype in order to validate basic aspects of the pancake design and manufacturing process.
As the previous prototype had less series turns that expected, the REBCO tapes was cut. There was therefore 2 short pieces of REBCO available to make new tests. An 8 m long REBCO tape was used to make a very short pancake. The Manufacturing process is globally the same that the one presented in part II-3.4.1.2. The internal radius of this pancake is 120 mm. The tape was soldered on the inner contact, then 3.5 turns of conductor were wounded. The winding tension was low. The conductor was soldered on the external contact, then the winding was going on for 3 turns. The last 2 series turns were glued together with Stycast®. The useful length of the pancake is therefore shorter than 3 meters.

This prototype was tested at 4.2 K (liquid helium bath), without background field. No compensation was required since our Sorensen® power sources behaves very well on loads with low inductances. The envelope of the noise of the pancake voltage was lower than 250 µV.
It has been possible to increase the current until 980 A at a rate of 1 A/s. At this value, a transition occurred and the coil was discharged at a rate of -100 A/s. The current of 980 A was reached a second time in the same conditions and with the same result. This shows that no degradation occurred during the first transition.

Even if these results were much more satisfying that the results of the previous prototype, we were still far from the calculated critical current. Based on the data from T. Benkel et al. (See part I-1.3.1), the critical current should have been around 2100 A. In a general way, transitions have been observed at much lower current than the calculated critical current in all our prototypes. Some answers to this problem are given in part III-3.2.3.5.

# 7. Tests performed on real size operational prototypes

The prototypes n°3 and 4 are two real size prototypes which showed satisfying performances compared to what is required for the high specific energy SMES of the BOSSE project. The results of these prototypes complement each other. That is why they are presented together in this part.

## 7.1. Design of prototypes n° 3 and 4

### 7.1.1. Prototype n°3: single pancake

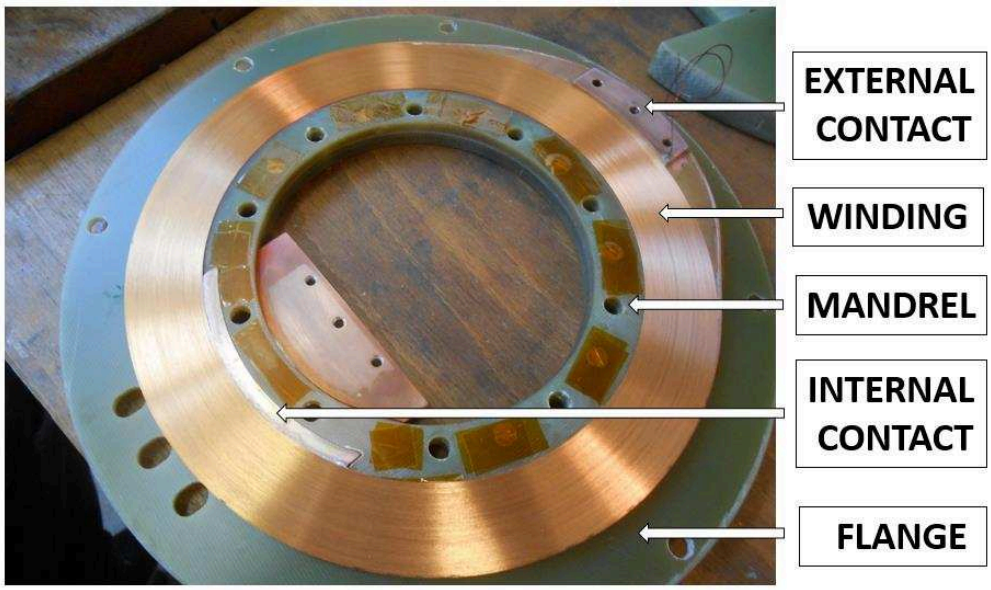


*Figure 120: Top view of the prototype pancake. The mandrel, the internal contact, the winding, the external contact and a flange are visible.*

| | Unit | Value |
|---|---|---|
| R | mm | 90 |
| H | mm | 6 |
| TH | mm | 30 |
| $B_{INT}/ I_{OPERATING}$ | mT/A | 5.57 |
| $B_R/ I_{OPERATING}$ | mT/A | 3.85 |
| Inductance | mH | 17.3 |
| Length of active conductor | m | 139 |
| Number of active series turns | | 211 |

*Table 15: Characteristics of the single pancake prototype.*

After the relative success of the short length prototype, we wanted to manufacture and test a real size single pancake. We manufactured a pancake with the dimensions of the design C (see part II-3.3.4), i.e. with an inner radius of 90 mm and an external radius of 120 mm. The tape is 6 mm wide. The manufacturing process was similar to the one presented in part II-3.4.1.2

The number of active series turns was 211, a little bit less than expected, which means that the average thickness of the tape was around 142 µm (see part). There are 4 additional free series turns after the soldered external contact then 3 more series turns glued with Stycast®.
This pancake generates a maximum field $B_{INT}$ of 5.57 mT/A and a maximum transverse field $B_R$ of 3.85 mT/A. The inductance is 17.3 mH. These values are calculated supposing a homogeneous distribution of the current density in the winding.

There are two compensation coils associated with the superconducting pancake (see part III-1.2). They are wound using insulated copper wire. They have the same geometric characteristics that the SW (superconducting winding): I.R. = 90 mm, O.R. = 120 mm, Width = 6 mm, 211 series turns. The first compensation coil is placed as close as possible from the SW, i.e. at 4 mm since it is the thickness of the flange holding the superconducting winding. The 2nd compensation coil is a bit further, at 52 mm of the superconducting winding. Both compensation coils are coaxial with the pancake.

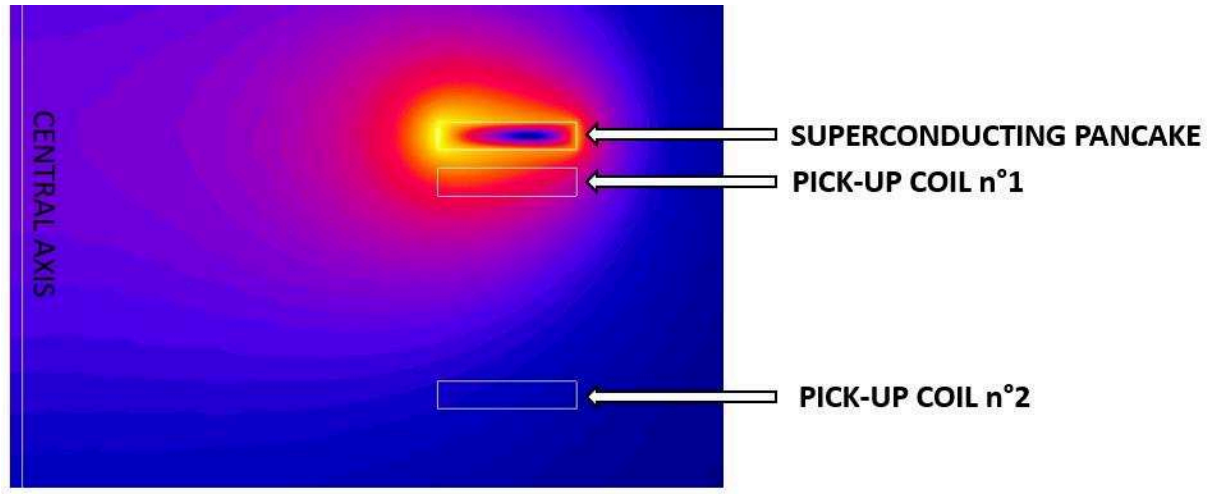


*Figure 121: Axisymmetric cross-section of the single pancake and its compensation coils. The B field distribution is visible. The current density is supposed to be homogeneous in the pancake.*

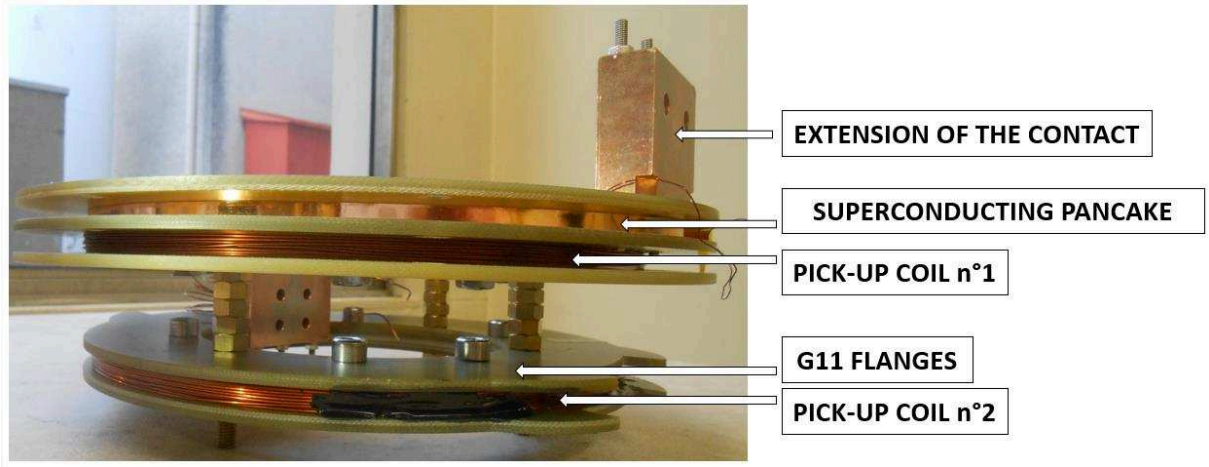


*Figure 122: View of the prototype pancake with its 2 compensation coils underneath. The rectangular blocks of copper and the copper contacts of the pancakes are pressed together by stainless steel screws passing through them. These blocks are then connected to the current leads.*

*Figure 123: The pancake and its compensation coils mounted on the 3 kA EuCARD probe (see part III-1.1). The extensions of the contacts are connected to the current leads of the probe by copper braids, which enables the connection to be partially flexible. This mounting is also visible in Fig. 104.b.*

### 7.1.2. Prototype n°4: double pancake

After the decision to make the design evolve from version C to version D, we wanted to make a prototype of a double pancake corresponding to the ones of the design D. We planned to make a double pancake made of 12 mm wide tapes with an inner radius of 96 mm and a thickness of 24 mm with 178 series turns per single pancake. The average thickness of the tapes was higher than expected, and was not the same for both unit length of conductor. The average thickness of the conductor is 167 µm for the upper coil and 140 µm for the lower coil. Consequently, the number of turns is therefore lower than expected. The characteristics of the double pancake are presented in table 16. $B_{MAX}$, $B_R$ and the inductance are calculated for a homogeneous distribution of the current density. $B_{MAX}$ is the maximum B field on each pancake. The manufacturing process is similar to the one presented in part II-3.4.1.2.

| | Unit | Value |
|---|---|---|
| R | mm | 96 |
| H | mm | 12 |
| TH (upper/lower) | mm | 25 / 23.5 |
| $B_{MAX}$/ $I_{OPERATING}$ (upper/lower) | mT/A | 5.04 / 5.40 |
| $B_R$/ $I_{OPERATING}$ (upper/lower) | mT/A | 4.08 / 4.39 |
| Inductance | mH | 31.4 |
| Length of active conductor (upper/lower) | m | 102 / 114 |
| Number of active turns (upper/lower) | | 150 / 168 |

*Table 16: Characteristics of the double pancake prototype*

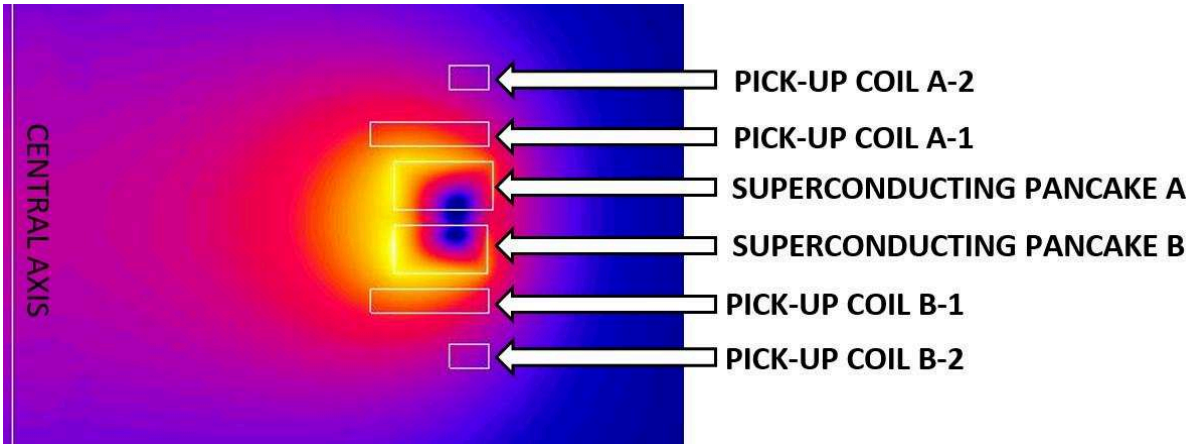


*Figure 124: Axisymmetric cross-section of the double pancake and its compensation coils. The B field distribution is visible. The current density is supposed to be homogeneous in each pancake.*

This double pancake is associated with 4 compensation coils, which enables to independently compensate the inductive voltage of each single under a noisy background field (see part III-1.2.4). The coils are similar in pairs. The coils A-1 and B-1 have 415 series turns, an inner radius of 90 mm, an outer radius of 120 mm and a thickness of 6 mm. The coils A-2 and B-2 have 231 turns, an inner radius of 110 mm, an outer radius of 120 mm and a thickness of 6 mm. The distance between the coils A-1 and B-1 and the superconducting pancakes is 4 mm. The distance between B-2 and B-1 or A-2 and A-1 is 8 mm.

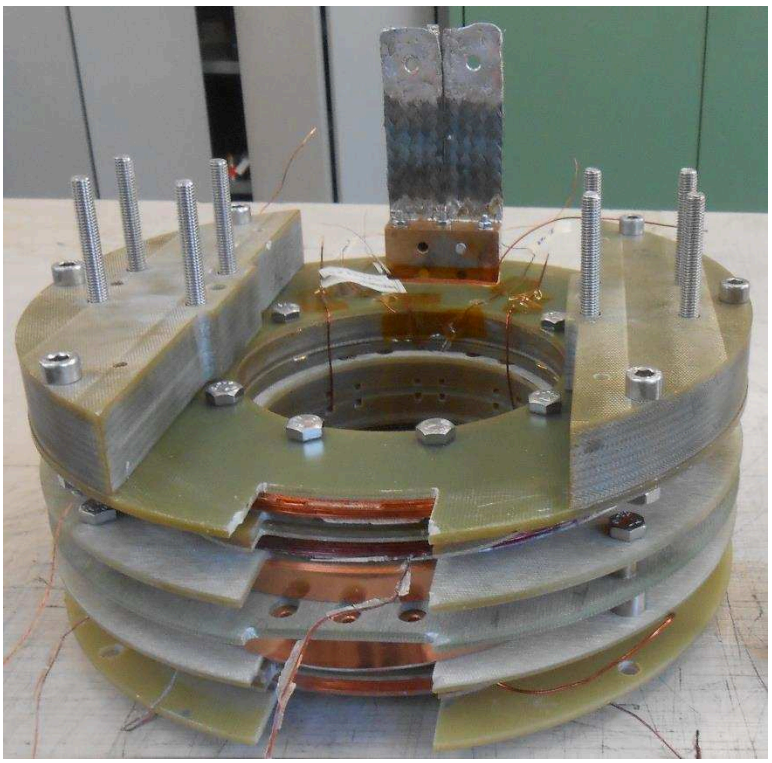

*Figure 125: The double pancake prototype with its compensation coils, ready to be mounted on the EuCARD probe.*

# 7.2. Experimental results of prototypes n° 3 and 4

## 7.2.1. General presentation and protocols of the tests.

### 7.2.1.1. Tests of the prototype n°3 (single pancake)

The single pancake has been tested in the 376 mm diameter bore resistive magnet of the Grenoble LNCMI. The data presented afterward have been obtained during this test under background magnetic field. The signals have been registered with the Yokogawa DL 850 oscilloscope. The Sorensen current source have been used (see part III-1.1). The first objective of this test was to submit the pancake to increasing hoop stress in order to test its mechanical resistance and its manufacturing process. The second objective was to demonstrate the possibility to protect insulated REBCO pancake under high current density.

| Ramp No | $B_{EXT}$ (T) | I (A) | I.R hoop stress (MPa) | O.R hoop stress (MPa) | Extra Voltage (μV) | Apparent n value |
|---|---|---|---|---|---|---|
| 1 | 0 | 480 | | | | |
| 2 | 1 | 486 | | | 336 | 60 |
| 3 | 8 | 282 | 300 | 290 | | |
| 4 | 6 | 341 | 300 | 240 | | |
| 5 | 5 | 379 | 300 | 200 | | |
| 6 | 4 | 424 | 300 | 155 | | |
| 7 | 3 | 476 | 300 | 91 | | |
| 8 | 8 | 321 | 350 | 322 | | |
| 9 | 6 | 386 | 350 | 262 | | |
| 10 | 4 | 473 | 350 | 160 | | |
| 11 | 6 | 428 | 400 | 280 | | |
| 12 | 0 | 560 | | | 418 | 140 |
| 13 | 4 | 504 | 382 | 162 | 911 | 60 |
| 14 | 2 | 516 | | | 376 | 40 |
| 15 | 6 | 469 | 450 | 297 | | |
| 16 | 7 | 433 | **453** | **347** | Saturation | >700 |

*Table 17: List of the performed current ramps in chronological order, with the background B field, the maximum current, the hoop stress at inner radius (I.R.) and outer radius (O.R.). The indicated stress is average stress on insulated conductor. For the ramps where a transition has been observed, the n value and the extra voltage (see part III-3.2.3.2.2) are also shown.*

During this test, the pancake has been submitted to 16 current ramps cycles (charge and discharge) under different background magnetic fields. The list of these ramps is presented in table 17. The successive combinations of current and background magnetic field have been chosen in order to minimize the risk of damaging the pancake for mechanical or electrical reasons. The choice was based on the expected electrical and mechanical performances of the pancake but also observations during the experiment. For each current ramp cycle, several current ramp rates were used. Generally at the beginning, the current rate was 4 A/s, then it was decreased to 3 A/s, then 2 A/s, 1 A/s and eventually 0.5 A/s. Current plateaus were performed between two different ramp rates. The reduction of ramp rate aims to limit the inductive voltage as the shift in the compensation of the inductive voltage

increases with the operating current (see Fig. 128 and part III-3.2.3). In this way, the most sensitive calibre of the oscilloscope can still be used.
During these 16 ramps, a transition (see part III-1.2.7) of the voltage curve has been observed 4 times (ramps No 2, 12, 13 and 14). Our original analysis was that these transitions were the sign of the loss of the superconducting state, i.e. that the critical current was reached, at least locally. In these four cases, the pancake has therefore been discharged quickly, at a rate around -130 A/s, which was the maximum controlled discharge speed of the current sources. In other cases, the pancake was discharged at slower rates.
At the 16th current ramping, the pancake has finally been damaged. As we will see in III-3.2.2.2, this damage likely occurred for mechanical reason and not for electrical one.
As we originally supposed that the transitions where related to the achievement of the critical current, we fitted the signal of the transition with a power law (see eq. 1). This fit aims to calculate the exponent "n" of the power law as well as the extra voltage, which is the additional voltage due solely to the transition. These values are reported in table 17. The way they are calculated is explained in III-3.2.3.2.2.

#### 7.2.1.2. Tests of the prototype n° 4 (double pancake)

Several unexpected phenomena were observed during the tests of the prototype n°3. In order to confirm these observations, more systematic tests have been led on the prototype n°4. Some of the results of these tests, in self-field or under background field, are presented in part III-3.2.3. The experimental set-up was very similar to the one used for the previous tests but the Bertha current source was used instead of the Sorensen current source (see part III-1.1).

During this test, a first transition was observed at 746 A in self-field. This value of current is higher than the maximum one reached with the prototype n°3 (560 A), but it should be reminded that the prototype n°3 is made of 6 mm wide tape while the prototype n°4 is made of 12 mm wide tape. So the reached current density was lower even if the operating current was higher. The fact that the maximum reached current density is lower for the prototype n°4 than for the prototype n°3 is likely due to the fact that the ratio between the maximum radial field $B_R$ and the operating current is higher for the prototype n°4 than for the prototype n°3 (see tables 15 and 16).
Another transition has been observed at 618 A under a 6 T background field, which corresponds to a maximum hoop stress of 325 MPa on the lower pancake. Consequently, the maximum hoop stress which had been reached during the tests performed on the prototype n°3 (450 MPa) had not been overtaken.

### 7.2.2. Mechanical considerations of the tests

#### 7.2.2.1. Calculation of the stress in the winding submitted to tests under background field

The hoop stress values indicated in table 17 are calculated but not measured. As the stress distribution depends on the current, the self-field and the background field, all of the 16 cases are different. In each case, 2 extreme models are compared: the Wilson formula, in which the stress of inner turns is reported rigidly on outer turns, and the "JBR" formula in which each turn acts independently without laying on other turns (see part I-4.1).
Figure 126 considers the case of the rupture point of the current ramp n°16, where the background field is 7 T and the operating current is 433 A. We can see the hoop stress calculated with the Wilson's formula is higher than the JBR formula. When the pancake is submitted to a background B field which is much higher than its self-field, the radial stress calculated by the Wilson's formula becomes tensile. As we have seen in part I-4.1.2, this means that the Wilson's formula cannot be used since the winding is not impregnated. In this case, the JBR product has to be used to calculate the real hoop stress. The

value of the JBR product is a little higher at the inner radius than at the outer radius. But as the inner series turns are smaller, the radial extension of these series turns, which is a percentage of their radius for a given magnetic load, is not sufficient for them to press on outer turns.
Furthermore, taking into account the polyimide insulation thermal contraction which untightens the winding during cooling down, it appears that the JBR formula has to be applied in most of cases. What is the pertinent model between the Wilson's formula or the JBR product is more ambiguous for cases of ramps No 1, 2, 12 and 14, but these cases are subject to low hoop stress anyway. The JBR product has to be used in all other cases of table 17.

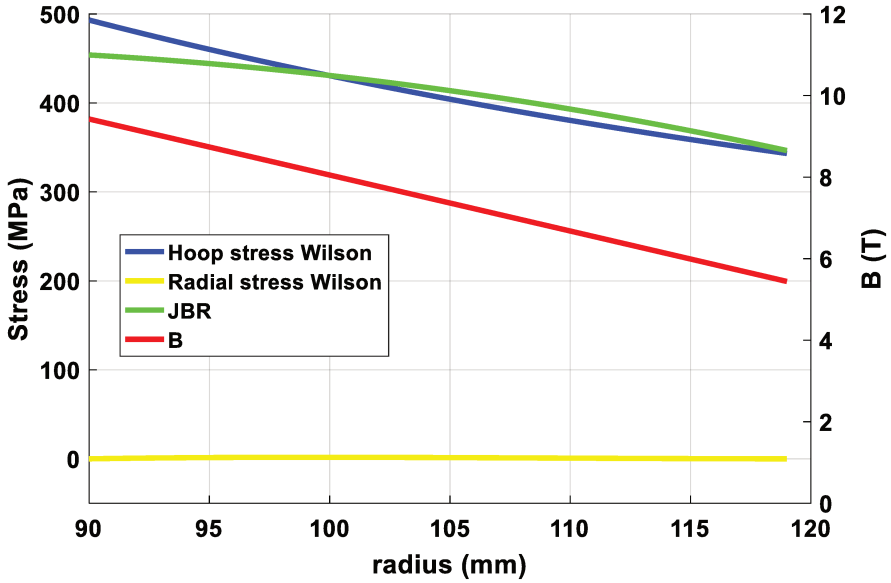


*Figure 126: Stresses and longitudinal B field along the radius of the pancake when the operating current is 433 A and the background field is 7 T. The radial stress calculated by the Wilson's formula is low and positive, with a maximum at 1.72 MPa.*

#### 7.2.2.2. Indications that the failure happened for mechanical reason

At the 16th current ramping, the current was maintained at 430 A for 24 s under a 7 T background magnetic field. The current was then increased again, but a very sharp increase of voltage happened at 433 A (see Fig. 129.e). The current discharge was triggered but the pancake was damaged during this event since a 17 µOhm resistance appeared permanently in the pancake. After the cryostat was opened and the pancake dismounted, traces of burned or damaged insulation were clearly visible on several square centimetres at the edge of the external contact.
For this event which damaged the pancake, it is not possible to fit the measured voltage by a power law with a n value lower than 700 while the n value of other transitions are comprised between 40 and 140. This event seems therefore fundamentally different from the previously observed transitions. Our interpretation is that this event happened for mechanical reasons rather than for electric ones (overstepping of critical current). This interpretation seems especially likely as the extremity of the rigid external contact, where the damage occurred, is a weak point from the mechanical point of view. From the electrical point of view, it is not supposed to be a weak point since the transverse field is low on the external contact.
This result is interesting since it seems to show that our measurement is precise enough to distinguish if the failure has an electrical or a mechanical origin. This distinction can indeed be difficult to perform for example when a damage occurs to a high field magnet, in which the REBCO conductor is used close to both its maximum electrical and mechanical performances [AWOM17]. Unfortunately but unsurprisingly, it also shows that it seems impossible to anticipate a mechanical failure of the winding by the observation of its voltage.

#### 7.2.2.3. Comparison between the results of the tests and the expected mechanical performance of the SMES

When the damage occurred, the outer turn of the pancake was theoretically submitted to a hoop stress of 347 MPa according to the JBR formula. But in the final configuration of the SMES, only submitted to self-field, the stress distribution is different and the outer turn will be submitted to lower hoop stress, around 270 MPa. The mechanical failure of our pancake is therefore not in contradiction with the expected performance of the SMES. But this mechanical failure prevented to reach higher hoop stress at the inner turn. Nevertheless, a hoop stress of 453 MPa has been reached at the inner turn while a hoop stress of 421 MPa is required to reach a specific energy of 20 kJ/kg and an energy of 1.1 MJ in the final configuration of the SMES (see Tab. 11 in part II-3.3.5). So even if the design of the pancake is a bit different in the final SMES since the thickness is 24 mm instead of 30 mm, the performed tests are largely contributing to validate the SMES design from a mechanical point of view.

### 7.2.3. Presentation of voltage measurements obtained during the tests.

In all the following figures and if not specified, the displayed signal is the compensated voltage, i.e. the voltage of the pancake combined with the voltages of the compensation coils (see part III-1.2), filtered by two successive filters (a sliding mean value filter and a low pass filter) as shown in Fig. 108.

If not specified, the displayed signals have been obtained during the tests performed on the prototype n°3 (single pancake).

#### 7.2.3.1. Introduction for adequate interpretation of the presented data

The voltage signals presented in the following parts are complex and their value is influenced by a set of phenomena. In order to make understandable the following figures, we first introduce some of these phenomena.

##### 7.2.3.1.1. Concept of apparent inductance

For all of our experiments, the compensation of the inductive voltage was imperfect. We have always observed a residual voltage which was proportional to the rate of the current ramp. For this reason, we will quantify this behaviour by what we will call an “apparent inductance” $L_{APP}$. But this apparent inductance depends on the state of the system and has different origins. The unit of the apparent inductance is the Henry (H).

###### 7.2.3.1.1.1. Evolution of the inductance and couplings

A first reason for that behaviour is, as it has already been explained in part III-1.2.6, that the inductance of the winding and its couplings with the compensation coils changes as the operating current is varying. The compensation had been optimised to be perfect at the beginning of the current ramp but as the current is increased, the residual inductance also increases.

###### 7.2.3.1.1.2. Voltage due to magnetisation losses

A second reason is that when the operating current is ramped, the winding is submitted to magnetisation losses (see part I-3.4.2.2). In steady state, these magnetisations losses, as well as the voltage due to this losses, are proportional to the rate of the current ramp [RBRM00]. For this reason, this voltage is quite uneasy to differentiate from the voltage due to the evolution of the inductance. This effect is therefore included in what we call the apparent inductance, even if it is totally different in nature with an inductance since it is a dissipative phenomenon.
In order to know what the respective parts of the inductance evolution and the magnetisation losses are in the evolution of the measured signal, it would be possible to perform a simulation of the tested

pancake with the simulation model developed by B. Rozier. This simulation has not been performed yet because of the required computation power.

#### 7.2.3.1.1.3. Influence of the background B field

Another phenomenon which has been observed is that the value of the background field of the Grenoble LNCMI magnet has a strong influence on the apparent inductance, which increases with the value of the background field. It is described in Fig. 132 and 135.

### 7.2.3.1.2. First magnetization of winding

Another phenomenon which has been observed is that the apparent inductance was much higher during a first ramp of current after cooling down than during the following current ramps with same ramp rate. This is true as far as the operating current does not overstep the maximum current which has been previously reached. If this value is overtaken, the voltage rises until the slope of previous current ramp is reached. This phenomenon has been understood during the analysis of the data obtained during the tests of the prototype n°3. Dedicated tests have been performed on the prototype n°4 to bring this phenomenon out. The results of these tests are presented in Fig. 127. During these tests, after the cooling down of the double pancake, some current ramps until 100 A have been performed in order to optimize the compensation system (see part III-1.2). These current ramps are not displayed in Fig. 127. The winding has then been submitted to 3 current ramps which are visible in this figure. The current has been increased until 200 A, decreased to 0 A, increased to 600 A, decreased to 0 A then increased until 746 A, at which a transition was observed. The negative voltage during the discharges is not visible. The drops at 300 A, 400 A and 500 A correspond to current plateaus. The current ramps have been performed at a rate of 1 A/s, except the current ramp in green which has been performed at 4 A/s until 500 A.

This phenomenon is likely related to magnetisation losses, which are known to be different between the first magnetisation cycle and the following cycles.

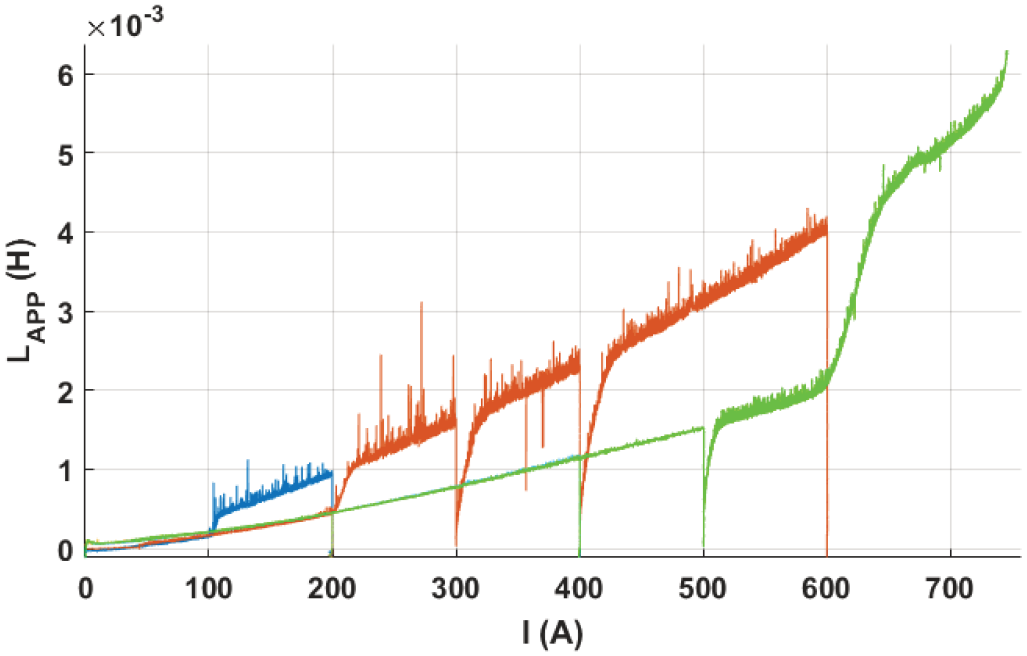


*Figure 127: Apparent inductance of the double pancake (prototype n°4) in self-field, submitted to three successive current ramps after cooling down.*

### 7.2.3.2. Validity of the concept of apparent inductance

#### 7.2.3.2.1. Example of a V(t) signal

Figure 128 shows a compensated voltage versus time. The signal corresponds to the current ramp n°13, under a 4 T background field. Another V(t) curve, corresponding to the current ramp n°2, under background field of 1 T, has already been shown in Fig. 108. If the compensation was perfect, the voltage should be zero until the dissipative transition. The voltage amplitude is indeed increasing with the current value, but go back to zero on current plateaus (when $t \in [-214\ s;-198\ s]$, $t \in [-165\ s;-155\ s]$, $t \in [-121\ s;-113\ s]$ and $t \in [-88\ s;-81\ s]$). We can clearly see that the voltage level is depending on the current ramp rate as expected for an inductance, but we can also see that this apparent inductance is increasing with the time (i.e. with the current).

At each beginning or end of the current plateaus, we can see that the voltage follows a smooth transition. These transitions are explained qualitatively by the simulations of B. Rozier [RBRM00] and are related to the magnetisation losses.

From -40 s, we can see that the dynamic of the evolution of the signal is really changing while the current rate is constant. It is what we have defined as a "transition" in part III-1.2.7. At 21 s, the pancake is discharged with a high current rate (-130 A/s). The voltage therefore becomes negative at this point but is not shown.

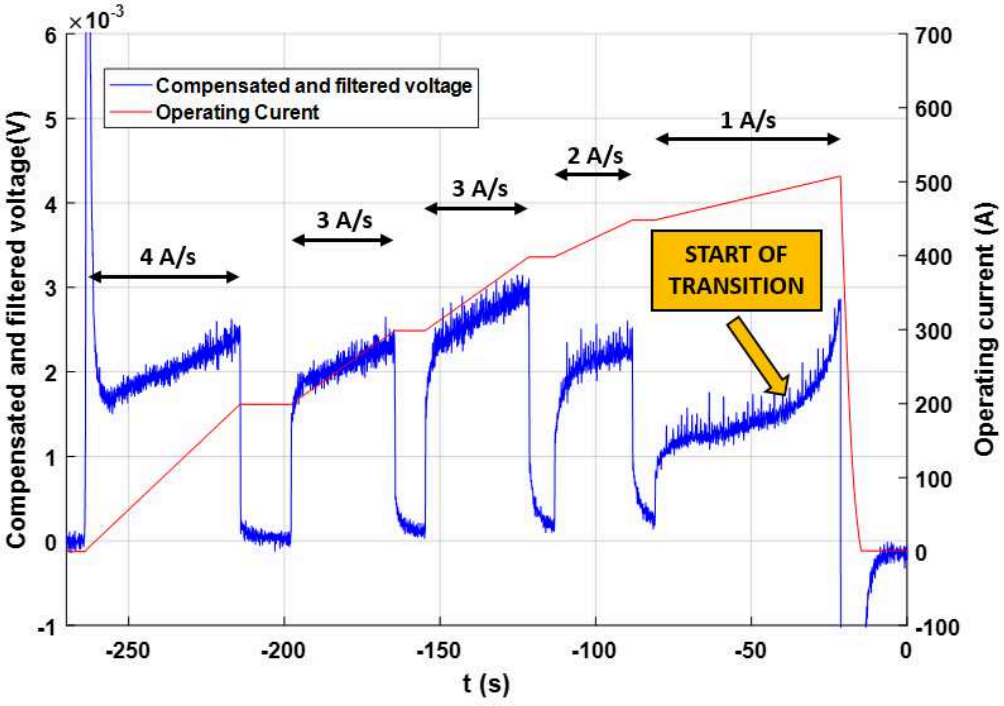


*Figure 128: Compensated voltage depending on time of the current ramp n°13 (prototype n°3).*

#### 7.2.3.2.2. Fit of V(I) curves by affine functions

In Fig. 128, the compensated voltage has been plotted in function of time, but it is of course possible to plot it depending on I. V(I) signals of the four cases for which a transition has occurred and the last current ramp (for which the pancake has been damaged) are displayed in Fig. 129. In this kind of representation, the current plateaus are reduced to only one point. They are the drops which reach zero volt for example at 300 and 400 A in Fig. 129.a.

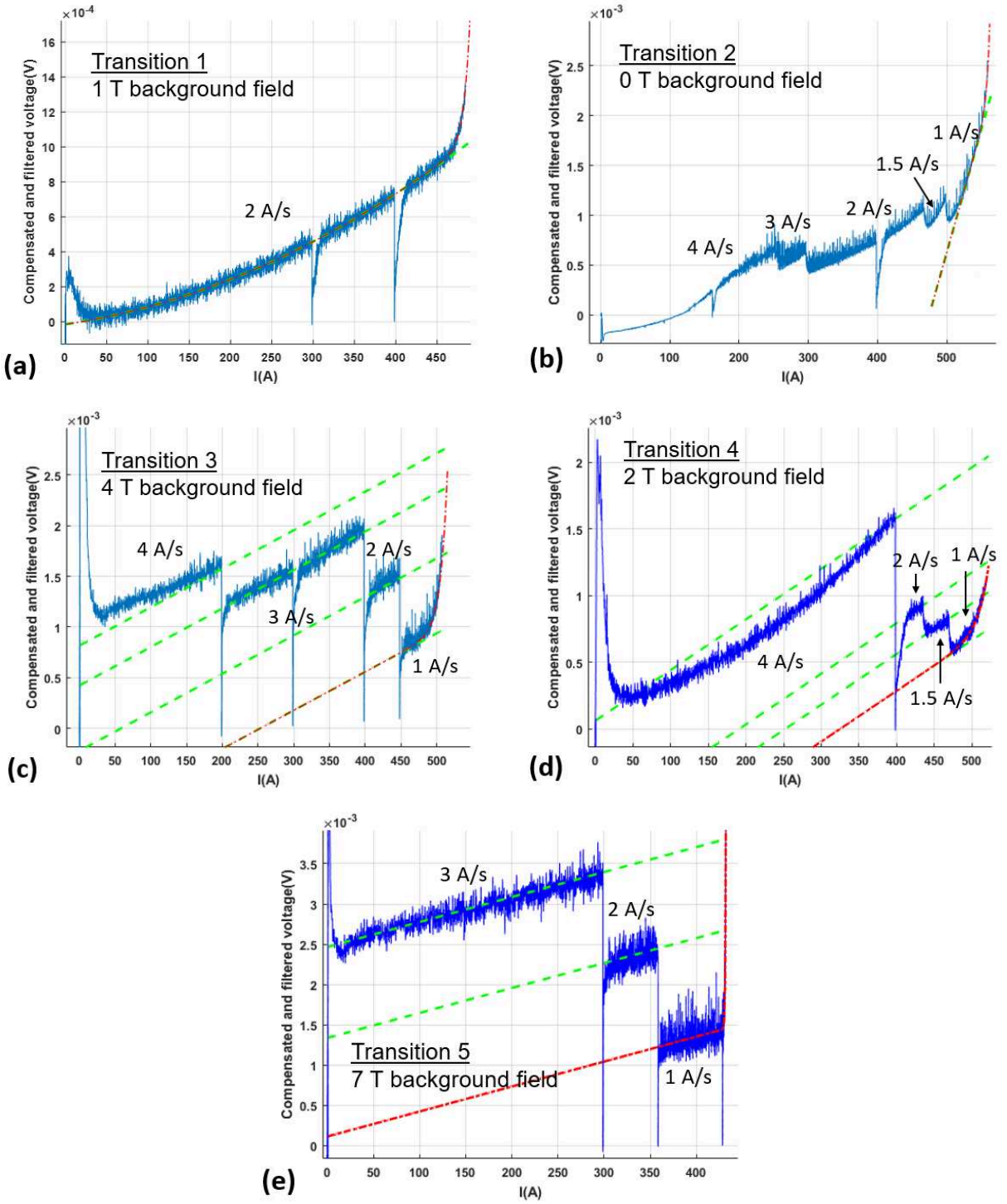


*Figure 129: V(I) curves of the 4 current ramps for which a transition has been observed (current ramps n° 2, 12, 13 and 14) and of the last current ramp for which the pancake has been damaged (current ramp n°16). The signals are shown until the discharge of the pancake has been triggered.*

The voltage curves have been fitted by a 2nd order polynomial for the first case (Fig. 129.a) and affine functions for other cases. These fit functions are the green dotted lines. This work has not been achieved for the curve of Fig. 129.b and only the last part has been fitted, which will be explained in III-3.2.3.5. In Fig. 129.c, d and e, there are several parallel affine functions. They are shifted following the rule that at the point where the current ramp rate is changed, the ratio of the values of two affine functions is the ratio of the current ramp rates. We can see that following this rule, the green affine

functions are effectively fitting the different sections of the voltage curve. So it shows that the voltage signal is proportional to the ramp rate and so that it can be characterised by an apparent inductance as we said in part III-3.2.3.1.1, but this apparent inductance is evolving with the current. In these figures, we can observe that the drift of the apparent inductance with the current is very regular under high background field while it is increasing under low background field, but we do not have explanation to this behaviour.

As we already said in part III-3.2.1.1, we originally supposed that the transitions where related to an overstepping of the critical current. We therefore tried to fit these transitions with a power law. These power laws are characterised by a value of critical current and a value for the exponent n. These power laws are added to the affine function which fits the last section of the voltage curves where the transition occurs. The result is displayed in red in Fig. 129 and 130. The figure 130 is a zoom on the end of the curve of the Fig. 129.c. The fit of the voltage curves aims to calculate the n value of the power law but also the extra voltage, which is the difference between the maximum voltage during the transition and the value of the apparent inductance at the corresponding current. A representation of this extra voltage is shown in Fig. 130. These two values (the n and the extra voltage) have already been reported in table 17. Under the assumption that the dissipative voltage is due to the resistivity of the superconductor, the extra voltage gives the value of the power dissipated in the winding during the transition.
Nevertheless, given our experimental results (see part III-3.2.3.5), it seems likely that a part of the apparent inductance is due to magnetisation losses. So a part of the additional voltage due to the evolution of the apparent inductance also corresponds to a dissipative voltage.

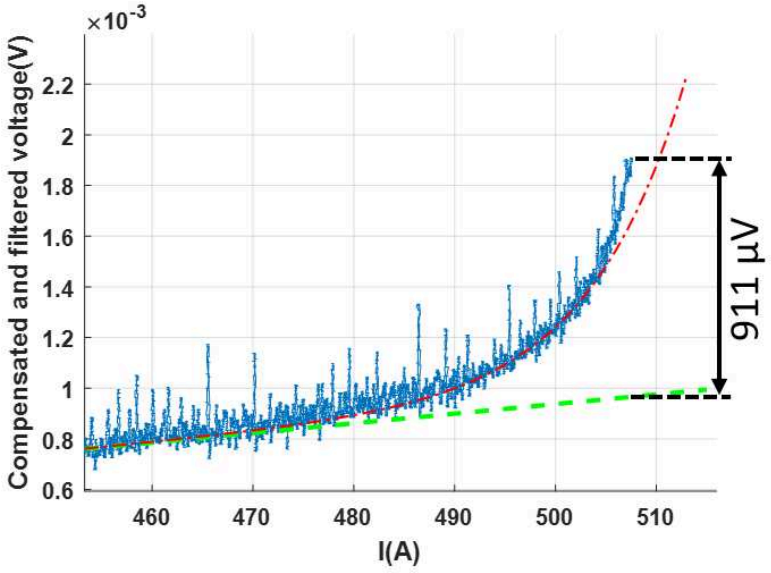


*Figure 130: V(I) curve of the 3rd observed transition. The voltage signal is in blue, the fit of the apparent inductance is in green and the fit of the transition with a power law is in red.*

#### 7.2.3.2.3. Cycles with different ramp rates

The compensated voltage signal can also be divided by the ramp rate. In this case, the obtained value is the apparent inductance.
After a current ramp until 600 A, the prototype n°4 has been submitted to 3 current ramps until 200 A. The ramp rate (during charge and discharge) was 2 A/s for the first cycle, 4 A/s for the second cycle and 8 A/s for the third cycle. The compensated voltage of these 3 cycles has been divided by their respective ramp rates in order to obtain the curves of their apparent inductance. These curves are displayed in Fig. 131. As we can see, they are perfectly superimposed. It shows the pertinence to use

an apparent inductance to describe the behaviour of the system since the voltage is perfectly proportional to the ramp rate. It also shows that the signals are perfectly reproducible and that there is no more modification of the apparent inductance after the first current ramp has been performed.

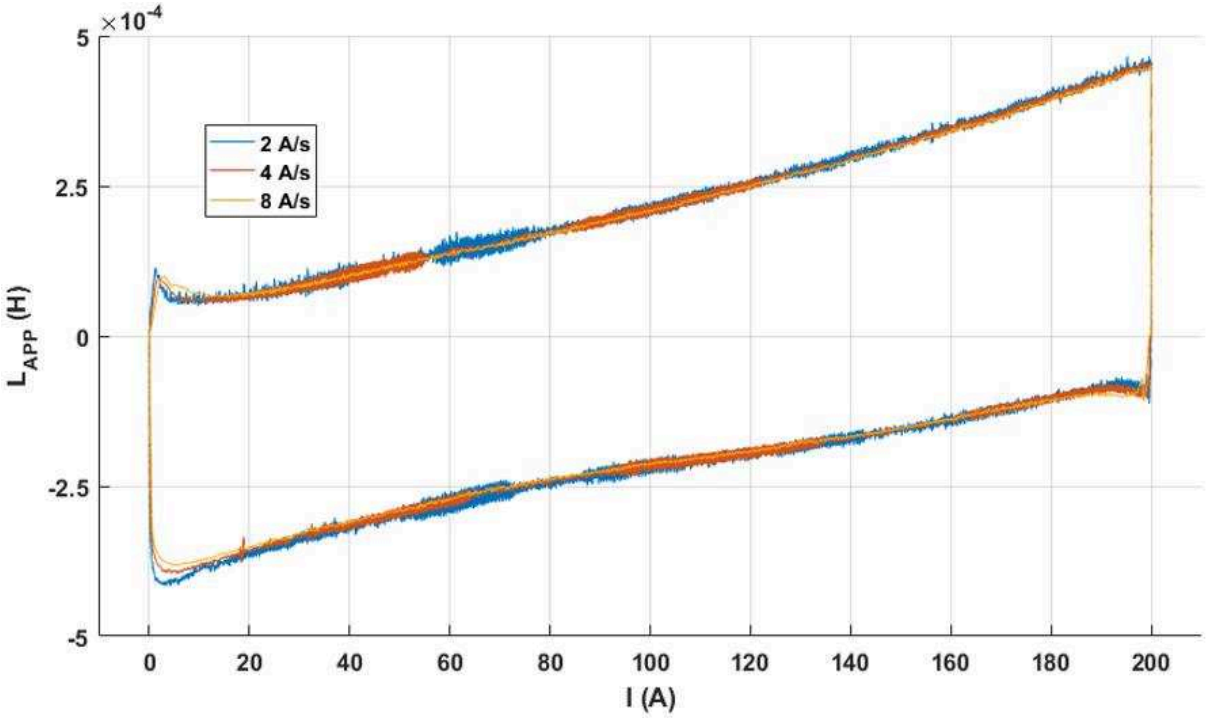


*Figure 131: Apparent inductance of 3 current cycles performed at different ramp rates on the prototype n°4 (double pancake). The prototype was previously magnetized by a current ramp until 600 A.*

#### 7.2.3.3. Comparison of the apparent inductance of several current ramps and influence of the background field

##### 7.2.3.3.1. Prototype n°3

Fig. 132 shows the evolution of the apparent inductances for some of the current ramps performed on the prototype n°3. For each of these curves is indicated the number of the current ramp (corresponding to the one indicated in the table 17) and the value of the background field during this current ramp. All of the 16 current ramps are not shown for clarity. The points corresponding to current plateaus have also been removed for the same reason.
The noise of the signal is higher at higher field because the higher magnetic fields of the background magnet are also noisier. On this figure, it can seem that the signal is noisier at higher current, but this is only due to the fact that the ramp rate is lower at higher current, so the original signal has been divided by lower values for data at high current.

On this figure, it is visible that except for the first current ramp (in red), all the curves are parallel, at least until the transitions. Another observation is that these curves are shifted to higher values when they are submitted to higher background fields. In other words, the apparent inductance is subject to an offset which increases with the background field. This is an offset of the apparent inductance and not of the signal itself since the value of the signals goes to zero on current plateaus. The value of this offset depending on the background field has been reported in Fig. 133. We have currently no explanation to this and we do not know if this is due to a dissipative phenomenon or not.

The fact that the curve of the first current ramp is quite different from the other signals is related to what have been explained in III-3.2.3.1.2. This first current ramp has been performed with different ramp rates, namely 2 A/s until 300 A, then 1 A/s and 0.5 A/s. The fact that all the sections of this curve

are aligned in Fig. 132 shows that the concept of apparent inductance also applies to the first current ramp after cooling down. Nevertheless, the value of the apparent inductance is different between the first cycle and the following cycles, which is logical if we consider that the voltage signal is due to magnetisation losses.

A partial interpretation of the transitions observed in this figure is proposed in part III-3.2.3.5.

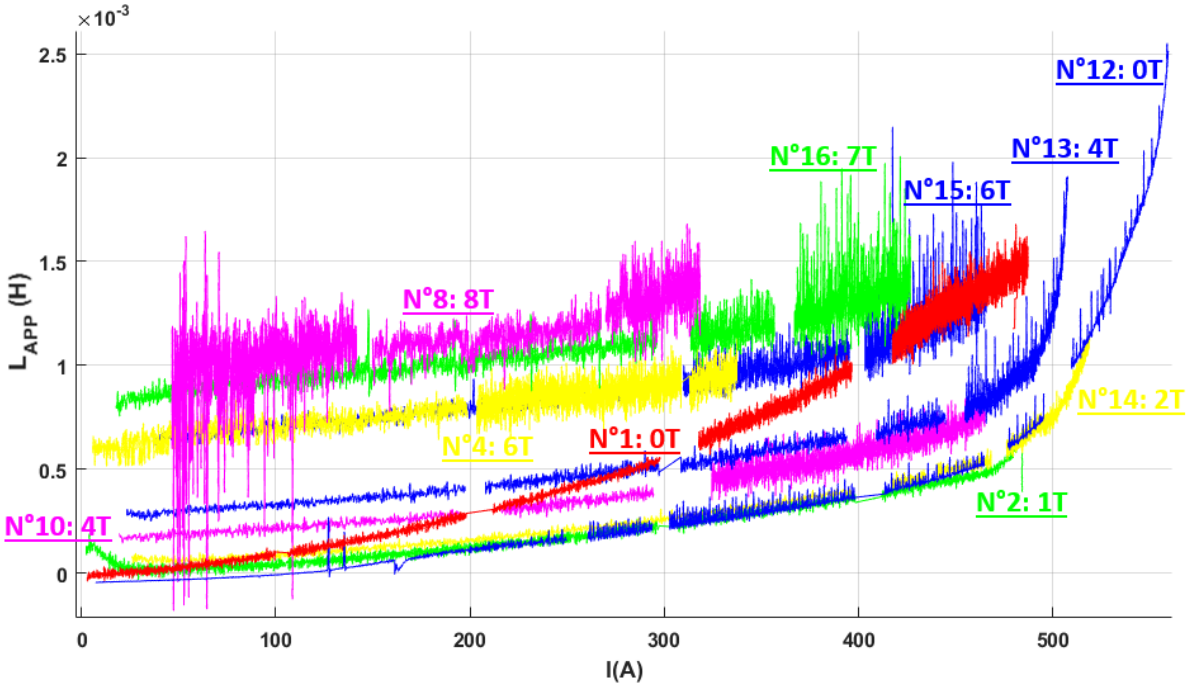


*Figure 132: Evolution of the apparent inductance, depending on the current and the background field. The current ramps have been performed on the prototype n°3 (single pancake). The red curve is the first current ramp.*

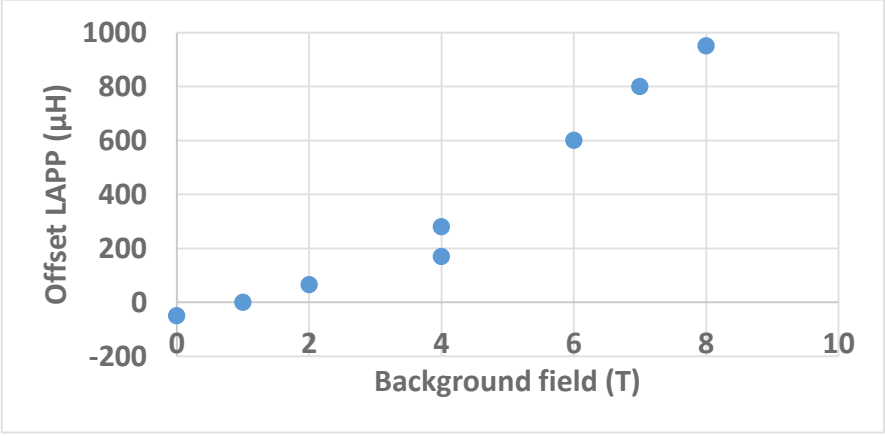


*Figure 133: Offset of the apparent inductance depending on the background field.*

#### 7.2.3.3.2. Prototype n°4

To confirm the influence of the background field on the apparent inductance, the prototype n°4 has also been submitted to current ramps under different background fields. After the cooling down and after a first current ramp until 650 A, the double pancake has been submitted to current ramps until 300 A under a background field increasing from 1 to 6 T. The ramp rate was 2 A/s. The measured compensated voltage is shown in Fig. 134. For a given background field, the current ramp has been performed twice. We can see that for each background field, the signals of the two current ramps are perfectly superimposed, which shows the perfect reproducibility of the phenomenon. As in the

previous paragraph (part III-3.2.3.3.1), we can see that the apparent inductance is increasing with the value of the background field.

But in comparison with Fig. 132, the signals are following a kind of “M”-shaped fluctuation before stabilizing at higher current. We do not have demonstrated explanations to this phenomenon, as well as we do not have explanations to the fact that the apparent inductance increases with the background field. Nevertheless, speculative elements of reflexion are given in appendix C-2.

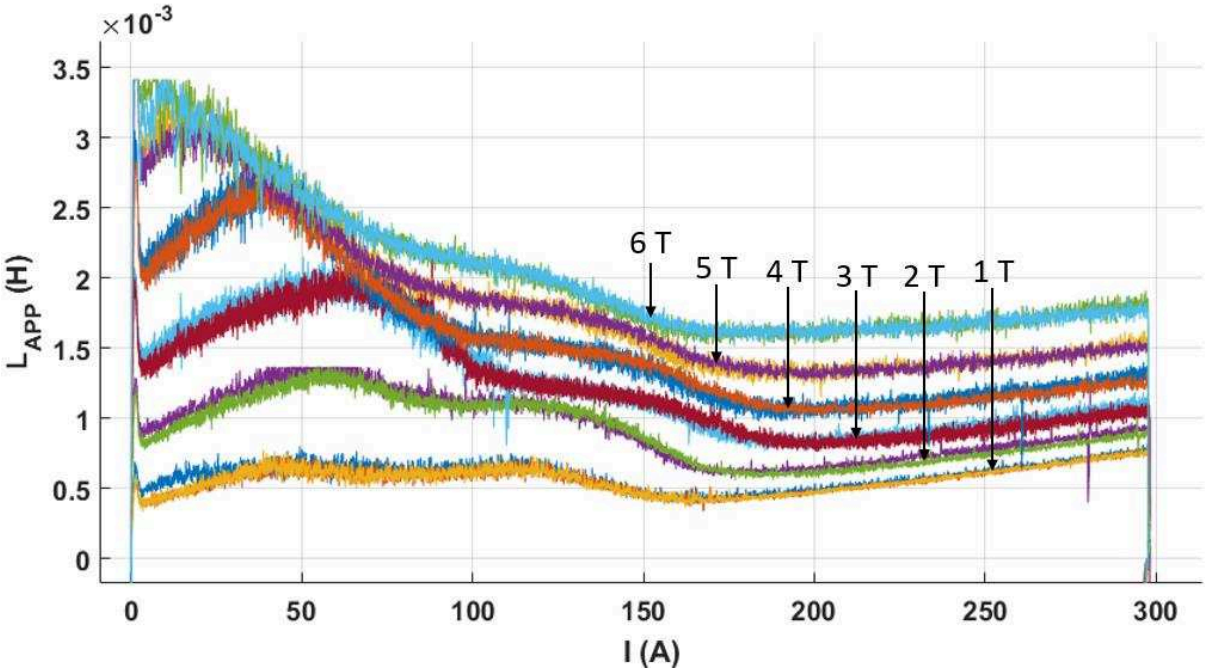


*Figure 134: Evolution of the apparent inductance, depending on the current and the background field, after a first current ramp until 650 A. The current ramps have been performed on the prototype n°4 (Double pancake).*

#### 7.2.3.4. Non-compensated signals and numerical compensation

Until now, we have showed the compensated voltage, which is a combination of the voltages of the superconducting winding and its compensation coils. Nevertheless, in order to interpret our results and to compare them with simulations, it can be interesting to determine independently the voltage of the superconducting winding, or, on the contrary, the voltage of each pick-up coil. As the non-compensated voltages are very noisy, it is necessary to highly filter the raw signals in order to extract useful signals. The result of such a treatment is visible in Fig. 108. It has been applied to the non-compensated signals of a current ramp from 0 A to 650 A performed on the prototype n°4. It was a first current ramp after cooling down of the double pancake. The ramp rate was 1 A/s. The raw signals had a sampling rate of 5000 points per second and have been submitted to a sliding average filter with a total window of 20 000. The three curves in the figure 135 are the voltage of the double pancake, the sum of the voltages of pick-up coils A1 and B1 and the sum of the pick-up coils A2 and B2 (see Fig. 124). The signals of the pick-up coils have been multiplied by the ratio between the inductance of the double pancake and their respective mutual inductance with the double pancake. In this way, they are normalised with the voltage of the double pancake at the beginning of the current ramp. Even if the result is still noisy, we can clearly see in Fig. 135 the trends of the signals. We can see that the voltages of the pick-up coils decrease during the current ramp. This is because their coupling with the current flowing in the double pancake decreases as the current drifts from the edges to the centre of the double pancake (see part III-1.2.6.1).

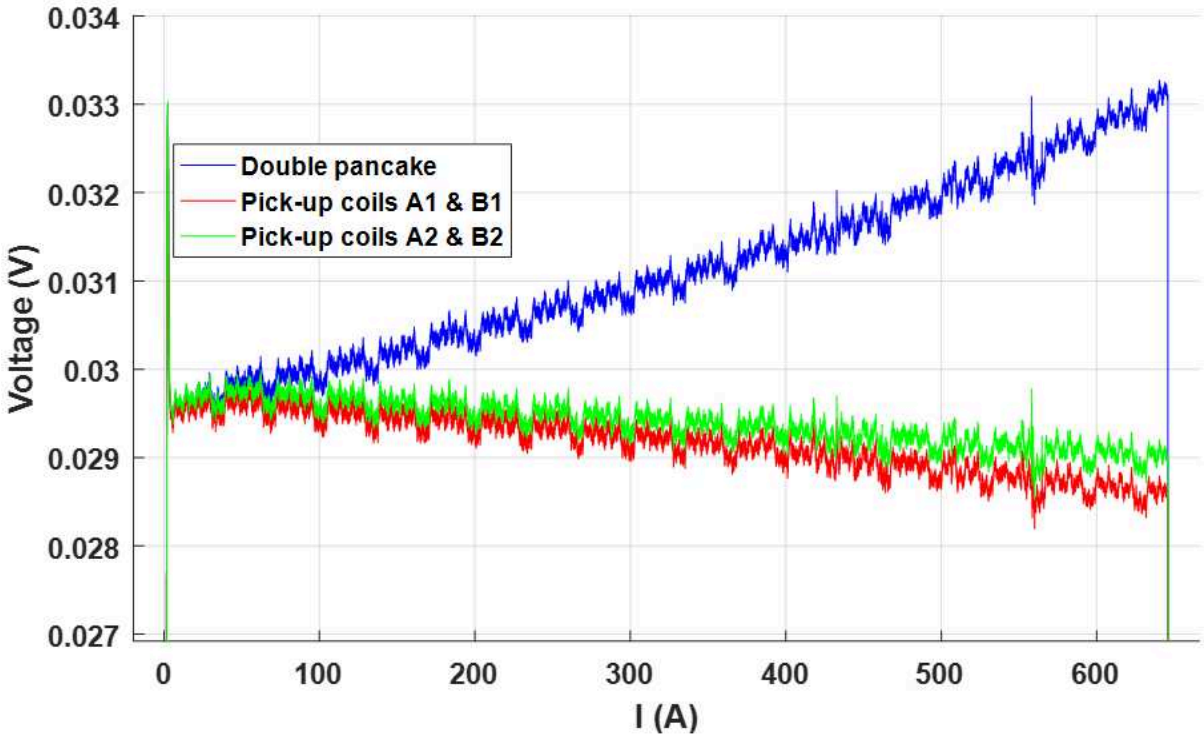


*Figure 135: Non-compensated filtered voltages of the double pancake (prototype n°4) and its pick up coils during a current ramp at 1 A/s.*

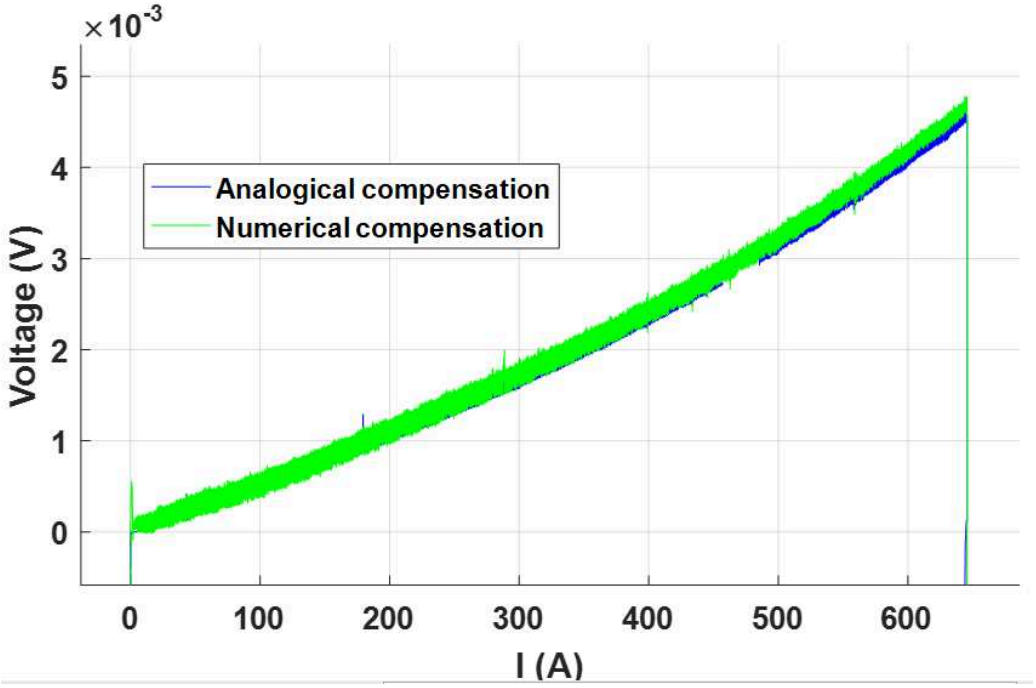


*Figure 136: Comparison between the compensated voltages of a current ramp obtained either by an analogical implementation or by a numerical weighted sum of the signals shown in Fig. 138.*

During the experiments, the compensation of the inductive voltage has been achieved by the mean of an analogical implementation (see Fig. 105 or 107). It is also possible to achieve the compensation of the inductive voltage by a numerical combination, with the same equation than the one used for analogical compensation (see eq. 72 or 92), of the filtered non-compensated signals. We can see in

Fig. 136 that the same result is obtained with both methods. The fact that we can obtain the same signals with two different methods participates to prove the reliability of the presented results.

It has to be noted that the processing of the non-compensated signals by a sliding mean value filter with a large window would add some delay to the detection of a transition if it was used in real time, i.e. during the experiment.

#### 7.2.3.5. Interpretation of the observed transitions

According to the data presented in Fig. 10.b. and based on a field distribution calculated for a homogeneous current density in the windings, the critical current in self field of the prototypes 1 to 4 should be respectively around 800 A, 2100 A, 950 A and 1550. In our tests, all the observed transitions occurred at currents which were much lower than the expected values (See table 18). Several explanations can be given

The first one is that the tape had been damaged during the winding process. It was obviously the case for the prototype n°1, but it seems unlikely for other prototypes. Another explanation is that the lift factor of the conductor was not the same in the case of the prototypes and for the samples used to obtain the data of Fig. 10.b. This can be a partial explanation of the problem. Some tests at 4.2 K on short samples taken at the beginning of unit lengths used to wind pancakes have shown performances 25 % lower in transverse field than what is shown in Fig. 10.b. This is a significant difference, but is not sufficient to explain the major difference between the expectations and the obtained results.

Another explanation can come from the effect of the inhomogeneity of the conductor (see part I-1.3.4 and II-3.1.1.3.1) [BRRM00] but data is missing about the statistics of the homogeneity at 4.2 K to quantify the influence of inhomogeneity on the global critical current.

| Prototype n° | 1 | 2 | 3 | 4 |
|---|---|---|---|---|
| Expected $I_C$ in self-field (A) | 800 | 2100 | 950 | 1550 |
| Current at which a transition has been observed in self-field and corresponding current ramp rate | 250 A (1 A/s) | 980 A (1 A/s) | 560 A (1 A/s) | 746 A or 971 A (1 A/s) (0.2 A/s) |

*Table 18: Comparison between the expected critical current and the current at which transitions have been observed, in self-field and for the 4 prototypes.*

In the case of the prototype n°3, it clearly seems that mistakes have been done on the interpretation of the observed transitions. As we have seen in part III-3.2.3.1.2, the voltage rises when the current overtakes the maximum current which has been reached in the previous current ramps. During the tests performed on this prototype, several of the observed transitions could be related to this phenomenon. As we can see in Fig. 132 and table 17, the first current ramp reached 480 A, without transition. At the second current ramp, a discharge had been triggered at 486 A because a transition was visible. The other transitions are also likely due, at least partially, to the same phenomenon. Nevertheless, in the transition of the current ramps n°12, the apparent inductance largely overtakes the apparent inductance of the current ramp n°1, which is not the case in the phenomenon described in part III-3.2.3.1.2. It therefore seems that another phenomenon plays a role. We can see in Fig. 130 and 132 that there is a second change in the dynamic of the voltage of the current ramp n°12 around 505 A, which makes it difficult to fit with a power law. It also explains why the n value calculated for current ramp n°12 is relatively higher than other ones. As the transition of the current ramp n°13 occurs at lower current than what have been reached in the current ramp n°12, it seems logical that this transition is not related to what is described in part III-3.2.3.1.2. It should also be the case for the transition of the current ramp n°14, but the curve of this transition strangely follows the curve of the ramp n°12.

In any case, it seems that the system was in an ambiguous situation during these tests. By the planning of the current ramps, such an ambiguity has been avoided in the tests of the prototype n°4. A transition has been observed at 746 A in self-field and at 618 A under a 6 T background field. These currents were reached with a current ramp rate of 1 A/s. According to the results of the simulations of B. Rozier [RBRM00], these transitions are related to dissipation due to magnetization losses, but their influence by the ramp rate and the vicinity of the critical current requires further investigation. Moreover, her model does not take into account the evolution of the temperature, which may play a significant role in these transitions.
Another test in self–field of the prototype n°4 has been performed later by A. Badel and A. J. Vialle. The current ramp rate was purposely reduced to 0.2 A/s. In these conditions, a transition occurred around 971 A instead of 746 A for a rate of 1 A/s. This additional test tends to confirm that the fact that a transition of the voltage occurs is related both to the value of the current and to the ramp rate. The dissipation and the voltage transitions can therefore not be predicted by a simple power law (see part I-1.1.3) or by a magneto static description of the problem.

# 8. Conclusion

The chapter III is dedicated to the experimental work. The experimental set-up is presented. A special attention is paid to the implementation of the analogical compensation of inductive voltage. The principle of the compensation of inductive voltage caused by two independent sources (current source and background B field) is described and the associated equations are given. This compensation principle has proven to be very effective during our tests. Nevertheless, it is not perfect and is influenced by the drift of the current in the width of the tape as well as the deformation of the pancake during the charge.

Prototype pancakes have been manufactured and tested. The first prototypes were degraded and had low performance, which is why the manufacturing process has significantly evolved over the time of the project. The different manufacturing processes are presented and discussed. The two last prototypes have shown electrical and mechanical performances satisfying enough to validate the design of the SMES and that a specific energy of 20 kJ/kg for the winding can be reached. It has been calculated that during a test of the third prototype, a hoop stress of 644 MPa (in average on the cross section of the bare conductor) has been reached at inner turn.

During the tests, it was possible, thanks to the inductive voltage compensation system, to observe steep transitions of the voltage signal. At least for some of them, it appears that these transitions are likely corresponding to a partial loss of the superconducting state. In these conditions, the discharge was triggered, ensuring the integrity of the pancake even with high curent density (980 A/mm$^2$).
The current at which a transition of the voltage was detected was depending on the current ramp rate. This value of current is therefore not the critical current of the pancake but depends on the dynamic of the charge of the system.

It has also been observed that the inductive voltage compensation was never perfect and that there was always a residual voltage whose value is proportional to the current ramp rate. For this reason, we decided to call this phenomenon “apparent inductance”, even if the observed residual voltage is not necessary due to an inductive phenomenon but can also be due to the dissipation of electrical power. Our interpretation is that the evolution of the apparent inductance is related to the gradual imbalance of the compensation during the charge of the pancake, but also depends on the magnetisation state and magnetisation losses. It also appeared that the value of the apparent inductance depends on the value of the external magnetic field, but we do not have satisfying explanation for this at this time.

# Final conclusion

## 1. General conclusion

This PhD has been dedicated to the BOSSE project, which has the challenging objective to beat the world record of specific energy for a superconducting winding. The design of the SMES is now achieved and the different tests performed on the prototypes pancakes have validated that the expected performance of the SMES, i.e. a specific energy of 20 kJ/kg for the winding, can be reached. The manufacturing of these pancakes has been highly instructive and improved our know-how about the winding of REBCO tapes.

A characteristic of the SMES of the BOSSE project is that the REBCO tapes are cooled at low temperature (4.2 K), but the magnetic field is only 12 T. Given the impressive performances of REBCO conductor, the current density in the bare conductor is very high (772 A/mm$^2$ for 880 A in the SMES). The protection of the SMES has therefore been an issue since the beginning of the project, all the more because the protection of REBCO windings is especially difficult. Our protection method is based on voltage measurement and a specific attention has been given to these measurement and about the noise reduction. The skills of our team on this topic has clearly progressed during this project.

A method, based on the use of two pick-up coils per pancake, has been developped to compensate the noise from both the current source and the background magnetic field during the tests of the prototype pancakes at the LNCMI Grenoble. This method has proven to be effective since transitions of the voltage, likely corresponding in some cases to a partial loss of the superconducting state, have been observed, even under noisy background magnetic field. In these cases, the discharge was triggered, ensuring the integrity of the pancake even with high curent density.

The measurements have shown to be sufficiently sensitive to observe the effects on the voltage of the AC losses and magnetisation of the pancakes.

## 2. Perspectives about the design of SMES

This work has been the opportunity to lead a global reflection on the design of SMES windings and on the compromise that has to be found between its different objectives (volume, mass, budget, etc…). Thanks to the equations presented in the chapter II, it is possible to quickly explore a wide domain of topological solutions, to evaluate the performances that can be achieved and to identify what are the advantages and drawbacks of the different topologies. We hope that the approach and reflexions presented in this manuscript can be useful for those who will have to develop a SMES, whatever are its purpose, its topology, its energy and the used superconductors. Some of the elements presented in this manuscript can be useful for the development of superconducting windings in general.

A special attention has been paid on the simple case of a solenoid with rectangular cross section and homogeneous current density. But the presented method and equations would be all the more interesting for more complex topologies described by more than two geometrical parameters. Some of the topologies presented in Part I-2.2.2 can offer intereting performances and should not be neglected solutions for an adanced project, even if they are more difficult to design and to develop.

In this manuscript, we did not developped our reflection about the use of nested windings (see part I-2.2.1.1.2). However, the spliting of a winding in several nested windings with different current densities and types of conductor is theoretically very interesting to optimize a SMES, in order to increase the specific energy and save some conductor. This concept does not only apply to solenoids but could be applied to toroids. Even if it was seen as uneasy to develop a solution based on nested

windings for the SMES of the BOSSE project, this kind of solution should be considered for the developpement of SMES with high energy. Of course, it increases the complexity of the optimisation since it increases the number of design parameters.
In the frame of this manuscript we focused on the optimization of a SMES windings. Nevertheless, in some cases, it could be interesting to design a SMES as a part of a supply chain which needs to be optimize as a whole. For example in the case of an electromagnetic launcher supplied by a SMES, the structure of the launcher and consequently its mass are related to the dynamic of the launch, which depends on the trade between the maximum current and stored energy of the SMES. The whole system should therefore be optimized as a whole in order to minimize its mass. The fast and simple approach we developed for the pre-design of SMES could be a starting point for such a task.
Another perspective to continue the reflexion about the design approach could be to try to integrate the effects of thermal contraction and mechanical anisotropy directly in the pre-design stage. It could be achieved thanks to analytical formulas for solenoids or by calculating the stress distribution thanks to a multiphysics simulation software for windings with more complex geometries.

# 3. Perspectives for experimental work

## 3.1. Evaluation and reduction of losses and magnetisation

During the experiments, it appeared that the influence of magnetisation and magnetisation losses on the observed voltage signal was more visible than what we initially expected. It seems necessary to improve the predictability and our understanding and this phenomenon. The electromagnetic calculation model developed by B. Rozier [RBRM00] can help us in this task. In order to validate this model, systematic tests should be performed on REBCO pancakes in varied conditions. In order to reduce the calculation time of the simulations, small size REBCO coils can be used. And in order to minimize the influence of eddy losses in these tests, REBCO coils without inner or outer copper contacts should be used. It appears clearly preferable to manufacture new REBCO coils dedicated to this work.
It has also been observed during the experiments that the current at which a transition of the voltage was detected was depending on the current ramp rate. This value of current was therefore not the critical current, but this conclusion is based only on a few observations. It would therefore be interesting to perform more systematic characterization in order to understand better this phenomenon, which is likely related to magnetisation losses but also to thermal considerations. These tests also offer the opportunity to verify if we are still able to protect the pancakes when we get closer of $I_C$ or if there is a high risk to locally burn the tapes because of a hotspot problem.
In a SMES which would be dedicated to pulse power or industrial applications, AC losses would be a major topic and the effect of magnetisation losses should be studied with care. Some solutions, such as striated conductor or transposed cables (See part I.3.5), have already been proposed to mitigate the problem of magnetisation losses in REBCO windings. These solutions can also be used to improve the operability of REBCO magnets (charging speed, field homogeneity…). The mastery and the development of models adapted to calculate the magnetisation losses in REBCO cables and their validation by experimental means is also a research axis for the development of REBCO SMES.

## 3.2. Reinforcement of winding and conductor

During the development of the prototype pancakes of the BOSSE project, we gave up the idea to prestress the pancake windings because of the poor results we obtained. Nevertheless, prestress can improve the mechanical strength of a superconducting winding and consequently its specific energy. It would therefore be interesting for our team to develop its knowhow about this technique. Reinforcement by external bracing should also be studied.
The reinforcement of the conductor is uneasy and of little interest in the case of the BOSSE project. But we have seen in part II-2.2.2 that when the energy of a SMES increases, the mechanical strength of the winding becomes the limiting factor against the current density to reach high specific energy. It can therefore be interesting to develop and test some reinforced REBCO cables if high energy REBCO SMES are considered

## 3.3. Detection of transitions and protection

A remaining task in the BOSSE project is to develop the protection system of the SMES, which principle is described in part II-3.4.4. The acquisition system and the compensation bridges have to be developed, as well as an algorithm able to detect a transition on one of the 21 acquisition channels. Ideally, this algorithm should be able to take into account the different effects on the voltage described in part III-3.2.3 in order to avoid false positive detections. But this is a very serious task and more likely during the tests of the SMES, the charge and discharge sequences will be adapted to avoid such false detections.
In this protection system, there are many compensation coils, one for each acquisition channel. The signals provided by these coils are proportional since they are proportional to the current variation of the SMES. In order to reduce the number of compensation coils, it could be interesting to explore solutions to duplicate with high fidelity the signal of one compensation coil by electronic or optoelectronic means (see part II-3.4.4.3). This approach is interesting for the protection of a high field magnet in which the volume of compensation coils would be a problem.
The compensation of inductive voltage by two pick-up coils has shown to be sensitive enough to see the effects of magnetisation on the voltage, even under noisy background field. It also made possible to protect the pancakes at high current density. Nevertheless, in this compensation system, it is not possible to differentiate the influence of magnetisation from the influence of the variation of inductance and couplings between the pancake and the compensation coils. The system could likely be improved by the use of a Rogowski coil instead of at least one pick-up coil.

# References


[ABFJ08] ALOTTO, P. ; BAUMGARTNER, U. ; FRESCHI, F. ; JAINDL, M. ; KOSTINGER, A. ; MAGELE, C. ; RENHART, W. ; REPETTO, M.: SMES Optimization Benchmark Extended: Introducing Pareto Optimal Solutions Into TEAM22. In: *IEEE Transactions on Magnetics* Bd. 44 (2008), Nr. 6, S. 1066–1069

[ABPH87] ABDELSALAM, M. ; BOOM, R. ; PETERSON, H. ; HELFRECHT, D. ; BRATLEY, W.: Operational aspects of superconductive magnetic energy storage (SMES). In: *IEEE Transactions on Magnetics* Bd. 23 (1987), Nr. 5, S. 3275–3277

[ACPV17] ARNAUD, A BADEL ; CICERON, J ; PASQUET, R ; VOISIN, E ; FOREST, F ; SCHNEIDER, M ; TIXADOR, P: Design of a Superconducting Self-Supplied Electromagnetic Launcher Proof of Concept Using HTS REBCO Conductor. In: *IEEE Transactions on Applied Superconductivity* Bd. 27 (2017), Nr. 4, S. 1–5

[Adva00] *Advanced conductor*. URL http://advancedconductor.com/

[AMBK07] AHMED, HAMID BEN ; MULTON, BERNARD ; BERNARD, NICOLAS ; KERZREHO, CORENTIN: Le stockage inertiel électromécanique. In: *revue 3EI* (2007), S. pp–18

[Amsc00] *AMSC*. URL https://www.amsc.com/

[Arp77] ARP, V: Stresses in superconducting solenoids. In: *Journal of Applied Physics* Bd. 48 (1977), Nr. 5, S. 2026–2036

[AVVS06] ANTONEVICI, ANCA ; VILLAUME, ALAIN ; VILLARD, CATHERINE ; SULPICE, ANDRÉ ; MARON, PIERRE BROSSE ; BOURGAULT, DANIEL ; PORCAR, LAURELINE: Coated conductors under tensile stress. In: *Journal of Physics: Conference Series*. Bd. 43 : IOP Publishing, 2006, S. 195

[AWOM17] AWAJI, SATOSHI ; WATANABE, KAZUO ; OGURO, HIDETOSHI ; MIYAZAKI, HIROSHI ; HANAI, SATOSHI ; TOSAKA, TAIZO ; IOKA, SHIGERU: First performance test of a 25 T cryogen-free superconducting magnet. In: *Superconductor Science and Technology* Bd. 30 (2017), Nr. 6, S. 065001

[BaCS57] BARDEEN, J. ; COOPER, L. N. ; SCHRIEFFER, J. R.: Theory of Superconductivity. In: *Physical Review* Bd. 108 (1957), Nr. 5, S. 1175–1204

[Bade10] BADEL, ARNAUD: Superconducting magnetic energy storage using high temperature superconductor for pulse power supply. In: *Doctor's Thesis, University of Grenoble* (2010)

[Ball13] BALLARINO, AMALIA: Development of Superconducting Links for the LHC Machine (2013), Nr. 4, S. 6

[BaMS15] BARTH, C ; MONDONICO, G ; SENATORE, C: Electro-mechanical properties of REBCO coated conductors from various industrial manufacturers at 77 K, self-field and 4.2 K, 19 T. In: *Superconductor Science and Technology* Bd. 28 (2015), Nr. 4, S. 045011

[Bart13] BARTH, CHRISTIAN: *High Temperature superconductor cable concepts for fusion magnets*. Bd. 7 : KIT Scientific Publishing, 2013

[BaTA11] BADEL, ARNAUD ; TIXADOR, PASCAL ; ARNIET, MICHEL: Optimized use of superconducting magnetic energy storage for electromagnetic rail launcher powering. In: *Superconductor Science and Technology* Bd. 25 (2011), Nr. 1, S. 014006

[BBWB13] BARTH, C ; BAGRETS, N ; WEISS, KP ; BAYER, CM ; BAST, T: Degradation free epoxy impregnation of REBCO coils and cables. In: *Superconductor Science and Technology* Bd. 26 (2013), Nr. 5, S. 055007

[BJRC18] BENKEL, T ; JACOLIN, X ; ROZIER, B ; CHAUD, X ; BADEL, A ; LÉCREVISSE, T ; FAZILLEAU, P ; TIXADOR, P: Characterization of HTS Insulated Coil for High Field Insert up to 19 T. In: *IEEE Transactions on Applied Superconductivity* Bd. 28 (2018), Nr. 3, S. 1–5

[BLSF17] BRINDZA, PAUL ; LASSITER, STEVEN ; SUN, ERIC ; FOWLER, MIKE ; FORREST, FREDERICK ; PORHEIL, AMAURY ; RAUMAGE, DAVID ; MALLARD, PIERRE-ERIC ; U. A.: Final Assembly and Factory Testing of the Jefferson Lab SHMS Spectrometer Quadrupole and Dipole Superconducting Magnets. In: *IEEE Transactions on Applied Superconductivity* Bd. 27 (2017), Nr. 4, S. 1–5

[BLTT11] BARZI, E ; LOMBARDO, V ; TOLLESTRUP, A ; TURRIONI, D: Study of effects of transverse deformation in BSCCO-2212 wires. In: *IEEE Transactions on Applied Superconductivity* Bd. 21 (2011), Nr. 3, S. 2808–2811

[BMCB17] BENKEL, TARA ; MIYOSHI, YASUYUKI ; CHAUD, XAVIER ; BADEL, ARNAUD ; TIXADOR, PASCAL: REBCO tape performance under high magnetic field. In: RAZEK, A. (Hrsg.) *The European Physical Journal Applied Physics* Bd. 79 (2017), Nr. 3, S. 30601

[Boui92] BOUILLARD, J.X.: *Preliminary investigation of force-reduced superconducting magnet configurations for advanced technology applications*, 1992

[BrRa96] BRAMMER, UWE ; RASCH, PETER: Optimization of ferromagnetic shields for solenoidal SMES. In: *IEEE transactions on magnetics* Bd. 32 (1996), Nr. 3, S. 1274–1277

[BRRM00] BADEL, ARNAUD ; ROZIER, BLANDINE ; RAMDANE, BRAHIM ; MEUNIER, GÉRARD ; TIXADOR, PASCAL: Modelling of “Quench” or the occurrence and propagation of Dissipative Zones in REBCO High Temperature Superconducting coils. In: *SUST* Bd. Submitted

[Bruk00] *Bruker*. URL https://www.bruker.com/products/superconductors-and-metal-composite-materials/superconductors/ybco-2g-hts-superconductors/overview.html

[BTAB12] BADEL, ARNAUD ; TIXADOR, PASCAL ; AMIET, MICHEL ; BROMMER, VOLKER: SMES to supply an electromagnetic launcher. In: *IEEE Transactions on Applied Superconductivity* Bd. 22 (2012), Nr. 3, S. 5700204–5700204

[CaCa97] CAMPBELL, AM ; CARDWELL, DA: Bulk high temperature superconductors for magnet applićations. In: *Cryogenics* Bd. 37 (1997), Nr. 10, S. 567–575

[CBTF17] CICERON, JEREMIE ; BADEL, ARNAUD ; TIXADOR, PASCAL ; FOREST, FREDERICK: Design Considerations for High-Energy Density SMES. In: *IEEE Transactions on Applied Superconductivity* Bd. 27 (2017), Nr. 4, S. 1–5

[CCKP15] CHOI, JU HUI ; CHOI, YOON HYUCK ; KANG, DONG-HYUNG ; PARK, YEONJOO ; SONG, JUNG-BIN ; HA, SUN-KYOUNG ; PARK, MINWON ; LEE, HAIGUN: Investigation of the key factors affecting the permanent damage of the REBCO coated conductor in overcurrent condition. In: *IEEE Transactions on Applied Superconductivity* Bd. 25 (2015), Nr. 3, S. 1–5

[ChJi14] CHEN, XIAO Y. ; JIN, JIAN X.: Evaluation of Step-Shaped Solenoidal Coils for Current-Enhanced SMES Applications. In: *IEEE Transactions on Applied Superconductivity* Bd. 24 (2014), Nr. 5, S. 1–4

[CiBT17] CICERON, JÉRÉMIE ; BADEL, ARNAUD ; TIXADOR, PASCAL: Superconducting magnetic energy storage and superconducting self-supplied electromagnetic launcher. In: *The European Physical Journal Applied Physics* Bd. 80 (2017), Nr. 2, S. 20901

[CJFX16] CHEN, XIAO YUAN ; JIN, JIAN XUN ; FENG, JUAN ; XU, QIANG ; TANG, MIAN GANG ; ZOU, HUI LIN: Performance Improvement of a Bi-2223 Solenoid Coil With Optimal Ferromagnetic Disks. In: *IEEE Transactions on Applied Superconductivity* Bd. 26 (2016), Nr. 7, S. 1–7

[CJXZ09] CHEN, XIAOYUAN ; JIN, JIANXUN ; XIN, YING ; ZHANG, JINGYIN: Design and optimization of HTS magnets for SMES applications. In: *2009 International Conference on Applied Superconductivity and Electromagnetic Devices*. Chengdu, China : IEEE, 2009 — ISBN 978-1-4244-3686-6, S. 26–29

[CoGn61] CORRUCCINI, ROBERT J ; GNIEWCK, JOHN J: Thermal expansion of technical solids at low temperatures: a compilation from the literature (1961)

[Cryo00] *CryoComp©*. URL http://www.eckelsengineering.com/

[CZCL18] CHEN, WEI ; ZHANG, HAIYANG ; CHEN, YONG ; LIU, LIYUAN ; SHI, JIANGTAO ; YANG, XINSHENG ; ZHAO, YONG: Fatigue Behavior of Critical Current Degradation for YBCO Tapes at 77 K. In: *IEEE Transactions on Applied Superconductivity* Bd. 28 (2018), Nr. 3, S. 1–5

[DAMD01] DECROUX, M ; ANTOGNAZZA, LOUIS ; MUSOLINO, NICOLAS ; DE CHAMBRIER, E ; REYMOND, S ; TRISCONE, J-M ; FISCHER, OYSTEIN ; PAUL, W ; U. A.: Properties of YBCO films at high current densities: Fault current limiter implications. In: *IEEE transactions on applied superconductivity* Bd. 11 (2001), Nr. 1, S. 2046–2049

[DBBT11] DEDIE, PHILIPP ; BROMMER, VOLKER ; BADEL, ARNAUD ; TIXADOR, PASCAL: Three-stage superconducting XRAM generator. In: *IEEE Transactions on Dielectrics and Electrical Insulation* Bd. 18 (2011), Nr. 4

[DeBS11] DEDIE, PHILIPP ; BROMMER, VOLKER ; SCHARNHOLZ, SIGO: Twenty-stage toroidal XRAM generator switched by countercurrent thyristors. In: *IEEE Transactions on Plasma Science* Bd. 39 (2011), Nr. 1, S. 263–267

[DETK15] DROZDOV, A. P. ; EREMETS, M. I. ; TROYAN, I. A. ; KSENOFONTOV, V. ; SHYLIN, S. I.: Conventional superconductivity at 203 kelvin at high pressures in the sulfur hydride system. In: *Nature* Bd. 525 (2015), Nr. 7567, S. 73–76

[DTZR15] DENG, X ; TANG, Y ; ZHANG, Y ; REN, L ; LIU, H ; GONG, Y ; LI, J: An experimental and numerical study on the inductance variation of HTS magnets. In: *IEEE Transactions on Applied Superconductivity* Bd. 25 (2015), Nr. 3, S. 1–5

[DZSC15] DIMITROV, IVO K. ; ZHANG, XIAO ; SOLOVYOV, VYACHESLAV F. ; CHUBAR, OLEG ; LI, QIANG: Rapid and Semi-analytical Design and Simulation of a Toroidal Magnet Made With YBCO and $MgB_2$ Superconductors. In: *IEEE Transactions on Applied Superconductivity* Bd. 25 (2015), Nr. 5, S. 1–8

[ESBM16] ESCAMEZ, GUILLAUME ; SIROIS, FRÉDÉRIC ; BADEL, ARNAUD ; MEUNIER, GÉRARD ; RAMDANE, BRAHIM ; TIXADOR, PASCAL: Numerical Impact of Using Different E (J) Relationships for 3-D Simulations of AC Losses in MgB2 Superconducting Wires. In: *IEEE Transactions on Magnetics* Bd. 52 (2016), Nr. 3, S. 1–4

[Esca16] ESCAMEZ, GUILLAUME: *AC losses in superconductors: a multi-scale approach for the design of high current cables*, Université Grenoble Alpes, 2016

[EyBo81] EYSSA, Y. ; BOOM, R.: Considerations of a large force balanced magnetic energy storage system. In: *IEEE Transactions on Magnetics* Bd. 17 (1981), Nr. 1, S. 460–462

[FANS03] FABBRI, M. ; AJIKI, D. ; NEGRINI, F. ; SHIMADA, R. ; TSUTSUI, H. ; VENTURI, F.: Tilted toroidal coils for superconducting magnetic energy storage systems. In: *IEEE Transactions on Magnetics* Bd. 39 (2003), Nr. 6, S. 3546–3550

[Fast00] *FastGrid*. URL https://www.fastgrid-h2020.eu/

[FBBD12] FAZILLEAU, P ; BERRIAUD, C ; BERTHIER, R ; DEBRAY, F ; HERVIEU, B ; JOSS, W ; JUSTER, FP ; MASSINGER, M ; U. A.: Final design of the new Grenoble hybrid magnet. In: *IEEE Transactions on Applied Superconductivity* Bd. 22 (2012), Nr. 3, S. 4300904–4300904

[FBCD18] FAZILLEAU, PHILIPPE ; BORGNIC, BENJAMIN ; CHAUD, XAVIER ; DEBRAY, FRANÇOIS ; LÉCREVISSE, THIBAULT ; SONG, JUNG-BIN: Metal-as-insulation sub-scale prototype tests under a high background magnetic field. In: *Superconductor Science and Technology* Bd. 31 (2018), Nr. 9, S. 095003

[Ferr69] FERRIER, M: Energy storage in a superconducting winding. In: *Low temperatures and electric power* (1969), S. 425–432

[FlBa00] FLEITER, J ; BALLARINO, A: Parameterization of the critical surface of REBCO conductors from Fujikura, S. 9

[Flei13] FLEITER, JEROME: *Étude de l'implémentation de supraconducteurs à haute température critique dans les aimants d'accélérateur*, Université de Grenoble, PhD Thesis, 2013

[Flux00] *Flux®*. URL https://altairhyperworks.com/product/flux

[Fu13] FU, SHAO-YUN: Cryogenic Properties of Polymer Materials. In: *Polymers at cryogenic temperatures* : Springer, 2013, S. 9–39

[Fuji00] *Fujikura*. URL https://www.fujikura.co.uk

[GAJH16] GUPTA, RAMESH ; ANERELLA, M ; JOSHI, P ; HIGGINS, J ; LALITHA, S ; SAMPSON, W ; SCHMALZLE, J ; WANDERER, P: Design, construction, and testing of a large-aperture high-field HTS SMES coil. In: *IEEE Transactions on Applied Superconductivity* Bd. 26 (2016), Nr. 4, S. 1–8

[GJKB06] GEHRING, R. ; JUENGST, K.-P. ; KUPERMAN, G. ; BORDRY, F. ; BURNET, J.-P. ; VOELKER, F.: A SMES-Based Power Supply for Accelerator Magnets. In: *IEEE Transactions on Applied Superconductivity* Bd. 16 (2006), Nr. 2, S. 594–597

[Good01] GOODZEIT, CARL L: Superconducting accelerator magnets. In: *USPAS, January* (2001)

[GySG18] GYURÁKI, ROLAND ; SIROIS, FRÉDÉRIC ; GRILLI, FRANCESCO: High-speed fluorescent thermal imaging of quench propagation in high temperature superconductor tapes. In: *Superconductor Science and Technology* Bd. 31 (2018), Nr. 3, S. 034003

[Hass83] HASSENZAHL, WILLIAM V: Superconducting magnetic energy storage. In: *Proceedings of the IEEE* Bd. 71 (1983), Nr. 9, S. 1089–1098

[Hass89] HASSENZAHL, W: A comparison of the conductor requirements for energy storage devices made with ideal coil geometries. In: *IEEE Transactions on Magnetics* Bd. 25 (1989), Nr. 2, S. 1799–1802

[Hfls00] *HFLSM*. URL http://www.hflsm.imr.tohoku.ac.jp/cgi-bin/index-e.cgi

[High00] *High Performance Polymer Inc.* URL http://www.hppolymer.com/

[Himb16] HIMBELE, JOHN: *HTS Dipole Insert using a Twisted Stacked Cable for a Particle Accelerator*, Université Grenoble Alpes, 2016

[HKIK14] HIGASHIKAWA, KOHEI ; KATAHIRA, KENTA ; INOUE, MASAYOSHI ; KISS, TAKANOBU ; SHINGAI, YUKI ; KONISHI, MASAYA ; OHMATSU, KAZUYA ; MACHI, TAKATO ; U. A.: Nondestructive Diagnostics of Narrow Coated Conductors for Electric Power Applications. In: *IEEE Transactions on Applied Superconductivity* Bd. 24 (2014), Nr. 3, S. 1–4

[HLIO02] HAID, BENJAMIN J ; LEE, HAIGUN ; IWASA, YUKIKAZU ; OH, SANG-SOO ; KWON, YOUNG-KIL ; RYU, KANG-SIK: A “permanent” high-temperature superconducting magnet operated in thermal communication with a mass of solid nitrogen. In: *Cryogenics* Bd. 42 (2002), Nr. 3–4, S. 229–244

[HNSH07] HIGASHIKAWA, KOHEI ; NAKAMURA, TAKETSUNE ; SHIKIMACHI, KOJI ; HIRANO, NAOKI ; NAGAYA, SHIGEO ; KISS, TAKANOBU ; INOUE, MASAYOSHI: Conceptual Design of HTS Coil for SMES Using YBCO Coated Conductor. In: *IEEE Transactions on Applied Superconductivity* Bd. 17 (2007), Nr. 2, S. 1990–1993

[HPBI11] HAHN, SEUNGYONG ; PARK, DONG KEUN ; BASCUÑÁN, JUAN ; IWASA, YUKIKAZU: HTS pancake coils without turn-to-turn insulation. In: *IEEE Trans. Appl. Supercond.* Bd. 21 (2011), Nr. 3, S. 1592–1595

[HSHW99] HAMAJIMA, T. ; SHIMADA, M. ; HANAI, S. ; WACHI, Y. ; TEZUKA, M. ; TAKANO, H.: SMES coil configurations with reduced stray field. In: *IEEE Transactions on Appiled Superconductivity* Bd. 9 (1999), Nr. 2, S. 346–349

[HTIW17] HANAI, SATOSHI ; TSUCHIHASHI, TAKAHIRO ; IOKA, SHIGERU ; WATANABE, KAZUO ; AWAJI, SATOSHI ; OGURO, HIDETOSHI: Development of an 11 T BSCCO insert coil for a 25 T cryogen-free superconducting magnet. In: *IEEE Transactions on Applied Superconductivity* Bd. 27 (2017), Nr. 4, S. 1–6

[Htsm00] *HTS modelling workgroup*. URL http://www.htsmodelling.com/

[HYHM17] HOSONO, HIDEO ; YAMAMOTO, AKIYASU ; HIRAMATSU, HIDENORI ; MA, YANWEI: Recent advances in iron-based superconductors toward applications. In: *Materials today* (2017)

[Hype00] *Hyper Tech Research*. URL http://www.hypertechresearch.com/

[IKIF17] IIJIMA, YASUHIRO ; KAKIMOTO, K ; IGARASHI, M ; FUJITA, S ; HIRATA, W ; MUTO, S ; YOSHIDA, T ; ADACHI, Y ; U. A.: BMO-Doped REBCO-Coated Conductors for Uniform In-Field Ic by Hot-Wall PLD Process Using IBAD Template. In: *IEEE Transactions on Applied Superconductivity* Bd. 27 (2017), Nr. 4, S. 1–4

[Iwas09] IWASA, YUKIKAZU: *Case studies in superconducting magnets: design and operational issues* : Springer Science & Business Media, 2009

[JFAM16] JIANG, JIANYI ; FRANCIS, ASHLEIGH ; ALICEA, RYAN ; MATRAS, MAXIME ; KAMETANI, FUMITAKE ; TROCIEWITZ, ULF P ; HELLSTROM, ERIC E ; LARBALESTIER, DAVID C: Effects of filament size on critical current density in overpressure processed Bi-2212 round wire. In: *IEEE Transactions on Applied Superconductivity* Bd. 27 (2016), Nr. 4, S. 1–4

[JGKK02] JUENGST, K.-P. ; GEHRING, R. ; KUDYMOW, A. ; KUPERMAN, G. ; SUESS, E.: 25 MW SMES-based power modulator. In: *IEEE Transactions on Appiled Superconductivity* Bd. 12 (2002), Nr. 1, S. 758–761

[JGKP02] JUENGST, K.-P. ; GEHRING, R. ; KUDYMOW, A. ; PFISTERER, H.-J. ; SUESS, E.: SMES compensator with a toroidal magnet system. In: *IEEE Transactions on Appiled Superconductivity* Bd. 12 (2002), Nr. 1, S. 754–757

[KIHS16] KISS, TAKANOBU ; INOUE, MASAYOSHI ; HIGASHIKAWA, KOHEI ; SUZUKI, TAKUMI ; LYU, LIN ; TAKASAKI, KEN ; IMAMURA, KAZUTAKA ; ONODERA, YUTA ; U. A.: Comparison between Bi-2223 tape and RE-123 coated conductor from the view point of current transport properties influencing thermal stability. In: *Cryogenics* Bd. 80 (2016), S. 221–228

[KKLC06] KIM, W.-S. ; KWAK, S.-Y. ; LEE, J.-K. ; CHOI, K.-D. ; JUNG, H.-K. ; SEONG, K.-C. ; HAHN, S.: Design of HTS Magnets for a 600 kJ SMES. In: *IEEE Transactions on Applied Superconductivity* Bd. 16 (2006), Nr. 2, S. 620–623

[KLJH12] KANDEL, HOM ; LU, JUN ; JIANG, JIANYI ; HAN, KE ; GUNDLACH, SCOTT ; VIOUCHKOV, YOURI ; MARKIEWICZ, WILLIAM DENIS ; WEIJERS, HUBERTUS: Sol-gel-Derived Al203-Si02 Composite Coating for Electrical Insulation in HTS Magnet Technology. In: *IEEE Transactions on Applied Superconductivity* Bd. 22 (2012), Nr. 5, S. 7701605–7701605

[Laan09] VAN DER LAAN, DANIEL C: YBa2Cu3O7- δ coated conductor cabling for low ac-loss and high-field magnet applications. In: *Superconductor Science and Technology* Bd. 22 (2009), Nr. 6, S. 065013

[LCSD13] LANGESLAG, SAE ; CURE, B ; SGOBBA, S ; DUDAREV, A ; TEN KATE, HHJ: Characterization of a large size co-extruded Al-Ni stabilized Nb-Ti superconducting cable for future detector magnets. In: *IEEE Transactions on Applied Superconductivity* Bd. 23 (2013), Nr. 3, S. 4500504–4500504

[LéBD18] LÉVÊQUE, JEAN ; BERGER, KÉVIN ; DOUINE, BRUNO: *Superconducting Motors and Generators* : Nova Science Publishers, 2018

[Lecr12] LECREVISSE, THIBAULT: *Contribution à l'étude des aimants supraconducteurs utilisant des matériaux supraconducteurs à haute température de transition*, Université de Grenoble, PhD Thesis, 2012

[LéIw16] LÉCREVISSE, THIBAULT ; IWASA, YUKIKAZU: A (RE) BCO pancake winding with metal-as-insulation. In: *IEEE Transactions on Applied Superconductivity* Bd. 26 (2016), Nr. 3, S. 1–5

[Lieb17] LIEBFRIED, OLIVER: Review of inductive pulsed power generators for railguns. In: *IEEE Transactions on Plasma Science* Bd. 45 (2017), Nr. 7, S. 1108–1114

[Lieu97] LIEURANCE, D.W.: Global cost optimization of 1-10 MWh toroidal SMES. In: *IEEE Transactions on Appiled Superconductivity* Bd. 7 (1997), Nr. 1, S. 14–17

[LJTK14] LARBALESTIER, DAVID C ; JIANG, J ; TROCIEWITZ, UP AL ; KAMETANI, F ; SCHEUERLEIN, C ; DALBAN-CANASSY, M ; MATRAS, M ; CHEN, P ; U. A.: Isotropic round-wire multifilament cuprate superconductor for generation of magnetic fields above 30 T. In: *Nature materials* Bd. 13 (2014), Nr. 4, S. 375

[LKHS12] LU, J ; KANDEL, H ; HAN, K ; SHEPPARD, WR ; MCRAE, DM ; VORAN, A ; PICKARD, KW ; GODDARD, RE ; U. A.: Insulation of coated conductors for high field magnet applications. In: *IEEE Transactions on Applied Superconductivity* Bd. 22 (2012), Nr. 3, S. 7700304–7700304

[Lncm00] *LNCMI Grenoble*. URL http://lncmi-g.grenoble.cnrs.fr/

[Luon96] LUONGO, C.A.: Superconducting storage systems: an overview. In: *IEEE Transactions on Magnetics* Bd. 32 (1996), Nr. 4, S. 2214–2223

[MaGo17] MARCHEVSKY, M ; GOURLAY, SA: Acoustic thermometry for detecting quenches in superconducting coils and conductor stacks. In: *Applied Physics Letters* Bd. 110 (2017), Nr. 1, S. 012601

[MaPV12] MAZURENKO, IRYNA ; PAVLYUK, ANDRIY ; VASETSKY, YURIY: Parameters of superconducting magnets with racetrack-shaped coils and support structure placed inside torus. In: *Przegląd Elektrotechniczny* Bd. 88 (2012), Nr. 3a, S. 67–69

[MBCB15] MIYOSHI, YASUYUKI ; BADEL, ARNAUD ; CHAUD, XAVIER ; BENKEL, TARA ; VINCENT, BENJAMIN ; TIXADOR, PASCAL ; MARPAUD, JULIEN ; DEBRAY, FRANÇOIS ; U. A.: Performance tests of prototype high-field HTS coils in Grenoble. In: *IEEE Transactions on Applied Superconductivity* Bd. 25 (2015), Nr. 3, S. 1–5

[MbSc08] MBARUKU, ABDALLAH L ; SCHWARTZ, JUSTIN: Fatigue behavior of Y–Ba–Cu–O/Hastelloy-C coated conductor at 77 K. In: *IEEE Transactions on Applied Superconductivity* Bd. 18 (2008), Nr. 3, S. 1743–1752

[MBTL07] MASSON, PHILIPPE J ; BRESCHI, MARCO ; TIXADOR, PASCAL ; LUONGO, CESAR A: Design of HTS axial flux motor for aircraft propulsion. In: *IEEE Transactions on Applied Superconductivity* Bd. 17 (2007), Nr. 2, S. 1533–1536

[Mgb215] MgB2 – An Intermediate-Temperature Superconductor. In: *Physical Properties of High-Temperature Superconductors* : Wiley-Blackwell, 2015 — ISBN 978-1-118-69664-4, S. 423–458

[MiMC16] MIKI, S ; MARSILI, F ; CASABURI, A: Recent research trends for superconducting detectors. In: *Superconductor Science and Technology* Bd. 29 (2016), Nr. 5

[MISB18] MANOLOPOULOS, CHARALAMPOS D ; IACCHETTI, MATTEO F ; SMITH, ALEXANDER C ; BERGER, KÉVIN ; HUSBAND, MARK ; MILLER, PAUL: Stator Design and Performance of Superconducting Motors for Aerospace Electric Propulsion Systems. In: *IEEE Transactions on Applied Superconductivity* Bd. 28 (2018), Nr. 4, S. 1–5

[MITT14] MIYAZAKI, HIROSHI ; IWAI, SADANORI ; TOSAKA, TAIZO ; TASAKI, KENJI ; ISHII, YUSUKE: Degradation-free impregnated YBCO pancake coils by decreasing radial stress in the windings and method for evaluating delamination strength of YBCO-coated conductors. In: *IEEE Transactions on Applied Superconductivity* Bd. 24 (2014), Nr. 3, S. 1–5

[MLWV12] MARKIEWICZ, W. D. ; LARBALESTIER, D. C. ; WEIJERS, H. W. ; VORAN, A. J. ; PICKARD, K. W. ; SHEPPARD, W. R. ; JAROSZYNSKI, J. ; AIXIA XU ; U. A.: Design of a Superconducting 32 T Magnet With REBCO High Field Coils. In: *IEEE Transactions on Applied Superconductivity* Bd. 22 (2012), Nr. 3, S. 4300704–4300704

[MoHF11] MOGHADASI, AMIR HASSAN ; HEYDARI, HOSSEIN ; FARHADI, MUSTAFA: Pareto Optimality for the Design of SMES Solenoid Coils Verified by Magnetic Field Analysis. In: *IEEE Transactions on Applied Superconductivity* Bd. 21 (2011), Nr. 1, S. 13–20

[Moon82] MOON, FRANCIS C: The virial theorem and scaling laws for superconducting magnet systems. In: *Journal of Applied Physics* Bd. 53 (1982), Nr. 12, S. 9112–9121

[MoWe69] MONTGOMERY, DONALD BRUCE ; WEGGEL, ROBERT J: *Solenoid magnet design: the magnetic and mechanical aspects of resistive and superconducting systems* : Wiley-Interscience, 1969

[Murg88] MURGATROYD, PN: Optimal designs for multilayer air-cored toroidal inductors with circular windows. In: *IEE Proceedings B-Electric Power Applications*. Bd. 135 : IET, 1988, S. 202–209

[Murg89] MURGATROYD, PAUL N: The optimal form for coreless inductors. In: *IEEE Transactions on Magnetics* Bd. 25 (1989), Nr. 3, S. 2670–2677

[Nasa88] NASA: *Lunar Base Applications of Superconductivity*, 1988

[NCTS13] NOMURA, S. ; CHIKARAICHI, H. ; TSUTSUI, H. ; SHIMADA, R.: Feasibility Study on Large Scale SMES for Daily Load Leveling Using Force-Balanced Helical Coils. In: *IEEE Transactions on Applied Superconductivity* Bd. 23 (2013), Nr. 3, S. 5700904–5700904

[NHKT04] NAGAYA, S. ; HIRANO, N. ; KONDO, M. ; TANAKA, T. ; NAKABAYASHI, H. ; SHIKIMACHI, K. ; HANAI, S. ; INAGAKI, J. ; U. A.: Development and Performance Results of 5 MVA SMES for Bridging Instantaneous Voltage Dips. In: *IEEE Transactions on Appiled Superconductivity* Bd. 14 (2004), Nr. 2, S. 699–704

[Nhmf00] *NHMFL*. URL https://nationalmaglab.org/

[NOKT99] NOMURA, S. ; OSAKI, T. ; KONDOH, J. ; TSUTSUI, H. ; TSUJI-IIO, S. ; SATO, Y. ; SHIMADA, R.: Force-balanced coil for large scale SMES. In: *IEEE Transactions on Appiled Superconductivity* Bd. 9 (1999), Nr. 2, S. 354–357

[NoTs17] NOMURA, SHINICHI ; TSUTSUI, HIROAKI: Structural Limitations of Energy Storage Systems Based on the Virial Theorem. In: *IEEE Transactions on Applied Superconductivity* Bd. 27 (2017), Nr. 4, S. 1–6

[NoYI02] NOGUCHI, S. ; YAMASHITA, H. ; ISHIYAMA, A.: An optimal design method for SMES coils using HTS tapes. In: *IEEE Transactions on Appiled Superconductivity* Bd. 12 (2002), Nr. 1, S. 1459–1462

[NZHH12] NIELSEN, GUNVER ; ZANGENBERG, NIKOLAJ ; HAZELTON, DREW ; HAUGE, NILS ; NIELSEN, BJARNE ROGER ; MØLLER, SØREN PAPE ; BAURICHTER, ARND: Dipole magnet from high Tc superconductor. In: *Physics Procedia* Bd. 36 (2012), S. 824–829

[ObPu14] OBRADORS, XAVIER ; PUIG, TERESA: Coated conductors for power applications: materials challenges. In: *Superconductor Science and Technology* Bd. 27 (2014), Nr. 4, S. 044003

[OgNT13] OGA, Y. ; NOGUCHI, S. ; TSUDA, M.: Comparison of Optimal Configuration of SMES Magnet Wound With $\hbox{MgB}_{2}$ and YBCO Conductors. In: *IEEE Transactions on Applied Superconductivity* Bd. 23 (2013), Nr. 3, S. 5700204–5700204

[Pasq15] PASQUET, RAPHAEL: *Contribution au développement des aimants supraconducteurs MgB2 R & W refroidis par conduction solide.*, Université Pierre et Marie Curie - Paris VI, 2015

[PLOL14] PARK, YJ ; LEE, MW ; OH, YK ; LEE, HG: Laser drilling: enhancing superconducting joint of GdBa2Cu3O7- δ coated conductors. In: *Superconductor Science and Technology* Bd. 27 (2014), Nr. 8, S. 085008

[Poli11] POLINDER, HENK: Overview of and trends in wind turbine generator systems. In: *Power and Energy Society General Meeting, 2011 IEEE* : IEEE, 2011, S. 1–8

[PPAK99] POLULYAKH, EP ; PLOTNIKOVA, LA ; AFANAS' EV, VA ; KHARINOV, MI ; KONDRATENCO, AK ; KLIMENCO, E YU ; NOVICOV, VI: Development of toroidal superconducting magnetic energy storages (SMES) for high-current pulsed power supplies. In: *Pulsed Power Conference, 1999. Digest of Technical Papers. 12th IEEE International*. Bd. 2 : IEEE, 1999, S. 1129–1132

[Rade09] RADEBAUGH, RAY: Cryocoolers: the state of the art and recent developments. In: *Journal of Physics: Condensed Matter* Bd. 21 (2009), Nr. 16, S. 164219

[RBBB15] ROSSI, L ; BADEL, A ; BAJKO, M ; BALLARINO, A ; BOTTURA, L ; DHALLE, MARC MJ ; DURANTE, M ; FAZILLEAU, PH ; U. A.: The EuCARD-2 future magnets European collaboration for accelerator-quality HTS magnets. In: *IEEE transactions on applied superconductivity* Bd. 25 (2015), Nr. 3, S. 1–7

[RBBC79] ROGERS, J ; BOENIG, H ; BRONSON, J ; COLYER, D ; HASSENZAHL, W ; TURNER, R ; SCHERMER, R: 30-MJ superconducting magnetic energy storage (SMES) unit for stabilizing an electric transmission system. In: *IEEE Transactions on Magnetics* Bd. 15 (1979), Nr. 1, S. 820–823

[RBBC83] ROGERS, J. ; BARRON, M. ; BOENIG, H. ; CRISCUOLO, A. ; DEAN, J. ; SCHERMER, R.: Superconducting magnetic energy storage for BPA transmission line stabilization. In: *IEEE Transactions on Magnetics* Bd. 19 (1983), Nr. 3, S. 1078–1080

[RBCD11] REY, J-M ; BRUCHON, M ; CHAUD, X ; DEBRAY, F ; LECREVISSE, THIBAULT ; MOSSANG, ERIC ; TIXADOR, PASCAL: Geometry optimization for SMES solenoids using HTS ribbons. In: *IEEE Transactions on Applied Superconductivity* Bd. 21 (2011), Nr. 3, S. 1670–1673

[RBMM16] RADOVINSKY, ALEXEY L. ; BROMBERG, LESLIE ; MINERVINI, JOSEPH V. ; MICHAEL, PHILIP C. ; SERVAIS, THOMAS ; FORTON, ERIC ; PEARSON, EMMA: Constant Field Toroidal SMES Magnet. In: *IEEE Transactions on Applied Superconductivity* Bd. 26 (2016), Nr. 3, S. 1–4

[RBRM00] ROZIER, BLANDINE ; BADEL, ARNAUD ; RAMDANE, BRAHIM ; MEUNIER, GÉRARD: Calculation of the local current density in HTS insulated REBCO coils using a Volume Integral Formulation and its contribution to coils protection. In: *SUST* Bd. Submitted

[Rode05] RODE, CLAUS H: Large superconducting radio frequency construction projects. In: *IEEE transactions on applied superconductivity* Bd. 15 (2005), Nr. 2, S. 2389–2392

[RuZC15] RUIZ, HAROLD STEVEN ; ZHANG, X ; COOMBS, TA: Resistive-type superconducting fault current limiters: concepts, materials, and numerical modeling. In: *IEEE Transactions on Applied Superconductivity* Bd. 25 (2015), Nr. 3, S. 1–5

[SaGN13] SANDER, M. ; GEHRING, R. ; NEUMANN, H.: LIQHYSMES—A 48 GJ Toroidal MgB2-SMES for Buffering Minute and Second Fluctuations. In: *IEEE Transactions on Applied Superconductivity* Bd. 23 (2013), Nr. 3, S. 5700505–5700505

[SALT14] SENATORE, CARMINE ; ALESSANDRINI, MATTEO ; LUCARELLI, ANDREA ; TEDIOSI, RICCARDO ; UGLIETTI, DAVIDE ; IWASA, YUKIKAZU: Progresses and challenges in the development of high-field solenoidal magnets based on RE123 coated conductors. In: *Superconductor Science and Technology* Bd. 27 (2014), Nr. 10, S. 103001

[SBBB15] SUGANO, MICHINAKA ; BALLARINO, AMALIA ; BARTOVA, BARBORA ; BJOERSTAD, ROGER ; GERARDIN, ALEXANDRE ; SCHEUERLEIN, CHRISTIAN: Evaluation of Young's modulus of MgB2 filaments in composite wires for the superconducting links for the high-luminosity LHC upgrade. In: *Superconductor Science and Technology* Bd. 29 (2015), Nr. 2, S. 025009

[SBBK16] SENATORE, CARMINE ; BARTH, CHRISTIAN ; BONURA, MARCO ; KULICH, MILOSLAV ; MONDONICO, GIORGIO: Field and temperature scaling of the critical current density in commercial REBCO coated conductors. In: *Superconductor Science and Technology* Bd. 29 (2016), Nr. 1, S. 014002

[ScAl00] SCHMIDT, F ; ALLAIS, A: SUPERCONDUCTING CABLES FOR POWER TRANSMISSION APPLICATIONS – A REVIEW, S. 6

[ScHa03] SCHOENUNG, SUSAN M. ; HASSENZAHL, WILLIAM V.: *Long- vs. short-term energy storage technologies analysis : a life-cycle cost study : a study for the DOE energy storage systems program.*, 2003

[Sena14] SENATORE, CARMINE: Tape performance summary from worldwide producers.

[SIFS16] SCURTI, F ; ISHMAEL, S ; FLANAGAN, G ; SCHWARTZ, J: Quench detection for high temperature superconductor magnets: a novel technique based on Rayleigh-backscattering interrogated optical fibers. In: *Superconductor Science and Technology* Bd. 29 (2016), Nr. 3, S. 03LT01

[Sigm00] *SigmaPhi*. URL https://www.sigmaphi.fr/

[SMFS92] SHIGEMATSU, T ; MORITA, K ; FUJII, Y ; SHIGI, T ; NAKAMURA, M ; YAMAGUCHI, M: Investigation of annealing effects of ultra pure copper. In: *Cryogenics* Bd. 32 (1992), Nr. 10, S. 913–915

[SMNH14] STEMMLE, MARK ; MERSCHEL, FRANK ; NOE, MATHIAS ; HOBL, ACHIM: AmpaCity 2014; Advanced superconducting medium voltage system for urban area power supply. In: *2014 IEEE PES T&D Conference and Exposition*. Chicago, IL, USA : IEEE, 2014 — ISBN 978-1-4799-3656-4, S. 1–5

[SMPP95] SCHONWETTER, G. ; MAGELE, C. ; PREIS, K. ; PAUL, C. ; RENHART, W. ; RICHTER, K.R.: Optimization of SMES solenoids with regard to their stray fields. In: *IEEE Transactions on Magnetics* Bd. 31 (1995), Nr. 3, S. 1940–1943

[SnGK05] SNITCHLER, GREG ; GAMBLE, BRUCE ; KALSI, SWARN S: The performance of a 5 MW high temperature superconductor ship propulsion motor. In: *IEEE Transactions on Applied Superconductivity* Bd. 15 (2005), Nr. 2, S. 2206–2209

[SoII08] SO NOGUCHI ; INABA, Y. ; IGARASHI, H.: An Optimal Configuration Design Method for HTS-SMES Coils Taking Account of Thermal and Electromagnetic Characteristics. In: *IEEE Transactions on Applied Superconductivity* Bd. 18 (2008), Nr. 2, S. 762–765

[SSSW09] SANGYEOP KWAK ; SEYEON LEE ; SANGYEOP LEE ; WOO-SEOK KIM ; JI-KWANG LEE ; CHAN PARK ; JOONHAN BAE ; JUNG-BIN SONG ; U. A.: Design of HTS Magnets for a 2.5 MJ SMES. In: *IEEE Transactions on Applied Superconductivity* Bd. 19 (2009), Nr. 3, S. 1985–1988

[Ştef00] ŞTEFĂNESCU, FLORIAN: GEOMETRY OPTIMIZATION OF SMES COIL

[Stro74] STROWBRIDGE, T R: *Cryogenic refrigerators — an updated survey*, 1974

[Suna00] *Sunam*. URL http://i-sunam.com/home/index_en.php

[Supe00a] *SuperOx*. URL http://www.superox.ru/en/

[Supe00b] *SuperPower*. URL http://www.superpower-inc.com/content/2g-hts-wire

[SvYo80] SVIATOSLAVSKY, I.N. ; YOUNG, W.C.: Structural design features for commercial fusion power reactor magnet systems. In: *Nuclear Engineering and Design* Bd. 58 (1980), Nr. 2, S. 207–218

[SYHS08] SUGANO, M ; YOSHIDA, Y ; HOJO, M ; SHIKIMACHI, K ; HIRANO, N ; NAGAYA, S: Two different mechanisms of fatigue damage due to cyclic stress loading at 77 K for MOCVD-YBCO-coated conductors. In: *Superconductor Science and Technology* Bd. 21 (2008), Nr. 5, S. 054006

[Tana06] TANAKA, SHOJI: High-Temperature Superconductivity. In: *Jpn. J. Appl. Phys.* Bd. 45 (2006), Nr. 12, S. 14

[TBDV07] TIXADOR, P.. ; BELLIN, B.. ; DELEGLISE, M.. ; VALLIER, J.C. ; BRUZEK, C.E. ; ALLAIS, A.. ; SAUGRAIN, J.M.: Design and First Tests of a 800 kJ HTS SMES. In: *IEEE Transactions on Applied Superconductivity* Bd. 17 (2007), Nr. 2, S. 1967–1972

[TeRT02] TEN HAKEN, BENNIE ; RABBERS, JAN-JAAP ; TEN KATE, HERMAN HJ: Magnetization and AC loss in a superconductor with an elliptical cross-section and arbitrary aspect ratio. In: *Physica C: Superconductivity* Bd. 377 (2002), Nr. 1–2, S. 156–164

[Thev00] *Theva*. URL https://www.theva.com/

[THTY10] TAKEMATSU, T ; HU, R ; TAKAO, T ; YANAGISAWA, Y ; NAKAGOME, H ; UGLIETTI, D ; KIYOSHI, T ; TAKAHASHI, M ; U. A.: Degradation of the performance of a YBCO-coated conductor double pancake coil due to epoxy impregnation. In: *Physica C: Superconductivity and its applications* Bd. 470 (2010), Nr. 17–18, S. 674–677

[Tixa10] TIXADOR, PASCAL: Development of superconducting power devices in Europe. In: *Physica C: Superconductivity and its Applications* Bd. 470 (2010), Nr. 20, S. 971–979

[Tixa95] TIXADOR, PASCAL: *Les supraconducteurs* : Ed. Techniques Ingénieur, 1995

[TsNS02] TSUTSUI, H. ; NOMURA, S. ; SHIMADA, R.: Optimization of SMES coil by using virial theorem. In: *IEEE Transactions on Appiled Superconductivity* Bd. 12 (2002), Nr. 1, S. 800–803

[Ullr95] ULLRICH, G.W.: Summary of the DNA SMES development program. In: *IEEE Transactions on Appiled Superconductivity* Bd. 5 (1995), Nr. 2, S. 416–421

[VDWK15] VAN NUGTEREN, J ; DHALLÉ, M ; WESSEL, S ; KROOSHOOP, E ; NIJHUIS, AREND ; TEN KATE, H: Measurement and analysis of normal zone propagation in a ReBCO coated conductor at temperatures below 50 K. In: *Physics procedia* Bd. 67 (2015), S. 945–951

[ViMT01] VINCENT-VIRY, O. ; MAILFERT, A. ; TRASSART, D.: New SMES coil configurations. In: *IEEE Transactions on Appiled Superconductivity* Bd. 11 (2001), Nr. 1, S. 1916–1919

[ViVS07] VINOD, K ; VARGHESE, NESON ; SYAMAPRASAD, U: Superconductivity of $MgB_2$ in the BCS framework with emphasis on extrinsic effects on critical temperature. In: *Superconductor Science and Technology* Bd. 20 (2007), Nr. 10, S. R31–R45

[VKBB18] VAN NUGTEREN, JEROEN ; KIRBY, GLYN ; BAJAS, HUGO ; BAJKO, MARTA ; BALLARINO, AMALIA ; BOTTURA, LUCA ; CHIUCHIOLO, ANTONELLA ; CONTAT, PA ; U. A.: Powering of an HTS dipole insert-magnet operated standalone in helium gas between 5 and 85 K. In: *Superconductor science and technology* Bd. 31 (2018), Nr. 6, S. 065002

[VRRK99] VENKATARATNAM, K ; RAO, VV ; RAO, KNV SUBBA ; KUMAR, A ARUN: Optimum design of superconducting magnet coil for a micro SMES unit. In: *IEEE transactions on applied superconductivity* Bd. 9 (1999), Nr. 2, S. 350–353

[Wils83] WILSON, MARTIN N: Superconducting magnets (1983)

[WMSS00] WADA, K ; MEGURO, S ; SAKAMOTO, H ; SHIMADA, T ; NAGASU, Y ; INOUE, I ; TSUNODA, K ; ENDO, S ; U. A.: Development of high-strength and high-RRR aluminum-stabilized superconductor for the ATLAS thin solenoid. In: *IEEE Transactions on applied superconductivity* Bd. 10 (2000), Nr. 1, S. 373–376

[WMSY00] WADA, KATSUNORI ; MEGURO, SHINICHIRO ; SAKAMOTO, HISAKI ; YAMAMOTO, AKIRA ; MAKIDA, YASUHIRO: High-strength and high-RRR Al-Ni alloy for aluminum-stabilized superconductor. In: *IEEE Transactions on applied superconductivity* Bd. 10 (2000), Nr. 1, S. 1012–1015

[WNHA15] WATANABE, TOMONORI ; NAGAYA, SHIGEO ; HIRANO, NAOKI ; AWAJI, SATOSHI ; OGURO, HIDETOSHI ; TSUCHIYA, YUJI ; OMURA, TAKUYA ; NIMORI, SHIGEKI ; U. A.: Strengthening effect of “Yoroi-coil structure” against electromagnetic force. In: *IEEE Trans. Appl. Supercond.* Bd. 25 (2015), Nr. 3

[XRTX17] XU, YING ; REN, LI ; TANG, YUEJIN ; XU, CHEN ; ZHANG, ZHONGPING ; CHEN, WEI ; LI, JINGDONG ; SHI, JING ; U. A.: A Study on the Design and Comparison of 1–100-MJ-Class SMES Magnet With Different Coil Configurations. In: *IEEE Transactions on Applied Superconductivity* Bd. 27 (2017), Nr. 5, S. 1–9

[YaMY95] YAMAOKA, H ; MIYATA, K ; YANO, O: Cryogenic properties of engineering plastic films. In: *Cryogenics* Bd. 35 (1995), Nr. 11, S. 787–789

[YIUO17] YANAMOTO, TOSHIYUKI ; IZUMI, MITSURU ; UMEMOTO, KATSUYA ; ORYU, TAMAMI ; MURASE, YOUHEI ; KAWAMURA, MASAHIDE: Load Test of 3-MW HTS Motor for Ship Propulsion. In: *IEEE Transactions on Applied Superconductivity* Bd. 27 (2017), Nr. 8, S. 1–5

[YKCL16] YOON, SANGWON ; KIM, JAEMIN ; CHEON, KYEKUN ; LEE, HUNJU ; HAHN, SEUNGYONG ; MOON, SEUNG-HYUN: 26 T 35 mm all-GdBa2Cu3O7–x multi-width no-insulation superconducting magnet. In: *Superconductor Science and Technology* Bd. 29 (2016), Nr. 4, S. 04LT04

[YMYO02] YAMAMOTO, A ; MAKIDA, Y ; YAMAOKA, H ; OHMIYA, H ; TANAKA, K ; HARUYAMA, T ; YOSHIDA, T ; YOSHIMURA, K ; U. A.: A thin superconducting solenoid magnet for particle astrophysics. In: *IEEE transactions on applied superconductivity* Bd. 12 (2002), Nr. 1, S. 438–442

[ZiYo17] ZIMMERMANN, ANDREAS W ; YOUNG, EDWARD A: Review of the State of the Art Superconducting Magnetic Energy Storage (SMES) in Renewable/Distributed Energy Systems (2017)

# Appendix

# APPENDIX A

## A-1.

Script (Matlab) to calculate the stresses in a solenoid according to the Wilson's formula (taken from WILSON, Martin N. Superconducting magnets. 1983).

```
Bmax=11.4% Axial B field at inner turn
Bext=-0.8% Axial B field at outer turn
J=520% Engineering current density
R=96% Internal radius (mmm)
EP=24% Thickness of the winding

v=0.32; % Poisson's ratio
R_a=R;
R_b=R+EP;
alpha=R_b/R_a;
K=(alpha*Bmax-Bext)*J*R_a/(alpha-1);
M=(Bmax-Bext)*J*R_a/(alpha-1);

N=200; % Number of discretization elements
for i=1:N+1
    r(i)=R_a+(R_b-R_a)*(i-1)/N; % Radius
    e=r(i)/R_a;
    epsilon(i)=e;

    B(i)=Bmax-(Bmax-Bext)*(i-1)/N;

    % Circumferential stress:
    sigma_theta(i)=(K*(2+v)/(3*(alpha+1))*(alpha^2+alpha+1+(alpha^2)/(e^2)-
e*(1+2*v)*(alpha+1)/(2+v)) - M*(3+v)/8*(alpha^2+1+(alpha^2)/(e^2)-
(1+3*v)/(3+v)*e^2))/1000;

    % Radial stress:
    sigma_r(i)=(K*(2+v)/(3*(alpha+1))*(alpha^2+alpha+1-(alpha^2)/(e^2)-
(alpha+1)*e) - M*(3+v)/8*(alpha^2+1-(alpha^2)/(e^2)-e^2))/1000;

    JBR(i)=J*B(i)*r(i)*1e-3;
end
```

# A-2.

Script (Matlab) to calculate the stresses resulting of the cooling down of a thermo-mechanically anisotropic solenoid. The formula comes from the article of V. Arp: “Stresses in superconducting solenoids)

```
% Formulas taken from ARP, V. Stresses in superconducting solenoids.
Journal of Applied Physics, 1977, vol. 48, no 5, p. 2026-2036.

Er=17e9% Radial Young modulus
Etheta=132e9;% Circumferential Young modulus
Poisson_theta_r=0.33; % Poisson's ratio
a=0.096; % internal radius (m)
b=0.120; % external radius (m)

l_r=-0.00480; % Radial thermal expansion (RT->4.2 K)
l_theta=-0.0029;% Circumferential thermal expansion (RT->4.2 K)

R=1/Er;
L=1/Etheta;
V=0;
k=(R/L)^(1/2);

N=1000; % Number of discretization elements

for i=1:(N+1)
r(i)=a+(b-a)*(i-1)/N;
end

c=(k*L-V)/(L*(b^k*a^(-k)-a^k*b^(-k)))*(l_r-l_theta)*(a*b^(-k)-b*a^(-k))/(1-
k^2);
d=(k*L+V)/(L*(b^k*a^(-k)-a^k*b^(-k)))*(l_r-l_theta)*(a*b^(k)-b*a^(k))/(1-
k^2);

for i=1:(N+1)

Sigma_r(i)=((c*(r(i)^(k-1))/(k*L-V))-(d*(r(i)^(-k-1))/(k*L+V)))+((l_r-
l_theta)/(L*(1-k^2)));

Sigma_theta(i)=(k*c*(r(i)^(k-1))/(k*L-V))+(k*d*(r(i)^(-k-
1))/(k*L+V))+((l_r-l_theta)/(L*(1-k^2)));

end
```

# A-3.

Script (Matlab) to calculate the stresses resulting of the winding under tension of a solenoid. The formula comes from the article of V. Arp: “Stresses in superconducting solenoids”.

Values of the parameters used in this calculation:

| | value | Unit |
|---|---|---|
| ID (Internal Diameter) mandrel | 58 | mm |
| ID winding | 60 | mm |
| ID reinforcement | 113.1 | mm |
| External diameter | 113.4 | mm |
| Nturns cowinding | 253 | |
| Nturns reinforcement | 5 | |
| Stress Cowinding | 50 | MPa |
| Stress reinforcement | 200 | MPa |
| E mandrel | 190 | GPa |
| E average cowinding | 172 | GPa |
| E reinforcement | 190 (used: 172) | GPa |
| Thickness REBCO tape | 75 | um |
| Thickness Stain. Steel tape | 30 | um |

Code:

```
% Formulas taken from ARP, V. Stresses in superconducting solenoids.
Journal of Applied Physics, 1977, vol. 48, no 5, p. 2026-2036.

Er=172e9;% radial Young modulus
Etheta=172e9;% Circumferential Young modulus
a=60e-3/2; % Inner radius
b=113.4e-3/2; % Outer radius
B=0.63e10 % Apparent radial Young modulus of the mandrel
Poisson_theta_r=0.33; % Poisson's ratio


N1=(253*(30+75)/5); %Number of discretization element in the
superconducting cowinding (1 node/5um)
N2=5*30/5; %Number of discretization element in the additional stainless
steel winding (1 node/5um)
N=N1+N2;

%Definition of the winding tension
for i=1:N1
Prestress(i)=50e6;% Winding tension (MPa)
end
for i=N1+1:N1+N2+1
Prestress(i)=200e6; %Winding tension (MPa)
end

R=1/Er;
L=1/Etheta;
V=0;
k=(R/L)^(1/2);
```

```
for i=1:(N+1)
r(i)=a+(b-a)*(i-1)/N;
end

for i=1:(N)
% Calculation of the integral I for each of the N points
% The average value between 2 points is used for r and Prestress
Integ(i)=(a*0.5*(Prestress(i)+Prestress(i+1))*((b/a-
1)/N))/((1+B*(k*L+V))*(0.5*(r(i)+r(i+1))/a)^k-(1-B*(k*L-
V))*(0.5*(r(i)+r(i+1))/a)^(-k));
end

I(N+1)=0;
for i=N:-1:1
I(i)=I(i+1)+Integ(i);
end

for i=1:(N+1)
C(i)=-(1+B*(k*L-V))*((r(i)/a)^k)*I(i);
D(i)=-(1-B*(k*L-V))*((a/r(i))^k)*I(i);

% Radial Stress:
Sigma_r(i)=(C(i)-D(i))/r(i);

% Hoop stress
Sigma_theta(i)=Prestress(i)+(k*(C(i)+D(i))/r(i));

%Radial displacement:
u(i)=(k*L-V)*C(i)+(k*L+V)*D(i);

end
```

# APPENDIX B

# B-1: Complementary data to the ones presented in Fig. 70 (part II-2.2.2)

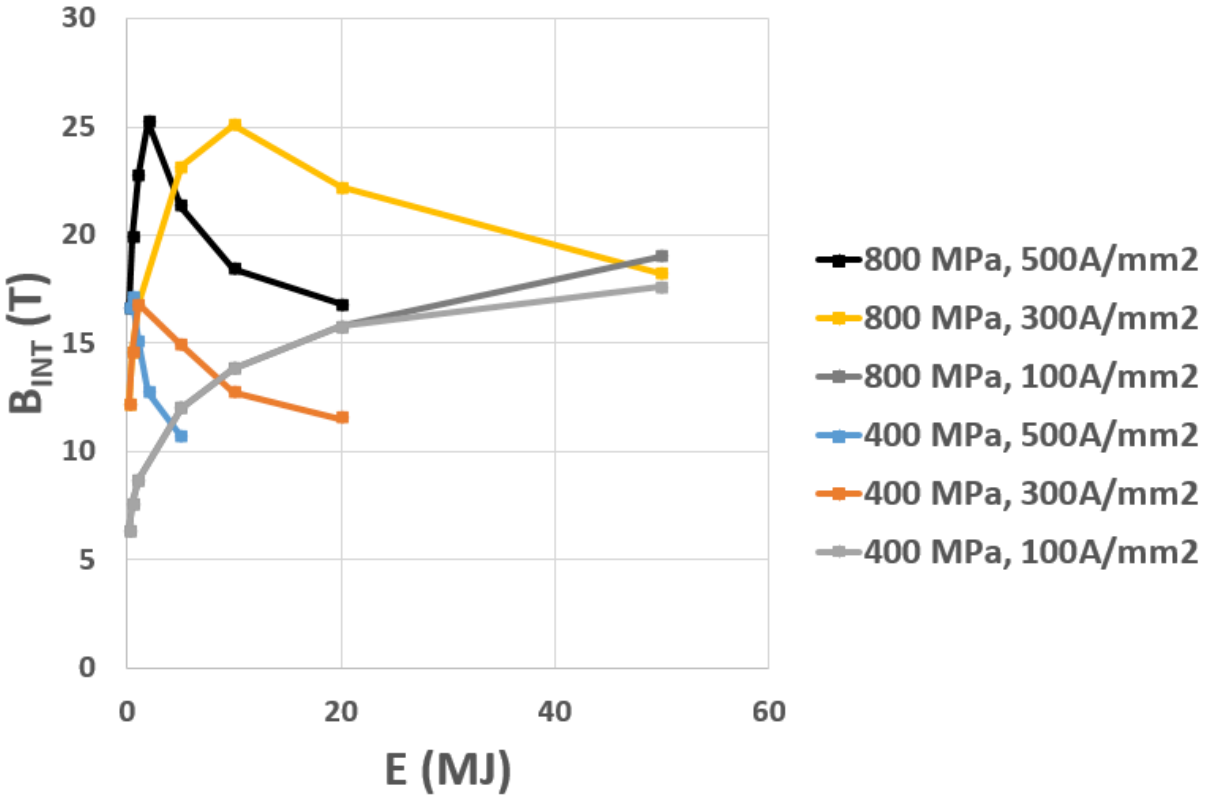


*Figure B-1. 1: Evolution of the magnetic field $B_{INT}$ at the inner radius and mid-plane of the solenoid. These data are corresponding to the ones presented in the Fig. 70, i.e. these are the values of $B_{INT}$ of the solenoids maximizing the specific energy while respecting a given maximum hoop stress. We can see that as far as $\alpha$=0.5 and $\beta$=1, the value of $B_{INT}$ increases as the power 1/5 of the stored energy (see eq. 37 and 38), then $B_{INT}$ decreases.*

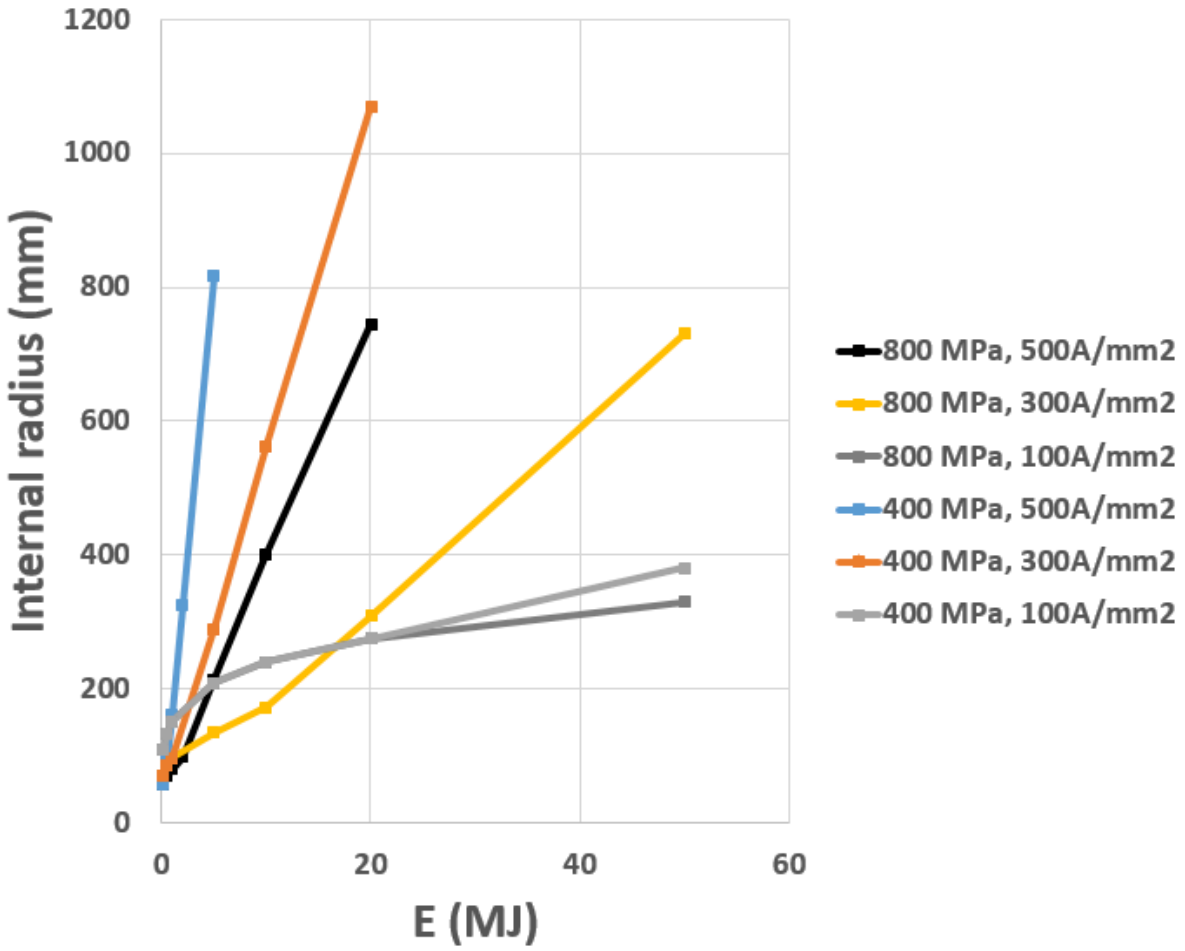


*Figure B-1. 2: Evolution of the inner radius of the solenoids. These data are corresponding to the ones presented in Fig. 70. As far as α=0.5 and β=1, the value of R increases as the power 1/5 of the stored energy (see eq. 38), then it increases more sharply.*

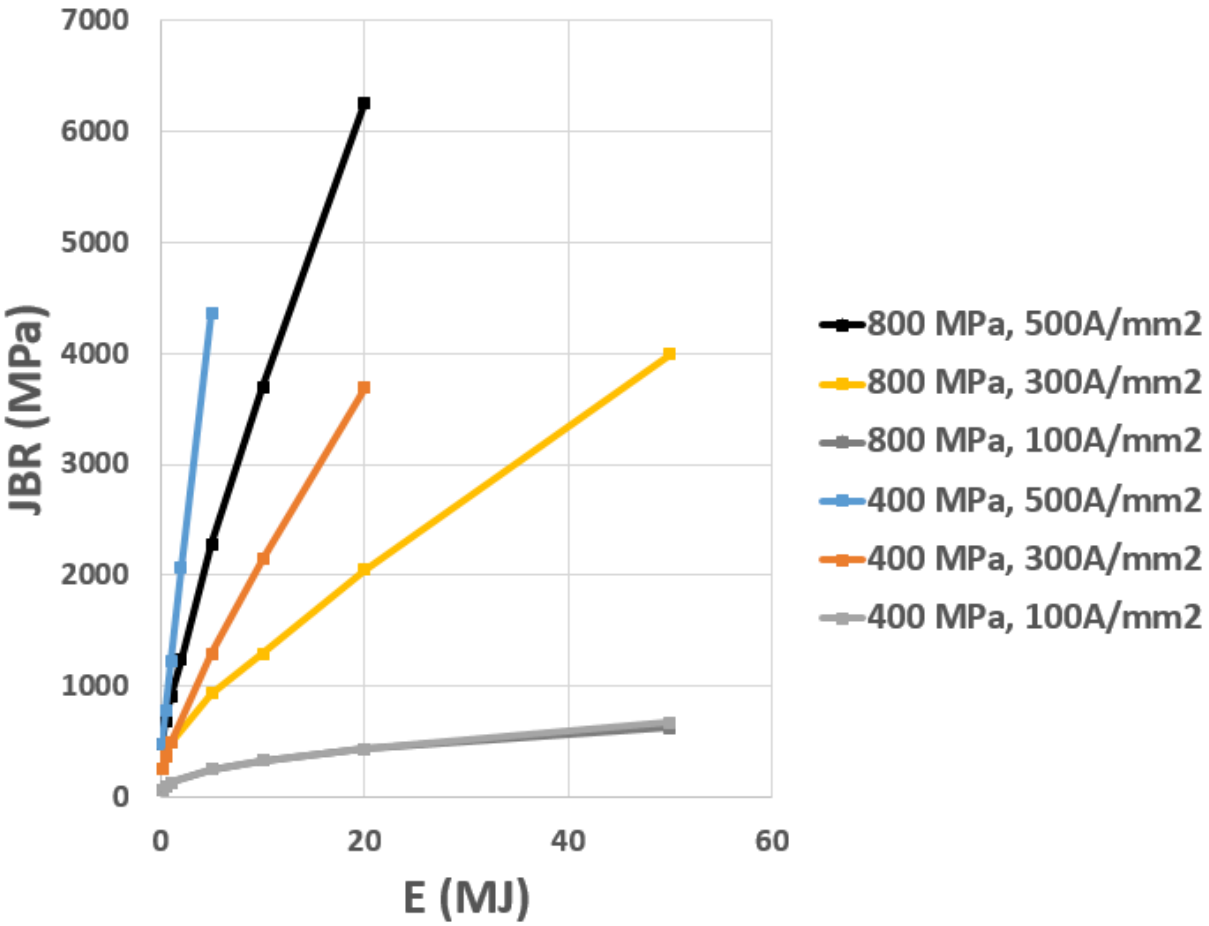


*Figure B-1. 3: Evolution of the JBR value (product of the current density by the B field by the radius) at the inner radius and mid-plane of the solenoids. These data are corresponding to the ones presented in Fig. 70. We can see that the JBR value is much higher than the hoop stress, which is always lower or equal to 400 MPa or 800 MPa depending on the considered curves. It means that the centrifugal magnetic force is very efficiently distributed in the whole structure by radial stress.*

# B-2: Complementary data to the ones presented in part II-2.2.3

The ratios of stresses presented in this annexe only depends on the topology of the solenoid (with rectangular cross section), i.e. it depends only on α and β. In other words, these data are valid whatever is the size or the current density of the solenoid. From the mechanical point of view, they are valid as far as the material of the body of the solenoid has a linear and isotropic stress/strain relation law.

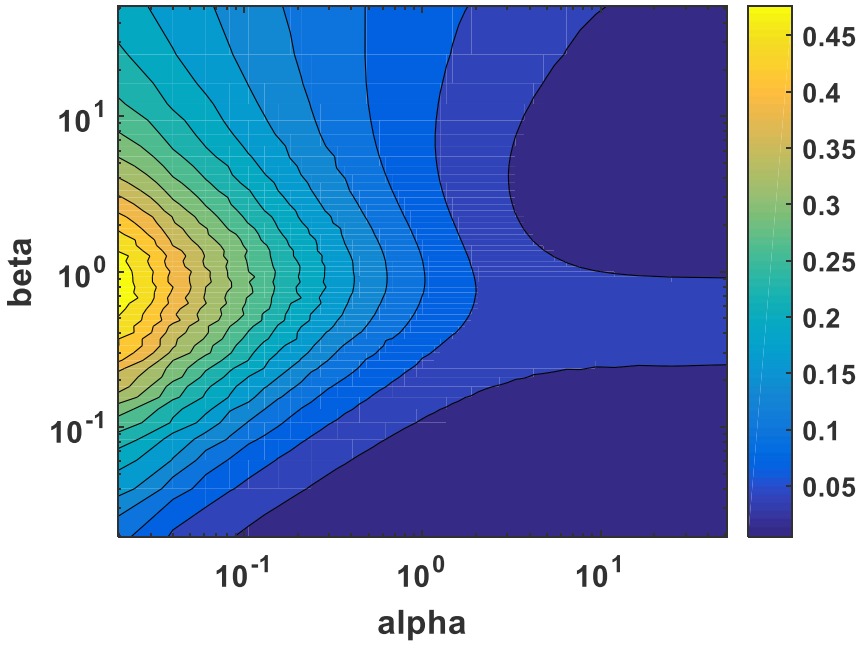


*Figure B-2. 1: Ratio between the maximal compressive radial stress and the maximum hoop stress calculated by the Wilson formula. The maximum of the hoop stress calculated by the Wilson formula is always reached at the inner radius of the solenoid. We can see that for some topologies, the compressive radial stress is not negligible compared to the hoop stress*

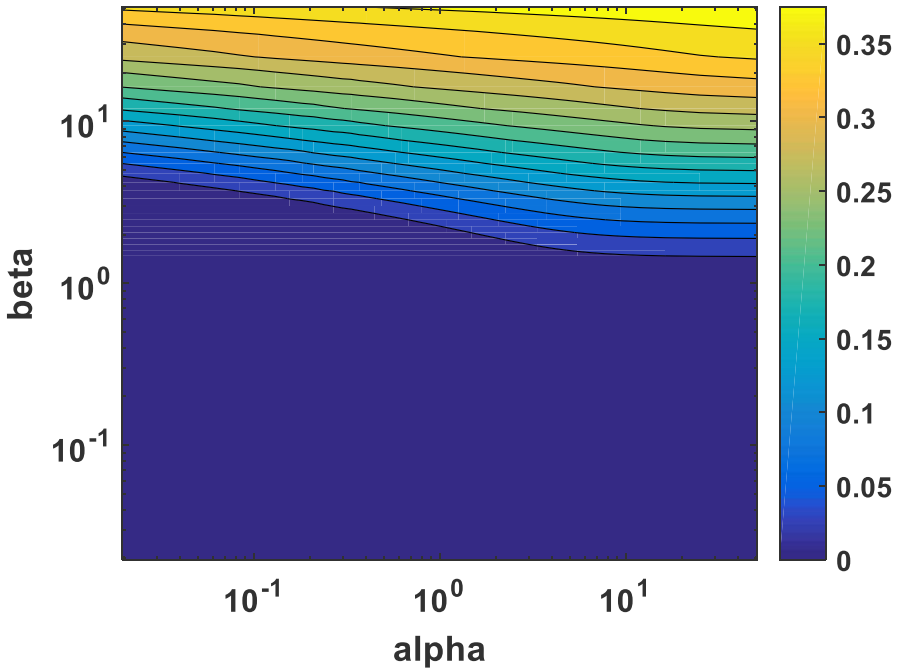


*Figure B-2. 2: Ratio between the maximal tensile radial stress and the maximum hoop stress calculated by the Wilson formula. For thin solenoids, the radial stress in the solenoid is only compressive. Having tensile radial stress increases the hoop stress. So solenoids with tensile radial stress should better be split in 2 independent solenoids.*

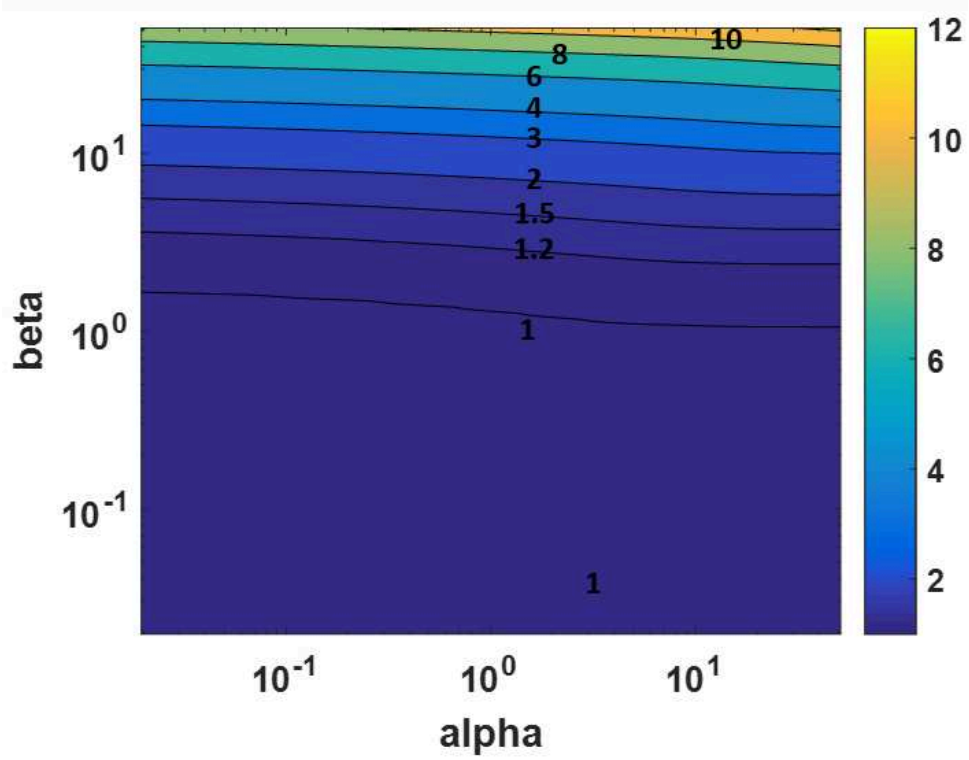


*Figure B-2. 3: Ratio of the maximum value of the JBR formula (across the mid-plane of the solenoid) and the value of JBR at the inner radius (and mid-plane) of the solenoid. We can see that for thick solenoids, the maximum value of JBR is not reached at the inner radius of the solenoid. This kind of situation is illustrated by the next figures.*

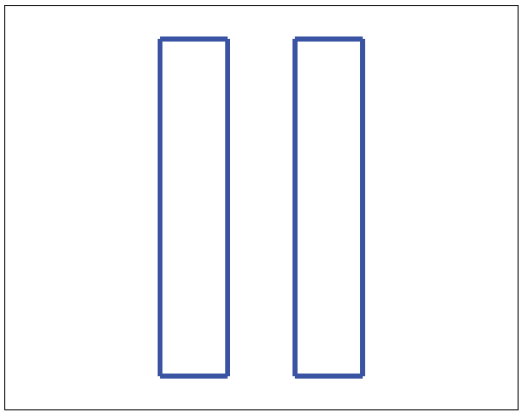

*Figure B-2. 4: Aspect ratio of a solenoid with α = 5 and β = 2.*

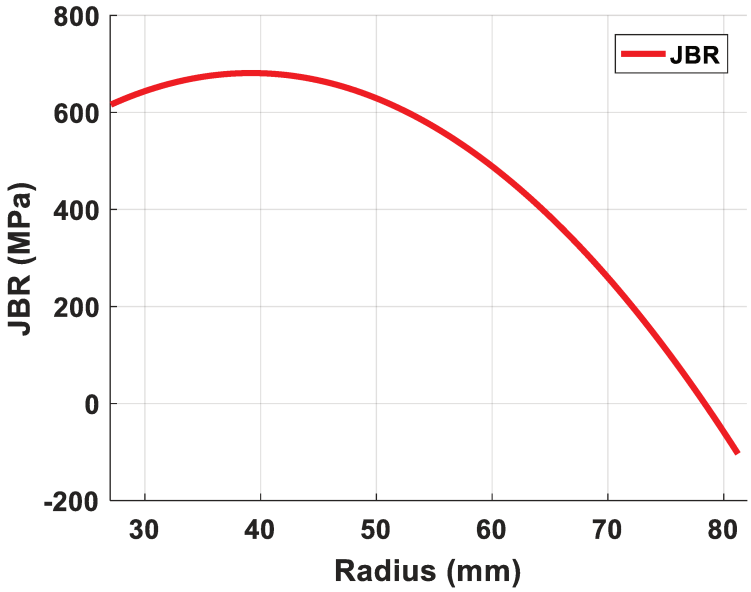


*Figure B-2. 5: Value of JBR along the cross section (at mi-plane) of a solenoid with α = 5 and β = 2. E=1 MJ and J=600 A/mm$^2$. We can see that the maximum of JBR is not reached at the internal radius.*

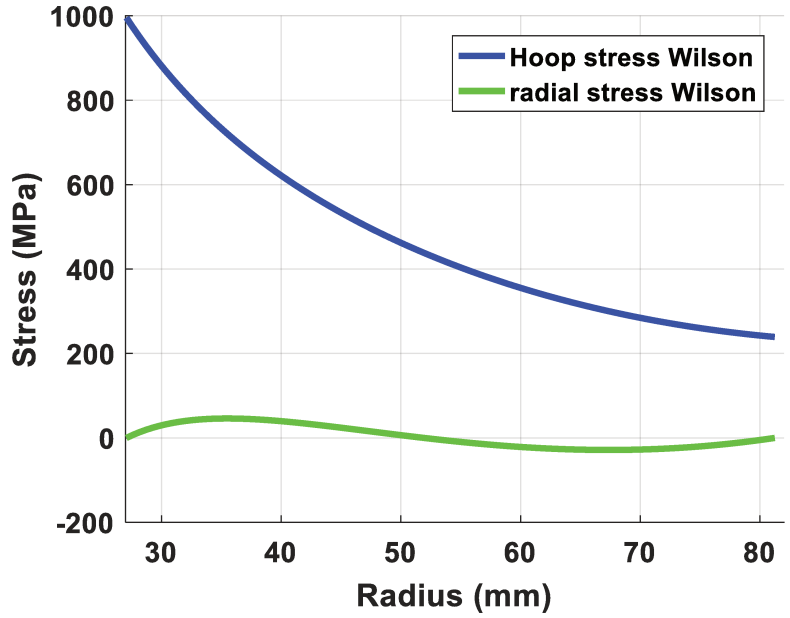


*Figure B-2. 6: Value of hoop stress and radial stress calculated by the Wilson formula along the cross section (at mi-plane) of a solenoid with α = 5 and β = 2. E=1 MJ and J=600 A/mm². We can see that the inner part of the solenoid is in radial traction (positive radial stress). Because of that, the hoop stress is higher than the JBR formula.*

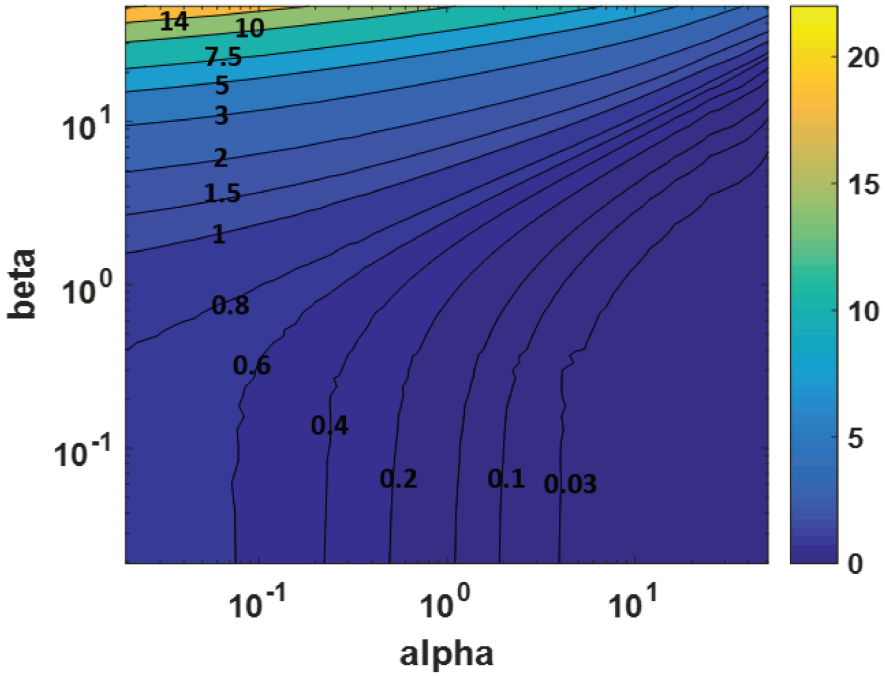


*Figure B-2. 7: Ratio of the amplitude of the compressive JBR at the outer radius of the solenoid (at mid-plane) and the value of JBR (tensile) at the inner radius of the solenoid (at mid-plane). We can see that the amplitude of JBR can be much higher at outer radius than at inner radius. Of course, the resulting forces on the body of the solenoid are always centrifugal forces, because the JBR at inner turn are not necessary the maximum value of JBR (see above).*

# B-3: Complementary information to part II-2.4.1

**Method to obtain data with constant energy and constant maximum hoop stress on a large set of topologies**

From part II-1-3, we know the following equations:

$$E = \lambda^5 \, \zeta^2 E_0$$

$$\vec{\sigma}(\lambda x_0, \lambda y_0, \lambda z_0) = \lambda^2 \, \zeta^2 \, \vec{\sigma}_0(x_0, y_0, z_0)$$

From these 2 equations above, if the energy is fixed, that the maximum hoop stress is fixed and that α and β are fixed, then λ and ζ are determined, hence J and R are determined.
For each (α, β) couple, we suppose that R=R0 and J =J0, where R0 and J0 are arbitrary values. We calculate the values E_tempo and σ_hoop_tempo, which are the energy and the maximum hoop stress calculated for R=R0 and J =J0. The values of R and J which will give an energy equal to E_target (1 MJ) and a hoop stress equal to σ_hoop_target are given by the following equations:

R=(( E_target / E_tempo * σ_hoop_tempo / σ_hoop_target)^(1/3))*R0;

J= (σ_hoop_target / σ_hoop_tempo *((R0/R)^2))^(1/2)*J0;

Once that R and J are determined, other physical parameters are calculated.

**Method to obtain data with constant energy and constant J/Jc(B_INT) on a large set of topologies**

From part II-1-3, we know the following equations:

$$E = \lambda^5 \, \zeta^2 E_0$$

$$\vec{B}(\lambda x_0, \lambda y_0, \lambda z_0) = \lambda \, \zeta \, \vec{B}_0(x_0, y_0, z_0)$$

Additionally, there is a relation between the critical current $J_C$ and the B field. From these 2 equations above and given the relation between Jc and B, then if the energy is fixed, if J/Jc is fixed and that α and β are fixed, then λ and ζ are determined, hence R and J (or B) are determined.
To determine the relation between Jc and B, we are using the data from T. Benkel et al. (See part. I-1.3.1). These data have been obtained by measurements on 4 mm wide REBCO tape from SuperOx®. These data can be very well fitted by a Kim law [Tixa95]. If the field B is parallel to the tape, the critical current is given by

$I_c$=1450 / (1+B/20)

If we suppose that the thickness of the tape is 95 um, then the critical current density in A/mm$^2$ is given by

$J_c$=1450 /(4*0.095* (1+B/20))

For each (α, β) couple, we suppose that R=R0 and J =J0, where R0 and J0 are arbitrary values. We calculate the values E_tempo and B_INT_tempo, which are the energy and the internal B field calculated for R=R0 and J =J0.

A and K are defined by the following equations,
A=((E_target/ E_tempo *J0^2)^(1/5))* B_INT_tempo /J0
K=JJc_target*1450/(4*0.095)

Where JJc_target is the desired ratio between the current density and the critical current density. JJc_target is smaller than 1.
We need to solve the following equation:
B_INT*(1+B_INT/20)^(3/5)-A*K^(3/5)=0
This equation is solved numerically.
The values of R and J which will give an energy equal to E_target (1 MJ) and a ratio J/Jc equal to JJc_target are given by the following equations:

```
J= K/(1+ B_INT /20);
R=R0* B_INT/ B_INT _tempo*J0/J;
```

Once that R and J are determined, other physical parameters are calculated.

# B-4: Complementary data to Fig. 82 (See part II-2.4)

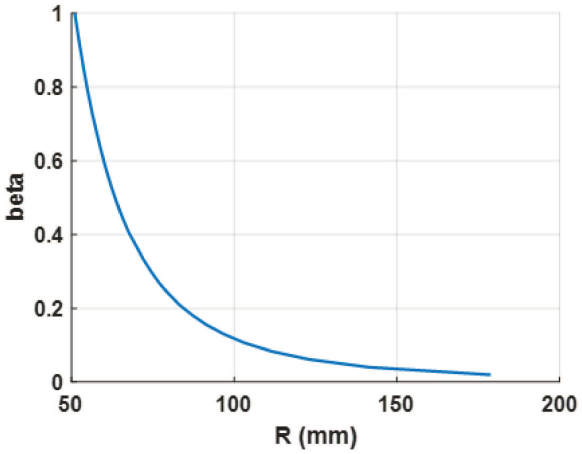


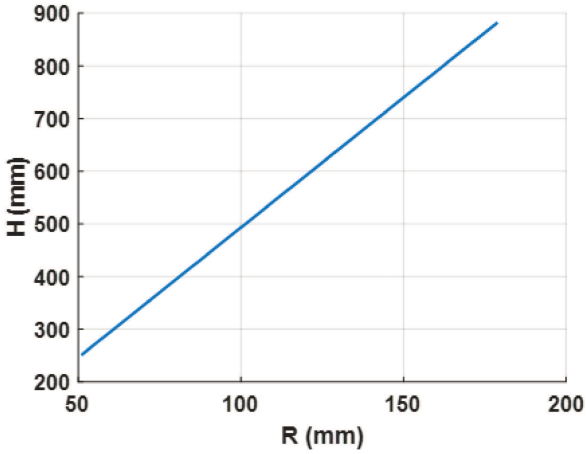


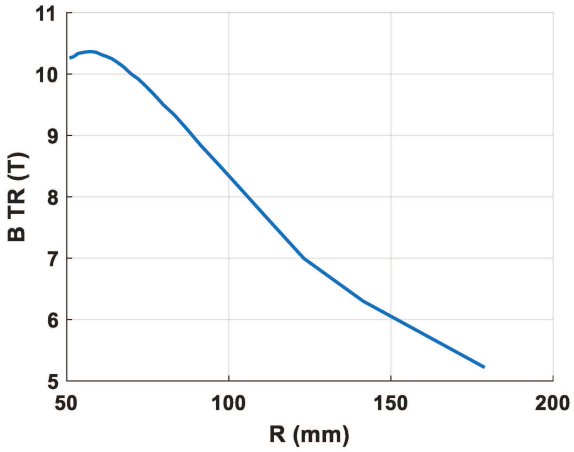


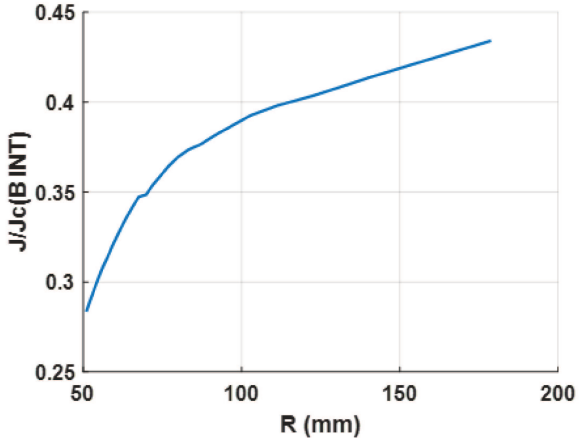


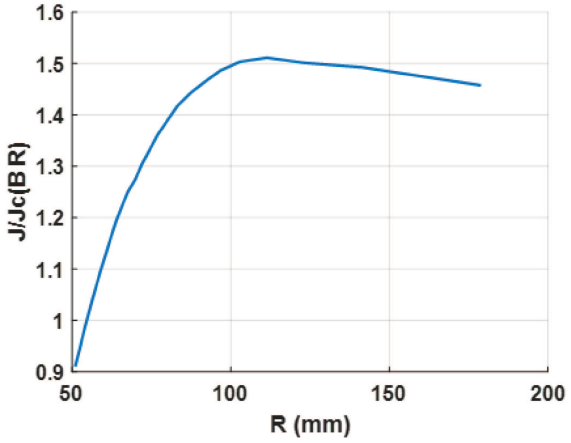

# B-5: Plans of a double pancake

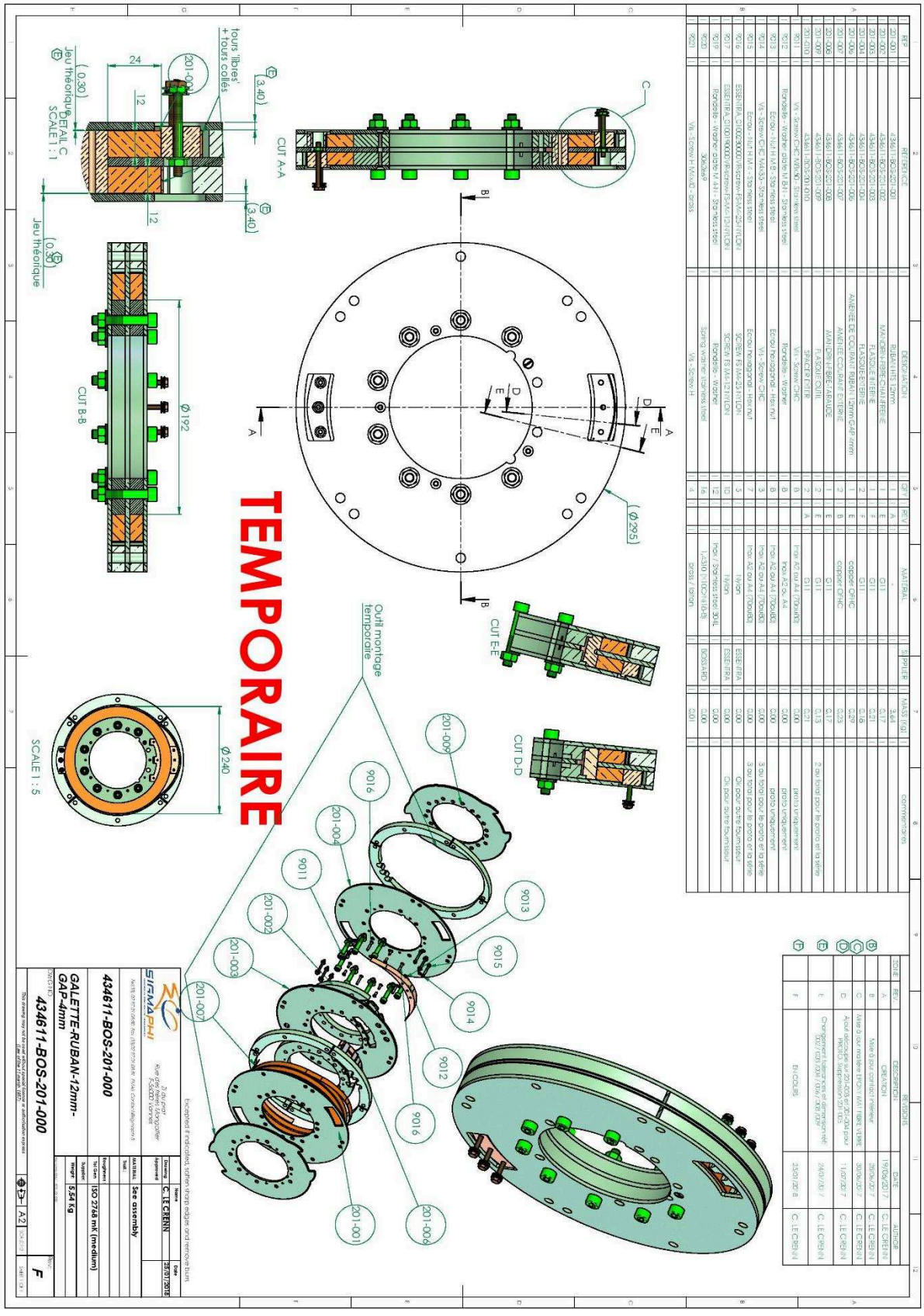

# B-6: Plans of the SMES

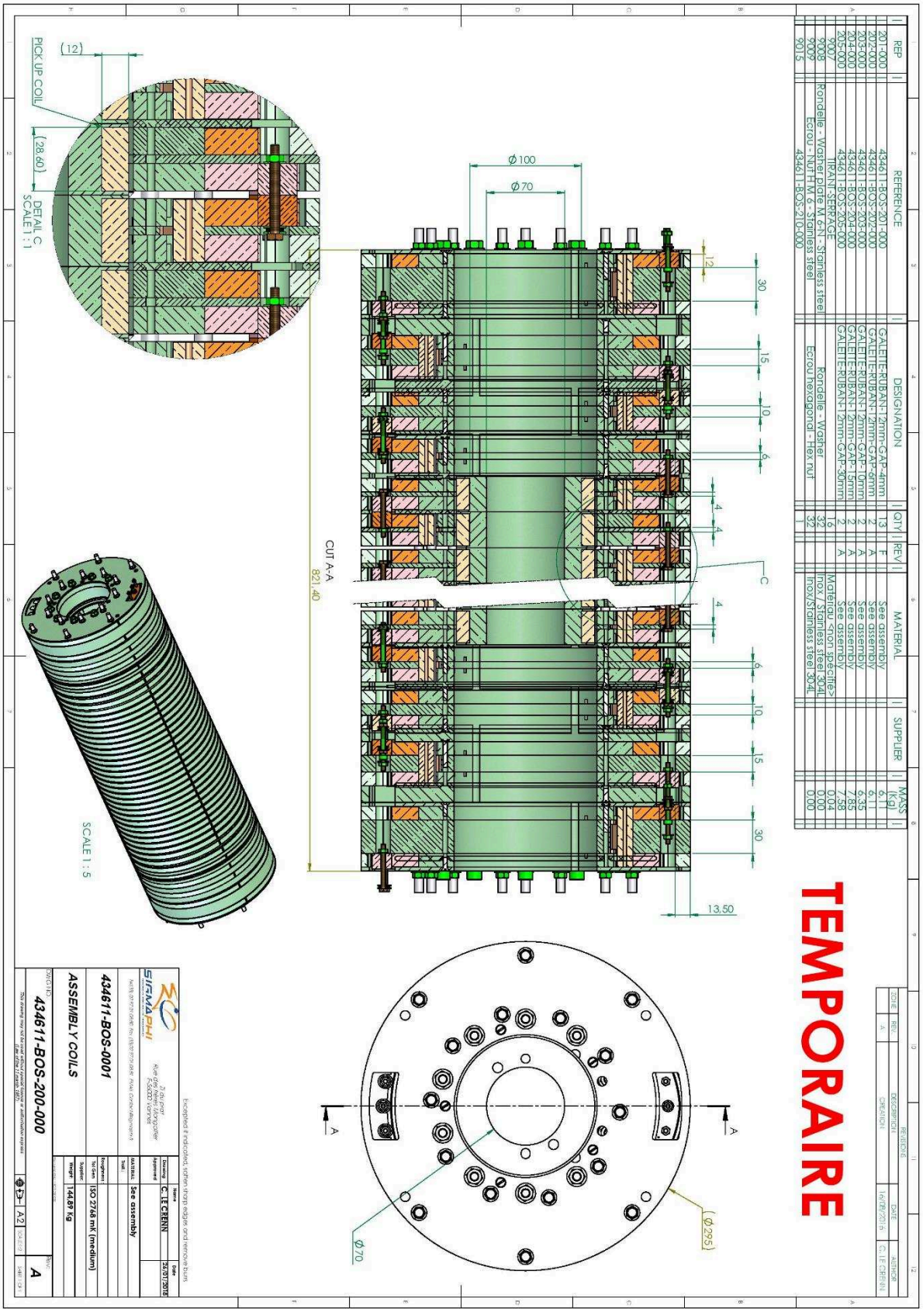


| REP | REFERENCE | DESIGNATION | QTY | REV | MATERIAL | SUPPLIER | MASS (kg) |
|---|---|---|---|---|---|---|---|
| 201-000 | 434611-BOS-201-000 | GALETTE-RUBAN-12mm-GAP-4mm | 13 | F | See assembly | | 6.11 |
| 202-000 | 434611-BOS-202-000 | GALETTE-RUBAN-12mm-GAP-6mm | 2 | A | See assembly | | 6.11 |
| 203-000 | 434611-BOS-203-000 | GALETTE-RUBAN-12mm-GAP-10mm | 2 | A | See assembly | | 6.35 |
| 204-000 | 434611-BOS-204-000 | GALETTE-RUBAN-12mm-GAP-15mm | 2 | A | See assembly | | 7.85 |
| 205-000 | 434611-BOS-205-000 | GALETTE-RUBAN-12mm-GAP-30mm | 2 | A | See assembly | | 7.58 |
| 9007 | TIRANT-SERRAGE | | 16 | | Matériau <non spécifié> | | 0.04 |
| 9008 | Rondelle - Washer plate M 6-N - Stainless steel | Rondelle - Washer | 32 | | Inox / Stainless steel 304L | | 0.00 |
| 9009 | Ecrou - Nut H M 6 - Stainless steel | Ecrou hexagonal - Hex nut | 32 | | Inox/Stainless steel 304L | | 0.00 |
| 9015 | 434611-BOS-210-000 | | 1 | | | | 0.00 |

# APPENDIX C

## C-1 : Plans of the EuCARD probe

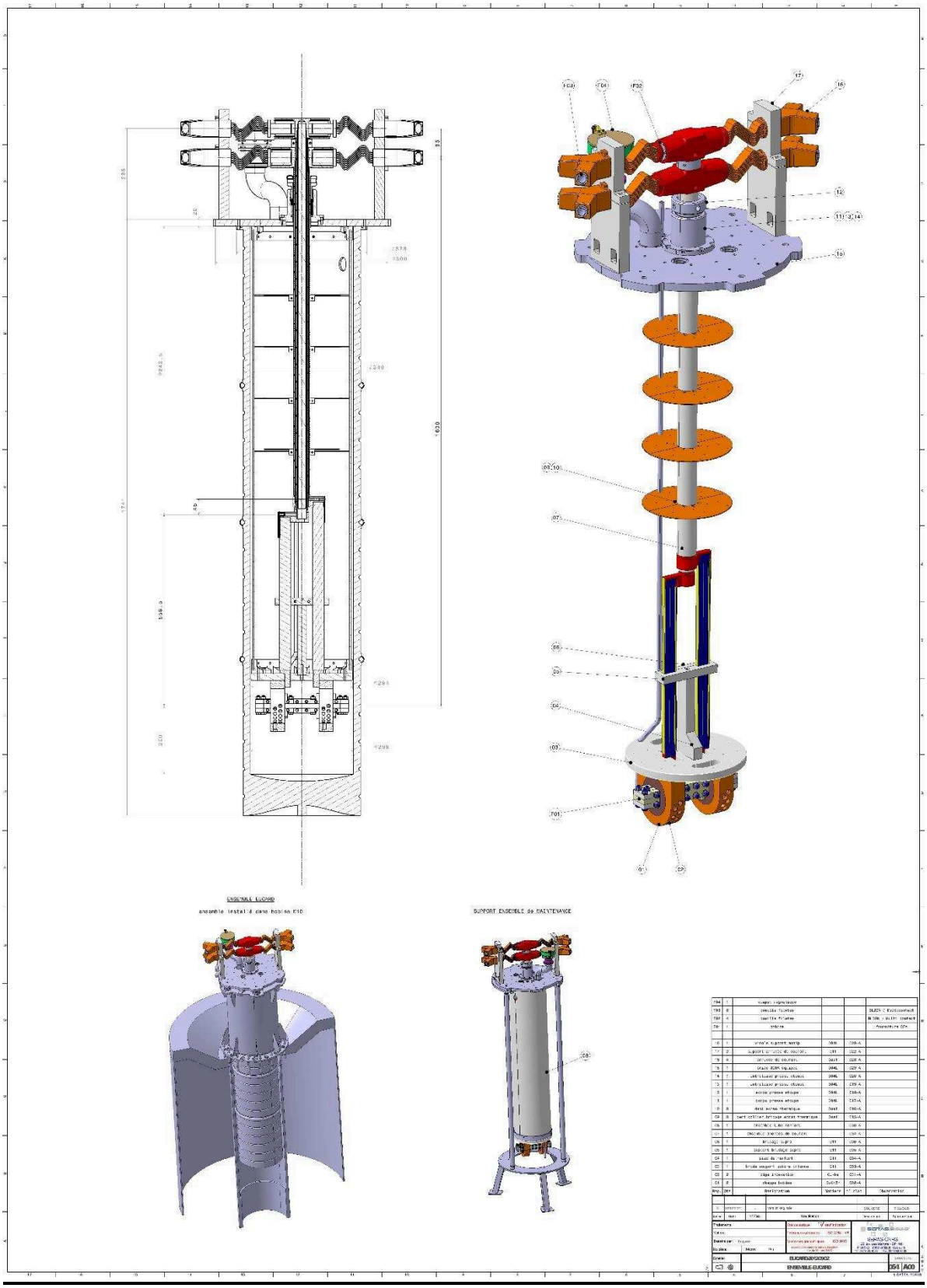

# C-2.

A difference between the tests on the prototype n°3 and the prototype n°4 is that a different current source was used in both cases. The Sorensen source was used in the first case and the “Bertha” source was used in the second case (see part III-1.1). The Bertha source was not optimized according to the inductance of our double pancake and had difficulty to regulate its current at low values. In tests without background field, the envelope of the voltage of the source was fluctuating in a way looking like the fluctuation of the value of the apparent inductance under field (see the figure below). This correlation can open an area of reflection to understand the behaviour of the curves in Fig. 134, but this is quite speculative.

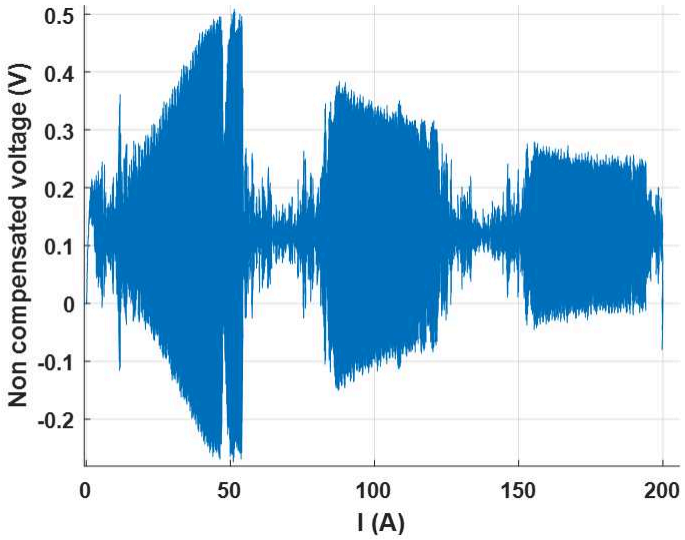


Non-filtered voltage of the Bertha source during a current ramp from 0 to 200 A, in self-field and at 4 A/s.

# Stockage d'Energie Magnétique par Supraconducteurs haute température critique de seconde génération

**Résumé:** En chargeant en courant une inductance supraconductrice, on stocke de l'énergie magnétique qui peut être déchargée à très haute puissance dans une charge. Ce système est appelé SMES pour Superconducting Magnetic Energy Storage. Le SMES est particulièrement adapté aux charges nécessitant un fort courant transitoire. Cette thèse s'inscrit dans le cadre du projet BOSSE, qui vise à mettre au point un démonstrateur de SMES dans la gamme du MJ. Ce SMES sera à la fois plus compacte que ses prédécesseurs et battra le record actuel d'énergie spécifique d'un bobinage supraconducteur en atteignant 20 kJ/kg. Cet objectif sera atteint grâce à l'utilisation de supraconducteurs haute température critique de seconde génération, dits conducteurs « REBCO ».
Cette thèse aborde de manière générale la problématique du design de SMES et propose des éléments de réflexion et des solutions pour un pré-design rapide du bobinage d'un SMES. Le design du SMES à haute densité d'énergie du projet BOSSE est détaillé.
Des éléments modulaires (galettes de ruban REBCO) du SMES ont été fabriqués et testés en champ propre et sous champ magnétique externe. Les méthodes et les résultats de détection de transition des galettes de l'état supraconducteur vers l'état normal sont présentés. Ces détections ont permis de garantir l'intégrité des galettes REBCO lors de transitions, même à très forte densité de courant (980 A/mm$^2$ dans le conducteur nu).
Ce travail est soutenu par la DGA (Direction Générale de l'Armement).

**Mots clefs:** *SMES, Supraconducteurs Haute Température Critique, Bobine supraconductrice, REBCO, Stockage d'énergie, Protection de bobinages supraconducteurs.*

---

# Superconducting Magnetic Energy Storage with second generation high temperature superconductors

**Abstract:** Magnetic energy is stored when a superconducting inductance is fed with current. This energy can be released with high power in a load. This principle is called SMES (Superconducting Magnetic Energy Storage). This kind of device is especially suitable when a high transient current is required. This PhD work has been conducted in the frame of the BOSSE project with the objective to develop a SMES demonstrator in the MJ range. This SMES will be especially compact and will reach a specific energy of 20 kJ/kg of winding, which is 50 % over the current world record for a superconducting coil. This performance is made possible by the use of 2$^{nd}$ generation high critical temperature superconductors, so-called "REBCO" conductors.
This work tackles the general problematic of SMES design and proposes elements of reflection and solutions for fast pre-design of a SMES winding. The design of the high specific energy SMES of the BOSSE project is presented in detail.
Modular elements (pancakes of REBCO tapes) of the SMES have been manufactured and tested in self-field and under background magnetic field. During these tests, transitions from superconducting state to normal state have been detected. These early detections have prevented the pancakes to be damaged when transitions occurred, even at very high current density (980 A/mm$^2$ in the bare conductor). The measurement method is presented, as well as the results of the tests.
The BOSSE project has been funded by the DGA (French Defence Procurement Agency).

**Keywords:** *SMES, High Critical Temperature Superconductors, Superconducting windings, REBCO, Energy storage, Protection of superconducting windings*